ENHANCING THE CONTROL OF TOKAMAKS VIA A CONTINUOUS NONLINEAR CONTROL LAW

THÈSE N^O 3034 (2004)

PRÉSENTÉE À LA FACULTÉ SCIENCES DE BASE

CRPP Association Euratom

SECTION DE PHYSIQUE

ÉCOLE POLYTECHNIQUE FÉDÉRALE DE LAUSANNE

POUR L'OBTENTION DU GRADE DE DOCTEUR ÈS SCIENCES

PAR

Jean-Yves FAVEZ

ingénieur électricien diplômé EPF
de nationalité suisse et originaire de Servion (VD)

accepteé sur proposition du jury:

Dr J. B. Lister, directeur de thèse
Prof. D. Bonvin, rapporteur
Prof A. Glattfelder, rapporteur
Dr A. Morris, rapporteur
Dr P. Muellhaupt, rapporteur
Prof. M. Q. Tran, rapporteur

Lausanne, EPFL
2004

Acknowledgements

During the completion of this thesis I was helped in different ways by many people. It is a pleasure to acknowledge some of those who contributed with their experience and support to this thesis work.

Firstly I thank my supervisor, Dr. Jo Lister, for his expertise, guidance and support in my work. His deep knowledge in the field of tokamaks in general and of tokamak control has been fundamental to this work.

Many thanks to Prof. Dominique Bonvin, Drs Philippe Mullhaupt and Bala Srinivasan from the Laboratoire d'Automatique at the EPFL for their precious expertise, advice, discussions and support in the field of control theory.

The work presented in the chapter dealing with AC losses (Chapter 5) results from a student diploma project carried out at the EPFL [46, 45]. I supervised this project, especially for everything that concerned control theory. Many thanks to my (now graduated) diploma student, Beat Schärz, for his essential contributions to this chapter and for his outstanding contributions to the topics of AC losses and control. In fact this is the first study which deals with the analysis of the effect of control on AC losses and which proposes a controller to reduce AC losses. I want to thank Dr. Pierluigi Bruzzone, who took time and effort to explain in a clear manner the basics of AC loss theory. Thanks are also due to Drs Yuri Gribov and Alfredo Portone for their support in providing the required technical information for the work described in this chapter.

Many thanks to Drs Victor Lukash, Rustam Khayrutdinov, Laurent Villard and Jean-Marc Moret for their help and advice concerning the DINA code description (Chapter 2).

Thanks are due to Drs A. Kavin and Y. Gribov for providing the linear tokamak model and the disturbances model for ITER-FEAT. Thanks to M. Ariola, A. Pironti and A. Portone for the reduced-order controller for the ITER-FEAT tokamak. Thanks to R. Albanese, G. Calabrò, F. Villone and M. Mattei for the CREATE-L model of JET and their shape controller.

Abstract

The control of the current, position and shape of an elongated cross-section tokamak plasma is complicated by the instability of the plasma vertical position. In this case the control becomes a significant problem when saturation of the power supplies is considered. Current saturation is relatively benign due to the integrating nature of the tokamak, resulting in a reasonable time horizon for strategically handling this problem. On the other hand, voltage saturation is produced by the feedback controller itself, with no intrinsic delay. In practice, during large plasma disturbances, such as sawteeth, ELMs and minor disruptions, voltage saturation of the power supply can occur and as a consequence the vertical position control can be lost. If such a loss of control happens the plasma displaces vertically and hits the wall of the vessel, which can cause damage to the tokamak. The consideration and study of voltage saturation is especially important for ITER. Due to the size and therefore the cost of ITER, there will naturally be smaller margins in the Poloidal Field coil power supplies implying that the feedback will experience actuator saturation during large transients due to a variety of plasma disturbances.

The next generation of tokamaks under construction will require vertical position and active shape control and will be fully superconducting. When the magnetic transverse field in superconducting magnets changes, the magnet generates two types of heat loss, the so-called coupling loss and the so-called hysteresis loss, grouped together as AC losses. Superconducting coils possess superconducting properties only below a critical temperature around a few K. AC losses are detrimental since they heat up the superconducting material. Thus, if AC losses are too large, the cryogenic plant can no longer hold the required temperature to maintain the superconductivity properties. Once the superconductivity is lost, the electric currents in the coils produce an enormous heat loss due to the ohmic resistivity, which can lead to a possible damage to the coils. In general, the coils are designed with enough margin to absorb all likely losses. A possible loss reduction could allow us to downsize the superconducting cross section in the cables, reducing the overall cost, or simply increase the operational cooling margin for given coils.

In this thesis we have tried to take into consideration these two major problems. The thesis is therefore focused on the following main objectives: i) the stability analysis of the tokamak considering voltage saturation of the power supplies and ii) the proposition of a new controller which enhances the stability properties of the tokamak under voltage saturation and iii) the proposition of a controller which takes into consideration the problem of reducing the AC losses. The subject of the thesis is therefore situated in an interdisciplinary framework and as a result the thesis is subdivided into two principal parts. The first part is devoted to tokamak physics and engineering, while the second part focuses on control theory.

In the tokamak physics and engineering part we present the linear tokamak models and the nonlinear tokamak code used for the controller design and the validation of the new proposed controller. The discussion is especially focused on the presence of a single unstable pole when the vertical plasma position is unstable since this characteristic is essential for the work presented in the control theory part.

In order to determine the enhancement of the stability properties we have to bring the new proposed controller to its stability limits by means of large disturbances. Validation by means of simulations with either linear or nonlinear tokamak models are imperatively required before considering the implementation of the new controller on a tokamak in

operation. A linear tokamak model will probably be inadequate since large disturbances can move its state outside its validity regions. A full nonlinear tokamak evolution code like DINA is indispensable for this purpose. We give a detailed description of the principal plasma physics implemented in the DINA code. Additionally, validation of DINA is provided by comparing TCV experimental VDE responses with DINA code simulations.

To allow a study of the AC losses reduction, the nature of the AC losses has to be reduced to a simplified form. We analyse to what extent the accumulated AC losses in ITER could be reduced by taking into account the losses themselves when designing the feedback control loops. In order to be able to carry out this investigation a simple and fast AC loss model, referred to as "AC-CRPP" model, is proposed.

In the control theory part we study the stability region in state space, referred to as the region of attraction, for linear tokamak-like systems with input saturation (voltage saturation) and a linear state feedback. Only linear systems with a single unstable pole (mode) and a single saturated input are considered. We demonstrate that the characterisation of the region of attraction is possible for a second order linear system with one unstable and one stable pole. For such systems the region of attraction possesses a topological bifurcation and we provide an analytical condition under which this bifurcation occurs. Since the analysis relies on methodologies like Poincaré and Bendixson's theorems which are unfortunately only valid for second order systems it is evident that there is no way to apply the results for second order systems to higher order systems. It turned out that the search for characterising the region of attraction for higher order systems was illusory and thus this research direction had to be abandoned.

We therefore focused on controllers for which the region of attraction is the maximal region of attraction that can be achieved under input saturation. This region is referred to as the null controllable region and its characterisation is simple for any arbitrary high order system possessing a single unstable pole. We present a new globally stabilising controller for which its region of attraction is equal to the null controllable region. This result is obtained by incorporating a simple continuous nonlinear function into a linear state feedback controller. There are several advantages linked to this new controller: i) the stability properties are enhanced, ii) the performance, AC loss reduction and fast disturbance rejection, can be taken into account, iii) the controller can be applied to any arbitrary high order system and iv) the controller possesses a simple structure which simplifies the design procedure.

We close the control theory part by focusing on the application of the proposed new controller to tokamaks. Since this controller is a state feedback controller one of the major problems is linked to the state reconstruction. Other pertinent topics are: i) the study of the effect of the disturbances on the closed-loop system stability, ii) the problem inherent to the nature of a state feedback controller when we want an output of the system to track a reference signal and iii) the discussion of the detrimental effects on stability if a pure time delay or a limited bandwidth are added to the closed-loop system, as is the case in reality.

The validation of the proposed controller is carried out by means of simulations. We present results for ITER-FEAT and JET using the linear tokamak model CREATE-L. Finally, we present a validation for the case of TCV using the nonlinear DINA-CH code.

Version Abrégée

Dans un tokamak, le contrôle du courant, de la position et de la forme d'un plasma allongé est compliqué par l'instabilité de la position verticale du plasma. En outre, le problème de contrôle s'accroît considérablement lors de la présence de saturation des alimentations. La saturation en courant est relativement bénigne due à l'effet intégrateur d'un tokamak permettant de faire face à ce problème au cours d'un horizon temporel raisonnablement long. Par contre, la saturation en tension est produite par le régulateur sans aucun délai intrinsèque. En pratique, durant des perturbations de plasma larges, comme les dents de scie, les ELMs et la disruption mineure, les tensions des alimentations peuvent être amenées en saturations impliquant une perte de contrôle de la position verticale. Dans ce cas, le plasma se déplace verticalement et entre inévitablement en contact avec la paroi de la coque, ce qui peut sérieusement endommager la machine. La considération et l'étude des saturations en tension sont particulièrement importantes pour ITER. Dû à la dimension et de ce fait au coût de ITER, les marges des alimentations des bobines poloidales seront naturellement plus petites engendrant des saturations en tension fréquentes durant les périodes transitoires dû à une variété de perturbations.

En vue de réduire la dimension et le coût des bobines et des alimentations, les futures machines, comme par exemple ITER, seront munies de bobines supraconductrices. Toutefois, la variation du champ magnétique transversal au sein des bobines supraconductrices engendre deux types de pertes calorifiques: i) les pertes dites de couplages et ii) les pertes dites d'hystérésis, toutes les deux regroupées sous la dénomination de pertes CA (courant alternatif). Ces pertes calorifiques entraînent inévitablement l'échauffement des bobines, ce qui peut engendrer la perte de la propriété supraconductrice des bobines provoquant la surchauffe, voire la destruction des bobines. En général, les bobines sont conçues avec assez de marge pour absorber toutes les pertes probables. Cependant, une réduction de pertes CA pourrait s'avérer utile en vue de permettre une réduction du diamètre des câbles supraconducteurs, la réduction des coûts en général ou l'augmentation de la marge opérationnelle du system de refroidissement des bobines.

Dans cette thèse, on a tenté de prendre en compte ces deux problèmes majeurs. Ainsi, il en découle les objectifs principaux suivants: i) l'analyse de la stabilité du tokamak en considérant les saturations en tension des alimentations, ii) la proposition d'un nouveau régulateur permettant d'augmenter les propriétés de stabilité en présence de saturations en tension et iii) la proposition d'un régulateur qui prend en compte le problème de la réduction des pertes CA. La thématique de cette thèse se trouve dans un cadre interdisciplinaire impliquant la division de la thèse en deux parties. La première partie traite la physique et l'ingénierie des tokamaks, quand à la deuxième partie, elle est dévouée à la théorie dans le domaine de l'automatique.

Dans la partie traitant la physique et l'ingénierie des tokamaks, on présente les modèles linéaires et le code non-linéaire utilisés pour le développement et la validation du nouveau régulateur proposé dans le cadre de cette thèse. La présentation est focalisée en particulier sur le fait que les modèles linéaires possèdent un unique pôle instable dû à l'instabilité de la position verticale du plasma. Cette caractéristique est primordiale en vue d'analyser la stabilité d'un système tokamak en boucle fermée en présence de saturations. Afin de pouvoir déterminer les améliorations en termes de stabilité, le régulateur proposé doit être conduit à la limite de son effet stabilisant en injectant de larges perturbations. Il est évident qu'une telle validation doit d'abord impérativement être mise en oeuvre par

voie de simulation avant de valider un nouveau régulateur sur un tokamak en opération. Les simulations à base d'un modèle linéaire sont dans ce cas présent inadéquates, car en présence de perturbations importantes, l'état du modèle linéaire peut quitter sa région de validité. Ainsi, un code non-linéaire, comme DINA, étant en mesure de reproduire toutes les non-linéarités principales d'un tokamak est indispensable. On présente une description détaillée de la physique des plasmas qui est implantée dans le code DINA. En plus, une validation de DINA est présentée en comparant sur TCV des réponses VDE expérimentales avec des simulations DINA.

En vue de pouvoir étudier la réduction des pertes CA, on présente la nature de ces pertes en une forme réduite et on propose un modèle réduit étant en mesure de calculer rapidement le montant des pertes CA.

Dans la partie dévouée à l'automatique, la région de stabilité dans l'espace des états, dite la région d'attraction, est étudiée pour des systèmes linéaires possédant un régulateur d'état linéaire dans la boucle de rétroaction. Des systèmes linéaires possédant uniquement une entrée saturée et un pôle instable sont considérés. On démontre qu'il est possible de caractériser la région d'attraction pour un système de deuxième ordre avec un pôle instable et un pôle stable. Pour de tels systèmes, la région d'attraction possède une bifurcation topologique et on fournit une condition analytique sous laquelle cette bifurcation apparaît. Du fait que ce résultat repose sur les théorèmes de Poincaré et de Bendixson, étant uniquement valides pour des systèmes de second ordre, il est évident qu'une démarche par analogie pour des systèmes d'ordre plus élevé n'est pas envisageable. Il se trouve que la recherche en vue de caractériser la région d'attraction pour des systèmes d'ordre plus élevé s'est avérée illusoire et cette direction de recherche a ainsi dû être abandonnée.

De ce fait une nouvelle stratégie a été adoptée visant à modifier un régulateur linéaire en vue d'obtenir une région d'attraction équivalente à la région d'attraction maximale atteignable en tenant compte de la saturation de l'entrée. Cet objectif est obtenu en incorporant une fonction simple, possédant une non-linéarité continue, dans un régulateur d'état linéaire. Plusieurs avantages sont liés à ce nouveau régulateur: i) les propriétés de stabilité sont augmentées, ii) la caractérisation de la région d'attraction maximale est facilitée pour n'importe quel système d'ordre arbitraire, iii) la performance, la réduction de pertes CA et le rejet de perturbations peuvent être incorporés, iv) le régulateur est applicable à des systèmes d'ordre arbitraire et v) le régulateur possède une structure simple, ce qui facilite la procédure de conception.

La partie consacrée à l'automatique s'achève par la discussion concernant l'application du nouveau régulateur aux tokamaks. Du fait que ce régulateur est un régulateur d'état, un des problèmes majeurs est lié à la reconstruction d'état. D'autres sujets pertinents sont i) l'étude des effets des perturbations sur la stabilité du système en boucle fermée, ii) le problème inhérent à la nature d'un régulateur d'état lors de la poursuite d'un signal de consigne et iii) les effets néfastes sur la stabilité provoqués par l'adjonction d'un retard pur ou d'une limitation de bande passante.

La validation du régulateur proposé dans cette thèse est accomplie à l'aide de simulations numériques. On présente des résultats pour ITER-FEAT et JET en utilisant le modèle linéaire CREATE-L. Finalement, on présente une validation accomplie sur TCV en utilisant le code non-linéaire DINA-CH.

Contents

5   The effect of feedback control on superconducting tokamak AC losses   89

II   Control theory   111

6   Region of attraction of one unstable and one stable pole planar systems with saturated feedback   113

III Validation   219

Chapter 1

Introduction

1.1 The tokamak: a thermonuclear fusion reactor

1.1.1 Principles of nuclear fusion

The basic principle of nuclear fusion is that the defect of mass resulting from the fusion of two light nuclei into a heavier and more stable nucleus is transformed into a large amount of energy. Nuclear fusion is the energy-producing process which takes place continuously in the sun and stars. In the core of the sun at temperatures of 10-15 million degrees Celsius, Hydrogen is converted to Helium providing enough energy to sustain life on earth.

For energy production on earth different fusion reactions are involved. The most suitable reaction occurs between the nuclei of the two heavy forms (isotopes) of hydrogen: Deuterium (D) and Tritium (T). This reaction, illustrated in Figure 1.1, is given by

$$^2_1D + ^2_1T \longrightarrow \ ^4_2He + n + 17.59 \text{ [MeV]}.$$

Eventually reactions involving just Deuterium or Deuterium and Helium may be used.
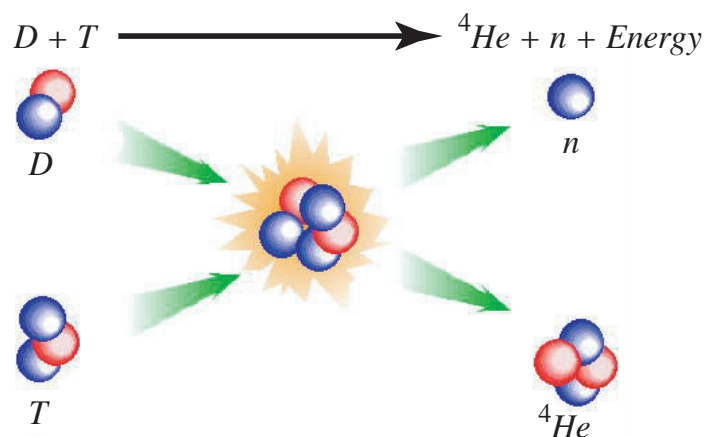
Figure 1.1: Illustration of the Deuterium (D) and Tritium (T) reaction.

In order to have a sufficiently high reaction rate, temperatures of the order of $100 \cdot 10^6$ $[^oC]$ (10^4[eV]) are required. Furthermore, in a reactor, the fuel density must be maintained

at about 10^{20} [m^{-3}] for a sufficiently long lapse of time. For these conditions the fuel changes its state from gas to PLASMA. In a plasma, electrons are separated from the atoms, which become charged ions.

1.1.1.1 Advantages of fusion

The fundamental advantages of fusion are as follows:

- A vast, new source of energy.

- Fuels are plentiful.

- Inherently safe since any malfunction results in a rapid shutdown.

- No atmospheric pollution leading to acid rain or "greenhouse" effect.

- Radioactivity of the reactor structure, caused by the neutrons, decays rapidly and can be minimised by careful selection of low-activation materials. Provision for geological time-span disposal is not needed.

1.1.1.2 Fuels

Deuterium is abundant as it can be extracted from all forms of water. If all the world's electricity were to be provided by fusion power stations, Deuterium supplies would last for millions of years.

Tritium does not occur naturally and will be manufactured from Lithium within the reactor. Lithium, the lightest metal, is plentiful in the earth's crust. If all the world's electricity were to be provided by fusion involving Lithium, known reserves would last for at least 1000 years. Once the reaction is established, even though it occurs between Deuterium and Tritium in the plasma, the consumables are Deuterium and Lithium.

Quantities:
For example, 10 grams of Deuterium which can be extracted from 500 litres of water and 15g of Tritium produced from 30g of Lithium would produce enough fuel for the lifetime electricity needs of an average person in an industrialised country.

1.1.2 The magnetic confinement

Since a plasma consists of two types of charged particles, ions and electrons, magnetic fields can be used to isolate the plasma from the vessel walls. In a magnetic field the particles readily spiral along the field lines but diffuse only slowly across them. The most promising magnetic confinement systems are toroidal (ring-shaped) and, of these, the most advanced is the tokamak. This is a device introduced in the late 60's in the ex Soviet Union by Sakharov and Tamm (tokamak is an acronym for the Russian TO*roidalnaya* KA*mera i* MA*gnitnaya* K*atushka* for toroidal chamber and magnetic coils) which has rapidly spread all over the world thanks to its relative technological simplicity and its high performance.

Figure 1.2 illustrates the basic components of the tokamak's magnetic confinement system. The magnetic field for the confinement is provided by the combination of a large **toroidal** field produced by the toroidal field coils (TF coils) and by a smaller **poloidal** field created by the plasma current and external coils. The plasma current is induced by
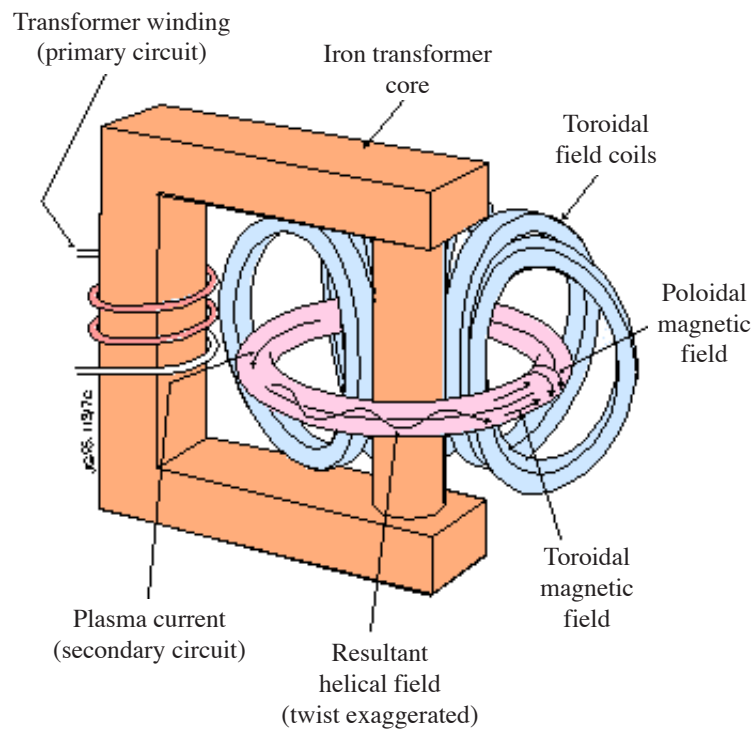
Figure 1.2: Illustration of the basic components of the tokamak's magnetic confinement system: i) the toroidal field which is produced by the toroidal field coils surrounding the vacuum vessel and ii) the poloidal field produced by a current in the plasma and in external coils; the plasma current is induced by transformer action

a magnetic field variation generated by a current injected in the central solenoid coil (CS coils). The central solenoid acts as the primary circuit winding of a transformer which drives the plasma current (**inductive current drive**). The combination of both field components, **toroidal** and **poloidal** fields, results in a helical magnetic field that contains the plasma; the surfaces covered by such fields are known as the magnetic surfaces (Figure 1.3). Since in a magnetic field the particles approximately spiral along the magnetic field lines the electric current in the plasma approximately flows parallel to the magnetic field [54]. Thus, the plasma current has a **toroidal** and a **poloidal** current component, too.

1.1.3   The heating of the plasma

In general, the following methods are used to heat the plasma:

- **Ohmic Heating due to the Driven Current**
  Due to the **current drive** discussed above currents up to 7 million amperes (for JET) flow in the plasma and deposit a few mega-watts of heating power.

- **Neutral Beam Heating**
  Beams of deuterium or tritium ions, accelerated by a potential of up to 1'000'000 volts, are injected into the plasma. In order to penetrate the confining magnetic field, the accelerated beams are neutralised. In the plasma, the beams become ionised and the fast ions give up their energy to the plasma. The power available is typically 20 MW.
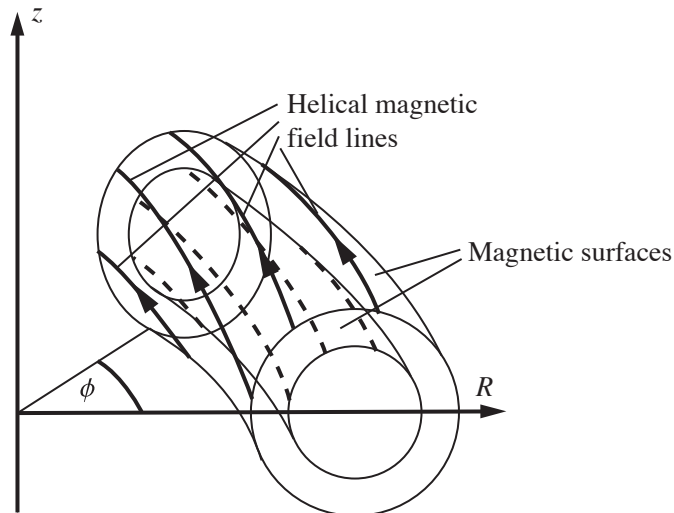
Figure 1.3: Illustration of two magnetic surfaces with the helical magnetic field lines.

- **Radio-Frequency Heating**
  The plasma ions and electrons rotate around in the magnetic field lines of the tokamak. Energy is given to the plasma where the radio waves resonate with the ion rotation. Antennae in the vacuum vessel propagate waves in the frequency range of 25-55 MHz (for JET) into the core of the plasma to increase the energy of the ions. This method can typically inject up to 20 MW of heating power.

- **Current Driven by Microwaves**
  Microwaves with several MW (≈ 10 MW) of power at frequencies around $1 \ldots 5$ GHz accelerate the plasma electrons to generate a plasma current. The name of the method, Lower Hybrid Current Drive (LHCD), refers to the particular waves excited in the plasma.

  Electron Cyclotron Resonance Heating (ECRH) and Electron Cyclotron Current Drive (ECCD) Gyrotrons are also powerful microwave sources. Typically, their output power is in order of hundreds of kW and their frequency around one hundred GHz.

- **Self Heating of Plasma**
  The helium nuclei (alpha-particles) produced when deuterium and tritium fuse remain within the plasma's magnetic trap. Their energy continues to heat the plasma to keep the fusion reaction going. When the power from the alpha-particles is sufficient to maintain the plasma temperature, the reaction becomes self-heating - a condition referred to as **IGNITION**.

1.1.4 Equilibrium in a tokamak with a circular plasma cross section

The toroidal structure of the magnetic field and the interaction of this field and the plasma necessitate the study of the equilibrium which permits the stability of the system. There are two major radial force components which have to be considered to determine the equilibrium of a circular toroidal shaped plasma:

1. **The force due to kinetic plasma pressure**
   We assume a constant mean value of the kinetic plasma pressure, referred to as p, in the whole plasma. Figure 1.4 illustrates the radial forces per unit of the toroidal angle ϕ, given by

   $$F_{p_{in}} = pS_{in} \qquad \text{and} \qquad F_{p_{out}} = pS_{out}, \tag{1.1}$$

   acting on the inner and outer plasma surfaces (magnetic surface), respectively. Due to the toroidal shape of the plasma the inner surface is smaller than the outer surface $(S_{in} < S_{out})$ and thus the forces satisfy the condition

   $$|F_{p_{in}}| < |F_{p_{out}}|. \tag{1.2}$$
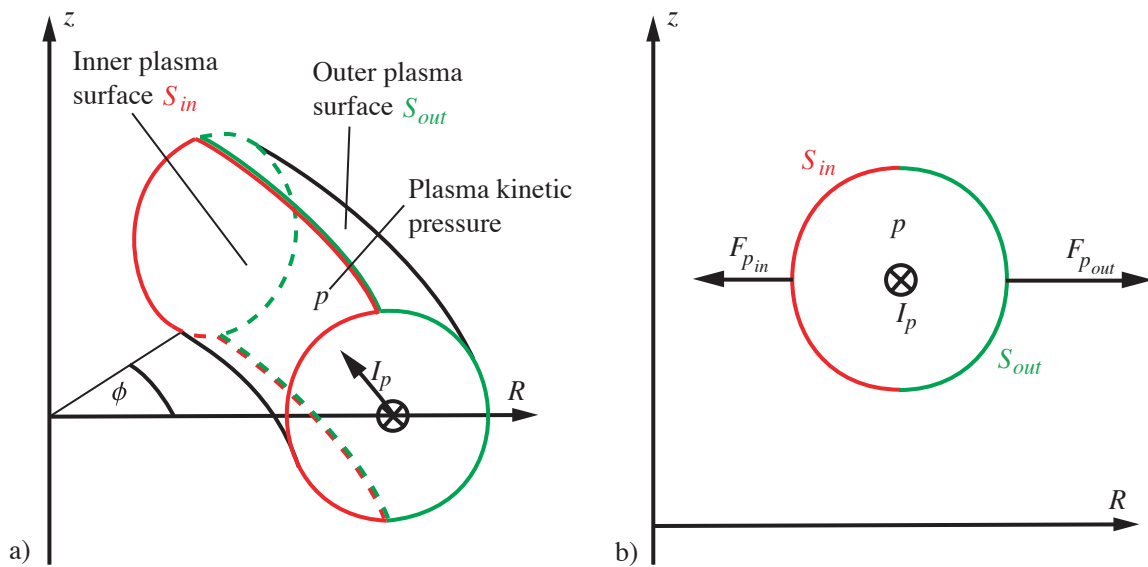
Figure 1.4: Radial forces due to the kinetic pressure.

2. **The force due to the poloidal magnetic field**
   Figure 1.5 illustrates schematically the radial forces acting on the plasma due to the poloidal magnetic field. The force can be interpreted as the result of the linear combination of the individual fields components created by the opposite currents I_p (right hand side of the z axis) and $-I_p$ (left hand side of the z axis) (Figure 1.5 a)). This leads to a poloidal magnetic field for which the vertical field at the inner surface, referred to as $B_{z_{in}}$, is larger than the field at the outer surface, referred to as $B_{z_{out}}$, since $B_{z_{in}}$ is the sum and $B_{z_{out}}$ is the difference of both field components.

   The force acting on the plasma is given by the Lorentz force law which can be expressed as a force per unit length, referred to as $\mathbf{F}'$, by

   $$\mathbf{F}' = \mathbf{I} \times \mathbf{B} \qquad \left[\frac{\text{N}}{\text{m}}\right], \tag{1.3}$$
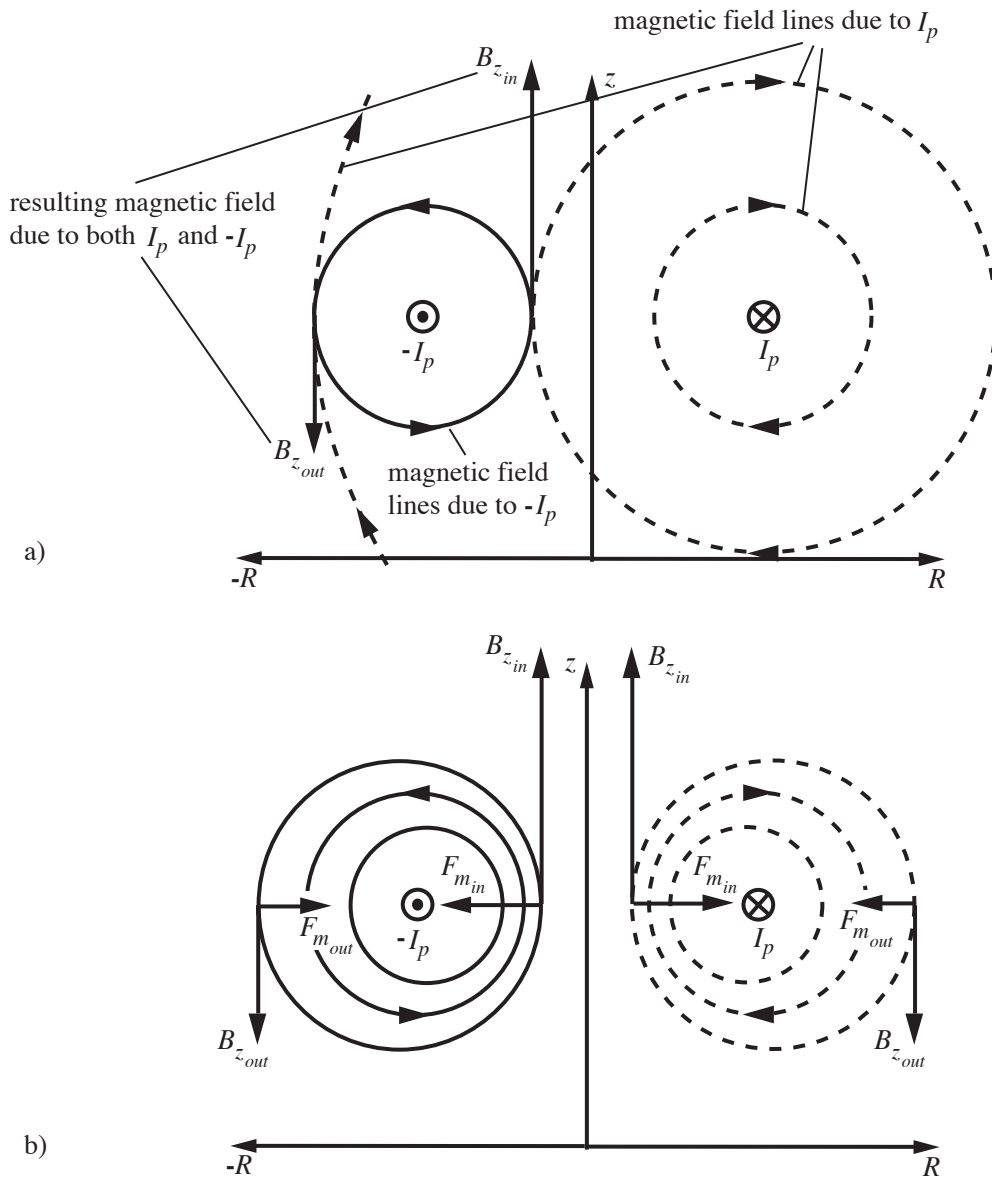
Figure 1.5: Radial forces due to the poloidal magnetic field: a) the magnetic field lines in dashed are due to the plasma current I_p only (right hand side of the z axis), while the magnetic field lines in solid are due to the current $-I_p$ only (left hand side of the z axis); b) the resulting magnetic field lines due to both current components I_p and $-I_p$.

where **I** is the current and **B** is the magnetic field. Thus, the radial force acting on the plasma is given by

$$F'_R = I_p B_z. \tag{1.4}$$

Since $|B_{z_{in}}| > |B_{z_{out}}|$ the resulting radial force at the inner surface, referred to as $F_{m_{in}}$, is larger than the field at the outer surface, referred to as $F_{m_{out}}$. i.e. $|F_{m_{in}}| > |F_{m_{out}}|$.

It turns out that both major radial forces, i.e. pressure and magnetic forces, contribute to an actual radial force, referred to as $F_{R_{tot}}$ acting on the plasma and which displaces the plasma radially to the outside (Figure 1.6). The avoid a radial displacement and therefore to keep the plasma in equilibrium, a reacting force, referred to as $F_{R_{ext}}$ is obtained by adding an external vertical field, referred to as B_v. Due to the Lorentz force law (Equation (1.3)) this radial force is given by

$$F_{R_{ext}} = -2\pi R I_p B_v, \tag{1.5}$$

where we assume that $I_p > 0$ and $B_v > 0$.
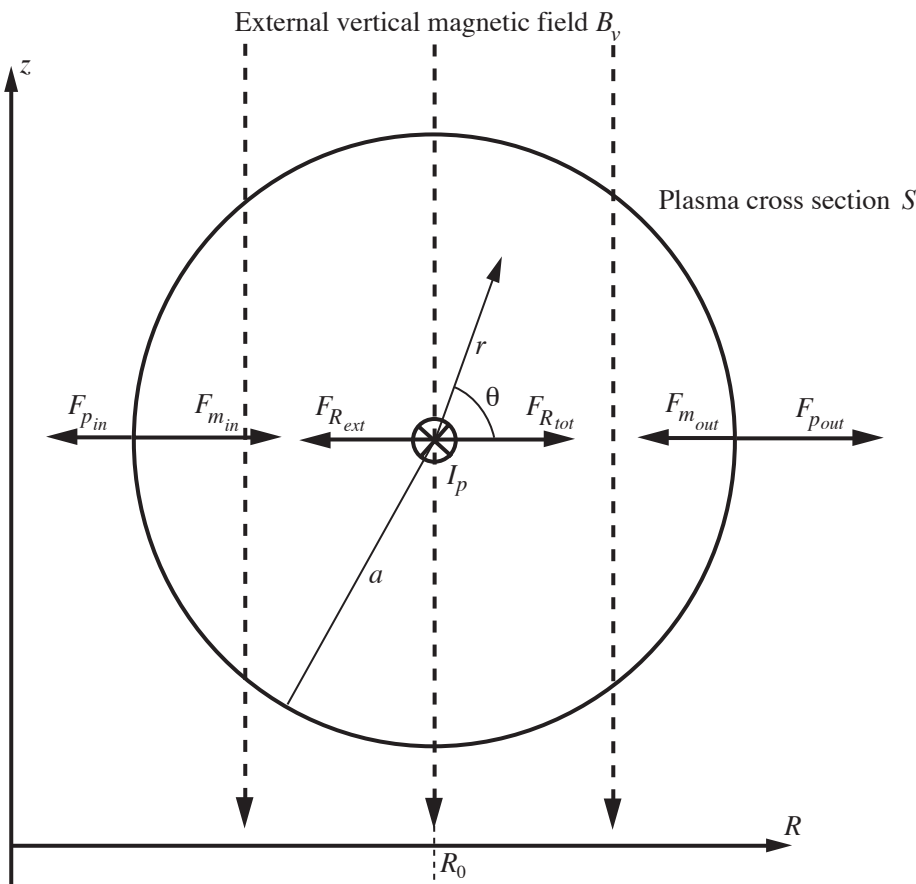
Figure 1.6: Illustration of the radial forces acting on the plasma.

The external vertical field is given by the Shafranov equation [54], i.e.

$$B_v = \frac{\mu_0}{4\pi R} I_p \left[\ln\left(\frac{8R}{a}\right) + \frac{l_i}{2} + \beta_p - \frac{3}{2} \right], \tag{1.6}$$

where a is the inner plasma radius and where we introduce two new plasma parameters [54]:

1. The ratio of the kinetic plasma pressure energy density to the poloidal magnetic field energy density, i.e.

$$\beta_p = 2\mu_0 \frac{<p>}{<B_\theta(a)^2>}, \tag{1.7}$$

   where $<p>$ is the mean value of the kinetic pressure and $B_\theta(a)$ the poloidal magnetic field at the plasma edge (position a).

2. The internal plasma inductance l_i is defined by means of the internal poloidal magnetic field energy per unit of the toroidal circumference given by

$$W'_{internal} = \frac{1}{2\mu_0} \int_S B_\theta(r,\theta)^2 dS = \frac{\mu_0}{2\pi} \frac{l_i}{2} I_p^2, \tag{1.8}$$

   where $B_\theta(r,\theta)$ is the total poloidal magnetic field (sum of the field due to I_p and the external vertical and poloidal field due to the PF coils) and S is the cross section of the plasma. Thus, the internal plasma inductance is given by

$$l_i = \frac{2\pi}{\mu_0^2 I_p^2} \int_S B_\theta(r,\theta)^2 dS. \tag{1.9}$$

The external vertical field is created by additional coils, referred to as the poloidal field coils (PF coils). These coils located around the outside of the vacuum vessel (Figure 1.7) are used for the shape and position control of the plasma.
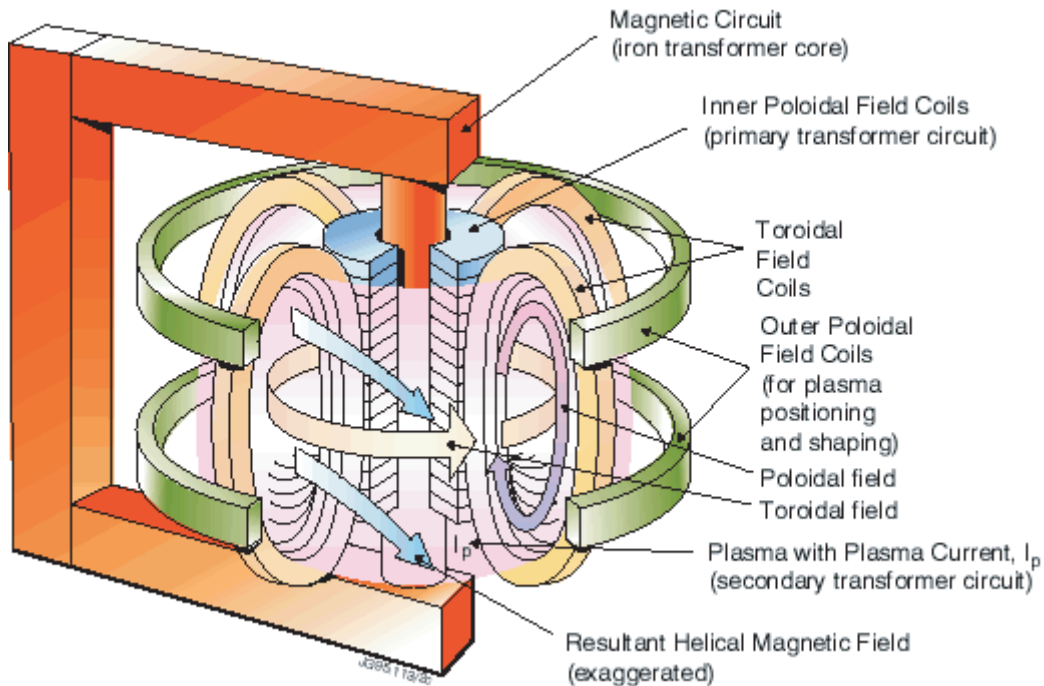
Figure 1.7: Schematic diagram of a tokamak with the poloidal field coils.

Note that the Shafranov equation (Equation (1.6)) depends on the parameters I_p, R, a, β_p and l_i which are all dependent of time. This implies that B_v varies as a function of time, too. Since the values of all these parameters are not known precisely a method is needed to maintain the equilibrium of the radial plasma position by controlling the vertical magnetic field B_v. Since the 70's feedback loops (controllers) are used for this purpose.

1.1.5 The elongated plasma and its vertical position instability

Tokamak plasmas with non-circular cross sections exhibit significant performance improvements. In fact, it can be shown that the vertical elongation, referred to as κ, allows larger plasma currents ($\propto \frac{1+\kappa^2}{2}$) to be carried for a given safety factor q and for given values of magnetic fields, major radius and minor radius, as well as producing large values of β ($\beta < \frac{I_p}{aB_\phi}$, where B_ϕ is the toroidal magnetic field). Note that β is the ratio of the kinetic plasma pressure energy density to the magnetic field energy density which is a measure of the effectiveness with which the magnetic field confines the plasma. Hence an increase in elongation leads to an increase in the maximum efficiency achievable. For what follows we will see that such plasmas are intrinsically vertical unstable and thus require a feedback control system to maintain the plasma in equilibrium.

In the last section we have seen that the external vertical magnetic field B_v permits us to maintain the plasma in equilibrium. In this section we show under which conditions the vertical plasma position, referred to as z, of this equilibrium is whether stable or not.

The shape of the plasma can be either flattened or elongated by adding a radial component to the vertical field B_v. Let us therefore decompose the external magnetic field into a radial and a vertical component, i.e.

$$\mathbf{B}_{ext} = B_{R_{ext}}\mathbf{e}_R + B_{z_{ext}}\mathbf{e}_z,$$

where $B_{R_{ext}}$ refers to as the radial magnetic field and $B_{z_{ext}}$ refers to as the vertical field which is given by

$$B_{z_{ext}} = -B_v. \tag{1.10}$$

Figure 1.8 illustrates that the shape modification is due to the Lorentz force (Equation (1.3)) induced by the external additional radial field in the upper and lower part of the plasma (B_{R_u} and B_{R_l}) and by the plasma current I_p. The additional external radial field leads to a curvature of the external magnetic field. The degree of the curvature is expressed by the decay index

$$n = -\frac{R}{B_{z_{ext}}}\frac{\partial B_{z_{ext}}}{\partial R}. \tag{1.11}$$

Figure 1.8 shows that for a positive decay index the plasma shape is flattened, while for a negative decay index the plasma is elongated. When there is no external radial magnetic field the resulting magnetic field is homogeneous, i.e. $\mathbf{B}_{ext}$ does not vary as a function of z and R, and the decay index is zero.

Due to Ampère's law given by $\mu_0\,\mathbf{j} = \nabla \times \mathbf{B}$, where $\mathbf{j}$ is the current density and $\mathbf{B}$ the magnetic field, and since the current creating $\mathbf{B}_{ext}$ is zero in the vacuum ($\mathbf{j} = 0$) we obtain the relation

$$\frac{\partial B_{z_{ext}}}{\partial R} - \frac{\partial B_{R_{ext}}}{\partial z} = 0. \tag{1.12}$$

The vertical force F_z acting on the plasma is given by

$$F_z = -2\pi R_0 B_{R_{ext}} I_p, \tag{1.13}$$

where R_0 is the radial position of the center of gravity of the plasma current density (Figure 1.8). By considering Equations (1.11)-(1.13) the partial derivative of the vertical force as a function of the vertical plasma position z becomes

$$\frac{\partial F_z}{\partial z} = 2\pi R_0 I_p \frac{n B_{z_{ext}}}{R}. \tag{1.14}$$
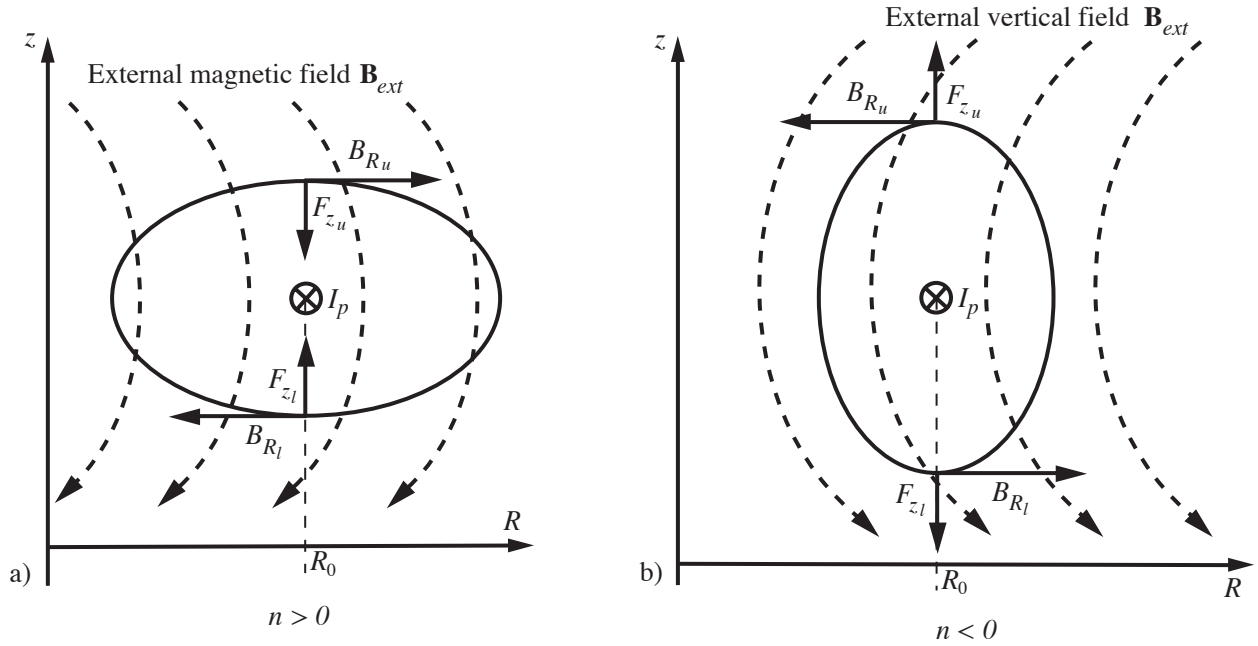
Figure 1.8: Illustration of curvature of the external vertical magnetic field: a) positive curvature leading to a flattened plasma and b) negative curvature leading to an elongated plasma.

Therefore, since $B_{z_{ext}} = -B_v < 0$ for the considered external magnetic field $\mathbf{B}_{ext}$ in Figure 1.8 the equilibrium possesses:

- a stable vertical plasma position ($\frac{\partial F_z}{\partial z} < 0$) if the decay index is positive ($n > 0$)

- an unstable vertical plasma position ($\frac{\partial F_z}{\partial z} > 0$) if the decay index is negative ($n < 0$)

- a marginally stable vertical plasma position ($\frac{\partial F_z}{\partial z} = 0$) if the decay index is positive ($n = 0$).

As mentioned before a plasma can only be made more elongated by means of a negative decay index and thus the vertical plasma position becomes unstable.

1.2 State of the art and current problems in the field of tokamak control

1.2.1 General vertical position stabilisation and plasma shape control

Most tokamaks separate vertical position stabilisation and shape control, in view of the different timescales and because most have a separate fast power supply for vertical control. The position and shape controllers are almost all of the PID type, with exception of JET, which uses a noisy bang-bang control of the vertical speed [36]. In general, the synthesis of these controllers relies on experience and the intuition of the physicist and operator. In fact, several methods have been proposed in the past for the synthesis of PID controllers. These studies are useful for the fundamental comprehension of the basic

tokamak feedback system. Furthermore, these results can be used for the basic controller design but in general the controller has to be refined by empirical tuning.

Recently, new plasma control approaches have been investigated in the domain of optimal controllers like $\mathcal{H}_2$ (LQG) and $\mathcal{H}_\infty$ and by increasing the controller robustness by means of loop shaping. The application of a $\mathcal{H}_2$ controller has solely been studied analytically without any experimental validation (carried out at JET by Garriba), while the application of a $\mathcal{H}_\infty$ loop shaping controller has been successfully validated on TCV [4, 5]. Nevertheless, its design on TCV has revealed itself to be rather complex.

For the ITER-FEAT tokamak a vertical stabilisation and plasma shape controller has been presented in [6] and a reduced order controller has been provided in [7].

1.2.2 Vertical position stabilisation by considering the saturation of the power supplies

As presented in section 1.1.5, the control of tokamaks is complicated by the instability of the plasma vertical position which is due to the elongation of the plasma. It turns out that all linearised tokamak models share the feature of a single unstable pole (Chapter 4).

In this case the control becomes a problem when we take into account the **voltage saturations** of the power supplies. In practice, during plasma disturbances, i.e. sawtooth crashes (changing β_p and l_i), Edge Localised Modes (ELMs, changing β_p especially) and minor disruptions (again changing β_p and l_i), the power supply can saturate and as a consequence the vertical position control can be lost. If such a loss of control happens the plasma position diverges vertically and thus hits the wall of the vessel (disruption), which can cause severe damage to the tokamak. The sole studies of the **voltage saturation** and its effect on the stability in the domain of plasma control are given in [49, 48]. The presented controller was successfully tested on the COMPASS-D tokamak in operation.

Note that **current saturation** is relatively benign due to the integrating nature of the tokamak, resulting in a reasonable time horizon for strategically handling this problem.

1.2.3 Reduction of the active control power

The reduction of the active control power demand is interesting with regard to enhance the efficiency of tokamaks. It could be for example taken into consideration to reduce the control effort during disturbance rejection for disturbances which have no destabilising effects on the tokamak.

1.2.4 Reduction of the AC losses in superconducting coils

The next generation of tokamaks under construction will require vertical position and active shape control and will be fully superconducting. The future large tokamak ITER is also naturally designed with superconducting coils. The interplay between the superconducting magnets and the plasma shape and position control will become important for these devices and presents one of their new features.

When the magnetic transverse field in superconducting magnets changes, the magnet generates two types of heat loss, the so-called coupling loss and the so-called hysteresis loss, grouped together as AC losses. Superconducting coils possess superconducting properties only below a critical temperature around a few K. For a temperature above

this critical temperature the coils show a non-negligible electric resistivity. AC losses are detrimental since they heat up the superconducting material. Thus, if AC losses are too large, the cryogenic plant can no longer hold the required temperature to maintain the superconductivity properties. Once the superconductivity is lost, the electric currents in the coils produce an enormous heat loss due to the ohmic resistivity, which can lead to possible damage to the coils. In general, the coils are designed with enough margin to absorb all likely losses. A possible loss reduction could allow us to downsize the super-conducting cross section in the cables, reducing the overall cost, or simply increase the operational cooling margin for given coils.

1.2.5   Strike point position control

The magnetic field confining the plasma occupies the entire volume of the plasma vessel. Consequently, the plasma also diffuses until it touches the vessel wall. The wall then absorbs at the areas of contact apart from the radiation the entire energy transported to the outside from the core of the plasma. As the wall is not normally suitable for this purpose, measures have to be taken to bound the plasma in a controlled manner.

The first wall is best safeguarded if the field lines do not impinge directly on the wall, but are directed, at an appropriate distance from the hot plasma core, to specially equipped plates, referred to as the divertor plates, which collect and neutralise the plasma particles.

In the ITER Tokamak, one of the most crucial components will be these divertor plates. To better distribute thermal load, the magnetic field could be varied in order to move the impact point (strike point) over the whole area of the plates. Figure 1.9 illustrates the plasma shape, the vacuum vessel, the divertor plates and the strike points for ITER. The divertor strike points are dynamically positioned in the ITER PF control system as part of the full plasma shape and position feedback controller. For ITER we consider among other control parameters 6 gaps between the edge of the plasma and the surrounding plasma facing components, referred to as g_1, g_2, ..., g_6 (Figure 1.9). By varying the gaps g_1 and g_2 by means of a reference signal the strike points on the divertor plates can be displaced as a function of time which allows us to distribute the thermal load on the whole divertor plates.

Moving the strike points to reduce the average local power loading has been demonstrated on JET. In ITER, such sweeping had been considered impractical due to the time varying magnetic fields on the PF coils, inducing hysteresis and coupling AC losses. Nevertheless, a recent elementary study we performed [38] provided encouraging results by showing that for ITER sweeping is still possible over an interesting range of frequencies for which the level of AC losses is not too important. Further, more rigorous studies on this topic have to be investigated in the future.

1.3   The subject of the thesis

This thesis is mainly focused on the vertical position stabilisation by considering the **voltage saturation** of the power supplies. The stability problem due to the voltage saturation can be characterised as follows.

From the observation that voltage saturation of power supplies leads to a loss of control one may at first sight guess that this problem might be solved by designing a controller
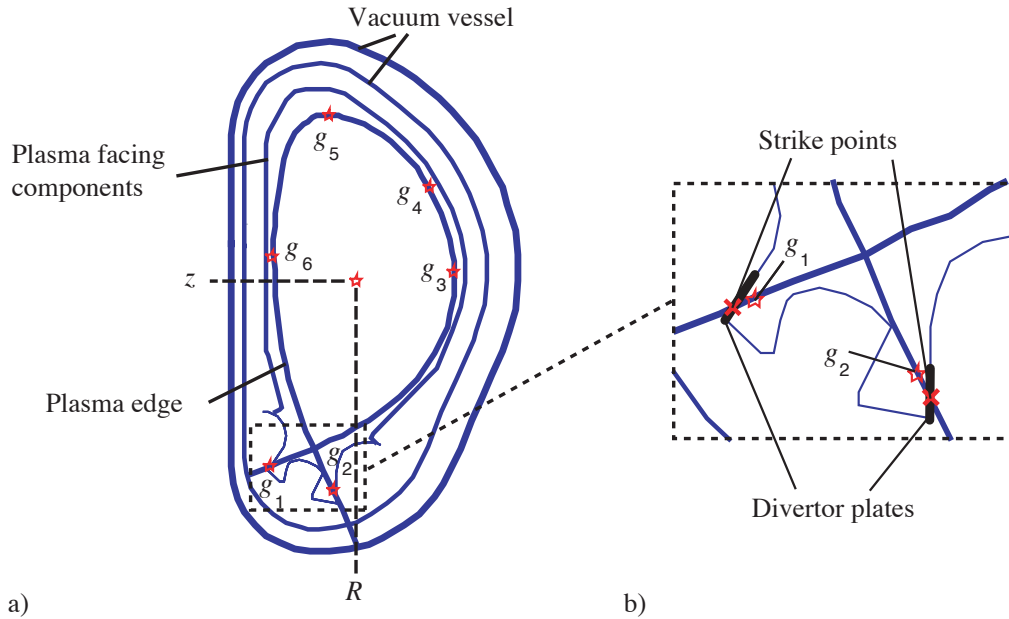
Figure 1.9: Illustration of a) the plasma control parameters like the vertical z and radial R positions and the gaps g_1, g_2, ..., g_6 and b) the gaps g_1 and g_2, the divertor plates and the strike points.

which completely avoids saturation of the power supplies. This suggestion reveals itself to be wrong if we take a look at the control problem in terms of control power. Consider that the plasma is affected by a disturbance which leads among other things to a vertical displacement of the plasma position. The plasma is in disequilibrium and thus a magnetic force acts on the plasma which accelerates the plasma away from the equilibrium point. The vacuum vessel provides a large restoring force, but a certain amount of power, we define it as control power, is necessary to stop and bring back the plasma to the nominal equilibrium position. Due to the voltage saturation of the power supplies this control power is limited (note that the control power is not exactly proportional to the control voltage). For small disturbances the displacement of the vertical plasma position and the destabilising magnetic force are small. Thus, the needed control power to bring the plasma back to equilibrium is low and the power supplies do not saturate. For larger disturbances the control power demand is higher and the power supplies begin to saturate. If a disturbance is too large then the amount of control power reaches its limit, due to the voltage saturation, and there is not sufficient power available to stabilise the plasma and the loss of control is inevitable. From the point of view of stability, we can conclude that it is not wrong to design a controller which often leads to voltage saturation of the power supplies. On the contrary, once voltage saturation is reached, we are sure to deliver the maximum available control power and there is no way to do better.

The work presented by Scibile in [49, 48] illustrates this very well. A sliding mode bang-bang controller for a simplified linear second order tokamak model with a single power supply was proposed. One of its properties is to ensure the maximum reachable stability performance under voltage saturation.

But it also demonstrates one important drawback which is linked to the minimisation of AC losses in superconducting coils (presented in Chapter 5). The main result of the AC losses analysis reveals that for reducing the AC losses we need to design a controller

which generates a non-oscillating, low amplitude and low frequency control voltage signal. Of course, a sliding mode bang-bang controller does just the contrary: it generates a non-smooth signal with a maximum amplitude and during sliding mode a highly oscillating signal with extreme high frequencies. Therefore, such a controller cannot be considered as suitable for tokamaks with superconducting coils.

Another drawback of the sliding mode controller presented in [49, 48] is the fact that considerable knowledge is required when designing and implementing this control algorithm. That is precisely what an operator wants to avoid, since he is interested in obtaining a functioning plant and not just in control theory. This is also one of the reasons why most implemented controllers for tokamaks are PID controllers.

Furthermore, the application of the proposed sliding mode bang-bang controller imperatively requires a linear second order tokamak model, while in general the linear models derived from RZIP [40] and CREATE-L [2] are of orders of 50 . . . 100.

1.3.1   State of the art in the field of dynamical systems with saturated (bounded) inputs

In control theory a dynamical system like the tokamak with voltage saturated power supplies is referred to as a **dynamical system with saturated (or bounded) inputs** since the power supplies are connected to the inputs (coils) of the tokamak.

In this thesis we study the stability of dynamical systems in state space. One of the most relevant notions that will accompany us throughout the control theory part of the thesis is the determination of the stability regions in state space. Therefore, two important concepts pertaining to the stability region have to be distinguished. First we have the *null controllable region*, i.e. the region in state space for which there exists an input that can steer the system to the origin [3, 27, 28, 49, 48]. The second is the *region of attraction with a given controller*, i.e. the region in state space from which the considered closed-loop system asymptotically reaches the origin [3, 27]. The null controllable region can be seen as the maximum region of attraction that can ever be attained by a controller. In other terms, there exists no controller for which the resulting region of attraction is larger than the null controllable region.

Linear systems with bounded inputs have been abundantly studied in the past. Most of the work focused on linear ANCBC (Asymptotically Null Controllable with Bounded Controls) systems where the open loop poles are all located in the closed left half plane (stable and marginally stable systems). It has been shown that such systems are globally stabilisable with nonlinear feedback laws [51]. Another approach dealing with the control of linear ANCBC systems is the semi-global asymptotic stabilisation which was introduced in [37]. The semi-global framework for stabilisation requires feedback laws that yield a closed-loop system which has an asymptotically stable equilibrium and whose domain of attraction includes an arbitrarily large bounded subset of the null controllable region. In [37], it was shown that semi-global asymptotic stabilisation in the null controllable region can be achieved using linear feedback laws.

By way of contrast, results for linear unstable systems with bounded inputs have been less frequently treated in the literature. The work in [49, 48] focuses on a simplified linear second order tokamak model, where essentially bang-bang controllers are analysed. In [3] second order systems in general with linear or nonlinear feedback are studied. It is shown that the number of open-loop unstable eigenvalues characterises the set of the equilibrium points and the shape of the region of attraction. The work in [27] presents an extensive

study of second order and higher order systems. Despite these publications it turns out that there remains a lot of work to be done in the field of control theory for such systems, of which the tokamak is a particular example.

1.3.2   Linear dynamical system with a single saturated input

Most of the results mentioned above [49, 48, 3, 27] are valid for exclusively **linear dynamical system** with **a single input under saturation**. In this thesis we also consider only linear systems (linearised tokamak models) with a single input under saturation, which of course, simplifies the analysis considerably. The justification of this choice is as follows:

- **The linear system**
  Most classical and powerful control theory results for the analysis of systems and the design of controllers are only valid for linear systems. Similar results for nonlinear systems can in general be achieved only partially or approximately. Moreover, the analysis of nonlinear systems requires more intellectual efforts.

  The tokamak is an intrinsically complicated and complex nonlinear dynamical system. It turns out that the analysis of such a system and the controller design for such a system by considering its nonlinearities is not practicable. For these purposes the use of linearised tokamak models (linear systems), e.g. RZIP [40] and CREATE-L [2] which already have been used with success in the past, is indispensable.

  For the purpose of this thesis we will consider linear systems for the analysis and linear tokamak models for the controller design. The sole nonlinearity that is considered is the voltage saturation of the power supplies, referred to as the saturated inputs of a linear system.

- **The single input under saturation**
  Beside the advantage for the theoretical work, it constitutes no major drawback in practice, since for many tokamaks, e.g. ITER, JET, MAST and TCV, the part of the control equipment responsible for plasma stabilisation is provided by only one power supply. For other tokamaks where no particular power supply but several power supplies are devoted for the plasma stabilisation, the power supplies have to be connected together in such a way that the resulting system becomes equivalent to a system with a single input under saturation. Note that the extension of the analysis presented in this thesis to systems with several saturated inputs constitutes a challenging task for future work.

1.3.3   Objectives of the thesis

In this thesis we have tried to take into consideration all of the points mentioned above. The thesis is therefore focused on the following objectives:

- The study of the stability of linear dynamical systems with a single unstable pole and a single saturated input.

- The proposition of a stabilising controller which takes into consideration

  1. the enhancement of the stability by increasing the region of attraction
  2. the problem of reducing the AC losses,

3. the application for linear tokamak models of arbitrary order (order ≥ 2) and

4. a simple design and implementation.

- Developing a nonlinear simulation to demonstrate the validity of these ideas.

1.4   Outline and survey of the thesis

Since the subject of the thesis is situated in an interdisciplinary framework the thesis is subdivided into three principal parts. The first part is devoted to the **tokamak physics and engineering**, while the second part focuses on the **control theory**. The validation of the results, obtained by means of simulations, is presented in the third part.

1.4.1   Part I: Tokamak physics and engineering

1.4.1.1   Chapters 2 and 3: The DINA code description and validation

The main objective of the thesis is to study the effect of the power supply saturation on the closed-loop stability and to provide a new controller with enhanced stability properties. In general, the loss of the vertical position control (loss of stability) is due to large plasma disturbances. Thus, in order to determine the enhancement of the stability properties we have to bring the new controller to its stability limits by means of large disturbances. Such validations cannot be carried out on a tokamak like ITER in operation since the loss of control leads to a disruption which can cause damage to the machine.

Therefore, simulations with either linear or nonlinear tokamak models are imperatively required before considering the implementation of the new controller on a tokamak in operation. A linear tokamak model will probably be inadequate since large disturbances can move its state outside its validity regions. Thus, an accurate nonlinear code like DINA is indispensable for this purpose. It is in particular important to focus on the vertical plasma displacement since a large disturbance leads to a large vertical plasma displacement. Therefore, a DINA validation by means of controlled Vertical Displacement Events (VDE) is particularly helpful for the purposes of this thesis. Chapter 2 gives a detailed description of the principal plasma physics implemented in the DINA code. In Chapter 3 a validation of DINA is provided by comparing TCV experimental VDE responses with DINA code simulations.

1.4.1.2   Chapter 4: Linear tokamak models

In this thesis the linear tokamak models RZIP and CREATE-L are used for controller design and validation of the controller. Thus, in this chapter we give a brief review of these linear models by describing their essence. The discussion is especially focused on the nature of the presence of a single unstable pole when the vertical plasma position is unstable since this characteristic is essential for the stabilising purposes addressed in Part II (Control theory).

1.4.1.3   Chapter 5: The effect of feedback control on superconducting toka-mak AC losses

In this chapter the nature of the AC losses is described in an elementary manner. Furthermore, we analyse to what extent the accumulated AC losses in ITER could be reduced

by taking into account the losses themselves when designing the feedback control loops. In order to be able to carry out this investigation an AC loss model is required which permits a fast estimation of the AC losses. Therefore, a simple and fast executable model of the AC losses, referred to as the "AC-CRPP" model, is proposed.

1.4.2   Part II: Control theory

1.4.2.1   Chapter 6: Region of attraction of one unstable and one stable pole planar systems with saturated feedback

The first approach during this work was to find a way to specify the region of attraction for linearised tokamak models with linear feedback subjected to saturation. The main idea behind this was to determine online if the state of a tokamak in operation was inside or outside the region of attraction. In the case where the state approaches the boundaries or even leaves the region of attraction, the future or inevitable loss of control could be detected early enough to switch on an emergency procedure which could avoid severe damage to the machine. The choice of a linear feedback is justified since most controllers implemented in tokamaks are of linear nature (PID controllers). It has to be pointed out that our aim was to describe the exact region of attraction in contrast to many previous studies where the state of the art is to approximately estimate the region of attraction mainly by making use of Lyapunov functions. The strategy on how to tackle this problem was to start with the most simple tokamak-like system, which is a second order system with one stable and one unstable pole, where the goal was to understand the fundamental nature of the problem linked to the characterisation of the region of attraction. The expectation was to be able to apply in a similar way this new knowledge for higher order systems with a single unstable pole. However it turned out that the analysis of the second order system itself was not as simple as at first sight. Nevertheless, the problem could be completely solved by applying:

- results about equilibrium points and the region of attraction given in [3],

- the fundamental theorems from Poincaré and Bendixson (Theorems A.1 - A.3), which give results on the existence of limit cycles for a second order system

- some results from contraction analysis of second order systems (see Section A.2), where one part is provided by [27] and the other part is a new contribution.

It is evident that there is no way to apply the results for second order systems to higher order systems, since the analysis rests on methodologies like Poincaré and Bendixson's theorems which are uniquely valid for second order systems. Thus, since the work for second order systems was not trivial at all, the search for characterising the region of attraction for higher order systems had to be abandoned. Note that other researchers also tried to work out some results for higher order systems without success [27]. It can therefore be concluded that the identification of the region of attraction by means of conservative methods like Lyapunov function analysis remains state of the art for higher order systems.

1.4.2.2   Chapter 7: A globally stabilising controller under saturated input for systems with one unstable pole

From this somewhat disappointing start a new idea arose. Is there a possibility to slightly modify an existing linear controller to derive a new controller for which its region of attraction is equivalent to the null controllable region? Designing a controller for which its region of attraction is equal to the null controllable region is an essential step since it gives rise to two major advantages:

- Since the null controllable region is the maximum possible region of attraction, there exists no controller for which the resulting closed-loop system possesses a larger region of attraction than the null controllable region. Thus, if the region of attraction is equal to the null controllable region, we can state that, as far as stability region is concerned, we can do no better. We call such a controller a globally stabilising controller.

- The exact determination of the null controllable region and consequently of the region of attraction is very simple. We will show that its boundaries are due only to the unstable state, while the stable states are unbounded in the state space. Thus, by only measuring the value of the unstable state we can determine whether the state of the tokamak in operation is inside or outside the region of attraction. This allows us to accomplish our first goal which is the detection of the loss of control.

We present a new globally stabilising controller, referred to as the Continuous Nonlinear Globally Stabilising Controller (CNGSC), resulting from the incorporation of a simple continuous nonlinear function into a linear controller. Note that the idea of designing a global stabilising controller for unstable saturated systems is not totally new. There are several results on this topic and we therefore present a (hopefully) complete survey of globally stabilising controllers. Moreover, we compare the various standard controllers, linear controllers included, against each other by considering 5 essential requirements which have to be taken into account for the design of a tokamak controller:

1. Global stability
   This requirement is achieved if the region of attraction is equivalent to the null controllable region. In terms of the region of attraction, there exists no better controller.

2. Performance
   There are many performances requirements one might impose on a controller. For our purposes we will consider the fast rejection of disturbances as the most essential performance indicator (recognised by ITER as a crucial and probably the dominant indicator). We will see that there is often a tradeoff between global stability and performance. Thus, for some controllers, we are not always able to satisfy the required performance over the whole region of attraction. We therefore define the notion of local performance where we guarantee the performance locally around the equilibrium point (the origin of the linearised behaviour). This means that for small enough disturbances the required performance is ensured, while for large disturbances some controllers may lose the required performance for the sake of guaranteeing global stability.

3. Reduction of AC losses

   The reduction of AC losses is an additional performance requirement. Since it is a most important aspect for tokamaks with superconducting coils we consider it separately. The results concerning the AC losses reduction are presented in Chapter 5 of Part I. The main goal for reducing AC losses is to design controllers which generate control signals with i) least possible oscillations, ii) amplitudes as small as possible and iii) signal frequencies as low as possible.

4. Control law applicable to higher order systems

   In general linear models like RZIP and CREATE-L generate models with 50 to 100 states. We tried to reduce such models with modal reduction techniques presented in [10] and with methods like balanced truncation and the optimal Hankel norm approximation [58]. We observed that for an accurate representation of a tokamak, a model with at least 10 to 15 states is required. It is definitely an illusion to seek a sufficiently accurate linear tokamak model of only second order. Thus, the controller design method should be able to handle higher order systems.

5. Simple design and implementation

   Experience shows that new controllers with complicated and complex structures are often not considered in practice, especially in the field of industrial applications. In general, there seems to be a fear of controllers for which considerable knowledge is required for design and implementation. We therefore have to focus on controllers for which the design and the implementation is simple and fairly intuitive.

   We will see that the major design difficulty of global stabilising controllers in general is linked to the fact that the unstable state imperatively has to be fed back to ensure global stability. Thus, these controllers are partial or full state feedback controllers, while in contrast, the state of the art controllers for tokamaks are input-output controllers, like PID controllers. The main effort which has to be undertaken is i) to acquire the knowledge on how to migrate from input-ouput controllers to state feedback controllers and ii) to obtain an accurate unstable state estimation, i.e. a dynamic or static observer. This might be considered as a major drawback, but there exists no alternative solution to ensure global stability.

This discussion and comparison of standard state of the art controllers ends by establishing that these controllers cannot satisfy all 5 requirements simultaneously. We are therefore proposing a new class of nonlinear controllers (CNGSC) which is able to satisfy these requirements. In a first approach, controllers for second order systems are analysed. We give intuitive explanations on how this class of controllers might satisfy the global stability and the performance requirements, AC loss reduction included. It is followed by an analytic proof of the global stability for slightly more conservative conditions. In fact, this means that we are not able to provide an analytic proof for the whole class of controllers but only for a large subset of the class. Nevertheless, we note that all results obtained from simulations seem to reveal a global stability for the whole class. We continue with a discussion on the performance and AC loss reduction, where we compare the CNGSC controller against the various standard controllers via simulation results. Finally, we will show that the extension of the new class of controllers to higher order systems is straightforward. But the quest for an analytic proof of the global stability is highly complicated in this case. Therefore, the proof of the global stability of the higher order systems is only based on numerical results by means of simulations. Nevertheless,

we provide an interesting property encouraging the search for a formal stability proof in the future.

1.4.2.3   Chapter 8: Tokamak control

The last chapter of the control theory part is devoted to the problem of applying the CNGSC controller to tokamaks. In general, we assume, for the controller design phase, a tokamak closed-loop system consisting of a linearised tokamak model with several saturated inputs and two input-output controllers. There is a slow controller which is responsible for the plasma shape control and a fast controller which ensures the so-called "vertical plasma position" stability. Although the terminology varies from one tokamak to another, this property is common to ITER, JET, MAST and TCV. In contrast to this, we consider in Chapter 7 a normalised closed-loop system which consists of a second or higher order normalised linear system with a single saturated input and a state feedback controller. Therefore, we first provide a scheme which describes a way to transform a tokamak closed-loop system into a normalised closed-loop system. This will allow us to apply the results of Chapter 7 straightforwardly for the design of the controller.

We then discuss the problem of the state reconstruction. Additionally, we will show that when considering the CNGSC controller it is sufficient to reconstruct or measure only the unstable state.

Another pertinent topic is the study of the effect of the disturbances on the closed-loop system. We will see that the determination of the closed-loop system stability by means of the region of attraction is only valid during time lapses where the system is not disturbed. This is due to the fact that the concept linked to the region of attraction is only applicable to autonomous closed-loop systems (autonomous systems are time-invariant systems [50]). However, in system theory a disturbance is interpreted as a time-varying external input to the closed-loop system. Another problem is due to the unknown evolution of the shape, the amplitude and the time duration of a disturbance. Thus, the evolution of the states is not predictable during a disturbance and we have to wait until the disturbance has vanished to determine whether the states are still in the region of attraction or not. Nevertheless, there are possibilities to improve the stability during disturbances by slightly modifying the controller.

A further problem lies in the nature of the state feedback controller when we want an output of the system to track a reference signal. For input-output systems, this is usually obtained by simply taking the error between the output and the reference. The resulting error signal is fed to the input-output controller which tries to cancel the error. We will see that this is not as simple for nonlinear state feedback controllers, since such controllers work for a well defined equilibrium point. Thus, if we want to track a reference signal then we have to move the equilibrium point as a function of the reference signal.

We end this chapter by discussing the detrimental effects on stability if a pure time delay or a limited bandwidth are added to the closed-loop system. This study is essential since there are inevitably a limited bandwidth and a pure time delay due to the power supply, which are in general not negligible. Furthermore, there is second pure time delay due to the computing time for the execution of the control algorithm. Therefore, we will suggest pragmatic solutions to avoid some detrimental effects on the stability properties of our CNGSC controller.

1.4.3 Part III: Validation

1.4.3.1 Chapter 9: Validation via simulations

In this chapter we validate the CNGSC controller provided in Part II (Control theory). Note that nowadays the control systems of many tokamaks do not allow for implementing nonlinear control laws. Since the CNGSC controller possesses a nonlinearity no experimental discharges could be carried out so far for the purpose of the validation. Therefore, the validation is restricted to simulations.

The validation is carried out for the following three tokamaks:

- **ITER-FEAT**:
  The controller design and the validation are carried out with the linear CREATE-L model.

- **JET**:
  The controller design and the validation are carried out with the linear CREATE-L model.

- **TCV**:
  The controller is designed with the linear RZIP model, while the validation is carried out with the nonlinear DINA code.

1.5 New contributions presented in this thesis

The new contributions in the field of tokamak physics and engineering are:

- the development of a simple and fast executable model for the estimation of AC losses,

- the validation of the DINA code by comparing TCV experimental VDE responses with DINA code simulations and

- the detailed description of the principal plasma physics implemented in the DINA code.

The new contributions in the field of tokamak control and control theory in general are:

- the analysis of the region of attraction of linear planar systems with one unstable and one stable pole and saturated feedback with the focus on:

  - the description of the shape of the region of attraction and

  - the analytic condition for the topological bifurcation of the region of attraction,

- the analysis to what extent the accumulated AC losses in ITER could be reduced by taking into account the losses themselves when designing the controller,

- the new continuous nonlinear controller (CNGSC) for an arbitrary high order (order ≥ 2) system with a single unstable pole which ensures:

  - the global stability,

  - the local performance and

     – the reduction of AC losses and

- the detailed description of the application of the proposed CNGSC controller to tokamak models with the focus on:

  – the transformation of tokamak closed-loop system into a normalised system

  – the state reconstruction

  – the tracking of a reference signal with a nonlinear state feedback controller

  – the closed-loop system stability during disturbances and

  – the deleterious effects on the closed-loop system stability due the presence of bandwidth limitation and time delay in the closed-loop system.

Part I

Tokamak physics and engineering

Chapter 2

The DINA code

2.1 Introduction

A non-linear time-evolution code is an essential tool for modelling existing or future toka-mak experiments in particular cases in which linearised models are inadequate. Such cases are dominated by those in which the excursions from the nominal equilibrium are large, excluding local linearisation of the plasma equilibrium response. Consider for example the study of the active control of an elongated plasma which is generally unstable to an axisymmetric vertical plasma displacement. The common way of designing a tokamak controller is to consider a linearised tokamak model. Of course, this controller will work perfectly for small vertical plasma displacements. On the other hand, for large vertical displacements the evolution of the vertical plasma position as a function of time shows that it no longer follows a linear dynamical behavior. If the controller, especially the vertical stabilisation part, fails then a disruption can occur which can cause considerable damage to the machine. Therefore, a nonlinear code is indispensable for the validation of a tokamak controller.

The DINA code [34] is a suitable code for such purposes. It simulates axisymmetric tokamaks in two-dimensional geometry, i.e. the variations as a function of the toroidal angle are not taken into account. It considers the resistivity in a magneto-hydrodynamic (MHD) plasma. It assumes zero plasma mass, eliminating the dilemma introduced by falsifying the plasma mass, typified by the TSC code [30]. It correctly treats the poloidal flux diffusion, avoiding the imposition of either a rigid current displacement, typified by the linear RZIP model [17], or the frequent assumption of constant normalised poloidal flux profiles but deformable equilibrium typified by DPM and CREATE-L [25, 2]. DINA uses an energy transport model and a simple sawtoothing model. The transport equations are solved by averaging the evolving quantities, i.e. flux, current, pressure and density, on the constant flux surfaces. Due to this averaging technique DINA is considered as a code dealing with a 1.5 dimensional geometrical problem, and not with a pure 2 dimensional problem. The main differences between DINA and other codes is the method that is employed for the solution of the equilibrium problem. The "inverse variable" technique [56] is used in the DINA code to find the coordinates of the equilibrium magnetic surfaces. This method permits the code to determine the flux very quickly and accurately. For all these reasons, DINA provides a suitable compromise for plasma equilibrium response modelling.

The DINA code calculation is divided into two distinct steps. The first one is the determination of the flux surfaces and profiles by solving the plasma equilibrium problem.

This is done by solving the partial differential Grad-Shafranov equation. The second part is the calculation of the evolution for the next iteration (time step) of the flux surfaces where the flux, current, pressure and density profiles are calculated by integrating the differential transport equations which consist of the magnetic field diffusion equation, the density equation and the power balance equations for the ions and electrons. With these profiles a new equilibrium is computed by solving the Grad-Shafranov equation. For the first equilibrium calculation initial profiles are needed.

In what follows we will first discuss the plasma equilibrium problem. Then the transport equations are described and in addition the circuit equations of the active coils, passive coils and vacuum vessel structure are presented. We end this chapter with the description of the functional structure of the DINA code.

2.2   Equations of MHD and the tokamak equilibrium

2.2.1   The MHD equations

Magneto-hydrodynamics (MHD) describes the behaviour of a fluid which on a macroscopic scale is neutral and conducts electrical currents. The set of MHD equations is given by the flow equation, the continuity equation and, since the considered fluid is a conductor, by the Maxwell equations and Ohm's law.

$$\varrho \frac{d\mathbf{u}}{dt} = \varrho \left(\frac{\partial}{\partial t} + \mathbf{u} \cdot \nabla \right) \mathbf{u} = \mathbf{j} \times \mathbf{B} - \nabla p \qquad \text{Flow equation}$$

$$\frac{\partial \varrho}{\partial t} + \nabla \cdot (\varrho \mathbf{u}) = 0 \qquad \text{Continuity equation}$$

$$\mathbf{E} + \mathbf{u} \times \mathbf{B} = \frac{1}{\sigma}\mathbf{j} \qquad \text{Ohm's law} \qquad (2.1)$$

$$\nabla \cdot \mathbf{B} = 0 \qquad \text{non-existence of magnetic monopoles}$$

$$\nabla \cdot \mathbf{E} = \boxed{\frac{\varrho_c}{\epsilon_0}} \qquad \text{Poisson's law}$$

$$\nabla \times \mathbf{E} = -\frac{\partial \mathbf{B}}{\partial t} \qquad \text{Faraday's law}$$

$$\frac{1}{\mu_0}\nabla \times \mathbf{B} = \mathbf{j} + \boxed{\varrho_c \mathbf{u} + \epsilon_0 \frac{\partial \mathbf{E}}{\partial t}} \qquad \text{Ampère's law corrected by Maxwell}$$

where ϱ is the mass density, ϱ_c the charge density, $\mathbf{u}$ the plasma velocity, $\mathbf{j}$ the current density, p the plasma pressure, $\mathbf{E}$ the electric field and $\mathbf{B}$ the magnetic field.

The terms in the boxes, and moreover the whole Poisson's law, can in general be neglected in MHD due to the quasi-static approximation. Although a plasma of ions and electrons is globally neutral, there are some possible gaps in the electrical neutrality for physics dealing with spatial scales less than the Debye length

$$\lambda_D = (\epsilon_0 k_B T / n e^2)^{1/2},$$

where k_B is the Boltzmann constant, T, n and e are the temperature, the density and the electron charge, respectively. MHD does not describe phenomena characterised by spatial scales less than $\sim \lambda_D$ and characteristic times shorter than $\sim \lambda_D/v_T$, where v_T is the thermal velocity of electrons $v_T = \sqrt{2k_B T/m}$. Therefore, for macroscopic scales the

assumption of $\varrho_c \approx 0$ can by considered for Poisson's law and the term $\varrho_c \mathbf{u} \approx 0$ in the Ampère-Maxwell equation. Moreover, if the characteristic velocities of the plasma flow are small compared to the speed of light $c = 1/\sqrt{\mu_0 \epsilon_0}$ the displacement current denoted by $\epsilon_0 \partial \mathbf{E}/\partial t$ in the Ampère-Maxwell equation can be neglected. Therefore, in what follows, we will consider the set of MHD equations (2.1) without the terms in the boxes.

In general the plasma is considered as a good electrical current conductor. Therefore, its resistivity $\eta = 1/\sigma$ is very low (about $2 \cdot 10^{-8}$ Ωm at a temperature of 100 eV comparable to the resistivity of copper $\eta = 10^{-8}$ Ωm). Sometimes the plasma is considered as an ideal conductor $\eta = 1/\sigma = 0$. This case is called the ideal MHD as opposed to resistive MHD.

We have to pay particular attention to the velocity. If we consider the ion velocity $\mathbf{u}_i$ and the electron velocity $\mathbf{u}_e$ separately then these velocities can be subdivided into two parts.

$$\mathbf{u}_i = \mathbf{u} + \mathbf{u}_{j_i},$$
$$\mathbf{u}_e = \mathbf{u} + \mathbf{u}_{j_e}.$$

The first part $\mathbf{u}$ is due to the movement of a infinite small volume of the plasma (or the flow). For such a movement the ions and electrons move in the same direction with the same velocities $\mathbf{u}$. The second part is linked to the current density $\mathbf{j}$ which is the sum of the current densities of the ions $\mathbf{j}_i$ and electrons $\mathbf{j}_e$

$$\mathbf{j} = \mathbf{j}_i + \mathbf{j}_e, \qquad \text{where}$$
$$\mathbf{j}_i = n_i e \mathbf{u}_{j_i} \qquad \text{and} \qquad \mathbf{j}_e = -n_e e \mathbf{u}_{j_e},$$

where e is the elementary electric charge and n_i and n_e are the densities of the ions and electrons, respectively. Since the plasma is assumed to be electrically neutral on the macroscopic scale the ion and electron density are equal $n = n_i = n_e$ (assuming $Z = 1$). This leads to the following relations

$$\mathbf{u}_i = \mathbf{u} + \mathbf{u}_{j_i} = \mathbf{u} + \frac{1}{en}\mathbf{j}_i, \tag{2.2}$$

$$\mathbf{u}_e = \mathbf{u} + \mathbf{u}_{j_e} = \mathbf{u} - \frac{1}{en}\mathbf{j}_e, \tag{2.3}$$

$$\mathbf{j} = \mathbf{j}_i + \mathbf{j}_e = ne(\mathbf{u}_{j_i} - \mathbf{u}_{j_e}) = ne(\mathbf{u}_i - \mathbf{u}_e) \tag{2.4}$$

For the MHD description of the plasma we do not consider the total ion and electron velocities, $\mathbf{u}_i$ and $\mathbf{u}_e$, but we consider the plasma velocity (flow) $\mathbf{u}$ and the current density $\mathbf{j}$ separately.

2.2.2 The tokamak equilibrium

The search for the plasma equilibrium is used to find a stationary solution in space and time of the MHD equations. We therefore assume that the plasma velocities at equilibrium are zero and consider ideal MHD. This leads to the observation that the density and magnetic field due to the continuity equation, Ohm's law and Faraday's law of (2.1) do not evolve in time

$$\frac{\partial \varrho}{\partial t} = 0, \quad \frac{\partial \mathbf{B}}{\partial t} = 0.$$

Moreover, the set of MHD equations (2.1) are reduced to the following 3 equations

$$\nabla p = \mathbf{j} \times \mathbf{B}$$
$$\nabla \cdot \mathbf{B} = 0 \tag{2.5}$$
$$\nabla \times \mathbf{B} = \mu_0 \mathbf{j},$$

where the first equation expresses the fact that in equilibrium the forces due to the pressure and to the magnetic field balance at all points in space, neglecting the flow $\mathbf{u}$.

The combination of the first and third equation of (2.5), by considering the vector identity

$$(\nabla \times \mathbf{B}) \times \mathbf{B} = (\mathbf{B} \cdot \nabla)\mathbf{B} - \frac{1}{2}\nabla(\mathbf{B}^2)$$

leads to following general expression

$$\nabla \left(p + \frac{\mathbf{B}^2}{2\mu_0} \right) = \frac{1}{\mu_0} \left(\mathbf{B} \cdot \nabla \right) \mathbf{B}. \tag{2.6}$$

The scalar products of the first equation of (2.5) with the magnetic field $\mathbf{B}$ or the current density $\mathbf{j}$ imply that

$$\mathbf{B} \cdot \nabla p = 0, \qquad \mathbf{j} \cdot \nabla p = 0, \tag{2.7}$$

Therefore, we can define magnetic surfaces composed of magnetic field lines along which the pressure p is constant, i.e. the gradient of the pressure (the variation of the pressure in space) is perpendicular to the magnetic surfaces. Furthermore, it follows that the direction of the current density lies on the magnetic surfaces, too.

At this point we introduce the poloidal magnetic flux function Ψ which is due to the poloidal magnetic field. Since the magnetic surfaces are constituted of magnetic field lines the poloidal magnetic flux function Ψ is constant on each magnetic surface which consequently leads to

$$\mathbf{B} \cdot \nabla \Psi = 0, \qquad \mathbf{j} \cdot \nabla \Psi = 0. \tag{2.8}$$

The remaining study of the equilibrium relies on the properties of axisymmetric geometry, since this is a feature of DINA and also of the linear models RZIP and CREATE-L. Therefore, we introduce the cylindrical coordinates (R, ϕ, z) for the spatial description of the tokamak. For the description of the magnetic surfaces, polar coordinates (r, θ) are introduced in the poloidal cross section of the plasma for which the origin $(R_0, \cdot, z_0)$ is located on the magnetic axis. The unit vectors of the cylindrical coordinates are given by $\mathbf{e}_R$, $\mathbf{e}_\phi$ and $\mathbf{e}_z$ and for the polar coordinates by $\mathbf{e}_r$ and $\mathbf{e}_\theta$. Figure 2.1 illustrates the plasma shape and the definition of the cylindrical and polar coordinates. For the axisymmetric configuration we define the z axis as the axis of revolution and we consider that any arbitrary quantity s, i.e. pressure, current density and magnetic field, do not vary as a function of the toroidal angle

$$\frac{\partial s}{\partial \phi} = 0.$$
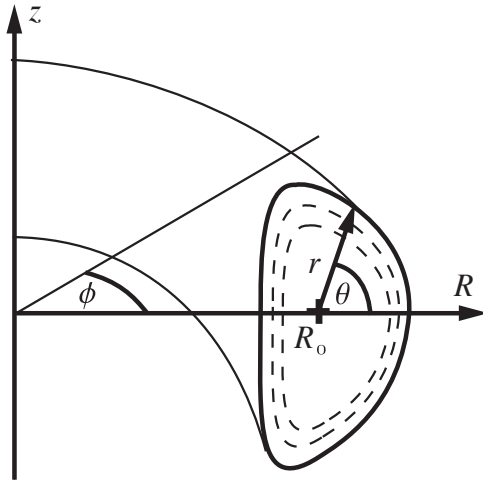
Figure 2.1: The axisymmetric configuration with the definition of the cylindrical coordinates (R, ϕ, z) and the polar coordinates (r, θ) in the poloidal sector. The dashed lines represent the magnetic surfaces (surfaces with constant pressure and magnetic flux) where the lines of the current and magnetic fields are located.

By defining the flux function Ψ as the poloidal flux per unit radian in ϕ we determine the poloidal magnetic field $\mathbf{B}_p = B_R \mathbf{e}_R + B_z \mathbf{e}_z$ which is related to (2.8) $\mathbf{B}_p \cdot \nabla \Psi = 0$ by

$$B_R = -\frac{1}{R}\frac{\partial \Psi}{\partial z}, \quad B_z = \frac{1}{R}\frac{\partial \Psi}{\partial R}. \tag{2.9}$$

Conforming to Maxwell's equations the poloidal magnetic field $\mathbf{B}_p$ satisfies

$$\nabla \cdot \mathbf{B} = \frac{1}{R}\frac{\partial (RB_R)}{\partial R} + \frac{\partial B_z}{\partial z} = 0.$$

The flux function Ψ is arbitrary with respect to an additive constant which is chosen for convenience. From the parallel properties of $\mathbf{j}$ and $\mathbf{B}$ it is clear that a current flux function also exists. We introduce such a function, denoted by f, which is related to the poloidal current density $\mathbf{j}_p = j_R \mathbf{e}_R + j_z \mathbf{e}_z$ by

$$j_R = -\frac{1}{R}\frac{\partial f}{\partial z}, \quad j_z = \frac{1}{R}\frac{\partial f}{\partial R}. \tag{2.10}$$

The comparison of (2.10) with Ampère's law $\nabla \times \mathbf{B} = \mu_0 \mathbf{j}$ leads to

$$j_R = -\frac{1}{\mu_0}\frac{\partial B_\phi}{\partial z}, \quad j_z = \frac{1}{\mu_0 R}\frac{\partial (RB_\phi)}{\partial R},$$

which gives the relation between f and the toroidal magnetic field as follows

$$f = \frac{RB_\phi}{\mu_0}. \tag{2.11}$$

Furthermore, it can be shown that f is a function of the flux Ψ. By taking the scalar product of $\mathbf{j}$ with the first equation of (2.5) to obtain $\mathbf{j} \cdot \nabla p = 0$, and by substituting $\mathbf{j}$ with (2.10) we obtain

$$\frac{\partial f}{\partial R}\frac{\partial p}{\partial z} - \frac{\partial f}{\partial z}\frac{\partial p}{\partial R} = 0,$$

which is equivalent to

$$\nabla f \times \nabla p = 0.$$

This proves that f is a function of p. Because of (2.7) and (2.8) resulting in $\mathbf{B} \cdot \nabla p = \mathbf{B} \cdot \nabla \Psi = 0$ the pressure is a function of the flux $p = p(\Psi)$ and therefore it follows that $f = f(\Psi)$.

We note that it is possible to define the total flux function over the whole torus circumference, denoted by Θ, by the simple substitution assuming axisymmetry

$$\Theta = 2\pi\Psi. \tag{2.12}$$

2.2.3   The Grad-Shafranov equation

The equilibrium of the tokamak plasma can be expressed as a partial differential equation, where the differentiated variable is the poloidal flux function Ψ. This equation, which contains two arbitrary functions, namely $p(\Psi)$ and $f(\Psi)$, is called the Grad-Shafranov equation.

The pressure and magnetic force balance equation (first equation of (2.5))

$$\nabla p = \mathbf{j} \times \mathbf{B}$$

can be written as

$$\mathbf{j}_p \times B_\phi \mathbf{e}_\phi + j_\phi \mathbf{e}_\phi \times \mathbf{B}_p = \nabla p, \tag{2.13}$$

where B_ϕ and j_ϕ are the toroidal components of the magnetic field and the current density, respectively. Equation (2.13) can be rewritten in terms of the flux function Ψ. We can express $\mathbf{B}_p$ defined by (2.9) and $\mathbf{j}_p$ defined by (2.10) more compactly

$$\mathbf{B}_p = \frac{1}{R}\left(\nabla\Psi \times \mathbf{e}_\phi\right) \tag{2.14}$$

and

$$\mathbf{j}_p = \frac{1}{R}\left(\nabla f \times \mathbf{e}_\phi\right). \tag{2.15}$$

Substituting these relations into (2.13) and noting that

$$\mathbf{e}_\phi \cdot \nabla\Psi = \mathbf{e}_\phi \cdot \nabla f = 0$$

gives

$$-\frac{B_\phi}{R}\nabla f + -\frac{j_\phi}{R}\nabla\Psi = \nabla p \tag{2.16}$$

We can write

$$\nabla f(\Psi) = \frac{df(\Psi)}{d\Psi}\nabla\Psi$$

and similarly for p

$$\nabla p(\Psi) = \frac{dp(\Psi)}{d\Psi}\nabla\Psi.$$

Substituting these relations into (2.16) gives

$$j_\phi = R\frac{dp}{d\Psi} + B_\phi\frac{df}{d\Psi}$$

and substituting (2.11) for B_ϕ gives

$$j_\phi = Rp'(\Psi) + \frac{\mu_0}{R}f(\Psi)f'(\Psi), \tag{2.17}$$

where $x'(\Psi)$ is defined as $\frac{dx(\Psi)}{d\Psi}$. To write j_ϕ as a function of Ψ we need Ampère's law (third equation of (2.5))

$$\mu_0\mathbf{j} = \nabla \times \mathbf{B}.$$

Substituting (2.9) into the toroidal component of the above equation results in

$$-\mu_0 Rj_\phi = R\frac{\partial}{\partial R}\left(\frac{1}{R}\frac{\partial\Psi}{\partial R}\right) + \frac{\partial^2\Psi}{\partial z^2}. \tag{2.18}$$

By substituting this for j_ϕ into (2.17) we obtain, finally, the Grad-Shafranov equation

$$R\frac{\partial}{\partial R}\left(\frac{1}{R}\frac{\partial\Psi}{\partial R}\right) + \frac{\partial^2\Psi}{\partial z^2} = -\mu_0 R^2 p'(\Psi) - \mu_0^2 f(\Psi)f'(\Psi). \tag{2.19}$$

In this equation the functions p and f, associated with the pressure and the poloidal current density can be chosen arbitrarily. The flux surfaces and profiles of j_ϕ, p and B_ϕ are typically obtained numerically.

The DINA code uses the "inverse variable" technique [56] to solve the Grad-Shafranov equation. For the first equilibrium calculation the functions Ψ, p and f are given by initial profiles (initial condition of the simulation). The time evolution of these three functions for the next iteration (time step) is then given by the transport equations which use the results of the equilibrium calculation. At this point a new equilibrium can be calculated.

2.3 The transport equations

The transport equations are required to compute the evolution in time of the plasma and the tokamak state in general. We will need the following 4 time differential equations which are derived from the fundamental physics:

- The magnetic field diffusion equation to compute the evolution of the magnetic fluxes and thus the magnetic fields.

- The density equation to get the evolution of the ion and electron density in the plasma.

- The energy balance equation to compute the evolution of the ion and electron pressure of the plasma.

- The electrical circuit equations to calculate the evolution of the currents (and thus current density) in the active and passive coils and the currents in the modelled filaments of the vacuum vessel.

To compute the evolution in time we have to integrate numerically this time differential equations. The pertinent question that can occur at this point is if we are seeking for partial time differential or absolute time differential equations. The absolute time derivation of a scalar or vectorial quantity $\mathbf{s}(\mathbf{r}, t)$ at position $\mathbf{r} = \begin{bmatrix} r_1 & r_2 & r_3 \end{bmatrix}^T$ and time t is defined by

$$\frac{d\mathbf{s}(\mathbf{r}, t)}{dt} = \lim_{\Delta t \to 0} \frac{\mathbf{s}(\mathbf{r} + \Delta \mathbf{r}, t + \Delta t) - \mathbf{s}(\mathbf{r}, t)}{\Delta t} = \lim_{\Delta t \to 0} \frac{\mathbf{s}(\mathbf{r} + \mathbf{u}(\mathbf{r})\Delta t, t + \Delta t) - \mathbf{s}(\mathbf{r}, t)}{\Delta t}, \quad (2.20)$$

where $\Delta \mathbf{r} = \mathbf{u}(\mathbf{r})\Delta t$ denotes the infinitesimal position variation and $\mathbf{u}(\mathbf{r}) = \frac{d\mathbf{r}}{dt}$ denotes the velocity of the quantity $\mathbf{s}(\mathbf{r}, t)$ at position $\mathbf{r}$. In contrast, the partial time derivation is defined by

$$\frac{\partial \mathbf{s}(\mathbf{r}, t)}{\partial t} = \lim_{\Delta t \to 0} \frac{\mathbf{s}(\mathbf{r}, t + \Delta t) - \mathbf{s}(\mathbf{r}, t)}{\Delta t}. \quad (2.21)$$

The link between a partial time derivation and an absolute time derivation is given by the relation

$$\begin{aligned}
\frac{d\mathbf{s}(\mathbf{r}, t)}{dt} &= \lim_{\Delta t \to 0} \frac{\mathbf{s}(\mathbf{r}, t + \Delta t) - \mathbf{s}(\mathbf{r}, t)}{\Delta t} + \lim_{\Delta t \to 0} \frac{\mathbf{s}(\mathbf{r} + \Delta \mathbf{r}, t) - \mathbf{s}(\mathbf{r}, t)}{\Delta t} \\
&= \frac{\partial \mathbf{s}(\mathbf{r}, t)}{\partial t} + \sum_{i=1}^{3} \frac{\partial \mathbf{s}(\mathbf{r}, t)}{\partial r_i} \frac{dr_i}{dt} \\
&= \frac{\partial \mathbf{s}(\mathbf{r}, t)}{\partial t} + (\mathbf{u} \cdot \nabla)\mathbf{s}(\mathbf{r}, t).
\end{aligned} \quad (2.22)$$

Consider Euler's first order integration method where the finite time step is denoted as Δt and where $\Delta \mathbf{r} = \mathbf{u}(\mathbf{r})\Delta t$. Then the integration of the absolute time derivative (2.20) results in

$$\mathbf{s}(\mathbf{r} + \Delta \mathbf{r}, t + \Delta t) = \mathbf{s}(\mathbf{r}, t) + \frac{d\mathbf{s}(\mathbf{r}, t)}{dt} \Delta t + \mathcal{O}(\Delta t^2), \quad (2.23)$$

while the integration of the partial time derivative (2.21) results in

$$\mathbf{s}(\mathbf{r}, t + \Delta t) = \mathbf{s}(\mathbf{r}, t) + \frac{\partial \mathbf{s}(\mathbf{r}, t)}{\partial t} \Delta t + \mathcal{O}(\Delta t^2). \quad (2.24)$$

Usually, the evolution in time at a fixed position $\mathbf{r}$ (fixed grid) is sought and thus we need to use time differential equations with partial time derivatives. Note, that there exists also integration methods with moving points (moving grid) where the absolute time derivatives are used. DINA uses a fixed grid numerical method and we therefore have to seek transport equations formulated with solely partial time derivatives.

2.3.1   Magnetic field diffusion equation

We apply the operator $\nabla \times$ to Ampère's law (2.1). By substituting $\mathbf{j}$ by Ohm's law (2.1) and assuming that the electrical conductivity σ is constant in space we obtain

$$\nabla \times \nabla \times \mathbf{B} = \mu_0 \sigma \left[\nabla \times \mathbf{E} + \nabla \times (\mathbf{u} \times \mathbf{B}) \right]. \quad (2.25)$$

We replace $\nabla \times \mathbf{E}$ by using Faraday's law (2.1). Then by using the vector identity relation

$$\nabla \times \nabla \times \mathbf{B} = -\nabla^2 \mathbf{B} + \nabla \nabla \cdot \mathbf{B}, \quad (2.26)$$

considering $\nabla \cdot \mathbf{B} = 0$ from (2.1) and rearranging the terms we obtain the fundamental equation of the MHD describing the magnetic field in a conducting fluid

$$\frac{\partial \mathbf{B}}{\partial t} = \nabla \times (\mathbf{u} \times \mathbf{B}) + \eta \nabla^2 \mathbf{B}, \tag{2.27}$$

where we define the magnetic diffusion factor

$$\eta = \frac{1}{\mu_0 \sigma}. \tag{2.28}$$

The first term in the right-hand side expression of (2.27) expresses that movements of the fluid ($\mathbf{u} \neq 0$) may amplify or reduce the magnetic field. On the other hand, the second term expresses that, if the magnetic diffusion factor $\eta \neq 0$, the spatial and temporal magnetic field fluctuations are dissipated. The dissipation is due to the Joule effect: the currents produced by the magnetic field $\mathbf{B}$ encounter a resistance which is not zero since the conductivity $\sigma \neq \infty$. The phenomenon of magnetic diffusion can also be expressed in terms of the partial time derivative of the magnetic flux $\partial \Theta / \partial t$, which constitutes the formulation used in the DINA code for calculating the evolution of the magnetic flux in time.

Consider an arbitrary area S and its contour L which is permeated by the magnetic field $\mathbf{B}$. Then the total flux Θ flowing through S is given by

$$\Theta = \int_S \mathbf{B} \cdot d\mathbf{S}.$$

By comparing with the magnetic field diffusion equation (2.27) it follows that the partial time derivative of the flux Θ depends only on the magnetic diffusion term

$$\frac{\partial \Theta}{\partial t} = \int_S \frac{\partial \mathbf{B}}{\partial t} \cdot d\mathbf{S} = \int_S \left(\nabla \times (\mathbf{u} \times \mathbf{B}) + \eta \nabla^2 \mathbf{B} \right) \cdot d\mathbf{S}. \tag{2.29}$$

Therefore, when the plasma is not moving, i.e. $\mathbf{u} = 0$, then for an ideal MHD, where $\sigma = \infty$ and thus $\eta = 0$, the flux Θ remains constant and we say that the magnetic field is "frozen".

We can reformulate equation (2.29) by applying the vector identity equation (2.26) with $\nabla \cdot \mathbf{B} = 0$ and Stokes's theorem which leads to

$$\frac{\partial \Theta}{\partial t} = \int_S \left(\nabla \times (\mathbf{u} \times \mathbf{B}) - \eta \nabla \times \nabla \times \mathbf{B} \right) \cdot d\mathbf{S} = \oint_L \left(\mathbf{u} \times \mathbf{B} - \eta \nabla \times \mathbf{B} \right) \cdot d\mathbf{l} \tag{2.30}$$

$$= \oint_L \left(\mathbf{u} \times \mathbf{B} - \frac{1}{\sigma} \mathbf{j} \right) \cdot d\mathbf{l}.$$

This is a general expression of the partial time derivative of the flux Θ as a function of the magnetic field due to the magnetic diffusion.

In the case of the axisymmetric tokamak the right-hand side of equation (2.30) can be reformulated as follows. Consider as illustrated in Figure 2.2 the points $A = (0, z_0)$, $B = (R_0, z_0)$, $C = (R, z)$ and $D = (0, z)$ in the (R,z) plane. We define the areas $S_{\overline{AB}}$, $S_{\overline{BC}}$ and $S_{\overline{CD}}$ as the revolving sections $\overline{AB}$, $\overline{BC}$ and $\overline{CD}$ around the z axis, respectively. The magnetic fluxes flowing through these areas are denoted by $\Theta_{\overline{AB}}$, $\Theta_{\overline{BC}}$ and $\Theta_{\overline{CD}}$. Note that the fluxes $\Theta_{\overline{BC}}$ and $\Theta_{\overline{CD}}$ are varying as functions of R and z while the flux $\Theta_{\overline{AB}}$ remains constant
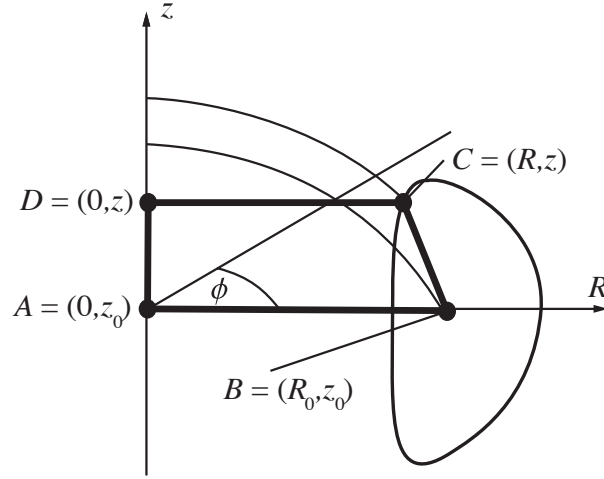
Figure 2.2: Illustration of the points $A = (0, z_0)$, $B = (R_0, z_0)$, $C = (R, z)$ and $D = (0, z)$ in the (R,z) plane.

$$\Theta_{\text{const}} = \Theta_{\overline{AB}} = \text{const.}$$

Moreover, the total poloidal flux Θ defined in (2.12) is

$$\Theta = \Theta_{\overline{BC}}.$$

Since due to the axisymmetry the section $\overline{DA}$ is part of a magnetic field line we can write the flux relation

$$\begin{aligned} \Theta_{\overline{CD}} &= \Theta_{\overline{AB}} - \Theta_{\overline{BC}} \\ &= \Theta_{\text{const}} - \Theta. \end{aligned} \tag{2.31}$$

Since the area $S_{\overline{CD}}$ is a disc parallel to the plane (R, ϕ) with the contour $L_{\overline{CD}}$ the infinitesimal length vector of $L_{\overline{CD}}$ is given by

$$d\mathbf{l} = \mathbf{e}_\phi \, R d\phi.$$

By means of (2.30) and since due to the axisymmetry $\mathbf{B}$ is not a function of ϕ we can express the partial time derivative of $\Theta_{\overline{CD}}$ as follows

$$\frac{\partial \Theta_{\overline{CD}}}{\partial t} = \oint_0^{2\pi} \left(\mathbf{u} \times \mathbf{B} - \frac{1}{\sigma}\mathbf{j} \right) \cdot \mathbf{e}_\phi \, R d\phi = 2\pi R \left(\mathbf{u} \times \mathbf{B} - \frac{1}{\sigma}\mathbf{j} \right) \cdot \mathbf{e}_\phi. \tag{2.32}$$

This equation shows that only the toroidal element of $\mathbf{u} \times \mathbf{B}$ and of $\mathbf{j}$ is relevant and thus

$$(\mathbf{u} \times \mathbf{B}) \cdot \mathbf{e}_\phi = u_z B_R - u_R B_z \qquad \text{and} \qquad \mathbf{j} \cdot \mathbf{e}_\phi = j_\phi.$$

By noting that due to (2.31) and (2.12) we have

$$\frac{\partial \Theta_{\overline{CD}}}{\partial t} = -\frac{\partial \Theta}{\partial t} = -2\pi \frac{\partial \Psi}{\partial t}$$

we finally obtain

$$\frac{\partial \Psi}{\partial t} = R \left(\frac{1}{\sigma} j_\phi + u_R B_z - u_z B_R \right). \tag{2.33}$$

2.3.2 Density equation

The density equation consists of the continuity equation to which we add a source term to describe an injection or a removal of ions and electrons. Therefore, the variation in time of the density of the ith ion species is described by

$$\frac{\partial n_i}{\partial t} + \nabla \cdot (n_i \mathbf{u}_i) = S_i, \tag{2.34}$$

where S_i denotes the source term, n_i the density and $\mathbf{u}_i$ the velocity of the flow of the ion species. The density equation for electrons is similarly given by

$$\frac{\partial n_e}{\partial t} + \nabla \cdot (n_e \mathbf{u}_e) = S_e. \tag{2.35}$$

The DINA code presently approximates the density equations (2.34) and (2.35) by assuming that the velocity of the electrons and ions can be neglected ($\mathbf{u}_i = \mathbf{u}_e = 0$), which results in a simplified form, i.e.

$$\frac{\partial n_i}{\partial t} = S_i \qquad \text{and} \qquad \frac{\partial n_e}{\partial t} = S_e. \tag{2.36}$$

2.3.3 Energy balance equation

If the viscosity terms are neglected, the energy balance equation or power balance equation is given by [12]

$$\frac{3}{2}\frac{\partial p_a}{\partial t} + \nabla \cdot \left(\frac{3}{2}p_a \mathbf{u}_a\right) + p_a \nabla \cdot \mathbf{u}_a + \nabla \cdot \mathbf{q}_a = \tilde{Q}_a, \tag{2.37}$$

where p_a is the pressure, $\mathbf{u}_a$ the velocity, $\mathbf{q}_a$ the heat flux and $\tilde{Q}_a$ expresses the heat generated in the plasma. The index a determines if we consider the energy balance equation of the ions (a=i) or electrons (a=e). With the relation

$$\nabla \cdot (p_a \mathbf{u}_a) = \mathbf{u}_a \cdot \nabla p_a + p_a \nabla \cdot \mathbf{u}_a \tag{2.38}$$

we can substitute the term $p_a \nabla \cdot \mathbf{u}_a$ in Equation (2.37) leading to

$$\frac{3}{2}\frac{\partial p_a}{\partial t} + \nabla \cdot \left(\frac{5}{2}p_a \mathbf{u}_a\right) - \mathbf{u}_a \cdot \nabla p_a + \nabla \cdot \mathbf{q}_a = \tilde{Q}_a. \tag{2.39}$$

From Equations (2.2) and (2.3) we can express the velocity $\mathbf{u}_a$ as

$$\mathbf{u}_a = \mathbf{u} + \mathbf{u}_{j_a} = \mathbf{u} + \epsilon(a)\frac{1}{en}\mathbf{j}_a, \tag{2.40}$$

where $\epsilon(i) = 1$ and $\epsilon(e) = -1$. By assuming a **quasi plasma equilibrium** we can simplify the terms $\mathbf{u}_a \cdot \nabla p_a$ and $p_a \nabla \cdot \mathbf{u}_a$ by means of Equation (2.7), i.e.

$$\mathbf{j} \cdot \nabla p = 0$$

and by using the fact that $\nabla \cdot \mathbf{j} = 0$ because of Ampère's law and the fact that $\nabla \cdot \nabla \times \mathbf{A} = 0$ for any arbitrary chosen vector field $\mathbf{A}$. This leads to following simplifications

$$\mathbf{u}_a \cdot \nabla p_a = (\mathbf{u} + \epsilon(a)\frac{1}{en}\mathbf{j}_a) \cdot \nabla p_a = \mathbf{u} \cdot \nabla p_a,$$

$$p_a \nabla \cdot \mathbf{u}_a = p_a \nabla \cdot (\mathbf{u} + \epsilon(a)\frac{1}{en}\mathbf{j}_a) = p_a \nabla \cdot \mathbf{u}$$

and Equation (2.39) becomes

$$\frac{3}{2}\frac{\partial p_a}{\partial t} + \nabla \cdot \left(\frac{5}{2}p_a\mathbf{u}\right) - \mathbf{u} \cdot \nabla p_a + \nabla \cdot \mathbf{q}_a = \tilde{Q}_a. \tag{2.41}$$

The heat generated in the plasma for the ions and the electrons is given by

$$\tilde{Q}_i = \mathbf{j}_i \cdot \mathbf{E} + Q_{ei} + Q_i$$

$$\tilde{Q}_e = \mathbf{j}_e \cdot \mathbf{E} - Q_{ei} + Q_e,$$

where $\mathbf{j}_i$ and $\mathbf{j}_e$ are the current densities due to the ions and the electrons, respectively. The first terms $\mathbf{j}_a \cdot \mathbf{E}$ express the heating due the ohmic resistivity of the plasma. Q_{ei} is the electron-ion heat exchange and Q_a are the source heating terms including charge-exchange losses for the ions and radiation losses for the electrons. Since $\mathbf{j}_e \gg \mathbf{j}_i$ and $\mathbf{j} = \mathbf{j}_e + \mathbf{j}_i$ we can approximate $\mathbf{j}_e \approx \mathbf{j}$ and $\mathbf{j}_i \approx 0$ which leads to

$$\tilde{Q}_i = Q_{ei} + Q_i \tag{2.42}$$

$$\tilde{Q}_e = \mathbf{j} \cdot \mathbf{E} - Q_{ei} + Q_e. \tag{2.43}$$

From Ohm's law of (2.1) and from the stationary flow equation (2.5) it can be deduced that

$$\mathbf{j} \cdot \mathbf{E} = \mathbf{u} \cdot (\mathbf{j} \times \mathbf{B}) + \frac{\mathbf{j}^2}{\sigma} = \mathbf{u} \cdot \nabla p_e + Q_{dg}, \tag{2.44}$$

where $Q_{dg} = \mathbf{j}^2/\sigma$.

From Equations (2.41)-(2.44) we obtain the energy balance equations for the ions and electrons

$$\frac{3}{2}\frac{\partial p_i}{\partial t} + \nabla \cdot \left(\mathbf{q}_i + \frac{5}{2}p_i\mathbf{u}\right) - \mathbf{u} \cdot \nabla p_i = Q_{ei} + Q_i, \tag{2.45}$$

$$\frac{3}{2}\frac{\partial p_e}{\partial t} + \nabla \cdot \left(\mathbf{q}_e + \frac{5}{2}p_e\mathbf{u}\right) - 2\,\mathbf{u} \cdot \nabla p_e = Q_{dg} - Q_{ei} + Q_e. \tag{2.46}$$

The DINA code presently approximates these energy balance equations by assuming that the velocity of the electrons and ions can be neglected ($\mathbf{u} = 0$). We usually also consider simplified expressions for both heat fluxes $\mathbf{q}_e$ and $\mathbf{q}_i$ by using the so-called "diagonal" model [34] where the fluxes are expressed as

$$\mathbf{q}_e = -\chi_e n_e \nabla T_e, \qquad \mathbf{q}_i = -\chi_i n_i \nabla T_i,$$

where χ_e and χ_i are the electron and ion thermal conductivities, respectively. By using the pressure temperature relation $n k_B T = p$ we obtain

$$\mathbf{q}_e = -\chi_e \frac{n_e}{k_B}\nabla\frac{p_e}{n_e}, \qquad \mathbf{q}_i = -\chi_i \frac{n_i}{k_B}\nabla\frac{p_i}{n_i}.$$

This results in the simplified energy balance equations

$$\frac{3}{2}\frac{\partial p_i}{\partial t} - \nabla \cdot (\chi_i \frac{n_i}{k_B}\nabla\frac{p_i}{n_i}) = Q_{ei} + Q_i \tag{2.47}$$

$$\frac{3}{2}\frac{\partial p_e}{\partial t} - \nabla \cdot (\chi_e \frac{n_e}{k_B}\nabla\frac{p_e}{n_e}) = Q_{dg} - Q_{ei} + Q_e, \tag{2.48}$$

$$\tag{2.49}$$

where the electron-ion heat exchange Q_{ei} is given by

$$Q_{ei} = 3\frac{m_e}{m_i}\frac{n_e}{\tau_e}(T_e - T_i) = \frac{3}{k_B}\frac{m_e}{m_i}\frac{n_e}{\tau_e}\left(\frac{p_e}{n_e} - \frac{p_i}{n_i}\right). \tag{2.50}$$

2.3.4 Electrical circuit equations for the active and passive coils and vacuum vessel

The active and passive toroidally axisymmetric coils and the vacuum vessel create a poloidal magnetic field. In what follows we define this poloidal magnetic field as the external magnetic field since it is not due to the toroidal plasma current but to the toroidal currents in the external conducting structure (active and passive coils and vacuum vessel). From Ohm's law we can write the toroidal current density creating the external poloidal field in the simple form

$$j_{\phi_{ext}} = \sigma E_{\phi_{ext}},$$

where $E_{\phi_{ext}}$ is the toroidal component of the electric field in the external conducting structure. The external conducting structure is subdivided in $n_c \in \mathbb{Z}^+$ small electrical circuits (filaments). For each ith circuit we define its position (R_i, z_i) (center of gravity point) in the (R, z) plane and its cross section $S_i = \Delta R_i \cdot \Delta z_i$ and we assume that the toroidal current density in each circuit j_i is homogeneous in the area S_i. With this, we define the toroidal current density in the external conducting structure as a function of (R, z)

$$j_{\phi_{ext}}(R, z) = \begin{cases} j_i & \text{if } (R, z) \in [R_i - \frac{\Delta R_i}{2}, R_i + \frac{\Delta R_i}{2}] \times [z_i - \frac{\Delta z_i}{2}, z_i + \frac{\Delta z_i}{2}] \\ & \text{for } i = 1, 2, 3 \ldots n_c \\ 0 & \text{elsewhere} \end{cases} \tag{2.51}$$

By considering Ohm's law for each circuit we obtain

$$j_i = \sigma_i E_i. \tag{2.52}$$

The electric field is given by

$$E_i = \frac{-\dot{\Psi}_i + V_i}{2\pi r_i},$$

where $-\dot{\Psi}_i$ is the induced voltage and V_i is the voltage applied to the ith circuit. By substituting the electric field with (2.52) we obtain

$$-\dot{\Psi}_i + V_i = \frac{2\pi r_i j_i}{\sigma_i}.$$

Since j_ϕ is homogeneous in every circuit the current density can be expressed as a function of the current $j_i = I_i/S_i$

$$-\dot{\Psi}_i + V_i = \Omega_i I_i \tag{2.53}$$

where $\Omega_i = 2\pi r_i / \sigma_i S_i$ is the resistivity of the element S_i.

The poloidal flux Ψ_i for each element is determined by

$$\Psi_i = L_i I_i + \sum_{j \neq i} M_{ij} I_j + \Psi_{ip},$$

where M_{ij} is the mutual inductance between the ith and jth circuit, L_i is the self-inductance of the ith circuit and Ψ_{ip} is the flux created by the plasma current in the

ith circuit. Applying equation (2.53) results in the differential equation expressing the time derivatives of the currents of the n_c circuits

$$L_i \dot{I}_i + \sum_{j \neq i} M_{ij} \dot{I}_j + \dot{\Psi}_{ip} + \Omega_i I_i = V_i, \tag{2.54}$$

where we assume that the mutual and self-inductances are time-independent since the circuits describe a solid conductor structure. This n_c differential equation can be expressed in a compact matrix form by defining a current, a voltage and a plasma-circuit flux vector

$$I = \begin{bmatrix} I_1 \\ I_2 \\ \vdots \\ I_{n_c} \end{bmatrix}, \qquad V = \begin{bmatrix} V_1 \\ V_2 \\ \vdots \\ V_{n_a} \\ 0 \\ \vdots \\ 0 \end{bmatrix} \quad \text{and} \quad \Psi_{cp} = \begin{bmatrix} \Psi_{1p} \\ \Psi_{2p} \\ \vdots \\ \Psi_{n_c p} \end{bmatrix}.$$

The first n_a circuits describe the active coil structure with their applied voltages $V_i \, \forall \, i \in \{1, 2, \ldots, n_a\}$, while the circuits for which $i > n_a$ describe the passive coil and vacuum vessel structure where the applied voltages are zero.

Similar to the conducting structure, the plasma area is subdivided in $n_{pl_c} \in \mathbb{Z}^+$ small electrical circuits (filaments). For each ith circuit we define its position (R_{pl_i}, z_{pl_i}) (center of gravity point) in the (R, z) plane and its cross section $S_{pl_i} = \Delta R_{pl_i} \cdot \Delta z_{pl_i}$ and we assume that the toroidal current density in each circuit j_{pl_i} is homogeneous in the area S_{pl_i}. With this, we define the plasma current density as a function of (R, z)

$$j_{\phi_{pl}}(R, z) = \begin{cases} j_{pl_i} & \text{if } (R, z) \in [R_{pl_i} - \frac{\Delta R_{pl_i}}{2}, R_{pl_i} + \frac{\Delta R_{pl_i}}{2}] \\ & \qquad \times [z_{pl_i} - \frac{\Delta z_{pl_i}}{2}, z_{pl_i} + \frac{\Delta z_{pl_i}}{2}] \quad \text{for } i = 1, 2, 3 \ldots n_{pl_c} \\ 0 & \text{elsewhere} \end{cases} \tag{2.55}$$

Furthermore, we define the plasma current vector

$$I_{pl} = \begin{bmatrix} I_{pl_1} \\ I_{pl_2} \\ \vdots \\ I_{pl_{n_{pl_c}}} \end{bmatrix},$$

where $I_{pl_i} = j_{pl_i} S_{pl_i}$ for $i = 1, 2, 3 \ldots n_{pl_c}$ represents the plasma current in each plasma circuit (filament). This allows us to express the plasma-circuit flux as a function of the plasma current

$$\Psi_{cp} = M_{cp} I_{pl},$$

where M_{cp} is the matrix containing the mutual inductances between the external conducting structure circuits and the plasma circuits.

The compact form of differential equations set (2.54) is given by

$$M\dot{I} + \frac{d\Psi_{cp}}{dt} + \Omega I = M\dot{I} + M_{cp}\frac{dI_{pl}}{dt} + \Omega I = V, \tag{2.56}$$

where

$$
M = \begin{bmatrix} L_1 & M_{12} & \cdots & M_{1n_c} \\ M_{12} & L_2 & \cdots & M_{2n_c} \\ \vdots & \vdots & \ddots & \vdots \\ M_{1n_c} & M_{2n_c} & \cdots & L_{n_c} \end{bmatrix} \quad \text{and} \quad \Omega = \begin{bmatrix} \Omega_1 & 0 & \cdots & 0 \\ 0 & \Omega_2 & \cdots & 0 \\ \vdots & \vdots & \ddots & \vdots \\ 0 & 0 & \cdots & \Omega_{n_c} \end{bmatrix}.
$$

By inverting the matrix M we obtain the derivative of the currents as a function of the currents, the voltages and the voltages induced by the plasma current

$$
\frac{dI}{dt} = -M^{-1}\Omega I + M^{-1}V - M^{-1}M_{cp}\frac{dI_{pl}}{dt}. \tag{2.57}
$$

Note that since the coils and the vacuum vessel are not moving the absolute time derivative is equal to the partial time derivative, i.e.

$$
\frac{\partial I}{\partial t} = \frac{dI}{dt}.
$$

2.4 Functional structure of DINA

2.4.1 Time step for the numerical integration

To express the evolution of the quantities, i.e. Ψ, n, p and j_ϕ, as a function of time we use the time variable t_n which corresponds to the time for the nth computing iteration. The time t_0 ($n = 0$) is defined as the inital time. The time interval between two iterations is given by $\Delta t_n = t_{n+1} - t_n$, referred to as the numerical integration time step. The time step Δt_n varies as a function of numerical integration convergence criteria presented in Section 2.4.5. There is a maximal and a minimal time step, referred to as Δt_{max} and Δt_{min}, respectively, which can be specified by the user. For each numerical integration step $\Delta t_n = t_{n+1} - t_n$ DINA starts with the maximal time step and reduces the time step if the convergence criteria are not satisfied until the minimal time step is reached. If for the minimal time step the convergence criteria are still not satisfied then DINA abandons the whole integration procedures with an error message. In this case the minimal time step has to be reduced by the user.

2.4.2 Normalised magnetic flux surface coordinate

For the description of the quantities in space we use the plane coordinates (R, z) and the normalised magnetic flux surface coordinate ρ. This coordinate takes values in the interval $\rho \in [0, 1]$ where each value corresponds to a constant poloidal magnetic flux surface ($\Psi = \text{const}$) which is located inside the plasma from the magnetic axis to the plasma edge (Figure 2.3). The definition of ρ relies on the toroidal flux Φ expressed as a function of the poloidal flux Ψ

$$
\Phi(\Psi) = \int_{S_\psi} \mathbf{B}_\phi \cdot d\mathbf{S}, \tag{2.58}
$$

where S_Ψ is the area enclosed by the magnetic contour $\Psi = c = \text{const}$ in the (R, z) plane. The toroidal magnetic field $\mathbf{B}_\phi = B_\phi(R, z)\mathbf{e}_\phi$ is derived from $f(\Psi)$ since it is given by

Equation (2.11), i.e.

$$B_\phi(R, z) = \frac{\mu_0 f(\Psi)}{R}.$$

Since we are seeking a ρ which is only defined in the plasma we define the fluxes at the two magnetic flux boundaries of the plasma:

1. The magnetic axis (R_0, z_0) where we consider $\Psi_0 = 0$, where the enclosed area is trivially $S_{\Psi 0} = 0$ and thus the toroidal magnetic flux $\Phi_0(\Psi_0) = 0$.

2. The plasma edge where we define the poloidal flux $\Psi_e = c_e \in \mathbb{R}^+$, the enclosed area $S_{\Psi e}$ and the toroidal magnetic flux $\Phi_e(\Psi_e) \in \mathbb{R}^+$.

This leads to the definition of the normalised magnetic flux surface coordinate

$$\rho(\Psi) = \sqrt{\frac{\Phi(\Psi)}{\Phi_e(\Psi_e)}} \in [0, 1]. \tag{2.59}$$

Since Ψ is a function of (R, z) the normalised magnetic flux surface coordinate ρ is also a function of (R, z), denoted as $\rho(R, z)$.
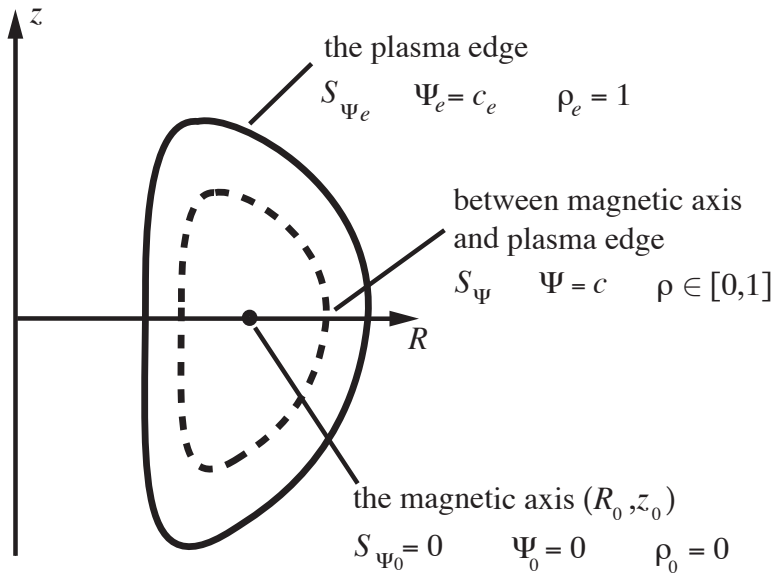
Figure 2.3: Illustration of the normalised magnetic flux surface coordinate ρ.

2.4.3 Computing the poloidal flux Ψ

The poloidal flux Ψ is computed by solving the **Grad-Shafranov** equation given by equation (2.18), i.e.

$$R\frac{\partial}{\partial R}\left(\frac{1}{R}\frac{\partial \Psi}{\partial R}\right) + \frac{\partial^2 \Psi}{\partial z^2} = -\mu_0 R j_\phi \tag{2.60}$$

by means of the "inverse variable" technique [56]. For the nth iteration we assume that the toroidal current density profile is given by

$$j_\phi(t_n, R, z) = j_{\phi_{ext}}(t_n, R, z) + j_{\phi_{pl}}(t_n, R, z), \tag{2.61}$$

where $j_{\phi_{ext}}(t_n, R, z)$, denoting the current density in the external conducting structure (active and passive coils and vacuum vessel), is given by equation (2.51). The quantity $j_{\phi_{pl}}(t_n, R, z)$ denotes the toroidal current density in the plasma which is given by equation (2.17) and expresses the toroidal current density as a function of the derivation of the pressure $p'(\Psi)$, the poloidal current density function $f(\Psi)$ and its derivative $f'(\Psi)$

$$j_{\phi_{pl}} = Rp'(\Psi) + \frac{\mu_0}{R} f(\Psi) f'(\Psi). \tag{2.62}$$

For the first iteration $n = 0$ at t_0, initial conditions are needed. For $j_{\phi_{ext}}(t_0, R, z)$ we use the initial currents in the active and passive coils and in the vacuum vessel (section 2.3.4). For the toroidal plasma current density $j_{\phi_{pl}}(t_0, R, z)$ we need an initial pressure profile $p(\Psi)$ to compute $p'(\Psi)$ and an initial poloidal current profile $f(\Psi)$ to compute $f(\Psi)f'(\Psi)$.

The numerical solution of the Grad-Shafranov equation (2.60) at the nth iteration gives the poloidal flux $\Psi(t_n, R, z)$. The constant flux surfaces are computed by solving $\Psi(t_n, R, z) = \text{const}$. This permits us to express the poloidal flux as a function of the normalised magnetic flux surface $\Psi(t_n, \rho) = \text{const}$.

2.4.4 Computing the evolution of the poloidal flux, the densities and the pressures

The evolution in time of the poloidal flux, the electron and ion densities and pressures are solely computed in one dimension, i.e. as a function of the normalised magnetic flux surface coordinate ρ. Thus, the partial time derivatives which are required to compute the evolution have to be averaged over the magnetic surfaces for which $\rho = \text{const}$ and $\Psi = \text{const}$. When we define any scalar or vectorial quantity as A then the average of A over a magnetic surface, referred to as S, is defined as

$$\langle A \rangle = \frac{\partial}{\partial V} \int_V A dV = \frac{1}{V'} \int_S A \frac{1}{|\nabla \rho|} dS, \tag{2.63}$$

where

$$V' = \frac{\partial V}{\partial \rho} = \int_S \frac{1}{|\nabla \rho|} dS \tag{2.64}$$

and V is the volume enclosed inside the magnetic surface S. A more detailed discussion concerning the average over magnetic surfaces is given in [34, 56].

The computation of the evolution in time from t_n to t_{n+1} of the flux $\Psi(\rho)$, the densities $n_{e,i}(\rho)$ and the electron and ion pressures $p_{e,i}(\rho)$ is done by numerical integration over the time step Δt_n, referred as to $\text{Int}(\cdot, \cdot, \Delta t_n)$. For the numerical integration the implicit first order integration method is used. The following 3 partial differential equations are applied:

- The **magnetic field diffusion** equation (2.33)

$$\frac{\partial \Psi(\rho)}{\partial t} = \left\langle R \left(\frac{1}{\sigma} j_\phi + u_R B_z - u_z B_R \right) \right\rangle, \tag{2.65}$$

where the poloidal flux for the next iteration $n + 1$ is computed by

$$\Psi(t_{n+1}, \rho) = \text{Int} \left(\Psi(t_n, \rho), \frac{\partial \Psi(\rho)}{\partial t}, \Delta t_n \right). \tag{2.66}$$

- The simplified **density** equations (2.36)

$$\frac{\partial n_{e,i}(\rho)}{\partial t} = \langle S_{e,i} \rangle. \tag{2.67}$$

where the densities for the next iteration $n+1$ is computed by

$$n_{e,i}(t_{n+1}, \rho) = \text{Int}\left(n_{e,i}(t_n, \rho), \frac{\partial n_{e,i}(\rho)}{\partial t}, \Delta t_n\right). \tag{2.68}$$

- The simplified **energy** equations for the electrons (2.48) and ions (2.47)

$$\frac{\partial p_e(\rho)}{\partial t} = \frac{2}{3}\left\langle \nabla \cdot \left(\chi_e \frac{n_e}{k_B} \nabla \frac{p_e}{n_e}\right) - Q_{ei} + Q_{dg} + Q_e \right\rangle \tag{2.69}$$

$$\frac{\partial p_i(\rho)}{\partial t} = \frac{2}{3}\left\langle \nabla \cdot \left(\chi_i \frac{n_i}{k_B} \nabla \frac{p_i}{n_i}\right) + Q_{ei} + Q_i \right\rangle, \tag{2.70}$$

where the pressures for the next iteration $n+1$ are computed by

$$p_{e,i}(t_{n+1}, \rho) = \text{Int}\left(p_{e,i}(t_n, \rho), \frac{\partial p_{e,i}(\rho)}{\partial t}, \Delta t_n\right). \tag{2.71}$$

Note that for the sake of simplicity the applied averaged technique presented here is somewhat simplified compared to the actual averaged technique used in DINA. For example, the average of the partial time derivative of the poloidal flux (Equation (2.65)) is derived in a different manner. It turns out that for DINA the plasma velocities u_R and u_z are neglected. The detailed derivation and application of the averaged technique for DINA is given in [34, 56].

The poloidal flux $\Psi(t_n, \rho)$ for every iteration results from the solution of the Grad-Shafranov equation. For the density and pressures initial profiles (iteration $n = 0$) are required, referred to as $n_{e,i}(t_0, \rho)$ and $p_{e,i}(t_0, \rho)$, respectively.

It remains to compute the evolution of $p' = \frac{\partial p}{\partial \Psi}$, f and $f' = \frac{\partial f}{\partial \Psi}$ to obtain the evolution of the toroidal current density of the plasma $j_{\phi_{pl}}(t_{n+1}, R, z)$ and the toroidal magnetic field $B_\phi(t_{n+1}, R, z)$.

The evolution of p' is straightforward since $p(t_{n+1}, \rho)$ is known from Equation (2.71). Note that the total pressure p is the sum of the electron and ion pressures ($p = p_e + p_i$). Thus, since $\rho(\Psi)$ is a function of Ψ we obtain

$$p'(t_{n+1}, \Psi) = \frac{\partial p(t_{n+1}, \Psi)}{\partial \Psi} = \frac{\partial p(t_{n+1}, \rho)}{\partial \rho} \frac{\partial \rho}{\partial \Psi}. \tag{2.72}$$

For the evolution of f' we have to apply the Grad-Shafranov equation (Equations (2.18) and (2.19)) and take the average over the magnetic surfaces ($\Psi = \text{const}$), i.e.

$$\left\langle \frac{j_{\phi_{pl}}}{R} \right\rangle = -\frac{1}{\mu_0}\left\langle \frac{1}{R}\left[\frac{\partial}{\partial R}\left(\frac{1}{R}\frac{\partial \Psi}{\partial R}\right) + \frac{1}{R}\frac{\partial^2 \Psi}{\partial z^2}\right]\right\rangle = p'(\Psi) + \mu_0 f(\Psi) f'(\Psi)\left\langle \frac{1}{R^2} \right\rangle. \tag{2.73}$$

Since $p'(t_{n+1}, \Psi)$ and $\Psi(t_{n+1}, \rho)$ (Equation (2.66)) are known and since ρ is a function of (R, z) we can solve Equation (2.73) for $f(t_{n+1}, \Psi) f'(t_{n+1}, \Psi)$, i.e.

$$f(t_{n+1}, \Psi) f'(t_{n+1}, \Psi) = \frac{1}{\mu_0 \left\langle \frac{1}{R^2} \right\rangle}\left(\left\langle \frac{j_{\phi_{pl}}(t_{n+1}, \Psi)}{R} \right\rangle - p'(t_{n+1}, \Psi)\right), \tag{2.74}$$

where

$$\left\langle \frac{j_{\phi_{pl}}(t_{n+1},\Psi)}{R} \right\rangle = -\frac{1}{\mu_0} \left\langle \frac{1}{R^2} \frac{\partial^2 \Psi(t_{n+1},\rho)}{\partial \rho^2} \left[\left(\frac{\partial \rho}{\partial R}\right)^2 + \left(\frac{\partial \rho}{\partial z}\right)^2 \right] \right\rangle \qquad (2.75)$$
$$-\frac{1}{\mu_0} \left\langle \frac{1}{R^2} \frac{\partial \Psi(t_{n+1},\rho)}{\partial \rho} \left[\frac{\partial^2 \rho}{\partial R^2} - \frac{1}{R}\frac{\partial \rho}{\partial R} + \frac{\partial^2 \rho}{\partial z^2} \right] \right\rangle.$$

From Equation (2.17) we obtain the toroidal current density in the plasma for the next iteration

$$j_{\phi_{pl}}(t_{n+1},R,z) = Rp'(t_{n+1},\Psi) + \frac{\mu_0}{R} f(t_{n+1},\Psi)f'(t_{n+1},\Psi). \qquad (2.76)$$

Furthermore, since

$$2ff' = \frac{\partial f^2}{\partial \Psi}$$

$f(t_{n+1},\Psi)$ is obtained by integrating and by taking the square root, i.e.

$$f(t_{n+1},\Psi) = \sqrt{\int \frac{\partial f^2(t_{n+1},\Psi)}{\partial \Psi} \frac{\partial \Psi}{\partial \rho} d\rho} = \sqrt{2 \int f(t_{n+1},\Psi)f'(t_{n+1},\Psi) \frac{\partial \Psi}{\partial \rho} d\rho}. \qquad (2.77)$$

Therefore from Equation (2.11) and since ρ and thus Ψ are functions of (R,z) we obtain the toroidal magnetic field in the plasma for the next iteration

$$B_\phi(t_{n+1},R,z) = \frac{\mu_0 f(t_{n+1},\Psi)}{R} = \frac{\mu_0 f(t_{n+1},R,z)}{R}. \qquad (2.78)$$

2.4.5   Convergence criteria

After each numerical integration step $\Delta t_n = t_{n+1} - t_n$ DINA checks by means of convergence criteria if the resulting evolution due to the numerical integration is self-consistent. There are a criterion on the evolution of the poloidal flux and two criteria on the evolution of the vertical plasma position, referred to as z_{pl}. The vertical plasma position is computed by deriving the center of gravity of the toroidal plasma current density $j_{\phi_{pl}}$, i.e.

$$z_{pl} = \frac{\int_{S_{\Psi_e}} z \, j_{\phi_{pl}}(R,z)dS}{\int_{S_{\Psi_e}} j_{\phi_{pl}}(R,z)dS},$$

where S_{Ψ_e} is the area in the (R,z) plane enclosed by the plasma edge. The 3 different criteria are defined as follows:

- The evolution of Ψ during Δt_n given by

$$\Delta \Psi_n(\rho) = \Psi(t_{n+1},\rho) - \Psi(t_n,\rho)$$

has to satisfy

$$|\Delta \Psi_n(\rho)| < \epsilon_{\Delta\Psi} \; \forall \rho \in [0,1] \quad \text{where} \quad \epsilon_{\Delta\Psi} \in \mathbb{R}^+.$$

- The evolution of z_{pl} during Δt_n given by

$$\Delta z_{pl_n} = z_{pl}(t_{n+1}) - z_{pl}(t_n)$$

  has to satisfy

$$|\Delta z_{pl_n}| < \epsilon_{\Delta z_{pl}} \quad \text{where} \quad \epsilon_{\Delta z_{pl}} \in \mathbb{R}^+.$$

- The average velocity of the vertical plasma position during Δt_n given by

$$\Delta \dot{z}_{pl_n} = \frac{\Delta z_{pl_n}}{\Delta t_n}$$

  has to satisfy

$$|\Delta \dot{z}_{pl_n}| < \epsilon_{\Delta \dot{z}_{pl}} \quad \text{where} \quad \epsilon_{\Delta \dot{z}_{pl}} \in \mathbb{R}^+.$$

The criteria constants $\epsilon_{\Delta \Psi}$, $\epsilon_{\Delta z_{pl}}$ and $\epsilon_{\Delta \dot{z}_{pl}}$ may be changed by the user.

If the criteria are not satisfied then the integration step Δt_n is reduced and the numerical integration procedure described in Section 2.4.4 has to be repeated.

2.4.6   Computing the evolution of the currents in the active and passive coils and the vacuum vessel

Once the convergence criteria are satisfied it remains for us to compute the evolution of the currents in the **active and passive coils and vacuum vessel circuits** by means of Equation (2.57), i.e.

$$\frac{dI}{dt} = -M^{-1}\Omega I + M^{-1}V - M^{-1}M_{cp}\frac{dI_{pl}}{dt}. \tag{2.79}$$

The time derivative of the plasma current filaments is approximated by taking the mean time derivative during Δt_n, i.e.

$$\frac{dI_{pl}}{dt} \approx \frac{I_{pl}(t_{n+1}) - I_{pl}(t_n)}{\Delta t_n},$$

where $I_{pl}(t_{n+1})$ and $I_{pl}(t_n)$ are derived from $j_{\phi_{pl}}(t_{n+1}, R, z)$ and $j_{\phi_{pl}}(t_n, R, z)$, respectively.

The circuit currents for the next iteration $n + 1$ are computed by

$$I(t_{n+1}) = \text{Int}\left(I(t_n), \frac{dI}{dt}, \Delta t_n\right). \tag{2.80}$$

From this the external toroidal current density $j_{\phi_{ext}}(t_{n+1}, R, z)$ can be derived as described in Section 2.3.4.

Finally, we obtain the whole toroidal current density

$$j_\phi(t_{n+1}, R, z) = j_{\phi_{ext}}(t_{n+1}, R, z) + j_{\phi_{pl}}(t_{n+1}, R, z). \tag{2.81}$$

2.4.7 The functional structure summary

Figure 2.4 illustrates schematically the functional structure of DINA. One iteration step of DINA can be summarised by following sequential main steps:

1. Solving the Grad-Shafranov equation by means of the toroidal current density $j_\phi(t_n, R, z)$ to get the poloidal flux $\Psi(t_n, R, z)$.

2. Computing the normalised magnetic flux surface coordinate to get $\Psi(t_n, \rho)$.

3. Integrating the flux diffusion, the density and the energy equations to get $\Psi(t_{n+1}, \rho)$, $n_{e,i}(t_{n+1}, \rho)$ and $p_{e,i}(t_{n+1}, \rho)$.

4. Computing the poloidal current function $f(t_{n+1}, \Psi)$ and the toroidal plasma current density $j_{\phi_{pl}}(t_{n+1}, R, z)$.

5. Verifying the convergence criteria. If the criteria are not satisfied then the integration time step Δt_n is reduced and the steps from step 3. have to be reiterated.

6. Integrating the active and passive coils and the vacuum structure equations to get the external toroidal current density $j_{\phi_{ext}}(t_{n+1}, R, z)$.

Initial poloidal
current function

$f(t_0, \Psi)$

Initial currents in the
circuit structure

$j_{\phi_{ext}}(t_o, R, z)$

Initial plasma current density
profile

$j_{\phi_{pl}}(t_o, R, z) = Rp'(\Psi) + \frac{\mu_0}{R}f(\Psi)f'(\Psi)$

Current density profile

| $j_\phi(t_n, R, z)$ | $=$ | $j_{\phi_{ext}}(t_n, R, z)$ | $+$ | $j_{\phi_{pl}}(t_n, R, z)$ |

Solving the
Grad−Shafranov
equation

Integration of active and
passive coils and vacuum
vessel equations

$\frac{dI_{pl}}{dt}$

Currents in
plasma filaments

$j_{\phi_{ext}}(t_{n+1}, R, z)$

$j_{\phi_{pl}}(t_{n+1}, R, z)$

$\Psi(t_n, R, z)$

Normalised magnetic
flux surface coordinate

satisfied

not satisfied   *Convergence*
                         criteria

Δt_n

$\Psi(t_n, \rho)$

Initial density
profile

$n_{e,i}(t_o, \rho)$

Initial pressure
profile

$p_{e,i}(t_o, \rho)$

Integration of
flux diffusion
equation

$n_{e,i}(t_n, \rho)$

$p_{e,i}(t_n, \rho)$

Integration of
density equation

Integration of
energy equation

$\Psi(t_{n+1}, \rho)$

$n_{e,i}(t_{n+1}, \rho)$

$p_{e,i}(t_{n+1}, \rho)$

$f(t_{n+1}, \Psi)$

Computing the toroidal
plasma current density
and the poloidal current
function f

Temperature
$T_{e,i}(t_{n+1}, \rho)$

$j_{\phi_{pl}}(t_{n+1}, R, z)$

Figure 2.4: Functional structure scheme of the DINA code.

Chapter 3

Comparing TCV experimental VDE responses with DINA code simulations

3.1   Introduction

In previous work [33] DINA showed good agreement with the effects of Poloidal Field (PF) control coil voltage pulses in TCV. A nonlinear response due to one of the perturbations significantly changing the vertical field decay index and driving the closed loop unstable gave a first demonstration of nonlinear behaviour correctly modelled by DINA, including the full TCV feedback and diagnostic systems. DINA had also been used in the past to study Vertical Displacement Events (VDE) in the DIII-D tokamak [29].

The DINA code simulations presented in this chapter exploit discharges with different cross-sectional shapes and different vertical instability growth rates which were subjected to controlled VDEs. We exploit the large height of the TCV vacuum vessel to explore a second nonlinearity, namely one in which the spatial variation of the vacuum field is large enough to invalidate local linearisation of the plasma equilibrium response. A set of experiments carried out earlier to compare experimental and modelled growth rates [23] provided suitable data. Subsequently, similar experiments at higher growth rate were performed, but are not analysed here [24]. In the previous work, the initial, small amplitude growth rate was evaluated. We extend that work by reproducing the behaviour during the complete large vertical plasma displacement. This case cannot be modeled with a linear model because of the large amplitude nonlinearities due to the final large vertical position displacement and non-time-invariant nonlinearities since the growth rate γ changes as a function of the position and therefore of time. The DINA code has been cross-checked against all 14 of the VDE experiments with different growth rates ranging approximately from 100 rad/s to 300 rad/s and different plasma shapes carried out on limited plasmas in the TCV tokamak.

The main aim of the thesis is to study the effect of the power supply saturation on the closed-loop stability and to provide a new controller with enhanced stability properties. In general, the loss of the vertical position control (loss of stability) is due to large plasma disturbances. Thus, in order to determine the enhancement of the stability properties we have to bring the new controller to its stability limits by means of large disturbances. Such validations cannot be carried out on a tokamak like ITER in operation since the loss of control leads to a disruption which will cause damage to the machine. Thus,

simulations with either linear or nonlinear tokamak models are imperatively required before considering the implementation of the new controller on a tokamak in operation. A linear tokamak model will probably be inadequate since large disturbances can move its state outside its validity regions. Thus, an accurate nonlinear model is indispensable for this purpose. It is in particular important to focus on the vertical plasma displacement since a large disturbance leads to a large vertical plasma displacement. Therefore, a DINA validation by means of triggered VDEs is particularly helpful for the purposes of this thesis.

The remainder of the chapter is laid out as follows. In Section 3.2 we describe the procedure that we used to initiate the VDE and discuss the potential disagreements which can arise when comparing the results between LIUQE (a tokamak equilibrium reconstruction code [26]) and DINA simulations. In Section 3.3 we present a comparison of the DINA simulation data with experimental data from the TCV tokamak focusing on the VDE experiments. We also present a comparison of common equilibrium parameters like the plasma current I_p, the elongation κ, the triangularity δ, the safety factor q, the ratio between the averaged plasma kinetic pressure and the pressure of the poloidal magnetic field at the edge of the plasma β_p and the internal self inductance l_i. Section 3.4 deals specifically with the non-time-invariant growth rate γ. We compare the time-varying growth rate of the TCV experiment and DINA simulation with the evolution of the closed-loop growth rate calculated with the RZIP model at each equilibrium point. Section 3.5 closes the chapter with a discussion.

3.2 Experimental conditions

3.2.1 Initiating the VDE

In the TCV experiments the VDE was initiated by interrupting the feedback control of both the radial and vertical position (to avoid all effect on the vertical position) at $t = 0.45$ s. The power supply demand signal becomes the preprogrammed signal and the power supply remains active. Because of the plasma disturbances and noise, mainly generated by the power supply and the diagnostics, and due to the fact that the plasma is unstable in vertical direction, the VDE is immediately initiated. In a DINA simulation, a break off of the control does not cause a VDE due to the fact that the plasma is in equilibrium and no noise and disturbances are added to the simulation. Therefore, a disturbance had to be injected to cause an early loss of equilibrium and a subsequent VDE. Several trials had to be undertaken to find out which disturbance least pollutes the results. For the first tests we applied a trapezoidal feedforward voltage disturbance at $t = 0.45$ s during $t_p = 4$ ms to the E1 coil (Figure 3.1 shows the TCV vacuum vessel and PF coils). The sign and amplitude of the disturbance voltage determine the direction of the vertical displacement: upwards or downwards. It was found that the amplitude has to be huge (1000 V) to make sure that the displacement goes in the same direction as the experiment. In addition to this problem, the disturbance generates an overshoot or undershoot of the plasma current, according to the displacement direction and thus to the sign of the voltage. This overshoot or undershoot can be explained by the net flux induced by the perturbation. An I_p overshoot is illustrated in Figure 3.2 (top). To avoid this problem we used an antisymmetric disturbance on the E1 and E8 coils (Figure 3.1) with the amplitude as small as possible and a period of only $t_p = 2$ ms. As

shown on Figure 3.2 (bottom), this solution clearly prevents the overshoot of the plasma current because of the vertical anti-symmetry of the perturbation. Figure 3.3 shows the trapezoidal disturbance voltage of +200 V and a period of $t_p = 2$ ms applied to coil E1 to produce an upward plasma displacement. The injected voltage in coil E8 has the same disturbance shape, but, since the two coils are driven antisymmetrically, it has a negative amplitude of -200 V. After this testing, this disturbance was subsequently applied for all discharges, except for discharges #9486 and #9490, in which the right movement direction could only be obtained with a longer ($t_p = 4$ ms) and bigger disturbance.
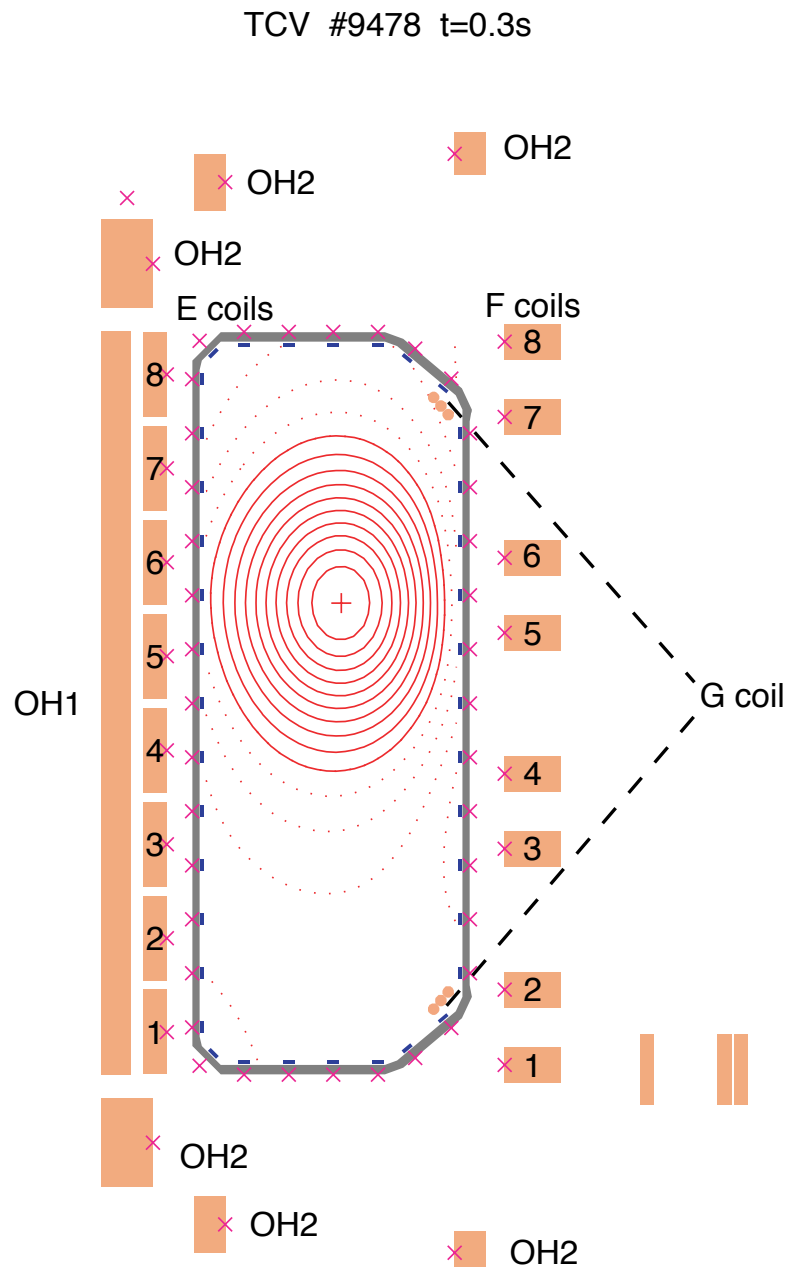
Figure 3.1: The TCV vacuum vessel, PF coils, poloidal field probes (marked '-' inside the tiles) and flux loops (marked 'x'). A modestly elongated plasma has a large volume available for a VDE before hitting the first wall
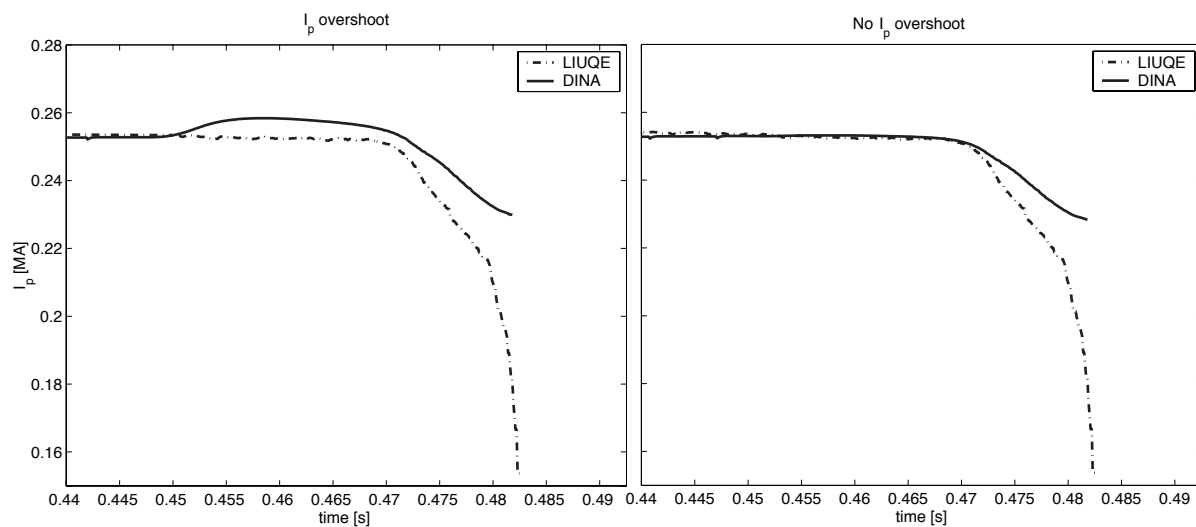
Figure 3.2: The figure on the left-hand side shows the plasma current I_p overshoot of DINA due to the large disturbance injected on the E1 coil only. The figure on the right-hand side shows no more overshoot because of the antisymmetric disturbance injection on coil E1 and E8.
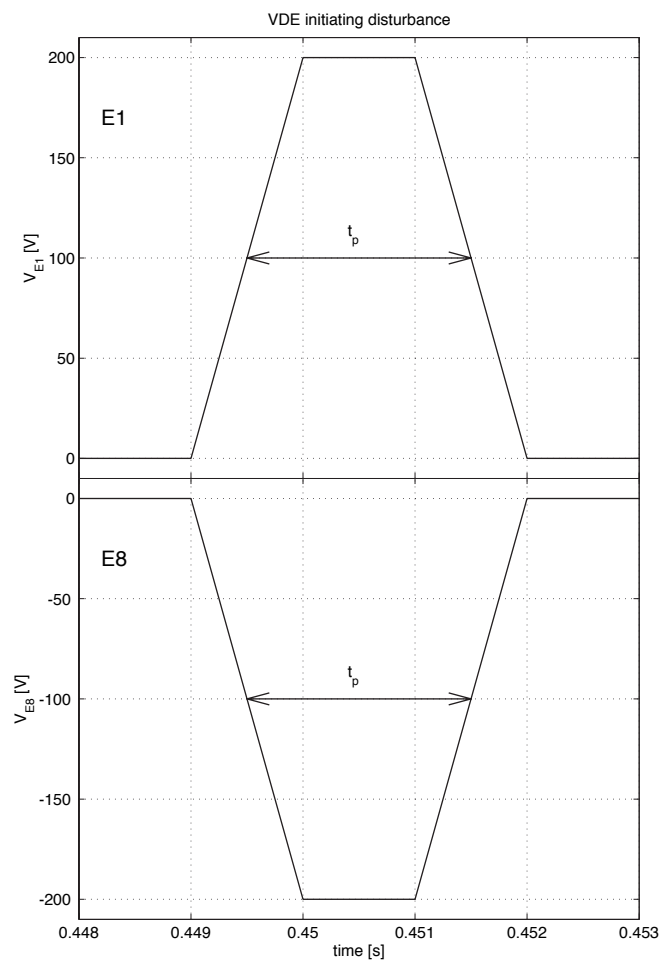
Figure 3.3: Disturbance shape initiating the VDE in DINA simulations.

3.2.2 Differences between the plasma equilibrium reconstructing code LIUQE and the simulation code DINA responses

Before comparing the TCV experiment results (LIUQE) and the DINA simulation predictions it is instructive to consider possible discrepancies. There are several potential reasons for disagreement between the responses represented by the experimental results and the DINA simulations.

1. Only the vertical and horizontal feedback control loops are interrupted during the VDE. The evolution of the PF currents remains controlled by other loops and determines the evolution of the vacuum field during the complete VDE. The agreement between the DINA and experimental evolution confirmed the correct modelling of these other feedback loops.

2. The electronics, particularly the amplifiers and integrators implemented in the diagnostics to evaluate the magnetic fields and the fluxes, may have small offsets. This adds offsets and constant slope drift errors to the measurements of the fields and fluxes. The power supply and electronics modelling are not considered to be a problem due to the precise agreement obtained for the linear response in previous work on TCV [33], approximating the power supply by a low-pass filter.

3. When starting the simulations with badly chosen initial states, a significant transient is observed before the simulation settled down to reproduce the TCV time traces more or less accurately [33]. This transient can be due to the different equilibrium parametrisation used by the LIUQE inverse equilibrium code and the DINA simulation code. However, it is difficult to find the right initial conditions to completely avoid this effect and there often remains a short transient before the equilibrium relaxes to a diffused DINA equilibrium. This can lead to an offset between the responses of the experiment and the DINA simulation. A comparison between DINA and LIUQE reconstruction of z, β_p and l_i for discharge #9480 is shown in Figure 3.4. There is a clear transient for all 3 parameters at the beginning of the DINA simulation. Furthermore, after the transient has decayed, an offset error remains at a level of about 5% for l_i and 1% for z. However, there is no offset error for β_p.

4. The equilibrium parameters (vertical and horizontal plasma position z and R, plasma current I_p, elongation κ, triangularity δ, the safety factor q, β_p and l_i) are not measured in a direct manner. They have to be estimated offline using the accessible measurements of the diagnostics (magnetic fields, fluxes and coil currents). The LIUQE code reconstructs the plasma evolution of a discharge by means of a parameterised function set for current and pressure profiles and a fitting algorithm calculating the parameter-values of these functions (constraints). This reconstruction method leads to results that mainly follow the experiment but cannot show all details of the plasma evolution. On the other hand, the simulation with the DINA code starts with a set of initial conditions and the profiles then evolve in a totally free manner. This leads to very detailed results but, of course, only for the features of the tokamak implemented in the DINA code. Figure 3.5 illustrates, as an example of the potential drawback of LIUQE using parameterised functions, the evolution of the plasma current profile across the plasma mid-plane. We clearly see the smooth gaussian-like shape of the LIUQE result due to the usage of parameterised functions, while the DINA simulation shows a more complex shape evolution. Without

additional experimental information we cannot determine whether the constrained or evolving profile is closer to the experimental reality. The finer structure is not 'visible' to the magnetics diagnostics outside the plasma which can measure the centroid, the total current and (less precisely) the internal inductance which varies with the current profile width.
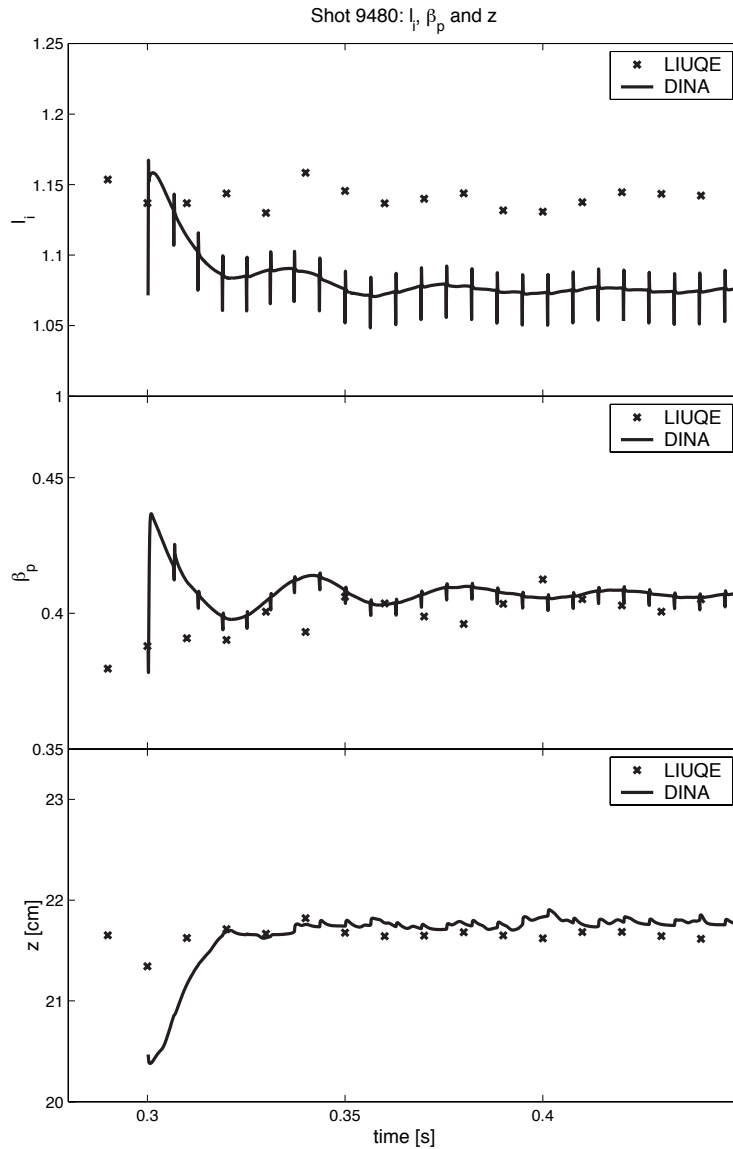
Figure 3.4: Discharge #9480, showing a short transient of l_i, β_p and the vertical position z at the beginning of the DINA simulation. The perturbation peaks on the simulation are due to sawteeth.

These problems have to be considered apart from the validation of the DINA code. Thus, a careful interpretation and treatment of the data are required to compare the results rigorously. Despite these numerous potential sources of error, the equilibrium parameters still show excellent agreement between DINA simulations and experiments, as we will see later. Additionally, two data treatment methods are adopted in order to avoid the residual offsets and drift errors. Firstly, when comparing raw diagnostic data such as magnetic fluxes and fields, the results are filtered by removing the linear part of the data, referred to
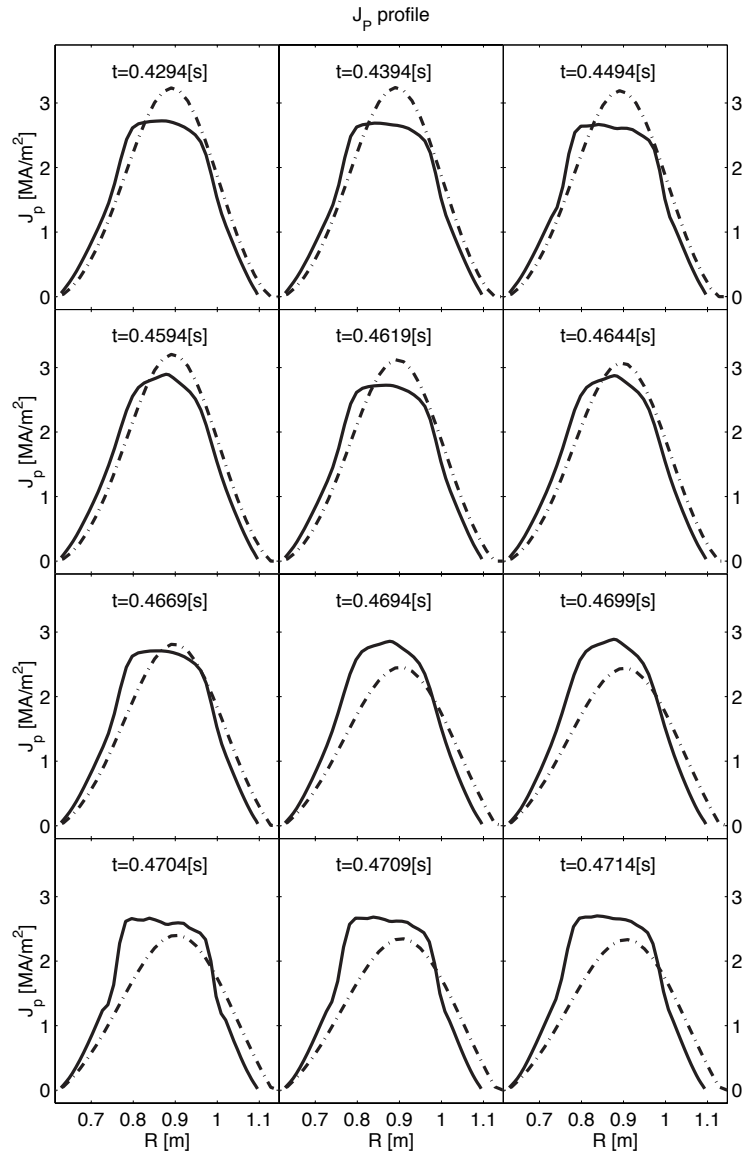
Figure 3.5: Plasma current density J_p profile of discharge #9487, estimated with LIUQE (dashed) and simulated with DINA (solid).

as 'detrending'. Secondly, for the equilibrium parameters, and especially for the vertical position, where we have only constant offsets, a more complete data adjustement method is proposed in Section 3.3.1.

Comparison during the final disruption itself are not as good. The most likely explanation is due to the LIUQE code which cannot deal with the significant profile evolution during disruptions without additional care. The comparison has therefore been limited to the time between the onset of the VDE up to the time just before the disruption occurs. The validation of DINA and LIUQE during the disruptive phase of TCV discharges will have to be treated in future work.

3.3   Comparison between TCV and DINA

3.3.1   Elimination of the offsets between experiment and DINA data

As mentioned in Section 3.2.2, there may be offset errors due to electronic offsets and the choice of the initial conditions. There is another mismatch shown up by the observation that the vertical plasma displacement of the DINA simulation usually begins earlier than the experimental data. In fact, the time of the beginning of the displacement is quite sensitive to the amplitude of the disturbance voltage applied to the coils E1 and E8 in the simulation (Section 3.2.1). Several DINA simulations with different disturbance amplitudes have shown that a bigger amplitude leads to an earlier vertical displacement as expected. As mentioned above (Section 3.2.1), we have to apply a disturbance with an amplitude that is large enough to ensure the correct direction, upwards or downwards, of the vertical plasma movement. This disturbance is bigger than the disturbances and noise of the experiment, leading to the observation that the vertical plasma displacement of DINA usually starts earlier than the one in the experiment. Before the comparison between the experimental and the DINA simulation data can be made, this time mismatch has to be corrected by means of data shifting. We chose to shift the DINA vertical position data by minimizing the cost function Q:

$$\min_{\delta t, \delta z} Q = \int_{t_1}^{t_2} \left\{ \min_{t_D} \left[w_t (t_D + \delta t - t_T)^2 + w_z (z_D(t_D) + \delta z - z_T(t_T))^2 \right] \right\} dt_T \qquad (3.1)$$

Where δt is the shifting of the time axis, δz the shifting of the z axis (vertical position), t_D and z_D are the time and vertical position of the DINA simulation and t_T and z_T are the time and vertical position of the TCV experiment. The integral interval is defined by $[t_1, \ t_2] = [0.35 \, s, \ t_{T_{end}}]$, where $t_{T_{end}}$ is the time of the last TCV experiment sample. The two weights w_t and w_z were chosen to attach more importance to the fitting accuracy of either the time axis by increasing w_t or the z axis by increasing w_z. Values of $\omega_t = 1 \ \text{s}^{-2}$ and $\omega_z = 4 \cdot 10^{-4} \ \text{m}^{-2}$ are suitable. The minimizations in the cases studied result values in the range of $\{-3.3 \dots 22.1\}$ ms for δt and $\{-1.75 \dots 6.64\}$ cm for δz. Only a single case exceeded $\delta z = 4.5$ cm and only the data are modified slightly, not the simulation itself.

3.3.2   Comparison of the vertical plasma position

Figure 3.6 shows the modelled and experimental evolution of the vertical plasma displacement of the whole set of 14 experiments with the simplest data mismatches between the DINA simulations and the experiments eliminated in the manner described. The most immediately striking feature is that all experiments with the plasma position going downwards have an S-like shape consisting of a fast exponential-like movement at the beginning and a slowing down part at the end just before the disruption occurs. Since the z position at equilibrium is located at $+20$ cm, the distance the plasma can move before the disruption is shorter for the experiments with an upward going vertical displacement. Therefore only these experiments show the initial exponential-like shape.

In general, especially considering the potential differences between the LIUQE and DINA codes already described, we consider the overall agreement for the evolution of the vertical plasma position as excellent. Nevertheless, to attempt a more rigorous assessment, we try to distinguish between good and less good agreement (Table 3.1). The curvature
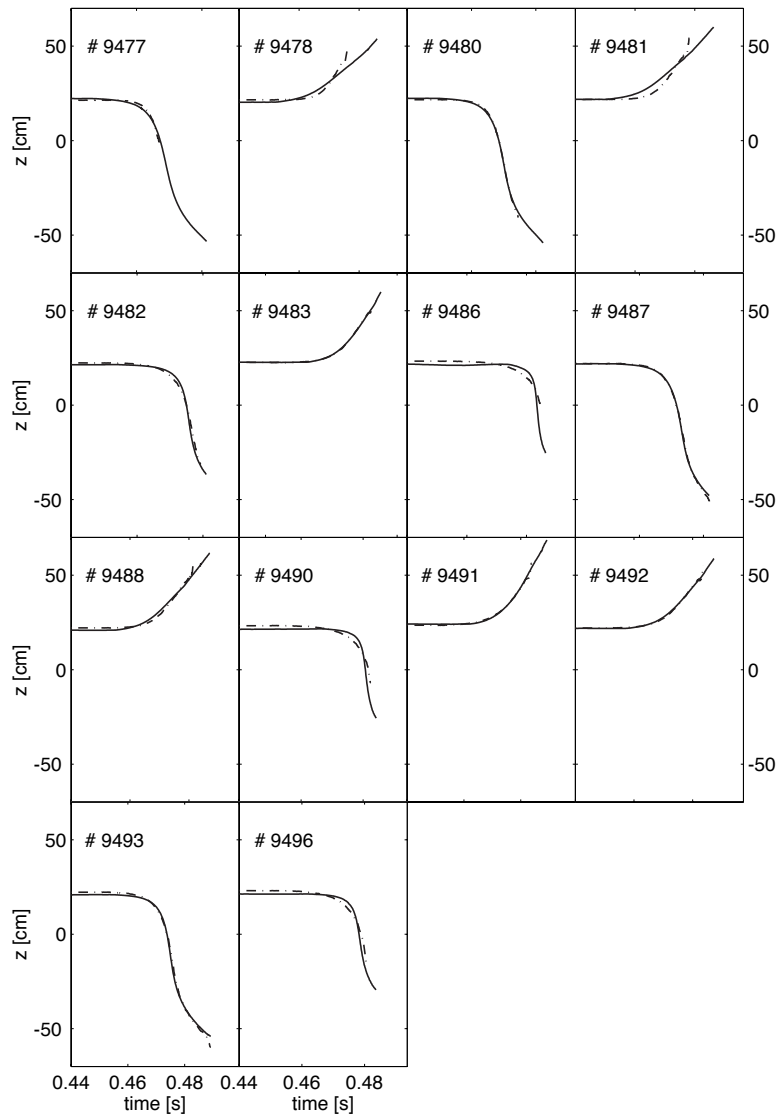
Figure 3.6: Comparison of the vertical displacement movement $z[cm]$. At $z = \pm 50$ cm a full minor radius circular plasma hits the top or bottom tiles. (solid: DINA, dashed: LIUQE)

of the exponential part (knee) of the vertical position is not always exactly reproduced by DINA, shown by a double crossing of the two traces. This curvature error seems to have a systematic property, because the DINA simulations show for every upward going displacement a softer knee than the experiments (e.g. #9478), while for the downward going movement we see a harder knee for DINA (e.g. #9486).

The correct reproduction of the S-like shape by DINA is an important nonlinear code feature. Such behaviour cannot be modelled by linear time-independent models because of the predominant exponential shape of the instability. These models only have one unstable pole corresponding to the vertical instability and although the set of stable poles could dominate the response during transient behaviour, the unstable pole and its residue have to dominate the behaviour at longer times.

For what follows, we aim to illustrate this statement by analysing the behaviour of the linearised tokamak model in closed-loop. Therefore, we consider the n order linear closed-

Good agreement	9477	9480	9482	9483	9487	9491	9492	9493
Less good agreement	9478	9481	9486	9488	9490	9496		

Table 3.1: Good and less good agreement between the experiment and DINA

loop system during the VDE experiment which is constituted by the linearised tokamak model and the feedback controller without the feedback of the radial and vertical plasma positions. We define the time relation $t_{-1} < t_0$, where t_{-1} and t_0 denote the time at which the VDE initiating disturbance starts and ends, respectively. It is assumed that at time t_{-1} the closed-loop tokamak system is in equilibrium and thus the linearised tokamak model can be derived at this time. We consider the time t_0 as the initial time from which we want to analyse the behaviour of the considered closed-loop system. From this time on there is no longer an external signal fed to the closed-loop system. Thus, the closed-loop system represents an autonomous system which can be described as a set of n independent differential equations

$$\dot{x}_i = \lambda_i x_i, \qquad i \in 1, 2, 3, \ldots, n \tag{3.2}$$

where x_i are the n states and λ_i are the n eigenvalues of the closed-loop system. We remark that every linear system can be put in such a form (for more detailed information see Section 8.3.6 of Part II). Furthermore, note that for the sake of simplicity we only consider pure real eigenvalues. In fact, for this demonstration it suffices to consider only the real parts of complex pole pairs, since we only want to analyse if the values of the states decrease or increase while the oscillatory behaviour of the states is not relevant here. Since we consider a system with a single unstable pole, we arbitrarily choose the state x_1 as the unstable state for which $\lambda_1 > 0$, while all other states represent the stable states for which $\lambda_2, \lambda_3, \ldots, \lambda_n < 0$.

The evolution of the vertical plasma position z is given by the linear state combination

$$\delta z = C_{z1} x_1 + C_{z2} x_2 + \ldots + C_{zn} x_n, \tag{3.3}$$

where $C_{zi} \in \mathbb{R} \ \forall i \in 1, 2, 3, \ldots, n$. In fact, the linear system given by Equations (3.2) and (3.3) describes only the linear vertical plasma displacement, denoted by δz, around the equilibrium plasma position z_0 which is equal to the vertical plasma position at the equilibrium time $z_0 = z(t_{-1})$. Thus, the evolution of z is given by

$$z(t) = z_0 + \delta z(t), \qquad t \geq t_{-1}. \tag{3.4}$$

A linear autonomous system possesses only a single equilibrium point which is trivially located at the origin since

$$\lim_{x_i \to 0} \dot{x}_i = \lim_{x_i \to 0} \lambda_i x_i = 0, \qquad i \in 1, 2, 3, \ldots, n. \tag{3.5}$$

From this it is obvious that at the equilibrium time t_{-1} the following equilibrium conditions

$$z(t_{-1}) = z_0$$
$$\delta z(t_{-1}) = 0$$
$$x_i(t_{-1}) = 0$$

have to be satisfied.

Just after the VDE initiating disturbance, at time t_0, the states and δz are no more in equilibrium ($x_i(t_0) \neq 0$ and $\delta z(t_0) \neq 0$) since they have been disturbed. We assume that the VDE initiating disturbance is small enough to ensure that the initial vertical plasma displacement $\delta z(t_0)$ is small. We define $x_i(t_0)$ as the initial conditions for the solution of System (3.2) which is given by

$$x_i(t) = x_i(t_0)e^{\lambda_i(t-t_0)}, \quad t \geq t_0, \quad i \in 1, 2, 3, \ldots, n. \tag{3.6}$$

The evolution of the vertical plasma displacement is therefore

$$\delta z(t) = C_{z1}x_1(t_0)e^{\lambda_1(t-t_0)} + C_{z2}x_2(t_0)e^{\lambda_2(t-t_0)} + \ldots + C_{zn}x_n(t_0)e^{\lambda_n(t-t_0)}, \quad t \geq t_0. \tag{3.7}$$

Since $\lambda_2, \lambda_3, \ldots, \lambda_n < 0$ the second to the nth terms on the right hand side are decreasing as a function of time and converge to zero if $t \to \infty$. Thus, for $t \gg t_0$ the vertical plasma displacement $\delta z(t)$ follows essentially the expression of the first term and we might approximate $z(t)$ by

$$z(t) = z_0 + \delta z(t) \approx z_0 + C_{z1}x_1(t_0)e^{\lambda_1(t-t_0)} \approx z_0 + \delta z(t_0)e^{\lambda_1(t-t_0)}, \quad t \geq t_0. \tag{3.8}$$

Note that the unstable eigenvalue λ_1 of the closed-loop system is equal to the unstable eigenvalue (also called the growth rate γ) of the open-loop linearised tokamak model if the considered feedback controller without the feedback of the radial and vertical plasma positions does not have a stabilising effect on the tokamak. The TCV controller considered verifies this condition and thus the growth rate γ of the open-loop linearised tokamak model is equal to $\gamma = \lambda_1$.

3.3.3 Comparison of the equilibrium parameters

In this section, we present a comparison of the most common equilibrium parameters. Figures 3.7 a) - c) show the evolution of the plasma current I_p, the elongation κ_{95}, the triangularity δ_{95} and the safety factor q_{95}, the last three parameters estimated at the 95 % flux surface. For completeness, the plasma vertical position z is added in the top row. As mentioned, we limit the comparison to the time before the final disruption occurs. To distinguish the instant of the final disruption we used the H_α signal, shown in the bottom row. The time when the disruption occurs is approximately determined by the maximum value of H_α, marked by a vertical line in the other plots. The time axis of the DINA data is shifted by δt, as described in Section 3.3.1, for all parameters. No shifting has been applied to the vertical axes.

For some discharges (#9477, #9478, #9480, #9481, #9483, #9488, #9491 and #9492), we observe a delay between DINA and LIUQE for some equilibrium parameters (an example is the plasma current) even after aligning the evolution of z as described. This may be due to the LIUQE code having difficulties reconstructing the plasma evolution correctly while the plasma current is rapidly decreasing and is not significant. Despite the fact that for discharge #9491 a short and low amplitude disturbance was applied, there remains an overshoot. This overshoot seems to also affect κ, δ and q.

Plasma current I_p : The agreement of the plasma current is good up to the time at which the final disruption occurs. The under- and overshoots of the DINA plasma current of discharge #9486 and #9490 are obvious because the initiating VDE disturbance is longer and larger.
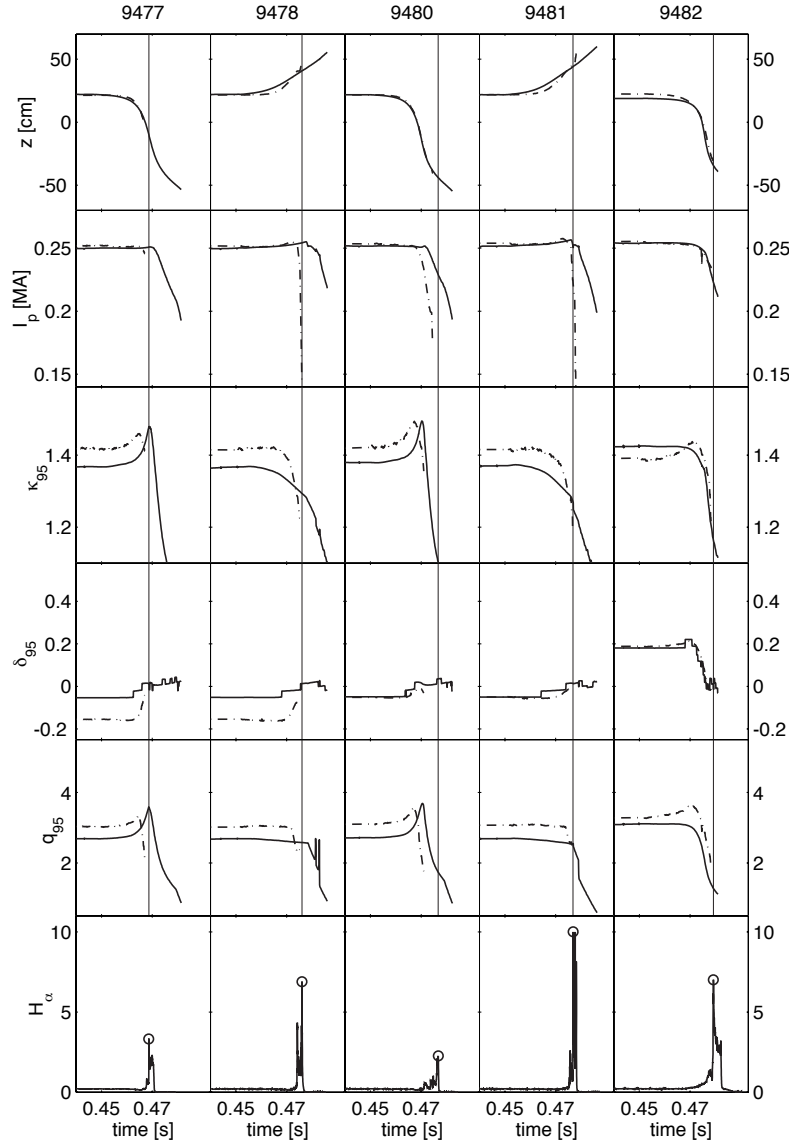
Figure 3.7: **a)** Comparison of the equilibrium parameters: vertical position z, plasma current I_p, elongation κ_{95}, triangularity δ_{95} and safety factor q_{95}. The peak of H_α indicates the disruption event, shown as a solid vertical line. (solid: DINA, dashed: LIUQE)

Elongation κ_{95} : For the TCV experiments, we observe a peak in κ when the plasma current decreases slowly (discharges #9477, #9480, #9482, #9487 and #9493). DINA reproduces this peak only for discharges #9477 and #9480. This is the most important disagreement and has not yet been explained. The most probable cause is differing evolutions of the LIUQE and DINA current profiles. The offset, which can be noticed for almost all discharges, is typically due to the problem of determining the right initial conditions for the simulations.

Triangularity δ_{95} : The agreement of the triangularity is excellent for all discharges, except for discharges #9477 and #9478. Despite the fact that the initial values start at $t = 0.3$ s with approximately the same values as the experiments for these discharges, the system relaxes to a DINA equilibrium, which induces a significant offset of δ_{95}. Like for
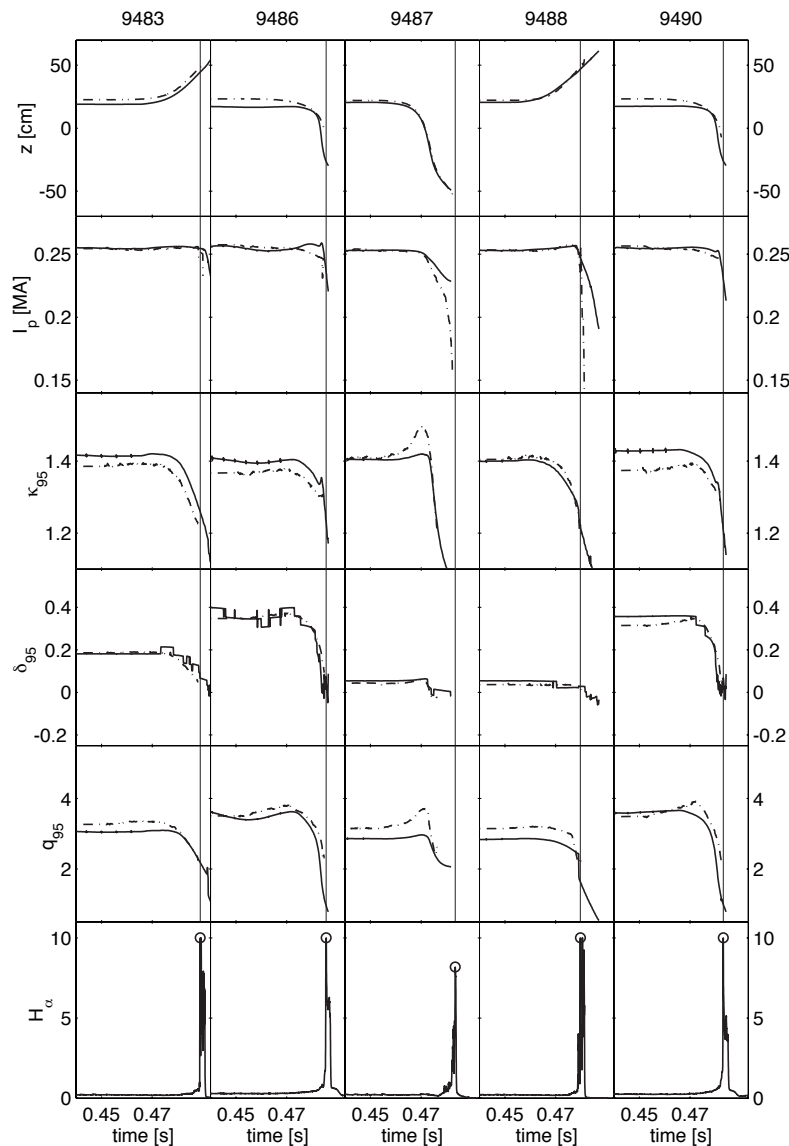
Figure 3.7: **b)** Comparison of the equilibrium parameters: vertical position z, plasma current I_p, elongation κ_{95}, triangularity δ_{95} and safety factor q_{95}. The peak of H_α indicates the disruption event, shown as a solid vertical line. (solid: DINA, dashed: LIUQE)

κ_{95}, this also belongs to the problem of determining the right initial conditions for the simulations.

Safety factor q_{95} : The safety factor inevitably behaves like the elongation, but with a less accentuated peak amplitude.

β_p and l_i : The two parameters β_p and l_i are shown in Figure 3.8. Besides the off-set errors, we establish that the decreasing behaviour of l_i is reproduced by DINA for all discharges, while for many discharges the direction of the change of β_p does not agree. This disagreement is most likely to be attributable to the LIUQE profiles, because it cannot accurately separate l_i and β_p for these modest elongations. To illustrate this problem, we compare the sum $\beta_p + \frac{l_i}{2}$ in Figure 3.9, which shows that the direction of the change is correct for all experiments.
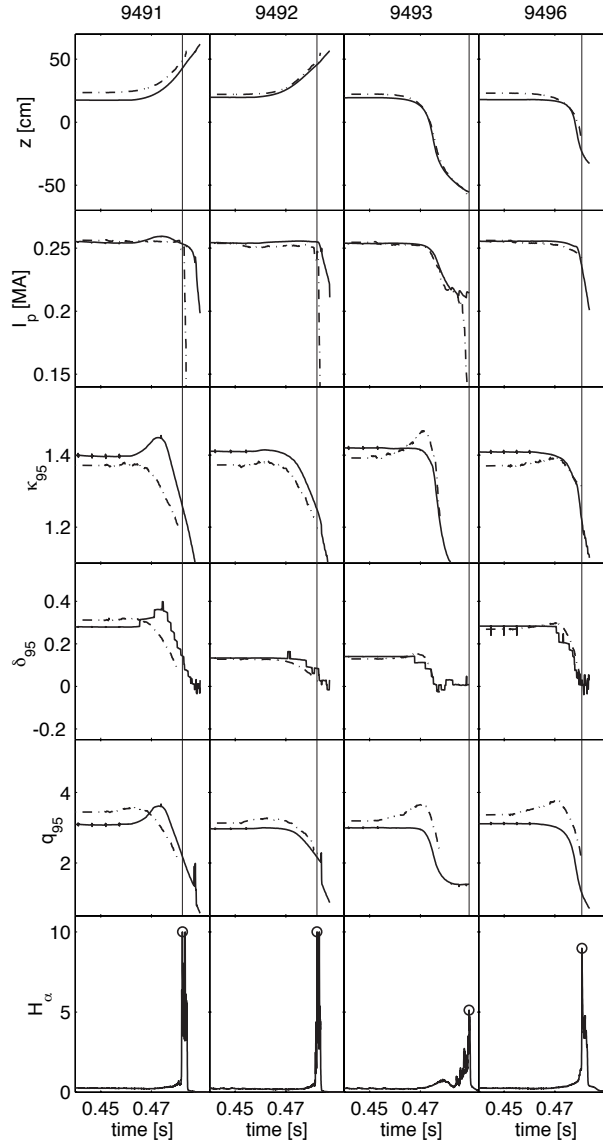
Figure 3.7: **c)** Comparison of the equilibrium parameters: vertical position z, plasma current I_p, elongation κ_{95}, triangularity δ_{95} and safety factor q_{95}. The peak of H_α indicates the disruption event, shown as a solid vertical line. (solid: DINA, dashed: LIUQE)

3.4 Comparison of the growth rate evolution

In this section, we compare the growth rate evolution of the TCV experiments, the DINA simulations and the simple RZIP linear model. The latter is based on the assumption of rigid displacement of the current distribution [17].

3.4.1 Computing the growth rate

The growth rates are established in RZIP by calculating the eigenvalues of the RZIP linear model in closed loop (with all feedback loops closed except for the vertical and radial positions). For the TCV experiment and the DINA simulations, the growth rates are calculated using the vertical plasma position data $z(t)$. The estimation is based on
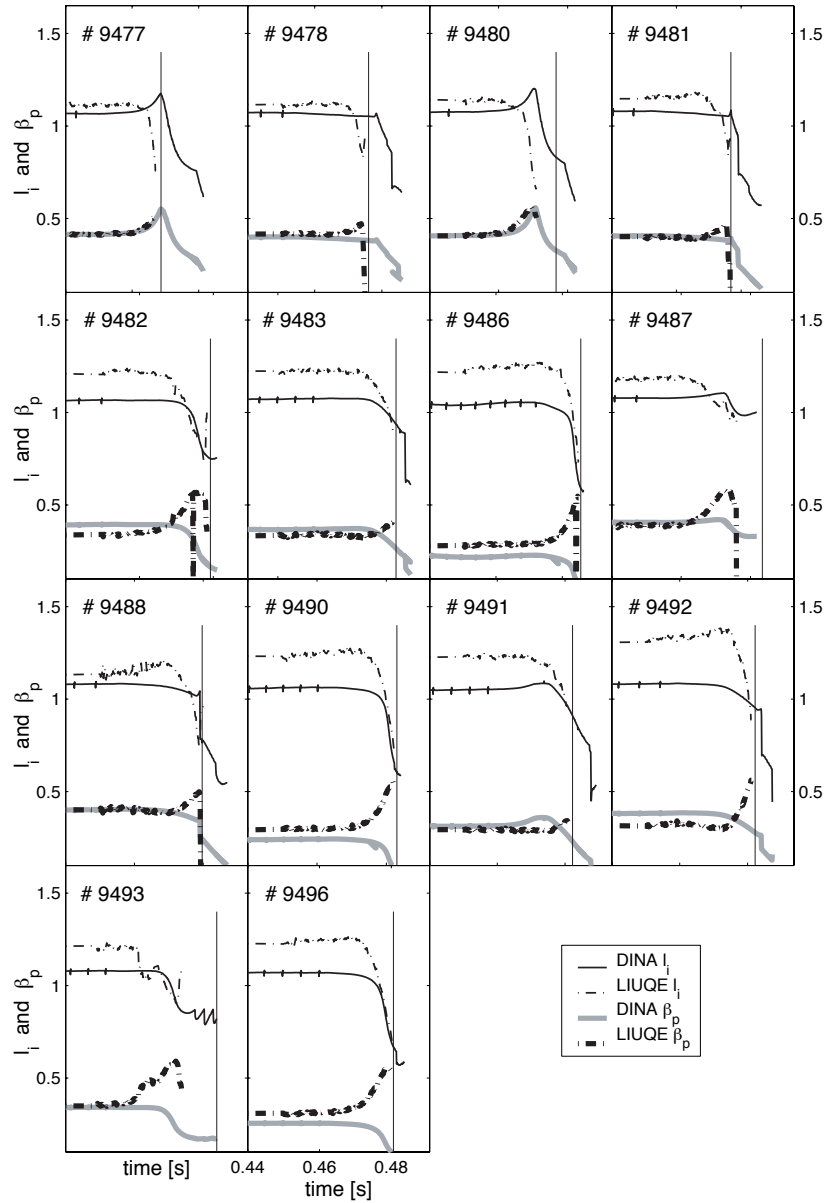
Figure 3.8: Comparison of l_i and β_p.

the assumption that $z(t)$ can be modeled by the function

$$z(t) = z_0 + \delta z \, e^{\int_{t_0}^{t} \gamma(\tau) d\tau} \tag{3.9}$$

which is the solution of the first order differential equation

$$\dot{z} = \frac{dz}{dt} = \gamma(t) \, \delta z \, e^{\int_{t_0}^{t} \gamma(\tau) d\tau} = \gamma(t)(z - z_0) \tag{3.10}$$

where we assume that z_0 and δz are constant in time and the growth rate γ is a function of time. The time t_0 is the time at which the VDE is initiated, in our case $t_0 = 0.45$ s, with a displacement δz from an equilibrium with zero passive structure currents.

If we assume that γ is time-independent, the exponent in Equation (3.9) is replaced by $\gamma(t - t_0)$. This gives us the approximated exponentially shaped response of a linear time-independent model (right hand side expression of Equation (3.8), where $\gamma = \lambda_1$).
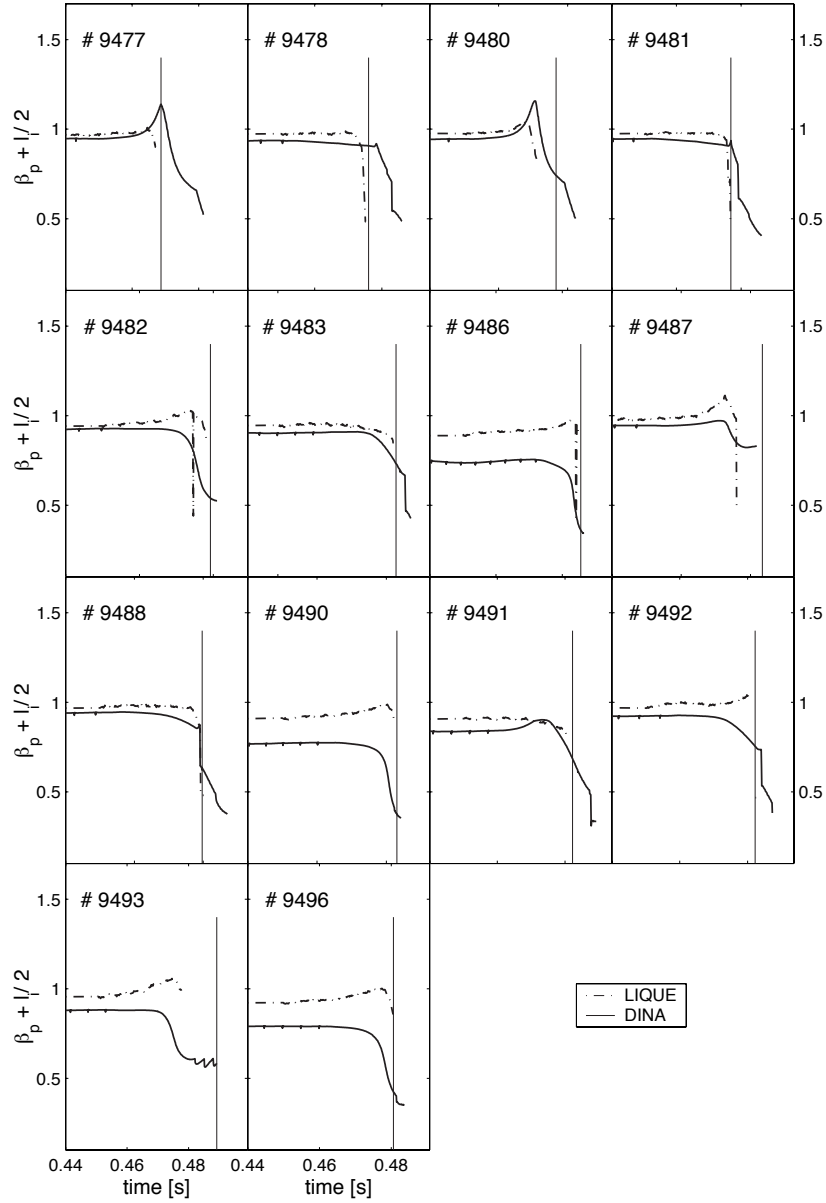
Figure 3.9: Comparison of $\beta_p + \frac{l_i}{2}$.

The aim of this section is to show that we can reproduce the nonlinear S-shape of the vertical displacement by taking this linear model and, additionally, assuming that only γ is a function of time. This assumption allows us to estimate the growth rate simply from the evolution of the vertical plasma position. We tested the following two different methods to compute $\gamma(t)$:

- **Logarithm method**
  First, the offset z_0 has to be subtracted from $z(t)$

$$\tilde{z}(t) = z(t) - z_0 = \delta z \, e^{\int_{t_0}^{t} \gamma(\tau)d\tau} \tag{3.11}$$

The logarithm of $\tilde{z}$ gives

$$\ln|\tilde{z}(t)| = \ln|\delta z| + \int_{t_0}^{t} \gamma(\tau)d\tau \tag{3.12}$$

We took the norm 1 of $\tilde{z}$ to avoid a logarithm of a negative value due to any noise and the arbitrary sign of the excursion. Finally, we obtain

$$\frac{d \ln |\tilde{z}|}{dt} = \gamma(t) \tag{3.13}$$

- **Quotient method**
  This method simply computes the growth rate by dividing Equation (3.10) by Equation (3.11) or by calculating directly $\frac{d \ln |\tilde{z}|}{dt}$ of Equation (3.13):

$$\frac{\dot{z}}{\tilde{z}} = \gamma(t) \tag{3.14}$$

The first derivative is used in both methods and thus noise in the data, especially the experimental data, is amplified. We therefore filter the vertical position data of both the DINA simulation and LIUQE reconstruction by means of a second order Butterworth filter with a cut-off frequency of $\omega_N/5$, where ω_N is the Nyquist frequency for the sampling period of the DINA data of $100\,\mu$s. Since LIUQE does not output data with a constant sampling rate, its data was interpolated linearly with the same sampling period as DINA and then filtered similarly.

In practice, the implementation of both methods exposed two problems:

1. The constant values z_0 and δz have to be determined. In fact, only one of these values has to be estimated because Equation (3.11) evaluated at $t = t_0$ simplifies to

$$z(t_0) = z_0 + \delta z \tag{3.15}$$

   where z is the known vertical position of either the DINA simulation or the LIUQE reconstruction data. The estimation is obtained by assuming that just after $t = t_0$ the growth rate $\gamma(t)$ remains time-independent over an interval defined by $[t_0, t_{lin}]$. This assumption is justified if the excursion of z over this interval is small and thus linear conditions can be assumed. This simplifies Equation (3.12) to

$$\ln |z(t) - z_0| = \ln |\delta z| + \gamma t \tag{3.16}$$

   In this case $\ln |z(t) - z_0|$ is linear and we simply tuned δz by hand until $\ln |z(t) - z_0|$ showed the expected linear behaviour in its initial phase defined by $[t_0, t_{lin}]$.

2. In principle, $\tilde{z} = z(t) - z_0$ should always remain positive or negative since δz is always positive for upward going VDEs and negative for downward going VDEs. In practice, there is noise in the $z(t)$ data and therefore, at the beginning where the vertical position is close to its initial value $z(t_0)$, the expression $z(t) - z_0$ oscillates around zero, which implies a number of zero crossings. To avoid zero crossings we add or subtract, according to the displacement direction of z, a small positive value to $z(t) - z_0$. Despite this precaution, the computed γ shows unavoidable rapid changes when noise is polluting the z data. This is due to the fact that when $\tilde{z} = z(t) - z_0$ is small and near zero the noise in the z data is amplified by the $\ln |\tilde{z}|$ function of the logarithm method (Equation (3.13)) and by the $1/\tilde{z}$ function of the quotient method (Equation (3.14)). Fortunately, we are mostly interested in the results of the nonlinear domain where γ varies in time and the distance $|z(t) - z_0|$ is large, under which condition the noise is no longer predominant.

For what follows, we only used the logarithm method, as it was found to provide less noise-polluted results than the quotient method.

3.4.2   Comparison of the growth rate

The comparison of the growth rate is shown in Figures 3.10 a) - c). The first and second rows illustrate $z(t) - z_0$ and $\ln|z(t) - z_0|$ of the LIUQE and the DINA data. The results of the second row can be used to find an appropriate value for δz and z_0, as described in point 1 of Section 3.4.1. The third row shows the evaluated growth rates for LIUQE, DINA and RZIP. As mentioned in point 2 of Section 3.4.1, we clearly see, especially for LIUQE, the noisy results in the initial phase where the growth rate is assumed to be constant. By inspecting the RZIP growth rate, we see that the assumption of a constant γ in the initial phase appears valid. Note that the curves of the RZIP growth rate stop at the end of the TCV pulse.

The RZIP model uses the reconstructed equilibrium and the instantaneous values of the PF coil currents to determine the growth rate. The vacuum poloidal magnetic field in the RZIP calculation therefore varies somewhat. But, if we analyse the radial magnetic field B_R, the height of the $B_R = 0$ line moves by a few cm, since the vertical position control is switched off. It is therefore not surprising that the modelled growth rate tracks the experimentally estimated evolution of the growth rate. On the other hand, the DINA code simulates the full evolution and the growth rate evaluated from the DINA results corresponds to the growth rate given the instantaneous PF coil currents in the DINA simulation and the instantaneous position of the plasma in the simulation. If the plasma evolution $z(t)$ is different, then the DINA simulation is at a different location at a given time. Since the growth rate itself is shown to be a function of the equilibrium position, then once there is any disagreement in $z(t)$, a disagreement in the estimated growth rate is inevitable for the remainder of the discharge. In spite of this, the ability of DINA to predict the evolution of all these plasma parameters during the large scale VDE is convincing.
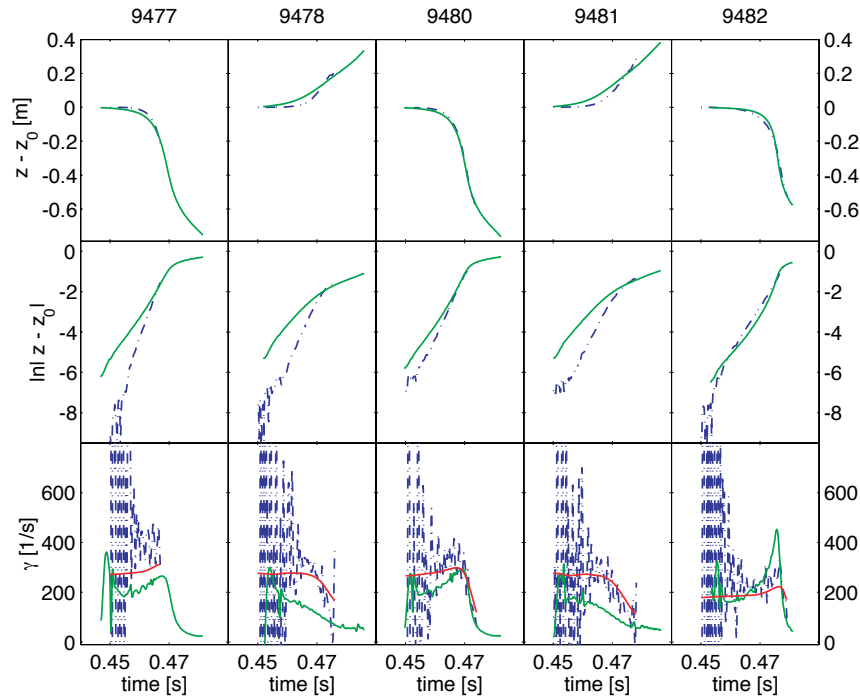
Figure 3.10: **a)** Computing growth rate of DINA (green solid) and LIUQE (blue dashed) and comparison with RZIP (red solid) growth rate.
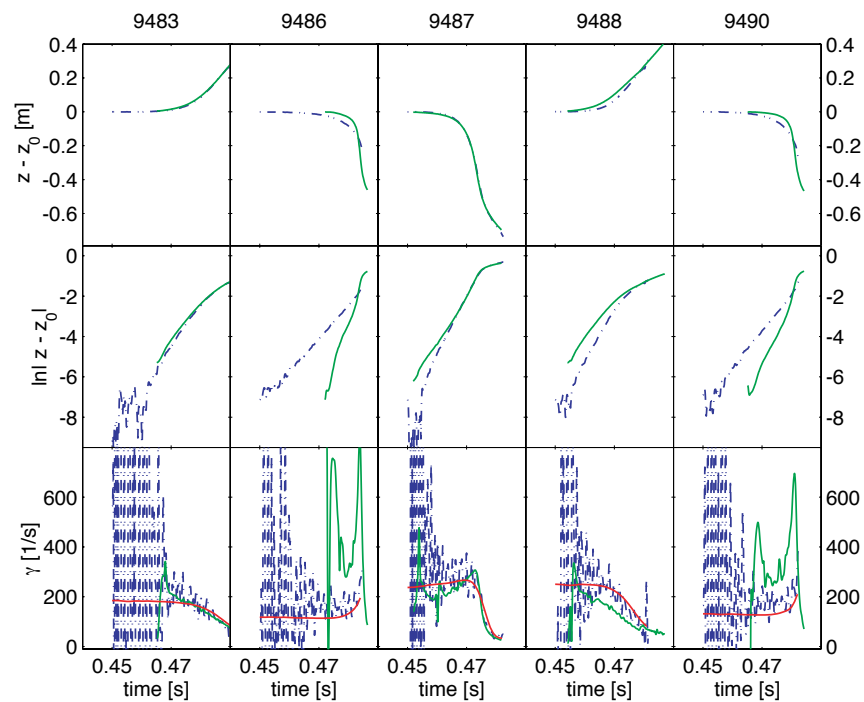
Figure 3.10: **b)** Computing growth rate of DINA (green solid) and LIUQE (blue dashed) and comparison with RZIP (red solid) growth rate.
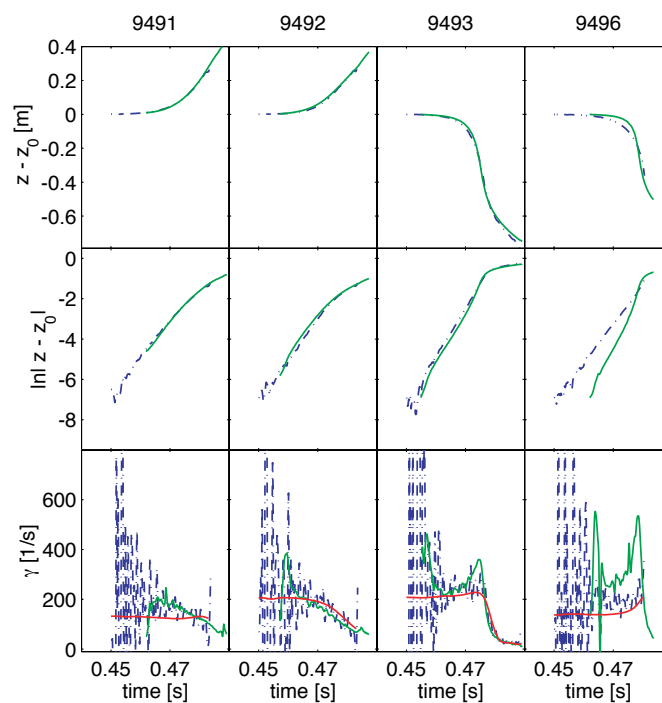
Figure 3.10: **c)** Computing growth rate of DINA (green solid) and LIUQE (blue dashed) and comparison with RZIP (red solid) growth rate.

Three candidate explanations are proposed for such a strong variation of the growth rate.

1. **The proximity of the vacuum vessel wall**
   The slowing down of the vertical displacement at the end of the downward going discharges could be attributable to the stabilising effect of the varying proximity of the vacuum vessel top and bottom wall.

2. **Variations in the plasma current profile**
   The effect on the growth rate of a varying plasma current profile is shown in Figure 3.11. The evolution of the RZIP growth rate assuming a fixed current profile is different from the 'normal' RZIP growth rate taking the deforming reconstructed current profile. The fixed current profile is taken before the break off of the vertical and radial position feedback control at $t = 0.43$ s. We previously established that the plasma current profile is not changing while the feedback control of the vertical and radial positions is active. After opening the position feedback control the deforming current profile growth rate peaks, while the fixed current profile growth rate already starts to decrease. This illustrates that the variation of the plasma current profile has a detectable impact on the evolution of the growth rate and therefore on the consequent vertical plasma displacement. Since the plasma current profiles of LIUQE and DINA are significantly different, Figure 3.5, it is natural that the agreement between the experiments and the DINA simulations is not perfect. Moreover, by inspecting the peaks of the RZIP growth rate in Figures 3.10 a) - c) we detect a systematic behaviour that discharges with large peaks (e.g. #9477, #9486, #9490 and #9496) show a less good agreement of the vertical movement. We also notice that the plasma current profile has some impact on the decrease of the growth rate at the end of the discharge, just before the disruption occurs. The deformable current profile growth rate shows a more pronounced rate of decrease (Figure 3.11).

3. **The spatial variation of the vertical field decay index n**
   The local vertical field decay index is

   $$n = -\frac{R}{B_z}\frac{\partial B_z}{\partial R},$$

   where B_z is the local vertical magnetic field and R is the local major radius. Figure 3.12 shows the spatial variation of the vacuum poloidal flux for discharge #9487 and does not vary significantly during the VDE since the poloidal field coil currents themselves do not vary significantly. The inhomogenity of the decay index is exceptional in TCV due to the large number of poloidal field coils allowing highly structured vacuum fields and to the elongation of the vacuum vessel.

The spatial effect of the varying plasma current profile is the smallest of these effects and the characteristic behaviour must reside in the first and third effects. To illustrate the origin of the pronounced S-curve in the downward moving VDEs, Figure 3.13 shows the vertical stabilising and destabilising forces per unit displacement on the plasma during the VDE. The variation in the stabilising forces is due to the variation of the coupling of the plasma current distribution to the passive and active circuits (vessel and PF coils) as the plasma moves. The destabilising force per unit displacement is simply due to

the weighted integral of the plasma current distribution multiplied with the decay index distribution over the plasma cross-section, deducible from Figure 3.12. In the case of the upward moving VDE, the stabilising force per unit displacement is reinforced almost immediately as the plasma current approaches the top wall of the vacuum vessel, while the destabilising force shows only a slight variation. In the case of the downward moving VDE, the stabilising force is slightly reduced as the plasma moves towards the mid-plane and only increases at the end of the trajectory when it couples more strongly to the lower vessel wall. During the downward moving disruption, the plasma feels an almost constant stabilising force, whereas the destabilising force varies significantly as different decay index regions are crossed. We can therefore predominantly attribute the pronounced S-curve in TCV downward moving VDEs to the spatial variation in the decay index rather than to the variation of the coupling to the vacuum vessel. TCV therefore differs from other devices in this respect, partly due to the large vertical height which reduces the sensitivity of the restoring force to plasma displacements compared with other tokamaks which have a more conformal vacuum vessel and partly due to the flexibility of its poloidal field coil system. A supporting confirmation comes from the elongation κ of the reconstructed plasma equilibrium, which drops to nearly 1.0 before disrupting, in the downward moving VDE. When κ drops to 1 the plasma becomes circular and it is therefore no more subjected to a vertical destabilising force.
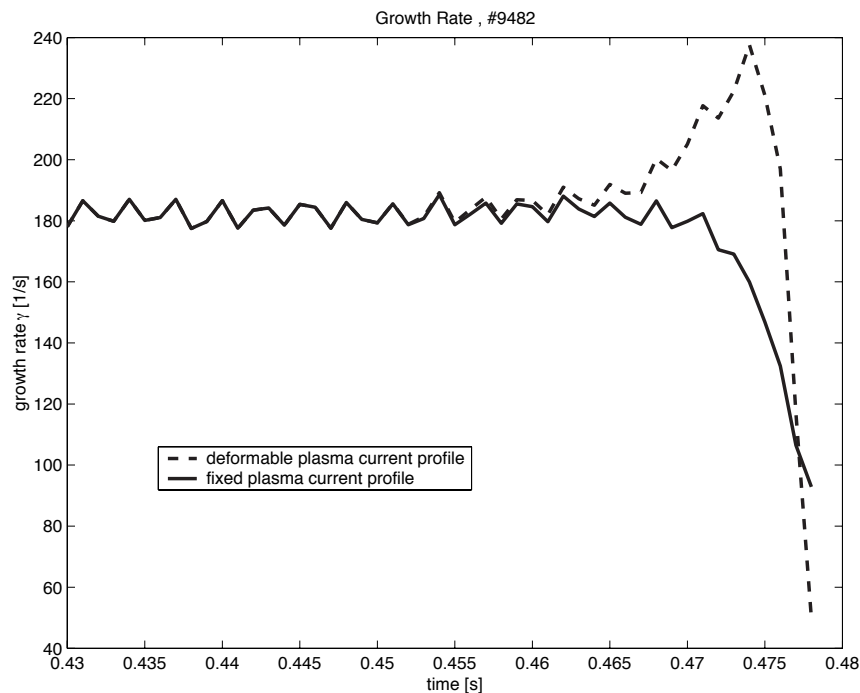
Figure 3.11: Evolution of the RZIP growth rate with a fixed plasma current profile (green solid) as against the 'normal' RZIP growth rate with a deformable reconstructed plasma current profile (blue dashed). The current profile of the fixed profile plot is taken at $t = 0.43$ s.
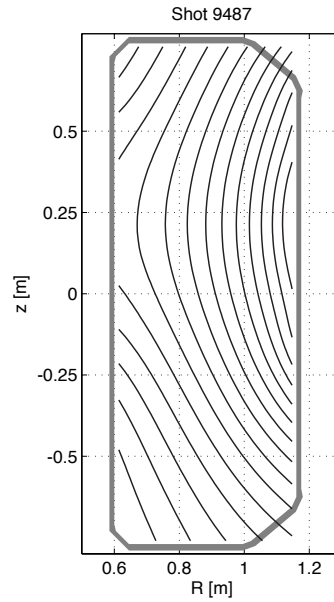
Figure 3.12: Spatial variation of the vacuum flux for the downward-going discharge #9487.
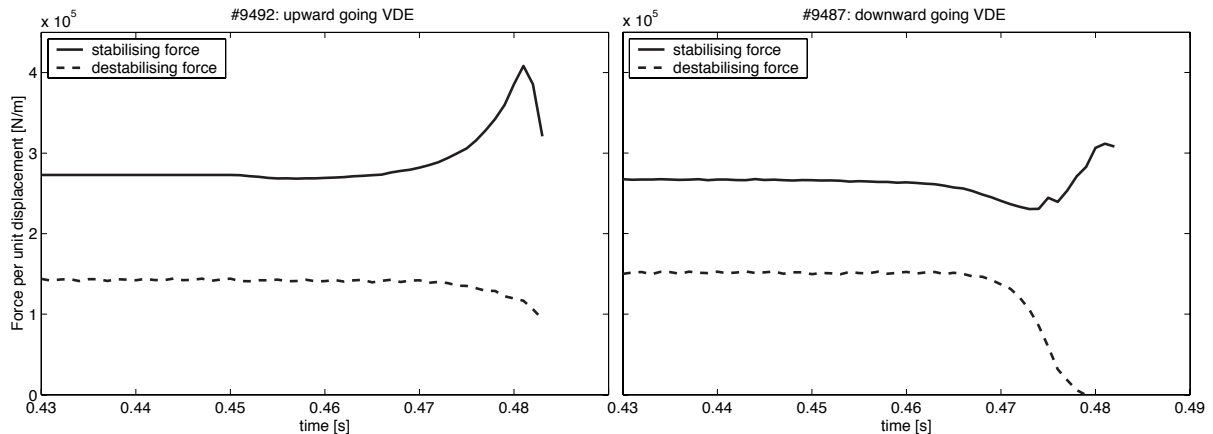
Figure 3.13: Evolution of the stabilising and destabilising forces per unit displacement for an upward-going VDE (left) and downward-going VDE (right).

3.5   Conclusion

In this chapter we have only had to make minor adjustments to the initial conditions of fully nonlinear DINA simulations of VDEs in TCV in order to obtain convincing agreement between the experimental and modelled data. The large number of TCV discharges modelled cover a range of triangularities and growth rates. The highly elongated TCV vacuum vessel has allowed us to follow VDEs over a large distance before a disruption ensues. The vacuum field curvature varies significantly over these large distances, implying a large modification of the vertical instability growth rate during the VDE. This feature is correctly modelled by DINA and the underlying reasons are brought out by inspecting the growth rate estimated by the RZIP rigid current displacement model which is accurate for the equilibria investigated. The presence of both upward and downward going disruptions shows that the proximity to the top and the bottom of the vessel is not the determining factor for varying growth rates. The evolution of the elongation and

triangularity in DINA does not agree perfectly with the LIUQE reconstructions and the multiple potential reasons are presented. Given these differences, it is impressive that the comparison shows such similar features and indeed, the inevitable differences illustrate the potential dangers of assuming absolute precision in nonlinear simulations of such a complex system. However, since the role of the complete plasma control feedback system is to hide such differences, the closed loop simulations will always be far more accurate than the "free fall" VDE simulations.

Chapter 4

Linear tokamak models

4.1 Introduction

As interest in modelling the combined plasma, vessel and PF coil system increased, many approaches were tried. Linearised models of the vertical instability were used during early JET operation, based on equivalent point currents to represent the stabilising property of the vacuum vessel [9]. This was extended for application to DIII-D to an eigenmode approximation to the vessel description, retaining the first up-down asymmetric eigenmode and exploring the controllability with a Proportional-Derivative feedback controller [35, 39]. These approaches considered the plasma as a filament or a non-deformable plasma, respectively. Deformation of the plasma was considered in the CREATE-L model , applied to the ITER design and validated on the TCV tokamak [52, 53]. An enhanced rigid current displacement model (RZIP) was developed and validated for TCV, considering changes to the plasma current and to its radial position [17, 40]. A deformable plasma model was developed for TCV highest growth rates [25].

In this present chapter, we make use of the single eigenmode representation [35] for its algebraic simplicity, of the linearised RZIP model [40] and of the linearised CREATE-L model for JET [2] and ITER [31]. A common feature of these linearised models is the presence of a single positive eigenvalue when the vertical plasma position is unstable. This point is essential for the stabilising purposes addressed in Part II (Control Theory) of the thesis.

4.2 Simple linear second order model

The simple second order model is based on a system consisting of a single-filament plasma within a vacuum vessel. The plasma is described by a total plasma current I_p and its nominal major radius R_0. The surrounding passive conductor has a current I_v flowing in an asymmetric mode (zero net current). The subscript v refers to the passive stabiliser due to the vessel, the subscript p refers to the plasma and the subscript z refers to the vertical plasma position. Later we introduce the subscribt a to refer to the active coil and the subscript R to refer the radial plasma position.

The stabilisation of the vertical plasma position is due to the Lorentz force which can be expressed as a force per unit length, referred to as $\mathbf{F}'$, by

$$\mathbf{F}' = \mathbf{I} \times \mathbf{B} \qquad \left[\frac{\text{N}}{\text{m}} \right], \qquad (4.1)$$

where $\mathbf{I}$ is the current and $\mathbf{B}$ is the magnetic field.

4.2.1 Linearisation notation

Let us define s as a variable standing for any varying quantities in a tokamak like the plasma current I_p, the vessel current I_v, the active coil current I_a, the radial R and vertical z plasma position, the radial magnetic field B_R and the vertical force F_z. For what follows we use the notation s for all the quantities describing the linearised model. The notation s_0 is used to describe the quantities at the equilibrium for which the linear model (linearisation equilibrium) is derived. The quantities which coincide with the actual quantities in a tokamak in operation is referred to as $\hat{s}$ and is given by

$$\hat{s} = s_0 + s.$$

We assume that when the state of the linear model is located at the linearisation equilibrium ($\hat{s} = s_0$) all quantities describing the linear model are zero ($s = 0$).

   To clarify this linearisation notation let us give an example by considering as quantity the plasma current: I_p describes the plasma current of the linearised model, I_{p_0} is the value of the plasma current at the linearisation equilibrium and $\hat{I}_p$ represents the actual plasma current in the tokamak.

4.2.2 The basic passive stabilisation due to the vacuum vessel

The vertical plasma position stabilising effect of the vacuum vessel is due to the currents in the vessel wall. These vessel currents are induced by a displacement of the plasma and create a magnetic field. But only a radial magnetic field, referred to as B_R, can contribute to the vertical plasma position stabilisation since from the Lorentz force equation a vertical force is solely due to the toroidal plasma current I_p and the radial magnetic field B_R, i.e.

$$F'_z \mathbf{e}_z = I_{p_0} \mathbf{e}_\phi \times B_R \mathbf{e}_R. \tag{4.2}$$

Figure 4.1 illustrates that the radial magnetic field B_R can solely be created by currents in the upper and lower halves of the vessel, schematically referred to as I_t and I_b. Furthermore, these currents have to have opposite signs, i.e. $I_t I_b < 0$, to obtain a radial magnetic field $B_R = B_t + B_b$, where B_t and B_b have the same sign. Such a current distribution in the vessel is referred to as the asymmetric up-down mode current distribution.

   For what follows we show that the vacuum vessel naturally possesses symmetric and asymmetric up-down eigenmodes. For this purpose we model the vacuum vessel by subdividing it into a finite number, referred to as n_{res}, of toroidal filaments. Figure 4.1 illustrates the vessel filament modelling of TCV. The system of the vessel filaments can be described as follows

$$M_{ves} \dot{I}_{ves} + \Omega_{ves} I_{ves} = 0, \tag{4.3}$$

where the currents of the n_{res} filaments are described by the current vector $I_{ves} \in \mathbb{R}^{n_{ves}}$, the ohmic resistances of the filaments by the diagonal matrix Ω_{ves} and the self-inductances of each filaments and the mutual inductances between the filaments by the matrix M_{ves}. Equation (4.3) can be expressed as

$$\dot{I}_{ves} = -M_{ves}^{-1} \Omega_{ves} I_{ves}$$
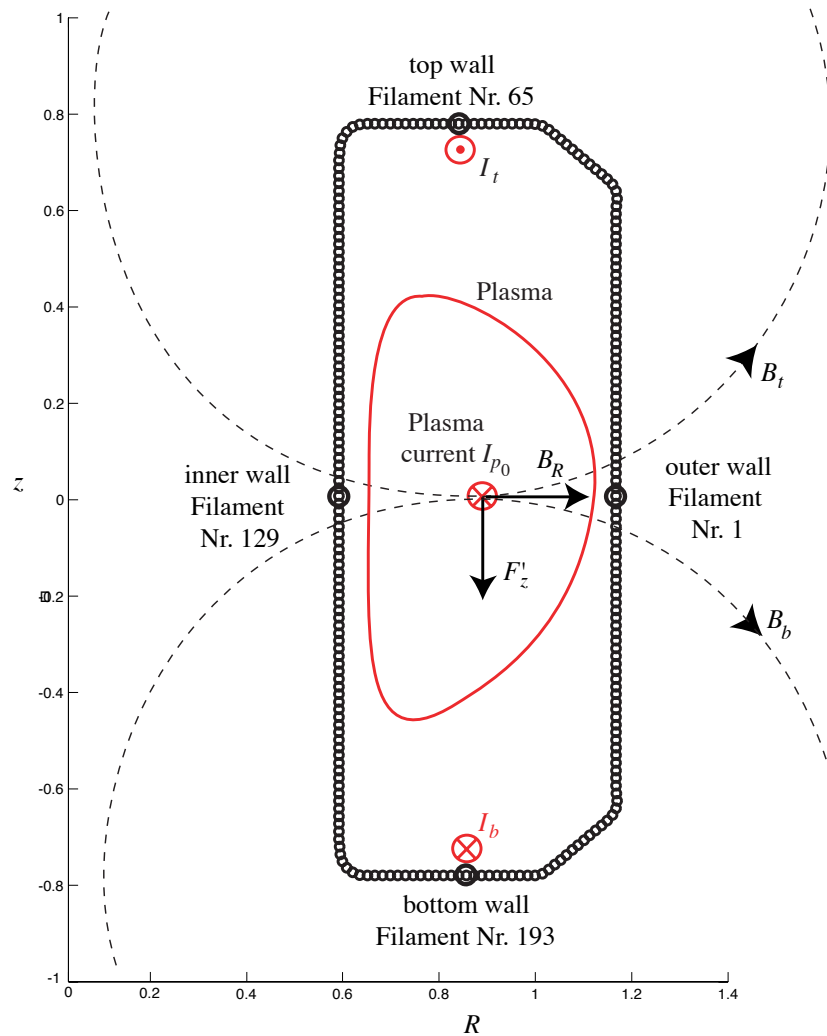
Figure 4.1: Illustration of the vertical position stabilisation due to the vacuum vessel and the vessel filament modelling.

and the vessel current eigenmodes are derived by diagonalising the matrix $M_{ves}^{-1}\Omega_{ves}$ by means of the linear transformation

$$I_{ves} = T_{ves}I_v, \tag{4.4}$$

where T_{ves} is the linear transformation matrix and the vector $I_v \in \mathbb{R}^{n_{ves}}$ refers to the currents of the vessel eigenmodes. With this linear transformation we obtain the diagonal matrix

$$L_v^{-1}\Omega_v = T_{ves}^{-1}M_{ves}^{-1}\Omega_{ves}T$$

and by choosing arbitrarily a diagonal constant vessel mode resistance matrix Ω_v the resulting diagonal matrix L_v describes the self-inductance of the vessel current eigenmodes. Thus, the system of the vessel filaments (Equation (4.3)) can be described as a function of the vessel eigenmode currents, i.e.

$$L_v\dot{I}_v + \Omega_v I_v = 0. \tag{4.5}$$

By means of Equation (4.4) the current distribution in the vessel wall can be deduced for every eigenmode current I_v. Figure 4.2 shows the vessel wall current distribution

of the first 6 eigenmodes of the TCV vessel. The filament numbering corresponds to the numbering in Figure 4.1. We see that the vessel eigenmodes 2 and 5 are up-down asymmetric modes while the other eigenmodes are up-down symmetric. Thus, the vertical plasma position stabilisation is essentially due to the modes 2 and 5.
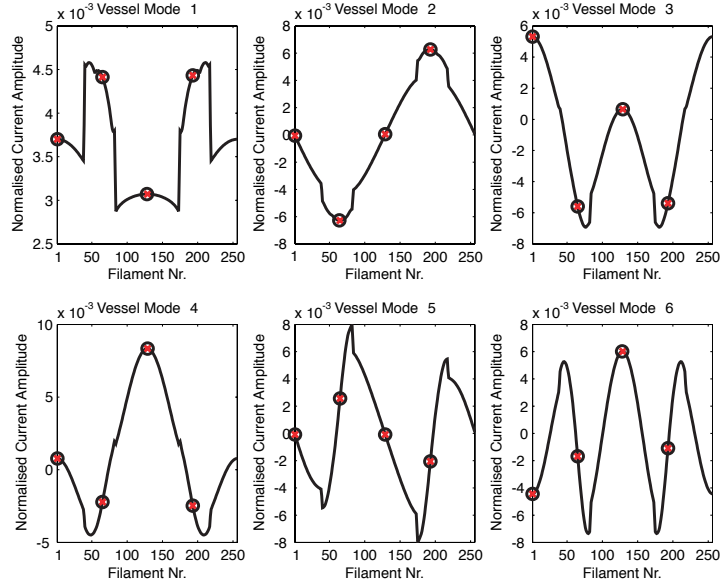
Figure 4.2: Current distribution in the vessel wall for the first 6 vessel eigenmodes.

4.2.3   The model of the basic passive stabilisation

The equations to be solved are: i) the vertical force balance equation for the plasma (Lorentz force)

$$m_p \frac{d^2 z}{dt^2} = F_z = -2\pi R_0 I_{p_0} B_R(z) \tag{4.6}$$

illustrated in Figure 4.3 a), where $B_R(z)$ denotes the radial magnetic field at the vertical plasma position z and ii) the circuit equation for the vacuum vessel

$$L_v \frac{dI_v}{dt} + \Omega_v I_v + \frac{dM_{vz}}{dt} I_{p_0} + M_{vz_0} \frac{dI_p}{dt} = 0, \tag{4.7}$$

where $I_v \in \mathbb{R}$, L_v and Ω_v represent solely the first up-down asymmetric vessel eigenmode current (mode 2 in Figure 4.2) and M_{vz} represents the mutual inductance between the vessel eigenmode current and the plasma current. In [35] it has been shown that when we assume a slowly varying plasma current the term with plasma current derivative $\dot{I}_p$ can be neglected which leads to

$$L_v \frac{dI_v}{dt} + \Omega_v I_v + M'_{vz} \frac{dz}{dt} I_{p_0} = 0 \tag{4.8}$$

where

$$M'_{vz} = \frac{\partial M_{vz}}{\partial z}$$

refers to the coupling coefficient between the plasma vertical position z and the vessel eigenmode current I_v (illustration in Figure 4.3 b)).

The radial magnetic field $B_R(z)$ in Equation (4.6) has two components:

1. The external field due to the equilibrium field coils that are producing the unstable curvature (see Section 1.1.5 in Chapter 1), referred to as $B_{R_{ext}}$. When the plasma is displaced vertically then the radial field component at z is varying as

$$B_{R_{ext}}(z) = \frac{\partial B_{R_{ext}}}{\partial z} z \qquad (4.9)$$

as a function of the vertical plasma position displacement z. By assuming stationary fields, it can be deduced from Ampère's law that the external magnetic field $\mathbf{B}_{ext}$ in the vacuum vessel satisfies

$$\nabla \times \mathbf{B}_{ext} = 0 \quad \text{implying that} \quad \frac{\partial B_{z_{ext}}}{\partial R} - \frac{\partial B_{R_{ext}}}{\partial z} = 0.$$

Thus Equation (4.9) becomes

$$B_{R_{ext}}(z) = -\frac{n B_{z_{ext}}}{R_0} z, \qquad (4.10)$$

where

$$n = -\frac{R_0}{B_{z_{ext}}} \frac{\partial B_{z_{ext}}}{\partial R}$$

is the decay index (Equation (1.11)) evaluated at the plasma radial position R_0. Furthermore, the external vertical magnetic field $B_{z_{ext}}$ is given by the Shafranov Relation (1.6) and by Equation (1.10), i.e.

$$B_{z_{ext}} = -B_v = -\frac{\mu_0}{4\pi R_0} I_p \left[\ln\left(\frac{8 R_0}{a}\right) + \frac{l_i}{2} + \beta_p - \frac{3}{2} \right].$$

This leads finally to

$$B_{R_{ext}}(z) = \frac{\mu_0 I_{p_0} \Gamma n}{4 \pi R_0^2} z, \qquad (4.11)$$

where

$$\Gamma = \left[\ln\left(\frac{8 R_0}{a}\right) + \frac{l_i}{2} + \beta_p - \frac{3}{2} \right] \qquad (4.12)$$

is the Shafranov coefficient.

2. The restoring radial magnetic field due to the currents induced in the vacuum vessel wall (I_v) by a vertical plasma displacement is referred to as $B_{R_{ves}}(I_v)$. By considering the magnetic flux $\Psi_{vz} = M_{vz} I_v$ due to the vessel eigenmode current I_v the radial magnetic field $B_{R_{ves}}(I_v)$ is deduced from

$$\partial \Psi_{vz} = B_{R_{ves}}(I_v) \mathbf{e}_R \cdot \partial \mathbf{S},$$

with the surface $\partial \mathbf{S} = 2\pi R_0 \partial z \mathbf{e}_R$ having a radial normal vector. This leads finally to

$$B_{R_{ves}}(I_v) = -\frac{1}{2\pi R_0} \frac{\partial M_{vz}}{\partial z} I_v, \qquad (4.13)$$

where the minus sign is due to following fact (we assume that $M'_{vz} > 0$, $L_v > 0$ and $I_{p_0} > 0$). When the plasma is displaced upwards ($\dot{z} > 0$) the current induced in the vessel becomes negative ($I_v < 0$) due to Equation (4.8). To stabilise the vertical plasma position the radial magnetic field has to be positive to induce by the Lorentz force law a downward pointing vertical force ($F'_z < 0$) (Figure 4.1). Thus, since $I_v < 0$ the negative sign in Equation (4.13) is required to satisfy $B_{R_{ves}}(I_v) > 0$.

The total radial magnetic field is given by

$$B_R(z) = B_{R_{ext}}(z) + B_{R_{ves}}(I_v) = \frac{\mu_0 I_{p_0} \Gamma n}{4\pi R_0^2} z - \frac{1}{2\pi R_0} \frac{\partial M_{vz}}{\partial z} I_v \tag{4.14}$$

Combining Equations (4.6) and (4.14) and considering Equation (4.8) leads to the linear third order dynamical system given by the following two differential equations

$$\ddot{z} + \frac{\mu_0 I_{p_0}^2 \Gamma n}{2R_0 m_p} z - \frac{M'_{vz} I_{p_0}}{m_p} I_v = 0 \tag{4.15}$$

and

$$L_v \dot{I}_v + \Omega_v I_v + M'_{vz} \dot{z} I_{p_0} = 0. \tag{4.16}$$

The study of the eigenvalue characteristics for this system is given in [35]. Furthermore, it is shown (in [35]) that this model can be simplified without any significant loss of accuracy by assuming a zero plasma mass ($m_p = 0$) which leads to the approximation of the instantaneous force balance. In this limit the only solution for the force balance equation (Equation 4.6) is $B_R(z) = 0$. Thus, we set $B_R(z) = 0$ in Equation (4.14) which leads to

$$\alpha z I_{p_0} + M'_{vz} I_v = 0, \tag{4.17}$$

where

$$\alpha = -\frac{\mu_0 \Gamma n}{2R_0} \tag{4.18}$$

is referred to as the field curvature. This simplification leads to a first order linear system given by substituting $\dot{z} I_{p_0}$ in Equation (4.16) by means of Equation (4.17), i.e.

$$\dot{I}_v + \frac{\Omega_v}{L_v - \frac{M'^2_{vz}}{\alpha}} I_v = 0, \tag{4.19}$$

where its eigenvalue given by

$$\lambda = \frac{\Omega_v}{L_v - \frac{M'^2_{vz}}{\alpha}}. \tag{4.20}$$

We see that System (4.19) is marginally stable if the ohmic resistance in the vessel wall is zero ($\Omega_v = 0$, superconducting vessel wall). Furthermore, we can deduce from the results presented in the next section that in the case of non-zero ohmic resistance, System (4.19) is always unstable ($\lambda > 0$) for elongated plasmas since $L_v - \frac{M'^2_{vz}}{\alpha} > 0$.
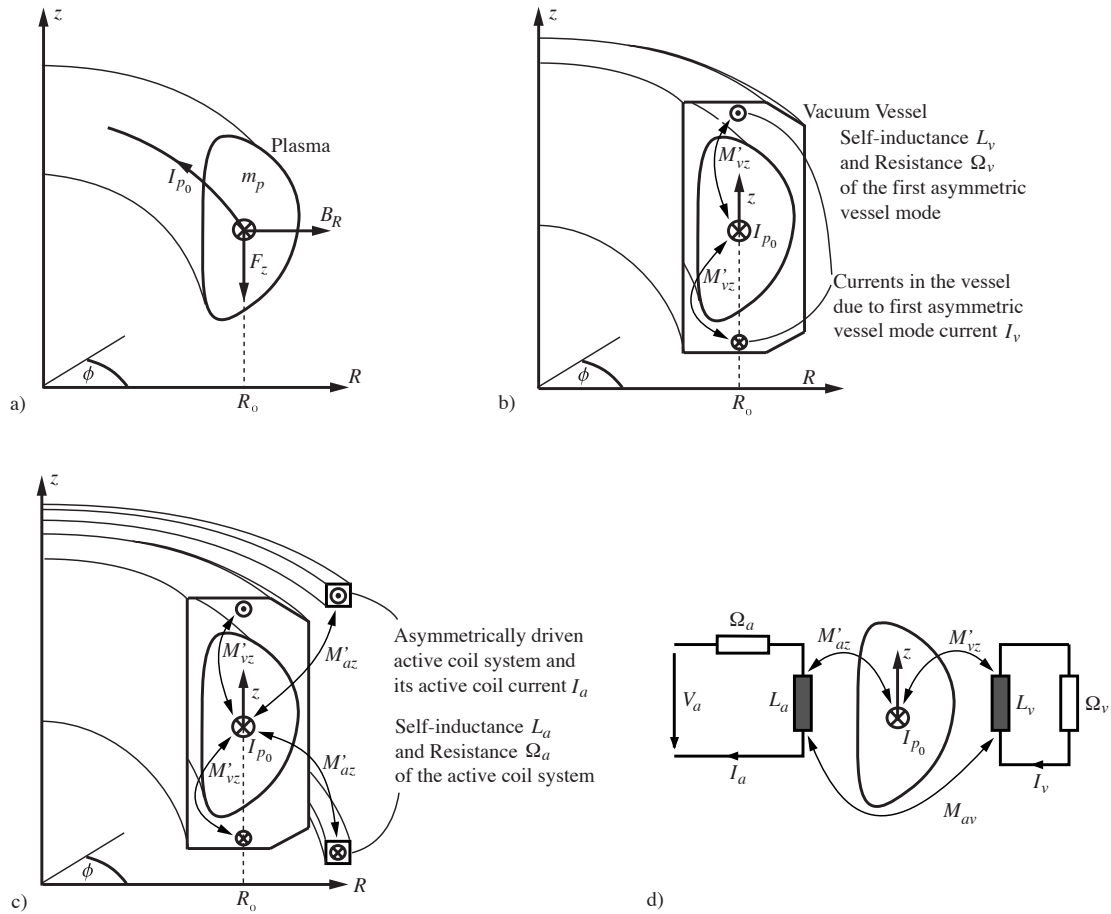
Figure 4.3: The simple second order model. a) the vertical force balance equation for the plasma; b) the vessel stabilisation; c) the active coil system stabilistion and d) the simplified second order model represented schematically.

4.2.4 The model for the plasma-vessel-active coil system

We extend the previous model by adding an active coil system. We therefore add a circuit equation for the active coil system and approximate similarly as in the previous section by considering the instantaneous force balance. This leads to the algebraic equation

$$\alpha z I_{p0} + M'_{vz} I_v + M'_{az} I_a = 0 \tag{4.21}$$

and to the two differential circuit equations

$$L_a \dot{I}_a + \Omega_a I_a + M_{av} \dot{I}_v + M'_{az} \dot{z} I_{p0} = V_a \tag{4.22}$$

$$L_v \dot{I}_v + \Omega_v I_v + M_{av} \dot{I}_a + M'_{vz} \dot{z} I_{p0} = 0, \tag{4.23}$$

where the radial field derivatives are given by

$$M'_{vz} = \frac{\partial M_{vp}}{\partial z} \quad \text{and} \quad M'_{az} = \frac{\partial M_{ap}}{\partial z}. \tag{4.24}$$

Figure 4.3 c) illustrates the stabilising active coil system and Figure 4.3 d) illustrates schematically the model described by Equations (4.21)-(4.23).

Tables 4.2-4.4 give a short description of all physical variables and constants used throughout the chapter.

By taking the derivative of equation (4.21) this set of equations can be written in matrix form

$$M\dot{x}_p + \Omega x_p = \begin{bmatrix} L_a & M_{av} & M'_{az} \\ M_{av} & L_v & M'_{vz} \\ M'_{az} & M'_{vz} & \alpha \end{bmatrix} \dot{x}_p + \begin{bmatrix} \Omega_a & 0 & 0 \\ 0 & \Omega_v & 0 \\ 0 & 0 & 0 \end{bmatrix} x_p = U, \tag{4.25}$$

where

$$x_p = \begin{bmatrix} I_a \\ I_v \\ zI_{p_0} \end{bmatrix} \quad \text{and} \quad U = \begin{bmatrix} V_a \\ 0 \\ 0 \end{bmatrix} \tag{4.26}$$

denote the physical state variables and the input voltage, respectively. This leads to the ODE system

$$\dot{x}_p = -M^{-1}\Omega x_p + M^{-1}U = A_p x_p + b_p V_a = A_p x_p + b_p u. \tag{4.27}$$

The tokamak outputs like the plasma parameters and the magnetic diagnostic measurements (about 100 sensors) are linear combinations of the state variables (all of which are current sources).

$$y = C_p x_p. \tag{4.28}$$

Remark:
The vector x_p represents the state variables. At first sight Equation (4.27) looks like a third order differential equation system since we have three state variables I_a, I_v and zI_{p_0}. But remember that the last line of (4.25) expresses only the algebraic Equation (4.21). Thus, we could reduce the system to a system where the matrices M and R are element of $\mathbb{R}^{2\times2}$ by substituting $\dot{z}I_{p_0}$ of the first two lines of System (4.25) with the algebraic equation which expresses $\dot{z}I_{p_0}$ in function $\dot{I}_a$ and $\dot{I}_v$. This would result in a second order system (also called the minimal realisation of the system) where I_a and I_v are its real state variables. It is also possible to get a minimal realisation of System (4.25) by substituting I_a or I_v. For our purposes we will consider the first variant and define I_a and I_v as state variables and call zI_{p_0} a pseudo state variable.

4.2.5 The modes of the second order system

It is well known that the elongated plasma of a tokamak possesses an unstable mode. We will show that this is due to the negative decay index $n < 0$ which is the only way to get a very elongated plasma [35] (Section 1.1.5). Usually this instability is called the vertical position instability. This denomination is somewhat confusing because it suggests that only the vertical position is unstable. But, at least for the linear model, all physical states x_p are unstable since they are all dependent of the unstable mode, as we will show later. The use of the vertical position instability has, so to speak, its legitimacy if we take into consideration that the unstable mode appears only if the algebraic Equation (4.21) defining the vertical position is added to the model.

The modes of System (4.27) are given by the eigenvalues of the matrix A_p. These eigenvalues are solely pure real values. This is due to the following theorem.

Theorem 1
Consider the symmetric real matrix S and the diagonal real matrix D with solely positive and zero elements. Then the eigenvalues of the matrix product SD are solely pure real.

Proof: Consider

$$Ax = SDx = \lambda x,$$

where x is any eigenvector of A and λ is its corresponding eigenvalue. By multiplying with x^*D and by observing that $D^{\frac{1}{2}^*} = D^{\frac{1}{2}}$ since the elements of D are positive or zero valued we obtain

$$x^*DSDx = \lambda x^*Dx = \lambda x^*D^{\frac{1}{2}}D^{\frac{1}{2}}x = \lambda x^*D^{\frac{1}{2}^*}D^{\frac{1}{2}}x = \lambda\|D^{\frac{1}{2}}x\|_2^2.$$

Since

$$(x^*DSDx)^* = x^*D^*S^*D^*x = x^*DSDx$$

we obtain

$$(\lambda\|D^{\frac{1}{2}}x\|_2^2)^* = \lambda^*\|D^{\frac{1}{2}}x\|_2^2 = \lambda\|D^{\frac{1}{2}}x\|_2^2$$

and thus λ possesses no imaginary part. ∎

Since M_2 and thus $-M_2^{-1}$ are symmetric and since Ω_2 is diagonal with positive and zero elements the eigenvalues of A_{2_p} given by

$$\lambda_0 = 0 \tag{4.29}$$

$$\lambda_1 = \frac{1}{2}\frac{N - \sqrt{N^2 - 4\Omega_a\Omega_v\alpha D}}{D} \tag{4.30}$$

$$\lambda_2 = \frac{1}{2}\frac{N + \sqrt{N^2 - 4\Omega_a\Omega_v\alpha D}}{D} \tag{4.31}$$

where

$$N = -\alpha(L_a\Omega_v + L_v\Omega_a) + M_{vz}'^2\Omega_a + M_{az}'^2\Omega_v \tag{4.32}$$

$$D = 2M_{av}M_{az}'M_{vz}' - L_aM_{vz}'^2 - L_vM_{az}'^2 + \alpha(L_aL_v - M_{av}^2). \tag{4.33}$$

are solely pure real valued. The first eigenvalue $\lambda_0 = 0$ is due the fact that the rank of A_{2_p} is equal 2 instead 3 because of the algebraic Equation (4.21). Physically it is not a mode of the system. Therefore, λ_1 and λ_2 are the two real modes of the second order system. Since the eigenvalues are real valued the expression in the square root is positive or zero

$$N^2 - 4\Omega_a\Omega_v\alpha D \geq 0 \tag{4.34}$$

Consider the system without the algebraic Equation (4.21) defining the vertical position by setting $\alpha = 1$ and $M_{az}' = M_{vz}' = 0$. This system results in a simple electromagnetic two coil coupled system, where the self-inductances L_a, $L_v > 0$, the resistances Ω_a, $\Omega_v > 0$ and the mutual inductances $M_{av} \in \mathbb{R}$. The eigenvalues of this system are given by Equations (4.30) and (4.31) with

$$N = N_0 = -(L_a\Omega_v + L_v\Omega_a) < 0 \tag{4.35}$$

$$D = D_0 = L_aL_v - M_{av}^2. \tag{4.36}$$

An electromagnetic coil coupled system is a passive system and is therefore stable. Moreover, such a system is not oscillating. Thus, both eigenvalues have to be pure real and negative. The pure real eigenvalue property is intrinsically given by the expression in the square root which is always positive

$$N_0^2 - 4\Omega_a\Omega_v D_0 = (L_a\Omega_v - L_a\Omega_v)^2 + 4\Omega_a\Omega_v M_{av}^2 > 0.$$

The negative eigenvalue property is given by imposing condition

$$D_0 = L_a L_v - M_{av}^2 > 0 \tag{4.37}$$

which assures that the square root expression verifies

$$N_0^2 > N_0^2 - 4\Omega_a\Omega_v D_0.$$

Condition (4.37) gives the well known coupling factor between two coils defined by

$$k = \frac{|M_{av}|}{\sqrt{L_a L_v}}$$

which is always $k \in [0, 1]$.

   By considering the algebraic Equation (4.21) defining the vertical position which results in the eigenvalues given by Equations (4.30)-(4.33) we will show that one eigenvalue can take a positive value depending on the parameters α, M'_{az} and M'_{vz}. The demonstration is given by analysing the eigenvalue's sign as a function of α.

   Before that, let us

1. introduce the critical value of α

$$\alpha_c = \frac{L_a M_{vz}'^2 + L_v M_{az}'^2 - 2M_{av}M'_{az}M'_{vz}}{L_a L_v - M_{av}^2} > 0, \tag{4.38}$$

   which occurs when D of Equation (4.33) is equal zero. The critical value of α is always positive since $L_a L_v - M_{av}^2 > 0$ condition (4.37) and since

$$L_a M_{vz}'^2 + L_v M_{az}'^2 - 2M_{av}M'_{az}M'_{vz} > 0. \tag{4.39}$$

   Condition (4.39) is easily verified when $M_{av}M'_{az}M'_{vz} < 0$. In the case where $M_{av}M'_{az}M'_{vz} > 0$ we can rewrite the condition by substituting $M_{av}M'_{az}M'_{vz}$ with $|M_{av}||M'_{az}M'_{vz}|$ and by the substitution

$$L_a M_{vz}'^2 + L_v M_{az}'^2 = (\sqrt{L_a}|M'_{vz}| - \sqrt{L_v}|M'_{az}|)^2 + 2\sqrt{L_a L_v}|M'_{az}M'_{vz}|$$

   which results in

$$(\sqrt{L_a}|M'_{vz}| - \sqrt{L_v}|M'_{az}|)^2 + 2\sqrt{L_a L_v}|M'_{az}M'_{vz}| - 2|M_{av}||M'_{az}M'_{vz}| > 0.$$

   Since the first term is quadratic it remains to show that

$$2\sqrt{L_a L_v}|M'_{az}M'_{vz}| - 2|M_{av}||M'_{az}M'_{vz}| > 0 \quad \Longrightarrow \quad L_a L_v - M_{av}^2 > 0$$

   which is Condition (4.37).

2. notice that D in Equation (4.33) is linearly dependent on α. Therefore, because of condition (4.37) we observe that

$$D > 0, \forall \alpha > \alpha_c \qquad \text{and} \qquad D < 0, \forall \alpha < \alpha_c.$$

3. notice that N in Equation (4.32) is also linearly dependent on α. For $N = 0$ the resulting expression in the square root has to be positive since the eigenvalues are pure real valued. Thus, for $N = 0$

$$-4\Omega_a\Omega_v\alpha D > 0 \qquad \Longrightarrow \qquad \alpha D < 0$$

which is verified if $\alpha \in (0, \alpha_c)$. Therefore, since $N > 0$ for $\alpha = 0$ it results that

$$N < 0, \forall \alpha \geq \alpha_c.$$

These preliminaries now allow the analysis of the eigenvalue's sign evolution as a function of α.

- $\alpha < 0$:
  Implies $N > 0$ and $D < 0$. Thus, the expression in the square root satisfies

  $$0 < N^2 - 4\Omega_a\Omega_v\alpha D < N^2$$

  which results in

  $$\lambda_1 < 0 \qquad \text{and} \qquad \lambda_2 < 0.$$

- $\alpha = 0$:
  Implies $N > 0$ and $D < 0$. The expression in the square root is equal to N^2 resulting in

  $$\lambda_1 = 0 \qquad \text{and} \qquad \lambda_2 = \frac{N}{D} < 0.$$

- $0 < \alpha < \alpha_c$:
  Implies $D < 0$. Thus, the expression in the square root satisfies

  $$N^2 - 4\Omega_a\Omega_v\alpha D > N^2$$

  which results in

  $$\lambda_1 > 0 \qquad \text{and} \qquad \lambda_2 < 0.$$

- $\alpha = \alpha_c$:
  Implies $N < 0$ and $D = 0$. Thus, the denominator of both eigenvalues (Equations (4.30) and (4.31)) are zero. For λ_1 the nominator is N and λ_1 is therefore not defined. For λ_2 the nominator converges to zero when $\alpha \to \alpha_c$. Therefor, it can be shown with de l'Hopital's rule that $\lambda_2 < 0$.

- $\alpha > \alpha_c$:
  Implies $N < 0$ and $D > 0$. Thus, the expression in the square root verifies

$$0 < N^2 - 4\Omega_a\Omega_v\alpha D < N^2$$

which results in

$$\lambda_1 < 0 \qquad \text{and} \qquad \lambda_2 < 0.$$

For an elongated plasma the decay index n is negative [35] (Section 1.1.5) which according to Equation (4.18) results in $\alpha > 0$. Therefore, the case where $\alpha < 0$ is not of interest for elongated plasma studies. When $\alpha = 0$ the decay index is equal to zero which means that the external magnetic field is not curved. This occurs when the plasma is circular (for large aspect ratio) and is therefore not relevant, too. For a strongly elongated plasma ($n < 0$, $\alpha > 0$) the linear model has two different ranges. It turns out that for the first part, where $0 < \alpha < \alpha_c$, one eigenvalue, i.e. λ_1, is positive resulting in an unstable system. According to the simple second order model the system becomes stable again for $\alpha > \alpha_c$. This is due to the fact that the force balance model does not consider the mass of the plasma. But for $\alpha > \alpha_c$ the plasma takes a considerable part in the dynamic of the plasma. In this case the plasma is still unstable and has a very fast unstable mode. Thus, the linear model is only valid in the range of $0 < \alpha < \alpha_c$ and its accuracy decreases when α approaches its critical value α_c. It turns out that the second order model is a good approximation since α is always below its critical value. This is due partly to the active coil system and mainly to the vessel.

Consider for example that there are no active coil and vessel. Then M'_{az} and M'_{vz} are both zero and thus α_c is zero as well according to Equation (4.38). This case can obviously not be represented with the simple linear model. By adding the active coil system and the vessel the coupling factors M'_{az} and M'_{vz} mostly reach sufficient important values to ensure that $\alpha < \alpha_c$. Therefore, the simple linear model is in most cases a good approximation. For what follows we will consider only cases for which $0 < \alpha < \alpha_c$ is satisfied.

Table 4.1 shows the summary of the discussed properties of λ_1 and λ_2 as a function of α. Furthermore, Figure 4.4 illustrates a numerical example of the evolution of λ_1 and λ_2 as a function of α with the intention of giving an impression of the shape of the evolution.

	$\alpha < 0$	$\alpha = 0$	$0 < \alpha < \alpha_c$	$\alpha = \alpha_c$	$\alpha > \alpha_c$
λ_1	< 0	$= 0$	> 0	$-$	< 0
λ_2	< 0	< 0	< 0	< 0	< 0

Table 4.1: Summary of the signs of the eigenvalues as a function of α.

4.3 The RZIP model

The RZIP model has a similar structure to the simple second model. The major difference lies in the following three improvements:
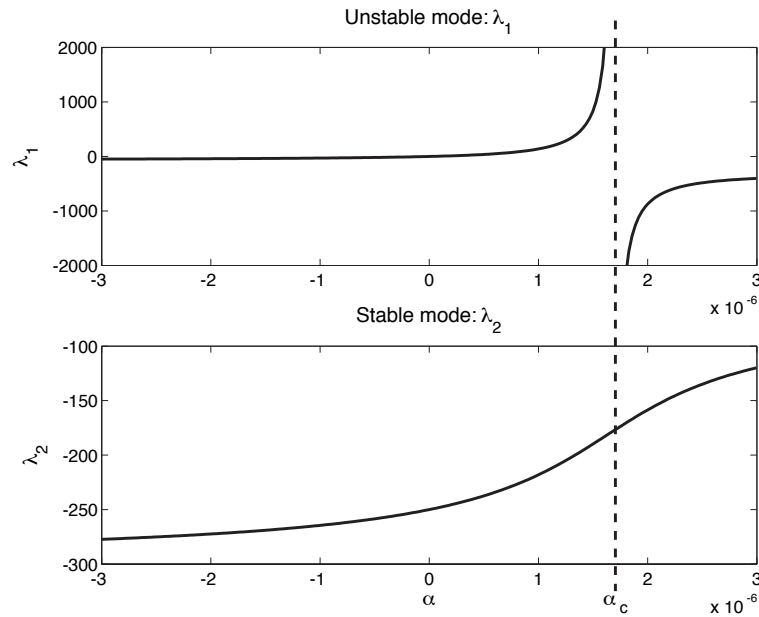
Figure 4.4: Numerical example of the evolution of λ_1 and λ_2 as a function of α.

1. The plasma current evolution is no longer neglected. Therefore the plasma current denoted by I_p is added to the state variables vector. The plasma current shows similar properties to a coil and therefore possesses a self-inductance, mutual inductances, coupling coefficients and an ohmic resistance.

2. The instantaneous radial force-balance equation is added. Similar to the vertical force-balance it is an algebraic expression. Thus, a pseudo state variable RI_{p0} denoting the radial plasma position is introduced into the model.

3. The number of active coil currents and vessel eigenmodes is unlimited. The variable $I_a \in \mathbb{R}^{n_a}$ consists of a vector for which every of the n_a elements expresses the current of a single coil or a structure of serial connected coils. This implies that the voltage input variable denoted by V_a is also a vector with n_a different corresponding voltage inputs. Similar to that, $I_v \in \mathbb{R}^{n_v}$ is a vector with n_v different vessel eigenmodes.

These additions result in the RZIP model formally described in [40].

$$M\dot{x}_p + \Omega x_p = \begin{bmatrix} L_a & M_{av} & M_{ap} & M'_{aR} & M'_{az} \\ M_{av} & L_v & M_{vp} & M'_{vR} & M'_{vz} \\ M_{ap} & M_{vp} & L_p & M'_{pR} & M'_{pz} \\ M'_{aR} & M'_{vR} & M'_{pR} & \beta & M'_{Rz} \\ M'_{az} & M'_{vz} & M'_{pz} & M'_{Rz} & \alpha \end{bmatrix} \dot{x}_p + \begin{bmatrix} \Omega_a & 0 & 0 & 0 & 0 \\ 0 & \Omega_v & 0 & 0 & 0 \\ 0 & 0 & \Omega_p & 0 & 0 \\ 0 & 0 & 0 & 0 & 0 \\ 0 & 0 & 0 & 0 & 0 \end{bmatrix} x = U, \tag{4.40}$$

where

$$x_p = \begin{bmatrix} I_a \\ I_v \\ I_p \\ RI_{p0} \\ zI_{p0} \end{bmatrix} \quad \text{and} \quad U = \begin{bmatrix} V_a \\ 0 \\ 0 \\ 0 \\ 0 \end{bmatrix}, \tag{4.41}$$

again leading to the ODEs in state space form

$$\dot{x}_p = -M^{-1}\Omega x_p + M^{-1}U = A_p x_p + B_p V_a = A_p x_p + B_p u. \tag{4.42}$$

Tables 4.2-4.4 give a short description of all physical variables and constants used.

As for the simple model the outputs, like plasma parameters and magnetic diagnostic measurements (about 100 sensors), of the tokamak are expressed as linear combinations of the state variables.

$$y = C_p x. \tag{4.43}$$

4.3.1   Unstable characteristic of the RZIP model

The matrix M is symmetric implying that its inverse M^{-1} is also symmetric and Ω is a diagonal semi-positive matrix (all its elements are positive or zero). Therefore by applying Theorem 1 the eigenvalues of $A_p = -M^{-1}\Omega$ cannot be imaginary. Similar to the simple second order model, the existence of the instability of the RZIP model depends on the value of the field curvature α.

Due to the structure of the model there exists at most only one unstable mode when the plasma is elongated, i.e. $\alpha > 0$. This behaviour of the RZIP model can be verified by taking numerical examples. All linear models derived so far with RZIP have shown the characteristic of a single unstable pole. So far, we are not able to provide a complete formal proof of this statement. Nevertheless, for what follows we give the principal ideas and the required assumptions for demonstrating the existence of a single unstable pole for elongated plasmas.

The eigenvalues of A_p are the n roots of its characteristic polynomial given by

$$\det(\lambda I - A_p) = \det(\lambda I + M^{-1}\Omega) = \det(M^{-1})\det(\lambda M + \Omega) \tag{4.44}$$

$$= \frac{1}{\det(M)}\det(\lambda M + \Omega),$$

where

$$\det(M\lambda + \Omega) = \left| \left[\begin{array}{ccc} \lambda M_p + \Omega_p & \lambda M_\beta^T & \lambda M_\alpha^T \\ \lambda M_\beta & \lambda\beta & \lambda M'_{Rz} \\ \lambda M_\alpha & \lambda M'_{Rz} & \lambda\alpha \end{array} \right] \right| \tag{4.45}$$

with

$$M_p = \left[\begin{array}{ccc} L_a & M_{av} & M_{ap} \\ M_{av} & L_v & M_{vp} \\ M_{ap} & M_{vp} & L_p \end{array} \right], \qquad \Omega_p = \left[\begin{array}{ccc} \Omega_a & 0 & 0 \\ 0 & \Omega_v & 0 \\ 0 & 0 & \Omega_p \end{array} \right],$$

$$M_\alpha = \left[\begin{array}{ccc} M'_{aR} & M'_{vR} & M'_{pR} \end{array} \right] \quad \text{and} \quad M_\beta = \left[\begin{array}{ccc} M'_{az} & M'_{vz} & M'_{pz} \end{array} \right].$$

We express the characteristic polynomial of $\det(M\lambda + \Omega)$ as

$$\det(M\lambda + \Omega) = a_n\lambda^n + \ldots + a_2\lambda^2 + a_1\lambda + a_0. \tag{4.46}$$

By identifying the coefficients of this polynomial with Equation (4.45) we obtain

$$a_0 = 0, \qquad a_1 = 0, \qquad a_2 = \text{Trace}(\Omega_p)\,\alpha\,\beta \quad \text{and} \quad a_n = \det(M), \tag{4.47}$$

where the two coefficients $a_0 = 0$ and $a_1 = 0$ are due to the simple fact that the dynamical System (4.42) possesses two algebraic equations linked to the vertical z and radial R plasma positions.

We reformulate the characteristic polynomial of A_p as

$$\det(I\lambda - A_p) = \frac{1}{\det(M)} \det(M\lambda + \Omega)$$

$$= \lambda^n + \frac{a_{n-1}}{\det(M)}\lambda^{n-1} + \ldots + \frac{a_3}{\det(M)}\lambda^3 + \frac{\text{Trace}(\Omega_p)\,\alpha\,\beta}{\det(M)}\,\lambda^2 \qquad (4.48)$$

$$= \lambda^2 C(\lambda),$$

where

$$C(\lambda) = \lambda^{n-2} + \frac{a_{n-1}}{\det(M)}\lambda^{n-3} + \ldots + \frac{a_3}{\det(M)}\lambda + \frac{\text{Trace}(\Omega_p)\,\alpha\,\beta}{\det(M)}. \qquad (4.49)$$

Since we already know that there are two eigenvalues at zero we only need to study the roots of the function $C(\lambda)$. Three cases depending on the sign of α can be distinguished:

1. $\alpha = 0$:
   $C(\lambda)$ has a root at zero. In this case we assume that System (4.42) is marginally stable and thus we consider that all other roots are negative. Furthermore, by observing that

   $$\lim_{\lambda \to +\infty} C(\lambda) = +\infty \qquad (4.50)$$

   the function $C(\lambda)$ can be qualitatively illustrated as in Figure 4.5 a). Since there is no positive root the function $C(\lambda)$ can never cross zero $(C(\lambda) = 0)$ for all $\lambda > 0$. Note that Figure 4.5 a) illustrates only the first two roots $\lambda_0 = 0$ and $\lambda_1 < 0$.

2. $\alpha < 0$:
   We consider the function $C(\lambda)$ at $\lambda = 0$, i.e.

   $$C(0) = \frac{\text{Trace}(\Omega_p)\,\alpha\,\beta}{\det(M)}. \qquad (4.51)$$

   Since all resistances of Ω_p are positive we have $\text{Trace}(\Omega_p) > 0$. Furthermore, we assume that $\frac{\beta}{\det(M)} < 0$. Thus, for $\alpha < 0$ condition $C(0) > 0$ is satisfied. Since the function $C(\lambda)$ is also a continuous function of α we consider first $C(\lambda)$ at $\alpha = 0$ and vary $C(\lambda)$ continuously by decreasing α ($\alpha < 0$). This leads to a function $C(\lambda)$ for $\alpha < 0$ which can be qualitatively illustrated as in Figure 4.5 b). Therefore, the roots of $C(\lambda)$ are strictly negative, i.e. $\lambda_2 < \lambda_1 < 0$.

3. $\alpha > 0$:
   Due to Equation (4.51) and by considering $\text{Trace}(\Omega_p) > 0$ and $\frac{\beta}{\det(M)} < 0$ condition $C(0) < 0$ is satisfied for $\alpha > 0$. Thus, similarly as for the case $\alpha < 0$, we consider first $C(\lambda)$ at $\alpha = 0$ and vary $C(\lambda)$ continuously by increasing α ($\alpha > 0$) which leads to a function $C(\lambda)$ for $\alpha > 0$ which can be qualitatively illustrated as in Figure 4.5 c). In this case we inevitably obtain a single positive root $\lambda_1 > 0$, while all other roots remain negative, i.e. $\lambda_2 < 0$.
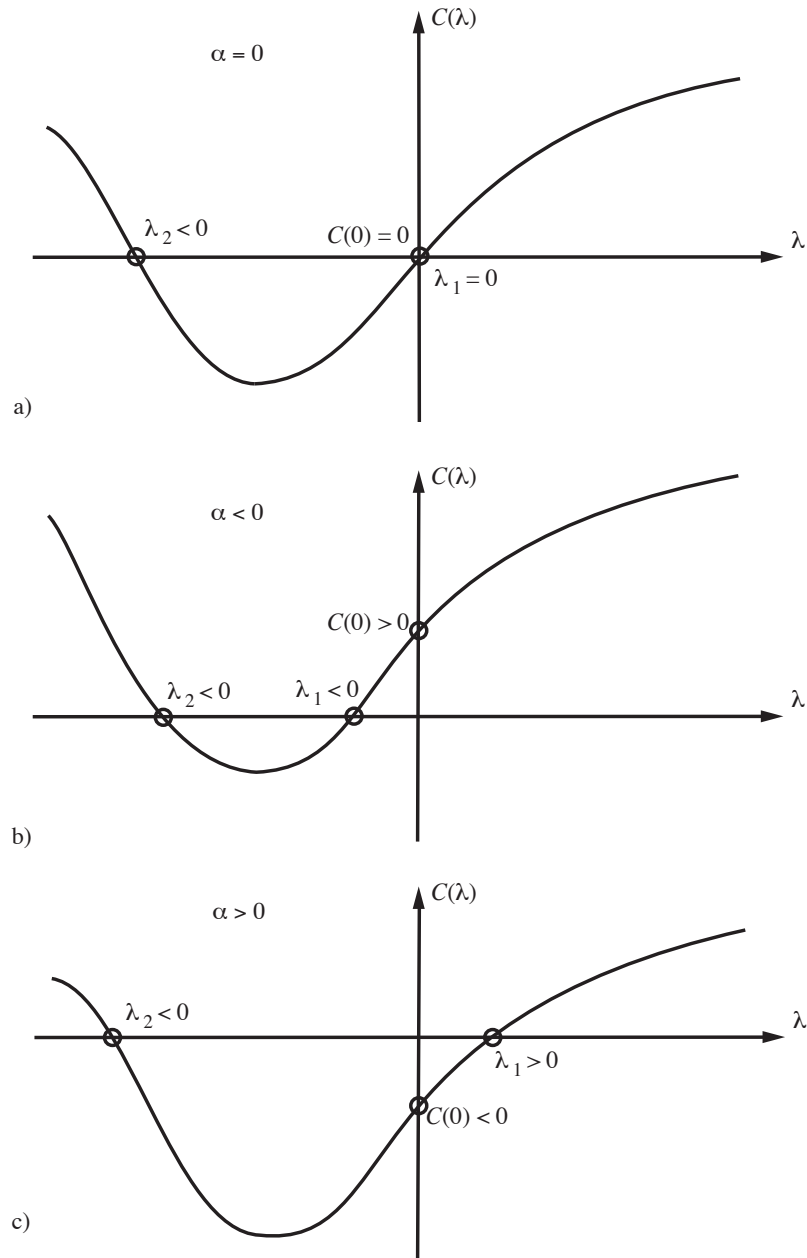
Figure 4.5: Qualitative illustration of the function $C(\lambda)$: a) for $\alpha = 0$, b) for $\alpha < 0$ and c) for $\alpha > 0$.

Note that $\det(M)$ varies as a function of α. It turns out that for $\alpha > 0$ there is a value of α for which $\det(M) = 0$. Compared with the simple second order model, this corresponds to the case for which α is equal to its critical value $(\alpha = \alpha_c)$.

To obtain a more rigorous and complete proof of the existence of a single positive root for $\alpha > 0$ further investigations are required. Among other things we will have to prove that

- there is no positive root for $\alpha = 0$ and

- $\frac{\beta}{\det(M)} < 0$ (Note that the RZIP model provides $\beta < 0$ and $\det(M) > 0$)

4.4 The CREATE-L model

Contrary to the RZIP model the CREATE-L model [2] allows plasma deformation by conserving an equilibrium of the plasma current distribution. In addition, the effect of changes to β_p and l_i are evaluated consistently. The constraints equations (algebraic equations expressing zI_{p_0} and RI_{p_0} in function of the currents for the RZIP model) are eliminated, but the model is expressed similarly to that of RZIP.

$I_a \in \mathbb{R}^{n_a}$	n_a active coil currents
$I_v \in \mathbb{R}^{n_v}$	n_v vessel eigenmode currents
$I_p \in \mathbb{R}$	Plasma current
$RI_{p_0} \in \mathbb{R}$	Radial plasma position times I_{p_0}
$zI_{p_0} \in \mathbb{R}$	Vertical plasma position times I_{p_0}

Table 4.2: The physical state variables.

Ω_a, Ω_v	Resistances of active coils and vessel eigenmodes (diagonal matrices)
L_a, L_v	Self and mutual inductances of active coils and vessel eigenmodes
M_{av}	Mutual inductances between active coils and vessel eigenmodes
Ω_p	Plasma resistance
L_p	Plasma self-inductance
M_{ap}, M_{vp}	Mutual inductances between plasma and active coils or vessel eigenmodes
M'_{aR}, M'_{vR}, M'_{pR}	Coupling coefficient between radial position and active coils, vessel eigenmodes or plasma
M'_{az}, M'_{vz}, M'_{pz}	Coupling coefficient between vertical position and active coils, vessel eigenmodes or plasma ($M'_{pz} = 0$ [40])
M'_{Rz}	Coupling coefficient between radial position and vertical position
β	The self-coupling coefficient of radial position (see [17, 40])
α	The field curvature: self-coupling coefficient of vertical position

Table 4.3: The parameters of mutual inductance matrix M and resistance matrix Ω.

I_{p_0}	Plasma current at equilibrium
R_0	Radial plasma position at equilibrium
n	Decay index $n = -\frac{R_0}{B_z}\frac{\partial B_z}{\partial R}$, where B_z is the vertical Field at R_0
Γ	Shafranov coefficient

Table 4.4: The plasma and magnetic field parameters at equilibrium.

Chapter 5

The effect of feedback control on superconducting tokamak AC losses

5.1   Introduction

Most present tokamaks use copper conductors for the creation of the magnetic fields required to provide the plasma equilibrium and to control the shape and position of the plasma cross section. Exceptions are Tore Supra, T-7 and T-15 which have superconducting toroidal field coils, the small tokamak TRIAM which has superconducting toroidal and poloidal field coils and the LHD Stellarator. These tokamaks operate with circular cross section plasmas and do not require active control of the vertical positional instability which is a property of vertically elongated plasma cross-sections.

The fusion power generated in a tokamak reactor plasma is less than the ohmic power which would be dissipated in copper poloidal and toroidal field coils, requiring superconducting magnets in any large device. The next generation of tokamaks under construction, K-STAR, SST-1 and HT-7U will require vertical position and active shape control and will be fully superconducting. The future large tokamak ITER is also naturally designed with superconducting coils. The interplay between the superconducting magnets and the plasma shape and position control will become important for these devices and presents one of their new features.

Superconducting coils possess superconducting properties only below a critical temperature around a few K. For a temperature above this critical temperature the coils show a non-negligible electric resistivity. AC losses are detrimental since they heat up the superconducting material. Thus, if AC losses are too large, the cryogenic plant can no longer hold the required temperature to maintain the superconductivity properties. Once the superconductivity is lost, the electric currents in the coils produce an enormous heat loss due to the ohmic resistivity, which leads to a possible damage of the coils. In general, the coils are designed with enough margin to absorb all likely losses. A possible loss reduction could allow us to downsize the superconducting cross section in the cables, reducing the overall cost, or simply increase the operational cooling margin for given coils.

When the magnetic transverse field in superconducting magnets changes, the magnet generates two types of heat loss, the so-called coupling loss and the so-called hysteresis loss, grouped together as AC losses and described in Section 5.2 of this chapter. The field variations which lead to losses are produced by the evolution of the equilibrium through the discharge, referred to as the scenario loss, and the action of the plasma position and shape controller, referred to as feedback losses. During the design of ITER,

studies were performed to estimate the effect of the action of the feedback control loops on the accumulated AC losses to determine the required cryogenic plant load and the local cooling requirements of the magnets. These estimates were performed with a complex code [57] which analysed the results of simulations of the plasma shape and position feedback control loops. The effect of the design of the controller on the AC losses had not previously been investigated.

The aim of this present chapter is to determine to what extent the accumulated AC losses in ITER could be reduced by taking into account the losses themselves when designing the feedback control loops. In order to be able to carry out this investigation an AC loss model is required which permits a fast estimation of the AC losses. Note that for the existing code [57] an execution time (computing and analysing time together) of about 6 months per AC losses estimation is typical. This is of course not practicable for our optimisation purposes. Therefore, a simpler and fast executable model of the AC losses, referred to as the "AC-CRPP" model, has been developed and is described in Section 5.2. At present, the AC losses are only calculated for the PF coils. This model was compared with detailed simulations available, in order to validate it. The action of the feedback control was simulated using a standard linearised model of the ITER tokamak [31] and using the standard ITER position and shape feedback controller [6, 7], described in Section 5.3. In order to evaluate the feedback controller performance, a set of standard disturbances was used, corresponding to the ITER design methodology [21] and summarised in Section 5.3.

In Section 5.4, the results of these simulations are presented, showing that the AC-CRPP model agrees well enough with the basic calculations of the detailed code [57] to have confidence in using the AC-CRPP model to refine the feedback controller. The distribution of the AC losses among the different coils is also discussed in Section 5.5.

These results allowed us to modify the feedback controller, especially the fast part which guarantees the vertical stability, showing that the hysteresis loss is only weakly affected by the controller design but that the coupling loss can be significantly reduced. A modified controller is proposed, to illustrate potential reductions using different design criteria.

In Section 5.6, we discuss the significance of these results for ITER, showing that the total AC losses are weakly dependent on controller design for the short 430 second flat-top, but that for longer pulse operation the AC losses could be usefully reduced by the approach presented.

5.2   AC loss model and validation

5.2.1   Superconductors and AC losses

5.2.1.1   Characterisation of superconductors

Below a certain critical temperature T_c, superconductors lose their electrical resistivity. Superconductors show the *Meissner-Ochsenfeld-effect* (diamagnetic behaviour) which is the expulsion of all external magnetic fields from their interior. The interior includes all the the material except for a very thin layer on the surface of the conductor (the London penetration depth λ). Inside this very thin surface layer an induced shielding current circulates, whose magnetic field compensates the external magnetic field.

Type I superconductors show a complete Meissner effect and expel all of the magnetic field from their interior up until a critical magnetic field B_c when they abruptly cease to behave like superconductors.

Type II superconductors only exhibit a partial Meissner effect except for weak magnetic fields up to a strength of B_{c1}, above they show progressively less expulsion until at a certain level of magnetic field B_{c2} they abruptly cease to behave as superconductors.

There is also a critical current density J_c above which the material loses superconductivity. T_c, B_c and J_c are interrelated.

Although there is no resistivity in superconducting cables, there are still AC losses in the presence of time-varying magnetic fields. The two most important types are hysteresis loss and coupling loss. They produce heat and are therefore important factors when designing the cryogenic system. Their relative importance depends on the application.

5.2.1.2 Hysteresis loss

In Figure 5.1 we illustrate a DC magnetisation curve for a type II superconductor, of the type proposed for ITER. When a magnetic field is initially applied (for this explanation we assume $B > 0$), the superconductor shows perfect diamagnetism, the shielding currents induced at the filament surface preventing the flux from penetrating ($-M = H > 0$) up until B_{c1}. Above B_{c1} the flux gradually penetrates into the filament until it reaches its center at the first penetration field B_{p1}. For a higher magnetic field B the magnetisation decreases and eventually becomes 0 at the upper critical field B_{c2} (upper branch, not illustrated in Figure 5.1). When the magnetic field is decreased, the average magnetisation begins to decrease rapidly, reverses its sign ($-M < 0$) and reaches the lower branch (Figure 5.1). The flux trapped at $B = 0$ is the residual magnetisation.
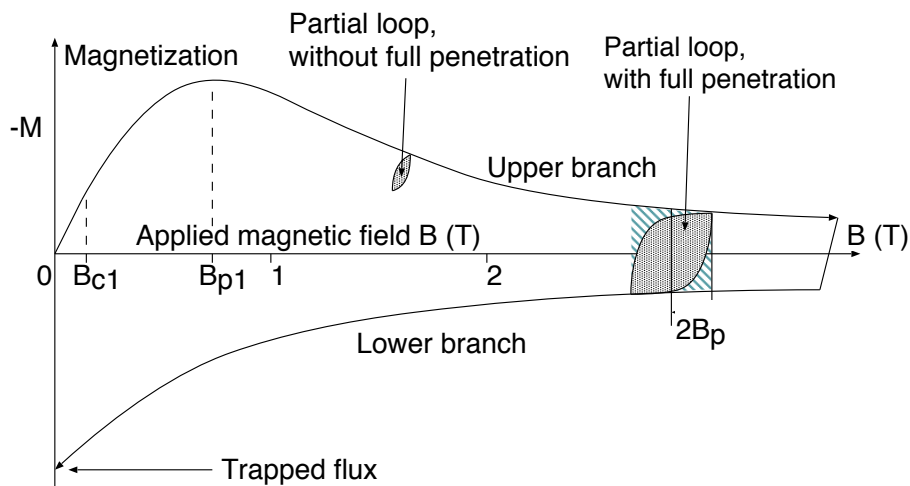
Figure 5.1: Magnetisation vs. applied magnetic field for a type II superconductor.

If the external magnetic field is reversed after the initial magnetisation (on the upper branche), there has to be a certain field difference until the field reversal reaches the center of the conductor. Figure 5.2 (a) shows the initial flux profile (dashed line) and the flux profile after a field reversal of $2B_p$ (solid line). B_p is the penetration field and is

the difference between the external field and the field at the electrical center line of the conductor. To fully reverse the flux profile, a field change of $2B_p$ is needed. Figure 5.1 includes a loop with full penetration. The shaded area between the demagnetisation and magnetisation path is the loss caused during the cycle. If the field difference is smaller, there is not full penetration and the resulting flux profile is like that shown in Figure 5.2 (b).
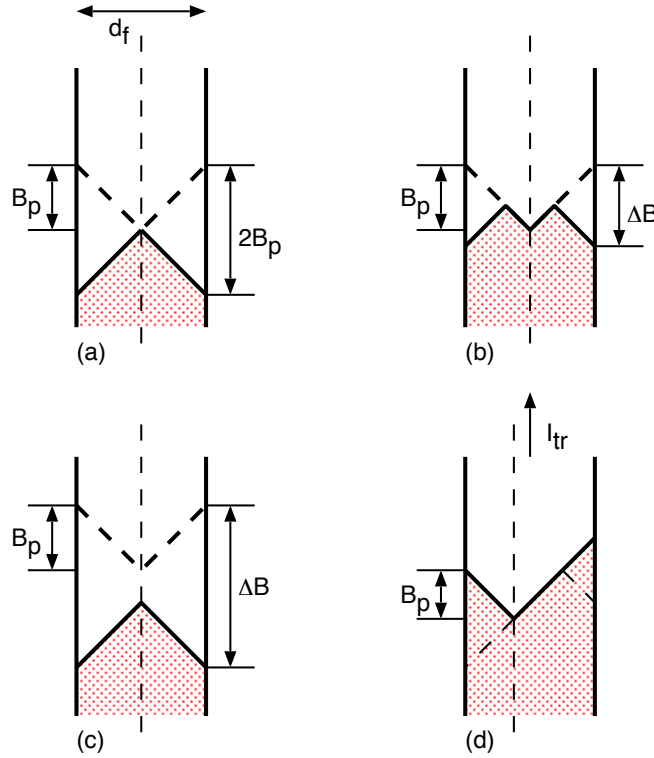
Figure 5.2: Penetration field without and with transport current. The dashed profile represents the situation on the upper branch of the magnetisation curve. The solid profile represents the lower branch.

It is assumed that the critical current density J_c is constant over the filament cross-section, so the flux profiles have a linear behaviour and Bean's model [8] can be used, in which for a cylinder of diameter d_f and with an external magnetic field perpendicular to the cylinder axis,

$$B_{p\perp} = \frac{\mu_0 j_{c\parallel}(B) d_f}{\pi}. \tag{5.1}$$

where $j_{c\parallel}$ is the critical current density of the superconductor, a function of temperature and external magnetic field, that can be obtained from measurements.

For closed cycles of magnetisation and demagnetisation, the energy loss q_h per unit volume of superconducting material is written as the integral of the magnetisation M versus the applied magnetic field B with M the average value of magnetisation,

$$q_h = \oint M(B) \, dB \qquad (\text{J/m}^3). \tag{5.2}$$

The hysteresis losses are independent of the magnetic field rate of change $\dot{B} = \frac{dB}{dt}$.

There are three simple cases considered for the calculation of the hysteresis loss, shown in Figure 5.1 and Figure 5.2:

For $\Delta B < 2B_{p\perp}$ (partial loop without full penetration, Figure 5.2 (b)):

$$q_{h,\perp} = \frac{\Delta B^3}{3\mu_0 B_{p\perp}} \left(1 - \frac{\Delta B}{4B_{p\perp}} \right) \qquad (\text{J/m}^3) \qquad (5.3)$$

For $\Delta B > 2B_{p\perp}$ (partial loop with full penetration, Figure 5.2 (c)):

$$q_{h,\perp} = \frac{4}{3}\frac{B_{p\perp}^2}{\mu_0} \left(\frac{\Delta B}{B_{p\perp}} - 1 \right) \qquad (\text{J/m}^3) \qquad (5.4)$$

For $\Delta B \gg 2B_{p\perp}$ (partial loop with full penetration, approximation for large ΔB)

$$q_{h,\perp} \approx \frac{4}{3}\frac{B_{p\perp}\Delta B}{\mu_0} \qquad (\text{J/m}^3) \qquad (5.5)$$

Hysteresis losses are calculated over a closed cycle of external magnetic field and are given per unit volume of superconductor (Joule/m^3).

The three cases are illustrated in Figure 5.1. From the figure, the third case (light shaded and approximatively squared area) overestimates the actual hysteresis loss.

If in a superconducting cylinder a longitudinal transport current I_{tr} is superimposed on the currents creating the transverse field magnetisation, the electric center line is moved from the geometric center to the periphery of the filament (Figure 5.2 (d)). The flux profile is asymmetric and the penetration field decreases by a factor $(1-k)$:

$$k = \frac{I_{tr}}{I_{c\parallel}}, \qquad B_{p\perp}^k = B_{p\perp}(1-k) \qquad (\text{T}) \qquad (5.6)$$

This also modifies the range of validity of Equation (5.3) and Equation (5.4) ($B_{p\perp}$ has to be replaced by $B_{p\perp}^k$). In addition, Equation (5.5) is modified to:

$$q_{h,\perp} \approx \frac{4}{3}\frac{B_{p\perp}\Delta B}{\mu_0}(1 + k^2) \qquad (\text{J/m}^3). \qquad (5.7)$$

These assumptions are used to estimate the hysteresis loss in the AC-CRPP model. Further information on hysteresis losses is presented in [55].

5.2.1.3 Coupling current loss

Superconducting cables used in industrial applications are composed of several bundled strands, each containing thousands of filaments. The reason for this is to avoid flux jumps that can occur in cables with large filament diameters and to reduce hysteresis loss. The drawback is the occurrence of a new class of losses, called coupling current losses, because of the magnetic coupling of strands and filaments in the presence of a time varying transverse magnetic field.

Two strands or filaments form an induction loop, in which the two superconducting parts are linked by two non-superconducting volumes. The induced loop current has to pass through this resistive area and thereby produces an ohmic loss (Figure 5.3). A time
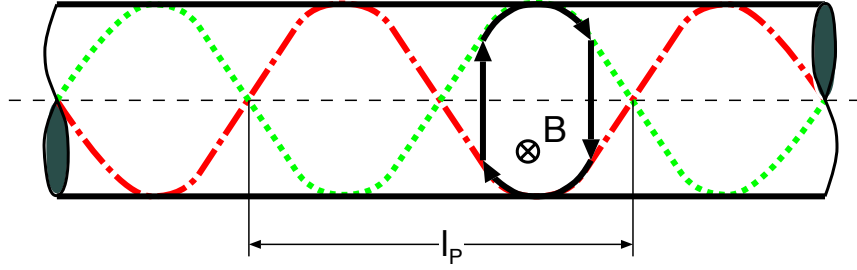
Figure 5.3: View inside a strand with two twisted filaments embedded in a non-superconducting matrix. The arrows illustrate a current loop caused by the varying transverse magnetic field. The twist pitch l_p is an average value and characterises the length of a typical loop.

constant can be assigned to such a loop, which allows linking the magnetic field rate of change $\dot{B}$ to the generated loss. This time constant for a twisted, multifilamentary composite can be expressed as

$$\tau = \frac{\mu_0 l_p^2}{8\pi^2 \rho} \qquad \text{(s)}, \tag{5.8}$$

which represents the ratio of the loop inductance to the loop resistance, a function of the twist pitch l_p and the matrix resistivity ρ.

A multistage cable has a multitude of different loops with different time constants τ_i. In this case, a dimensionless geometry factor n_i is associated to every time constant τ_i. An overall time constant has to be used for coupling loss calculations, expressed as

$$n\tau = \sum_i n_i \tau_i \qquad \text{(s)}. \tag{5.9}$$

Due to the uncertitude in the resistance of the different loops, it is not reliable to estimate the time constant directly from the conductor geometrical data, so it has to be measured.

For a linear ramp of the transverse magnetic field ($\dot{B} = \text{const}$), the coupling power loss per unit volume of strand material is given by

$$p_c = \frac{n\tau}{\mu_0} \dot{B}^2 \qquad \text{(W/m}^3\text{)}, \tag{5.10}$$

from which we extract the essential information that the coupling loss increases with the square of the field rate of change. This equation is called the steady state formula since it is exact only for ramps with infinite duration. Steady state conditions can be assumed if the time scale for the field change is much larger than the overall time constant factor $n\tau$. To illustrate this we consider the coupling loss during a finite time laps of Δt. During the time Δt the change of the magnetic field is given by $\Delta B = \dot{B} \Delta t$ since we assume a linear ramp for which $\dot{B} = \text{const}$. The coupling energy density loss during Δt is given by multiplying Equation (5.10) with Δt

$$q_c = \frac{n\tau}{\mu_0} \dot{B}^2 \Delta t = \frac{n\tau}{\mu_0} \Delta B \dot{B} = \frac{1}{2} \frac{1}{\mu_0} \Delta B \dot{B} \, 2n\tau \qquad \text{(J/m}^3\text{)}. \tag{5.11}$$

In contrast to it, the magnetic energy density accumulated during Δt is given by

$$q_m = \frac{1}{2} \frac{1}{\mu_0} \Delta B^2 = \frac{1}{2} \frac{1}{\mu_0} \Delta B \dot{B} \, \Delta t \qquad \text{(J/m}^3\text{)}. \tag{5.12}$$

By comparing Equation (5.11) with Equation (5.12) we observe that when the duration of the ramp is small $\Delta t < 2n\tau$ the coupling loss energy density q_c becomes larger than the magnetic energy density q_m. Of course, from the point of view of physics this is not possible. The explanation lies in the fact that for short magnetic field ramps (small Δt) the induced coupling currents cannot penetrate completely into the conductor during the time Δt. A certain amount of time is required, denoted by t_{pen}, after which the conductor can be considered as fully penetrated. The steady state formula is derived by assuming that the coupling currents fully penetrate the conductor, which only happens when $\Delta t \gg t_{pen}$ is satisfied and thus t_{pen} can by neglected. Therefore, for short Δt the actual coupling losses are always smaller that their estimation by means of the steady state formula.

If the duration of the ramp Δt is larger than $10n\tau$ the steady state formula is accurate enough. As an indication for the estimation error consider that the coupling losses are overestimated by $\approx 10\%$ in the case for which $\Delta t \approx 10n\tau$. For shorter ramps, the steady state formulas should be replaced by transient formulas [16]. But since these formulas are complicated and their implementation is far from evident, we will focus in this study only on the steady state formula.

For further informations on coupling current losses refer to [16]. Scaling laws for the critical properties of NbTi can be found in [11].

5.2.1.4   ITER magnet cables

The conductors to be used for the ITER PF coils (ITER version 1998) are made out of 864, 1080 or 1440 strands with different winding schemes. The strands are composed of sub-elements and the actual superconducting filaments are between $5\,\mu$m and $7\,\mu$m, embedded in a copper matrix. These strands are surrounded by a steel jacket to absorb the high mechanical forces, Figure 5.4.
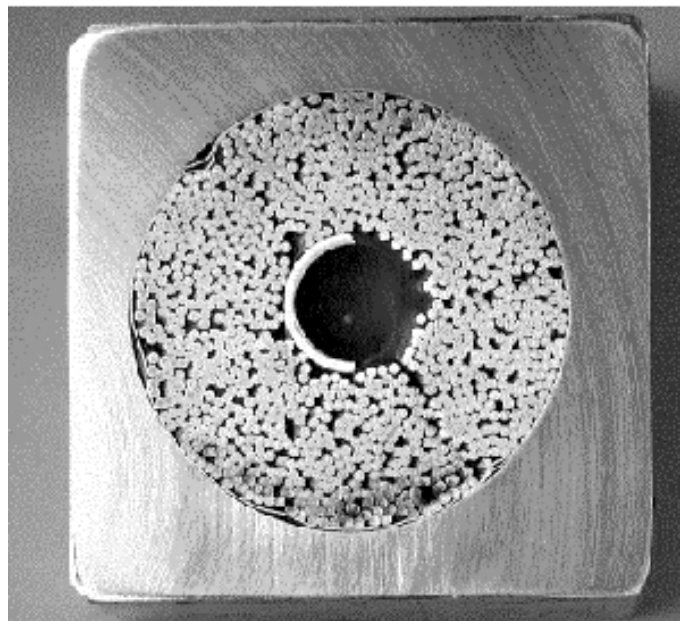
Figure 5.4: Cable-in-conduit (CICC) superconductor developed for the ITER Tokamak.

The central hole is a metal helix that carries most of the forced flow of supercritical helium. At the inlet, the coolant is at $4.5\,\mathrm{K}$ and reaches a temperature of up to $5.5\,\mathrm{K}$ at the outlet, leaving a margin of $1-2\,\mathrm{K}$ to the current sharing temperature.

The time between inlet and outlet is long in comparison with the time scale of all loss mechanisms, so the coolant temperature can be considered as an integrator of the loss history during the time the coolant is inside the conductor. The conductor is designed with enough margin to absorb all likely losses. The possible reduction could allow downsizing the superconducting cross section in the cables, reducing the overall cost.

Currently used filament diameters are around $7\,\mu\mathrm{m}$ and could be as low as $5\,\mu\mathrm{m}$ for the ITER coils. To reduce the conductor cost, it would be interesting to increase the filament diameter to at least $10\,\mu\mathrm{m}$, allowing a potentially simpler and cheaper manufacturing process.

Other loss sources include conduction, thermal and nuclear radiation. The non superconducting joints also generate losses due to ohmic heating. For ITER, the cryogenic system will have approximately $150\,\mathrm{kW}$ cooling power.

5.2.2 Evaluation method and AC-CRPP model

5.2.2.1 Magnetic field evaluation

The AC losses in the PF coils are a function of the transverse magnetic field and its time derivative at the center of every turn. Sources of the transverse magnetic field are the toroidal currents in the PF and CS coils, the plasma and the conducting vacuum vessel. These sources are modeled as discrete sets of stationary current carrying circular filaments, illustrated in Figure 5.5 where the crosses represent the filaments that model the coils, the circles represent the filaments that model the vessel and the dots represent the filaments that model the plasma. Simulations have shown that the influence of plasma position variations is small, so the plasma is assumed to be stationary. The TF coils also contribute to the transverse field because their field is not uniform along the perimeter, but this influence is small and therefore neglected in the model. The TF coil current itself is considered constant.

The filaments representing the PF coil currents are distributed uniformly over the whole area of each PF coil and the PF coil current is the sum of the nominal equilibrium current plus the transient variations due to the action of the shape and position feedback controller. The vessel is modeled as a set of 56 filaments that are identical to the states of the ITER state-space model used for control purposes. The plasma is modeled as a grid of filaments that carry a current defined by the plasma configuration and scaled according to the total plasma current variation.

The field over the cross section of a coil has significant spatial variations. While the field is maximum at the outside, it tends to zero at the center. This requires a certain minimum number of evaluation points for a good representation of the field distribution. In the AC-CRPP Model, a data point is sited at the center of every filament. The field at each point is evaluated as the sum of all contributions from all other filaments of all coils, plus the contribution from the vessel and the plasma. The influence of the particular filament itself is neglected, because its influence is small.
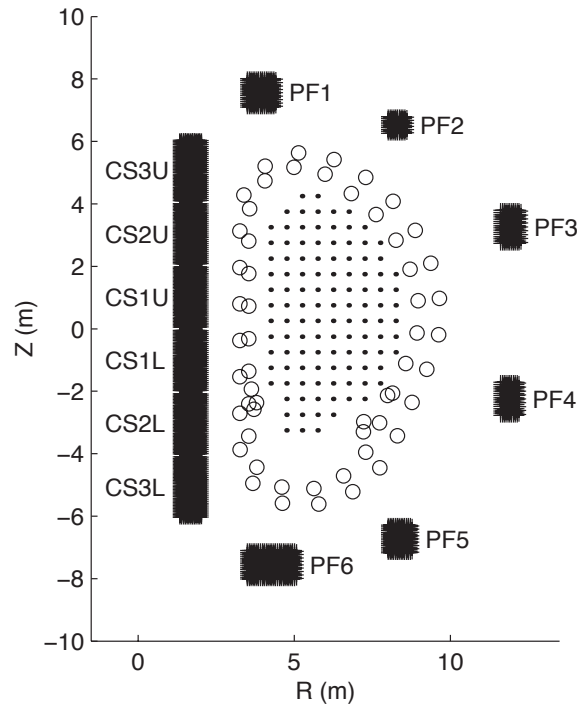
Figure 5.5: Current filament layout representing the magnetic field sources for the ITER tokamak. Crosses represent the coils, circles the vacuum vessel and dots the plasma.

5.2.2.2 Hysteresis loss evaluation

A tricky question when evaluating hysteresis loss is the definition of the cycles. In most simulations, the field does not return to its initial value. Figure 5.6 (a) shows the evolution of the poloidal magnetic field during a minor disruption of the plasma current. Candidate starting and ending points for cycles are the maxima and the minima of the magnetic field, as well as the starting and the ending point of the simulation.

If entire cycles have to be defined, a large part of the evolution is not taken into account. In Figure 5.6 (a) only the small cycle from t_0 to t_2 at the beginning is complete, although during the larger, incomplete second cycle from t_2 to t_3 losses are also produced. To resolve this, half cycles are defined in the AC-CRPP model, which allows us to cover the whole range of magnetic field change. The ending and starting points of the half cycles are all the points for which the derivative of the magnetic field is zero as well as the starting point and the ending point of the simulation. Figure 5.6 (b) shows two half cycles, the first from t_0 to t_1 and the second from t_1 to t_3. The loss is calculated with the same formulae as for entire cycles, but only half of the calculated loss is added.

The second issue with the evaluation of hysteresis loss is how to distribute the loss over the length of the cycle. The formulas only give the loss at the end of a half cycle. To provide a value for the instantaneous hysteresis loss power, the method illustrated in Figure 5.6 (c) is proposed. First, the field change with respect to the starting point is evaluated for every time step of the cycle (top, arrows) and the loss energy corresponding to that field change is calculated (middle, dashed lines) by means of the half cycle method. The difference between two consecutive loss energy calculations (middle and bottom, solid lines) divided by the time interval gives us the average loss power during a time step (bottom, shaded area).
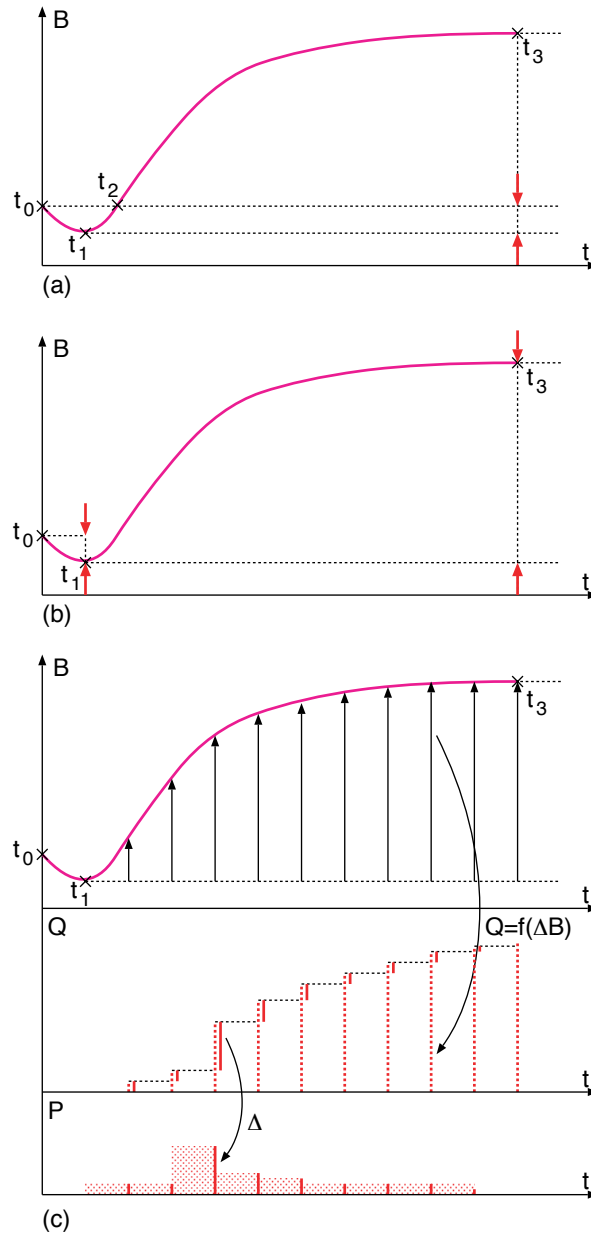
Figure 5.6: Magnetisation loop definition and hysteresis loss evaluation method.

5.2.2.3 Coupling current loss evaluation

Equation (5.10) allows a direct calculation of the coupling loss power during a time step via the magnetic field rate of change, approximated by dividing the magnetic field difference by the time difference.

When the time scale of the magnetic field change is much longer than any of the conductor time constants, steady state conditions can be assumed for the coupling currents. In some cases for which the magnetic field changes very fast, the steady state assumption leads to an overestimation of the loss (see Section 5.2.1).

5.2.2.4 Estimated quantities

The AC-CRPP model provides several output values for each PF coil, where the index $i \in \{1, 2, 3, 4, 5, 6\}$ denotes the coil number.

Time evolution of loss power for each coil $P_i(t)$: Contributions of the individual coils to the loss, suited for controller analysis.

Loss power P_i: Average loss power produced during the simulation.

Loss energy Q_i: Loss energy produced during the simulation. If divided by the number of disturbances it is an indicator of how lossy the controller is.

Maximum peak power $\hat{P}_i$: Maximum over all filaments of a coil of the peak loss power.

Integral of the square field rate $\int \dot{B}_i^2 \mathrm{d}t$: Measures the control action. The maximum value occurring in a coil over the cross-section is indicated.

All the estimated loss quantities are provided for hysteresis, coupling and total loss.

5.2.3 Validation

The AC-CRPP model is implemented in Matlab and consists of two main parts, the magnetic field calculation and the loss calculation. The validation of the model was performed in two steps.

5.2.3.1 Simple benchmark

First a simple benchmark was performed to check the formulae used in the loss calculation part. A sawtooth waveform for the assumed magnetic field variation, with an amplitude of 0.3 T and a field rate of 0.3 T/s was superimposed on a DC background field of 5 T at a magnet operating temperature of 5 K.

The results from the model agreed with manual calculations with zero difference for the coupling loss and $< 2\%$ difference for the hysteresis loss.

5.2.3.2 Disturbances during flat-top

To check the entire model, ITER simulation data [19] has been used and the results were compared with the complete AC loss model [57]. Two parameters determine an effective internal disturbance to the plasma equilibrium. The internal inductance, referred to as l_i, represents the degree of peaking of the plasma current profile. For a low value of l_i the plasma current profile is rather flat and it gets gradually a more peaked shape when l_i is increased. A drop in l_i and thus a flattening of the plasma current profile is frequently observed during plasma disturbances. The ratio of plasma pressure to the poloidal field magnetic energy, referred to as β_p, usually drops during a plasma disturbance when kinetic plasma energy is lost. The magnitude and time evolution of l_i and β_p changes generate different classes of disturbances for validating the ability of the feedback controller to reject them. Here $l_{i,0}$ and $\beta_{p,0}$ are the nominal values of l_i and β_p.

The three cases of disturbances used are [21]:

- A minor plasma current disruption (MD) at the start of burn (SOB) (start of flat-top) in the ITER scenario is modeled by an instantaneous l_i drop of $0.2(l_{i,0} - 0.5)$ without recovery simultaneous with a β_p drop of 20 % of the equilibrium β_p, followed by 3 s exponential recovery. One Minor Disruption is considered during the flat-top and two Minor Disruptions are considered during the plasma ramp-up and ramp-down phases. The duration of the simulation is 15 s.

- Compound edge localised modes (CELM) are a feature of tokamak operation in the H-mode and are specified during the sustained flat-top as an instantaneous l_i drop of $0.06(l_{i,0} - 0.5)$ followed by a 1 s linear recovery simultaneous with a β_p drop of $0.03\beta_{p,0}$ followed by a 0.2 s linear recovery. The repetition time is about 10 s and the simulation lasts 9.99 s.

- Type I edge localised modes (ELM1) also occur during H-mode and are specified during the flat-top as an instantaneous β_p drop of $0.03\beta_{p,0}$ followed by a 0.1 s linear recovery. They occur with a frequency of 3 Hz and the simulation lasts 9.99 s.

The simulations produce the waveforms of the PF coil current variations, the vessel current variations and the plasma current variations.

The AC-CRPP code first calculates the magnetic field at the centers of the filaments. This part is validated by comparing the maximum fields over the cross-section of each coil (Figure 5.7), showing good agreement.
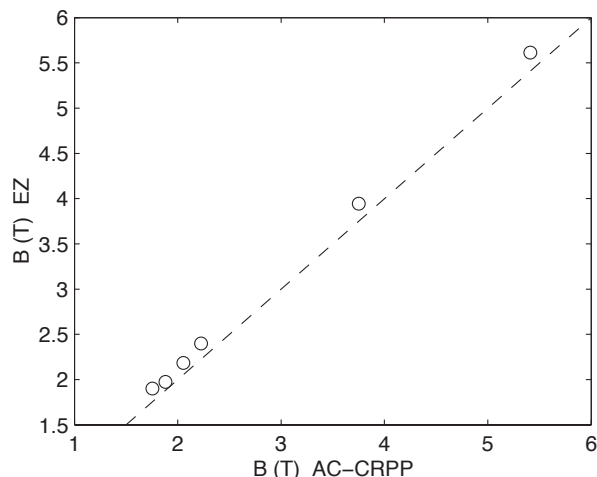
Figure 5.7: Maximum magnetic field occurring in the cross-section of the six coils calculated by [57], denoted as EZ, vs. values obtained with the AC-CRPP Model.

From the evolution of the magnetic field, the average AC losses are calculated and compared in Figure 5.8. Although there are differences of up to a factor of three, the results can be considered adequate given the general uncertainties in the AC loss modeling. The important feature for studying the effect of the feedback controller is that smaller losses in the AC-CRPP model correspond to smaller losses in the full and accurate model.

In Figure 5.8, the CELM and ELM Type 1 disturbances show a coupling current AC loss overestimation larger than for the Minor Disruption case. This is because CELM and ELM Type 1 provoque fast reactions of the control system and high frequencies are overestimated by the steady state formula. The agreement is again adequate for studying the feedback controller design.
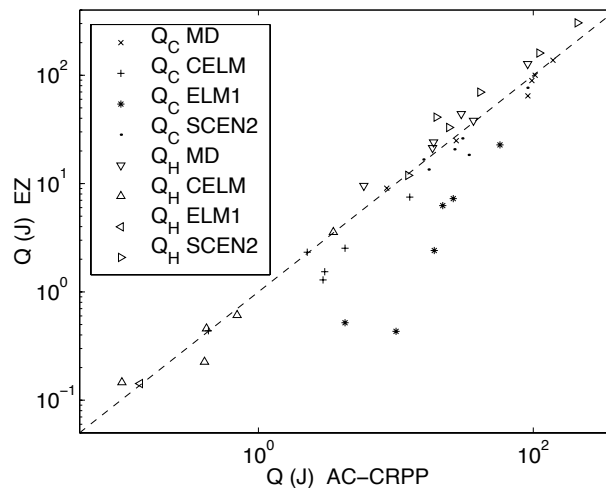
Figure 5.8: AC loss energy calculated by [57], denoted as EZ, vs. results from AC-CRPP. Comparison of the six PF coils for the three disturbance classes and the entire scenario.

5.2.3.3 Simulation of an ITER pulse

The reference ITER pulse has a length of $1800\,\text{s}$ with a flattop of $430\,\text{s}$. The AC losses calculated on the basis of the complete plasma discharge were calculated without disturbances, referred to as the scenario loss, averaged over the pulse length to produce a scenario loss power, included in Figure 5.8. The scenario losses have the highest hysteresis loss to coupling loss ratio. This is due to the very large field variations during ramp-up and ramp-down and the slow evolution of the scenario.

5.3 Structure of the reference feedback controller

For the closed-loop system simulations the setup shown in Figure 5.9 has been used. The linear ITER tokamak model is from [31], the disturbance model from [21], the CS and PF coil model from [22] and the controller from [6]. The AC-CRPP model losses were evaluated after each completed simulation.

This model was compared with detailed simulations available, in order to validate it. The action of the feedback control was simulated using a standard linearised model of the ITER tokamak [31] and using the standard ITER position and shape feedback controller [6, 7]. In order to evaluate the feedback controller performance, a set of standard disturbances was used, corresponding to the ITER design methodology [21].

The tokamak is a linearised model and all the variables represent variations with respect to an equilibrium configuration. The power supplies are modeled with first order dynamics plus saturation and delay.

Since the plasma is vertically unstable, the control system must stabilise it. The solution used in the current design is to use one fast power supply for vertical stabilisation (VS circuit) connected in series with the slower main converters (MC circuit) used for plasma shaping (see Figure 5.10). The fast vertical stabilisation system stops the vertical motion and the slower main converter system recovers the displacement.

In the reference controller, the vertical stabilisation is achieved by a gain on the vertical speed to control the fast power supply. The plasma current and shape control uses the coil currents, the gaps and the plasma current to control the main power supplies.
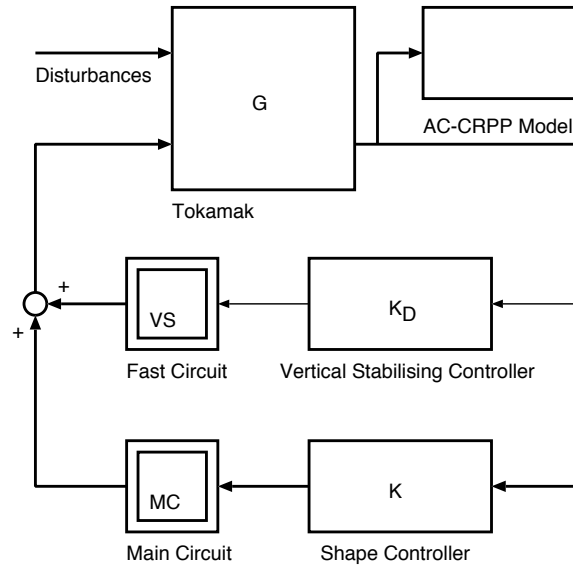
Figure 5.9: Setup for the simulations.

$$I_{imb} = I_2 - I_5 + I_3 - I_4$$
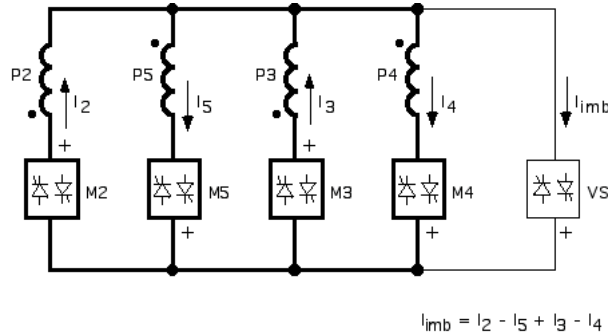
Figure 5.10: The vertical stabilisation circuit is connected to the PF coils 2-5.

5.4   Simulation and evaluation

The simulations show that the AC loss characteristics depends on the disturbance type (Figure 5.11). Whereas for the weak but fast ELM type I the coupling current losses dominate, the hysteresis loss is more important for the stronger compound ELM and becomes almost equally important for the minor disruption.

There are two main reasons for a significant difference in the distribution of the AC losses. First, for small amplitude magnetic field changes, the hysteresis loss is small, whereas for larger amplitudes it grows linearly. Second, the small disturbances provoke a stronger reaction by the fast coil system, which produces high coupling losses, due to its higher bandwidth.

A common feature of all disturbance classes is the immediate occurrence of the peak loss which is mainly due to coupling losses, Figure 5.12. This peak is caused by the action of the fast stabilising system to stop the plasma movement. The slower shaping system, which brings the plasma back to its original position does not create high coupling losses because of its lower bandwidth.

The distribution of the losses among the different PF coils shows some important points. PF coils 2 to 5 have high losses due to their use in the fast stabilising system, whereas the high losses in PF 6 are due to its size and the fact that it is used to fix the
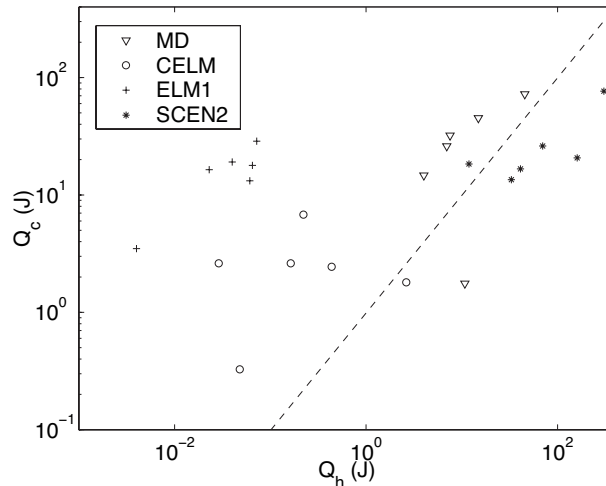
Figure 5.11: Loss characterisation of the six PF coils for different disturbances. The horizontal axis shows the coupling current AC loss and the vertical axis the hysteresis loss. The scenario loss is shown for comparison.
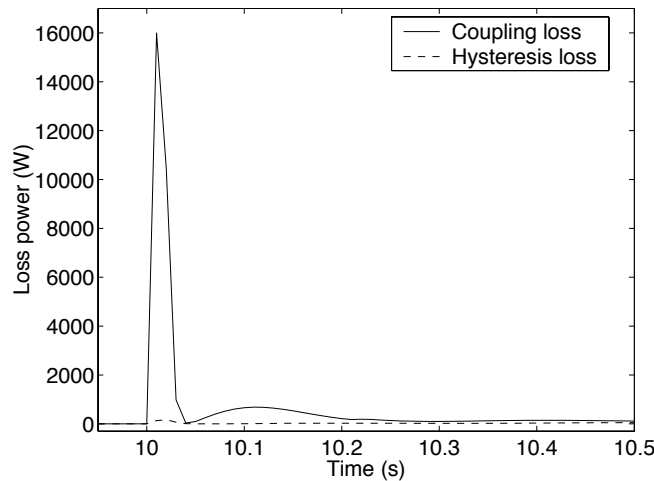
Figure 5.12: The time evolution of loss power in the case of a CELM disturbance shows a strong peak at the beginning of a disturbance.

divertor configuration. Its coupling loss is relatively small, whereas the hysteresis loss is 5 to 10 times higher than in the other coils. The PF 2 coil has few turns and to compensate this, the controller gain on this coil has to be higher, which leads to coupling losses 5 to 10 times higher than in all other coils (when looking at loss power per unit length).

When looking at an entire shot (scenario), the hysteresis losses dominate, Figures 5.8 and 5.11. This is due to the fact that during ramp-up and ramp-down we have large variations of the magnetic field B but at a low rate of change $\dot{B}$ (the ramp-up and ramp-down are of long durations with a relative flat slopes). Thus, the large magnetic field variations lead to large hysteresis losses while the flat slopes imply a low $\dot{B}$ which leads to low coupling losses. To compare the AC losses during the entire scenario with losses from the different disturbances, the following scenario has been assumed:

- A description of the equilibrium currents for $t = [0\,\mathrm{s} : 1800\,\mathrm{s}]$ according to scenario 2 from [20]

- One Minor Disruption during ramp-up
- One Minor Disruption during ramp-down
- A flat-top of 400 s, with
- One Minor Disruption at the start of the flat-top
- Compound ELMs every 10 s during the flat-top
- ELM type I with a frequency of 3 Hz during the flat-top
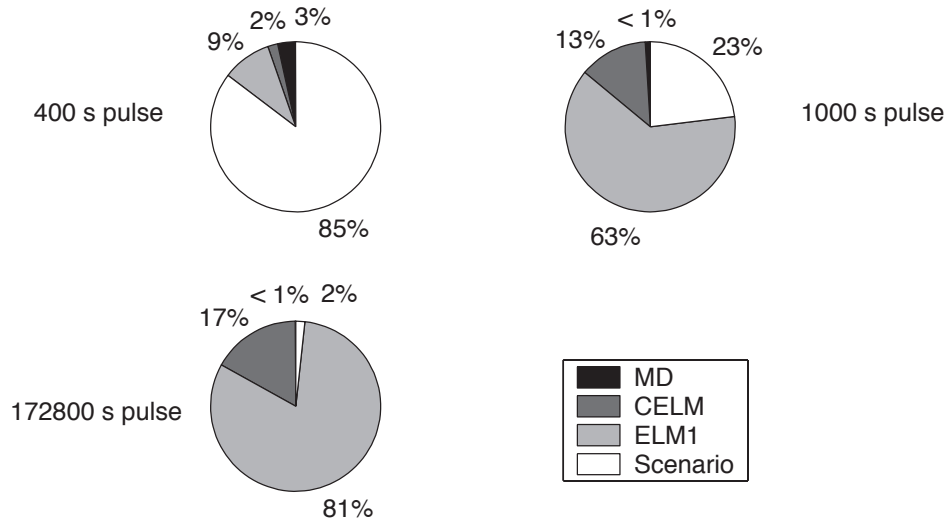
Figure 5.13: The importance of the irreducible scenario losses decreases with increasing flat-top durations. Shown are the distributions for 400 s, 10000 s and 172800 s pulses.

Figure 5.13 compares the scenario losses with the disturbance losses. The scenario losses dominate for the duration of the ITER pulse (top left) and therefore AC losses of the disturbances are not an issue. The scenario losses, essentially of hysteresis type, can only be reduced by changing the conductor, but not with controller adaptations.

If we assume longer pulse durations with flat-tops of 10000 s and 172800 s (48 hours), the AC losses caused during disturbance rejection become more important and AC loss reduction by controller adjustment becomes even more interesting (Figure 5.13, top right and bottom left).

5.5 Design of an improved controller

The hysteresis losses are proportional to the magnetic field variation ΔB and the coupling losses increase with the magnetic field rate of change $\dot{B}$. An optimised controller should therefore try to reduce these two values.

When looking at the output voltages (Figure 5.14), we can see that, since the magnetic field variation is linked to the voltage variation, the vertical stabilising controller (VS) produces most of the fast magnetic field variations. We therefore focus the analysis of the controller influences on AC loss on the VS controller.

The simplest way to reduce the magnetic field rate of change and thus the coupling losses is to reduce the bandwidth of the controller. This would lead to a damping of the high frequency response and therefore reduce the higher frequencies of the magnetic field variations. On the other hand, a fast reacting controller reduces the excursions of
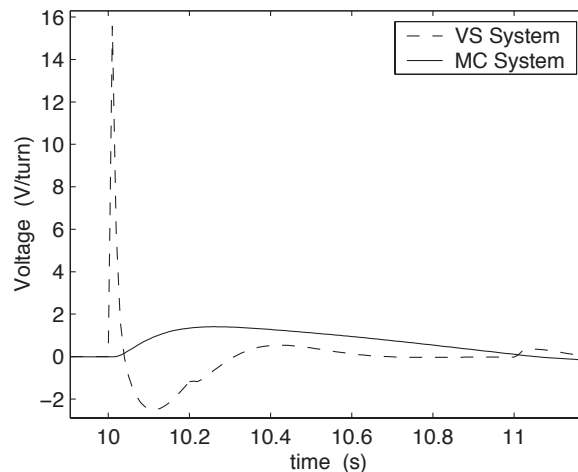
Figure 5.14: Comparison of the voltages from the VS and MC controllers to drive the PF3 coil in the case of a CELM.

the controlled variables and thus of the magnetic field variations, which should reduce the hysteresis loss. We therefore have to examine if there exists an optimal controller between a low bandwidth and a fast controller.

The vertical stabilising controller is given by:

$$K_D(s) = \frac{k_D s}{\tau_i s + 1} = \frac{150\, s}{0.003\, s + 1}. \tag{5.13}$$

The output voltage of the power supplies is limited due to the saturation, imposing a minimum gain and bandwidth on the controller. Once the plasma is out of equilibrium it is accelerated and if the controller does not react immediately, it will become too fast to be stopped by the saturated voltage.

When varying the gain of the controller k_D, some interesting observations can be made (Figure 5.15). The minimum k_D to guarantee stability depends on the disturbance type. While for the type I ELM this minimum gain is around 80, the minor disruption requires a minimum of 100. In the case of a type I ELM, the gain reduction leads to an important reduction of coupling loss, whereas in the case of a minor disruption, the benefit is smaller (see Figure 5.18).

If the gain is reduced in order to reduce the AC losses, the three disturbance classes have different requirements. The idea used for the design of an improved controller is to adapt the gain to the disturbance type. This requires a real-time estimation of the disturbance amplitude. Disturbances in tokamaks are almost instantaneous and move the system to a state which is located some distance from the equilibrium. As described in Chapter 4 (linear model discussion) the state variable vector $x = \begin{bmatrix} I_a & I_v \end{bmatrix}^T$ consists of a vector describing the active coil currents, denoted as I_a, and a vector describing the passive vacuum vessel currents, denoted as I_v. If the plasma is in equilibrium the equilibrium point is characterised by the active currents $I_a = I_{a_e}$ only while the passive currents are equal to zero $I_v = 0$. For the estimation of the disturbance we essentially need the vertical plasma position z which depends linearly of the state variables and the disturbance w (Section 8.3.1)

$$z = C_{za}I_a + C_{zv}I_v + F_z w,$$
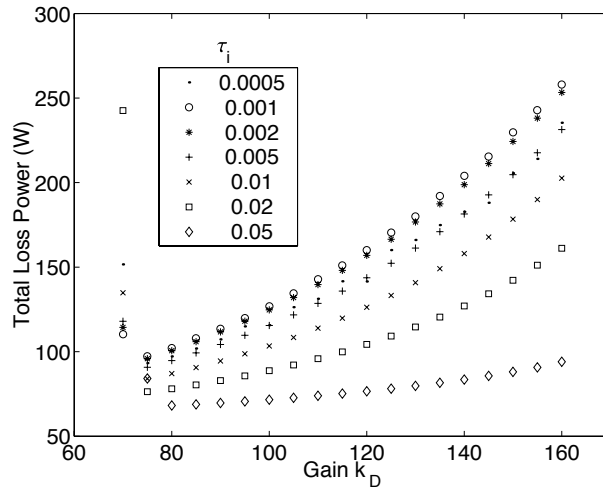
Figure 5.15: Total loss power as a function of the gain k_d for different time constants τ_i in the case of a type 1 ELM.

where $w = 0$ if the plasma is in equilibrium. An occurring disturbance $w \neq 0$ implies a disturbance of both $I_a = I_{a_e} + \delta I_a$ and $I_v = \delta I_v$, where the amplitude of δI_a and δI_v denote the effect of the disturbances. For the disturbance estimation we only want the information linked to the disturbance and we do not care about the equilibrium information given by I_{a_e}. Since I_a can be measured and since C_{za} is known from the linearised model the estimation of the disturbance can be given by

$$d_e = z - C_{za}I_a.$$

The output of such an estimator d_e is larger for disturbances requiring a higher gain (Figure 5.16). The new controller is designed to slide between two different vertical stabilising controllers, according to the estimator output d_e (Figure 5.17). To guarantee a high gain to stop the plasma movement, the maximum value of the estimator output is held for a certain time, $5\,\text{s}$ in the tested configuration.
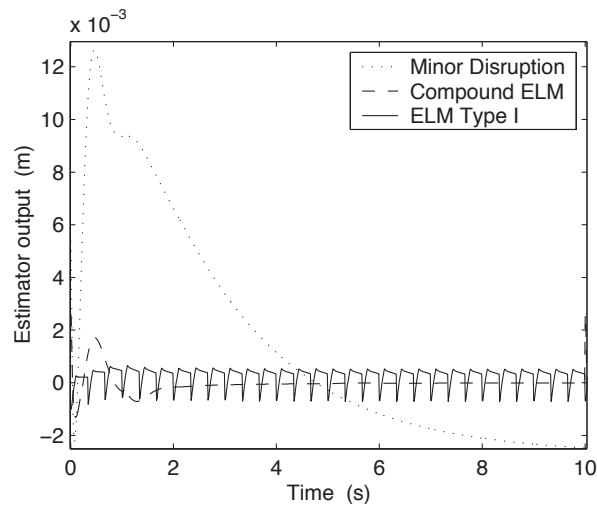
Figure 5.16: Output of the disturbance estimator d_e for the three disturbance classes.
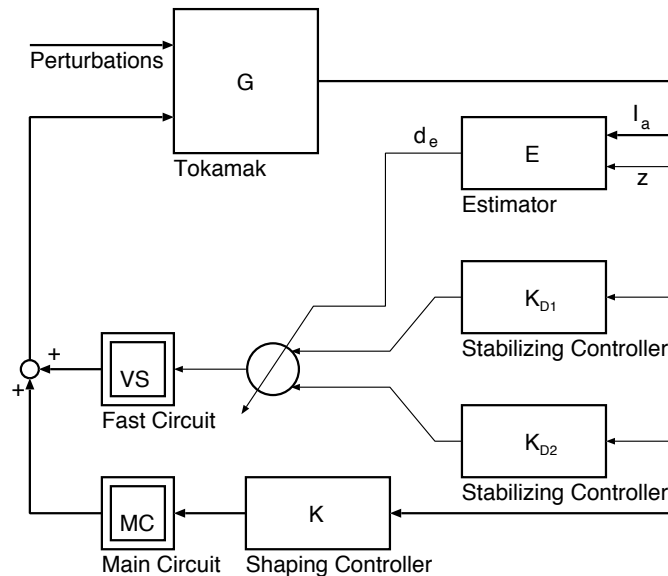
Figure 5.17: Structure of the AC loss reduced control system.

This improved controller considerably reduces the AC losses, especially in the case of the two weaker disturbances, the CELM and ELM1. The performances for the defined disturbances are comparable and the system is stable, but because here even the stronger controller has a lower gain than the original controller, its stability characteristics to very strong disturbances is reduced. The actual choice of the stronger and weaker controller is a trade-off between stability and performance on one side and AC loss reduction on the other side. As seen in Figure 5.15 many possible combinations of time constant and gain exist that have comparable AC losses, but not necesarily the same performance. The best choice depends on the actual tokamak and can only be made once a model based on the real tokamak has been established.

Although the effect of AC loss reduction may be small compared with other losses, it minimises heating inside the cable and thus improves conductor stability. Additionally, the importance of this reduction increases with increasing pulse duration, since the inevitable scenario AC losses remain constant, whereas the disturbance AC losses accumulate with the shot duration.

The loss per turn of conductor gives us a better idea of how much loss is generated before an exchange of the coolant and allows a comparison of the temperature rise from inlet to outlet (Figure 5.18). The PF2 coil has a much higher per turn AC loss than the other coils. This is because it has only very few turns and must therefore undergo higher current variations to produce the same effect on the plasma as the other coils, resulting in higher AC losses. To compensate this, the gains of the fast controller can be changed to shift a part of the control action from the PF2 and PF5 coils to the PF3 and PF4 coils. The result is that all the coils have comparable levels of per turn AC losses with the same amount of total AC losses. This would require a change to the turns and current specifications of the coils, since they share a common fast voltage.
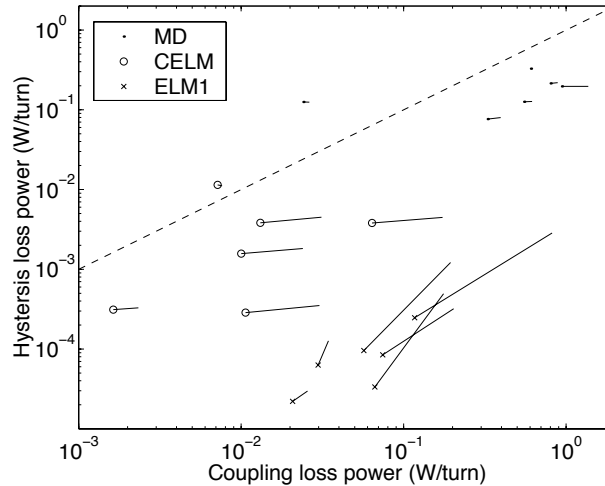
Figure 5.18: AC loss comparison of the original and improved controller. Starting points show the original values and the end points with the bullets the reduced values.

5.5.1 A general remark on the tradeoff between stability and AC loss reduction

In Part II of this thesis we will show that the reduced stability margin in a tokamak system is linked to two properties: i) the unstable pole (mode) of the linearised tokamak model and ii) the saturation of the power supplies. Remark that for systems which possess only one of these two properties its closed-loop systems remain stable under any disturbances. We will see that for systems like tokamaks the best stability properties can be obtained by means of bang-bang controllers. As an illustration for a bang-bang controller we take the vertical stabilising controller given by Equation (5.13), where for the sake of simplicity we neglect the low-pass filter by assuming $\tau_i = 0$. Taking the invert Laplace transformation of (5.13) with $\tau_i = 0$ leads to the control law

$$u = k_d \frac{dz_e}{dt},$$

where u is the control signal which is fed to the power supply and where $z_e = z - z_{ref}$ is vertical plasma position error. By considering the saturation of the power supply $\tilde{u} = \text{sat}(u)$, where $\tilde{u}$ is the voltage fed to the vertical stabilising coils, we obtain

$$\tilde{u} = \text{sat}\left(k_d \frac{dz_e}{dt}\right).$$

If we increase the controller gain to its positive infinite limit $k_d \rightarrow \infty$ then we obtain the bang-bang controller

$$\tilde{u} = \text{sgn}\left(\frac{dz_e}{dt}\right).$$

But from the results of this chapter we know that an increasing of the controller gain k_d leads to an increase of AC loss. Therefore, bang-bang controllers cannot be considered for tokamaks with superconducting coils.

Of course this example is very illustrative since it is an extreme case. In the general case, we can derive from the results of this chapter the following main statement: AC

losses can be reduced and kept weak by designing controllers which generate control signals with i) the least as possible oscillations, ii) amplitudes as small as possible and iii) signal frequencies as low as possible.

5.6 Discussion and conclusion

Using existing models of the ITER tokamak and its control system, it has been shown that the AC losses in the superconducting coils can be reduced by adapting the control strategy.

AC losses are due to the reactions of the control system to disturbances of the plasma and noise in the plasma and in the measurement system. Disturbances are almost instantaneous events that move the state of the tokamak away from the equilibrium position. Most of the AC losses occur during and immediately after the disturbance, leading to sharp peaks in the AC loss evolution. Therefore, a significant reduction has to target these peaks, that are essentially due to the fast stabilising control system.

The need for stability of the plasma position imposes a strong and rapid reaction to strong disturbances. Current control system designs also apply the same strong reactions to weaker disturbances and noise. While this does not influence traditional performance and stability criteria, it causes unnecessary AC losses in the superconducting coils. Weaker controllers allow reductions of the AC losses during weak disturbances to a fifth of their original value.

While the losses due to disturbances can be influenced, the losses due to the ramp-up and ramp-down of the scenario currents cannot be reduced, since they are due to the overall magnetic field changes, which is are defined by the operating scenario.

While the scenario AC losses remain constant, the losses due to disturbances are proportional to the duration of the discharge. Considering a discharge of 1800 s, with a flattop of 430 s the influence of AC loss reduction would be small compared with the total loss. As the discharge becomes longer, the AC loss reduction becomes more significant.

Additionally, the reduction of the peak loss power also improves the transient thermal behaviour of the conductor.

The price of the AC loss reduction is a smaller stability margin, but only a slightly reduced performance. Establishing the optimal tradeoff between reducing the AC losses and maximising the stability margin will be made when the true disturbance and noise spectra are measured.

From the point of view of controller design in general, the main result of the AC losses analysis reveals that for reducing the AC losses we need to design a controller which generates a small oscillating, low amplitude and low frequency control voltage signal.

Part II

Control theory

Chapter 6

Region of attraction of one unstable and one stable pole planar systems with saturated feedback

Linear systems with bounded inputs have been widely studied [51, 37, 27]. This type of study is important since, in most practical situations, the range of inputs is in fact limited.

Two important concepts pertaining to these systems have to be distinguished. First is the *null controllable region*, i.e. the region in state space where there exists an open-loop input that can steer the system to the origin [3, 27, 28, 49]. The second is the *region of attraction with a given controller*, i.e. the region in state space from which the closed-loop system asymptotically reaches the origin [3, 27]. In this chapter, only the issues pertaining to the latter, i.e. the region of attraction, will be studied. Also, designing controllers for which the region of attraction is arbitrarily close to the null controllable region [37] will not be studied here.

Single input linear planar systems (systems with 2 states) with saturated linear feedback will be considered. It will be assumed that the linear feedback makes the origin globally asymptotically stable in the absence of saturation.

The shape of the region of attraction depends on the location of the open-loop poles. With respect to the region of attraction, the poles on the imaginary axis have the same characteristics as the stables ones. If both poles are stable, then the system is globally stabilisable [3, 51]. If both poles are unstable, then the boundary of the region of attraction is a closed trajectory [3]. A method for finding this closed trajectory (limit cycle) is provided in [27, 28]. For systems with one stable and one unstable pole, it has been shown in [3] that topological bifurcation of the region of attraction occurs, i.e. the region of attraction changes between being a hyperbolic type region and a region bounded by a limit cycle. The characteristics of the region of attraction are summarised in Table 6.1.

Pole configuration	Region of attraction
Both stable	$\mathbb{R}^2$
One stable, one unstable	bifurcation
Both unstable	closed by a limit cycle

Table 6.1: Characteristics of the region of attraction

Only the case with one stable and one unstable pole is of interest here since it corre-

113

sponds to a linearised second order tokamak model. Concerning its region of attraction, less work can be found in the literature. Although the bifurcation problem was studied in [3], the bifurcation result presented therein is only existential. Also, no condition for bifurcation is provided. The main contribution of this chapter is to derive an analytical condition under which bifurcation occurs. Furthermore, a qualitative description of the region of attraction and the way how to compute its exact shape is provided. In fact we show that the condition for bifurcation and the shape of the region of attraction are strongly linked to the stable and unstable manifolds of the equilibrium points of the considered closed-loop system. It turns out that this closed-loop system possesses three equilibrium points: a stable one at the origin and two saddle points. The stable equilibrium point at the origin is due to the fact that we assume a linear feedback making the origin globally asymptotically stable. The two saddle points are due to the saturation and to the system possessing one stable and one unstable pole. Their stable and unstable manifolds provide the informations to formulate analytically a condition for bifurcation. Furthermore, their stable manifolds constitute the boundaries of the region of attraction if the region of attraction is a hyperbolic type region. In the case of a region of attraction bounded by a limit cycle, the limit cycle is located inside the region bounded by the unstable manifolds of the saddle points and all trajectories starting in this region asymptotically reach the limit cycle in reversed time. The proofs for this results rest partly on Poincaré's and Bendixson's theorems (they are stated as a reminder in Section A.1 of the Appendix). We mainly need to show that: i) there exists no limit cycle in the region bounded by the stable manifolds and that ii) there exists one and only one limit cycle in the region bounded by the unstable manifolds. Since Bendixson's theorem gives only a sufficient condition for the non-existence of a limit cycle we additionally need contraction analysis to complete the proofs. This analyses rests on the study of the contractive behaviour of two trajectories with respect to a line in the state space. In other terms, we study if the distance between two trajectories, with respect to a line, decreases (contraction) or increases. Since this contraction analysis development is encumbering it is presented in Section A.2 of the Appendix.

The chapter is organised as follows. In Section 6.1, definitions and terms used in this chapter are introduced. The important result concerning the equilibrium points of the considered closed-loop system is provided. Section 6.2 provides the definition of the stable and unstable manifolds of equilibrium points. A qualitative description of the stable and unstable manifolds of the saddle points is given. Section 6.3 provides the condition under which the bifurcation of the region of attraction appears. In Section 6.4, the shape of the region of attraction as a function of the condition for bifurcation is given. Conclusions are drawn in Section 6.5.

6.1   Preliminaries

6.1.1   System

Consider a single input second-order linear system with a stable and an unstable pole. Upon state transformation, the system can be written as:

$$\dot{x} = Ax + bu = \begin{bmatrix} \lambda_1 & 0 \\ 0 & \lambda_2 \end{bmatrix} x + \begin{bmatrix} \lambda_1 \\ \lambda_2 \end{bmatrix} u \tag{6.1}$$

where, $x \in \mathbb{R}^2$ is the state vector, u the input, A and b appropriate matrices, and λ_1, λ_2 the eigenvalues of the open-loop system. Assume that $\lambda_1 > 0$ and $\lambda_2 < 0$.

The notion of a system evolving in reversed time leading to the notion of a reversed time system is frequently used. If nothing is specified then the evolution of a dynamic system is considered in forward time. By considering system (6.1) the evolution in forward time of the state from an initial condition x_0 at time t_0 is denoted by $x(t_0 + t)$ for all $t \geq 0$. On the other hand, its evolution in reversed time is given by $x(t_0 - t)$ for all $t \geq 0$. If we consider the time reversed system of (6.1), defined by

$$\dot{x}_r = -Ax_r - bu_r, \quad \text{where } u_r(t_0 + t) = u(t_0 - t) \text{ for all } t \geq 0, \tag{6.2}$$

then the state evolution in reversed time can be expressed in forward time

$$x_r(t_0 + t) = x(t_0 - t) \quad \text{for all } t \geq 0.$$

Remark that sometimes it is more convenient to consider the evolution in forward time of the time reversed system instead of the evolution of the system in reversed time.

For the input saturation, the symmetric saturation function with unity saturation level will be used:

$$u = \text{sat}(\tilde{u}) = \begin{cases} -1 & \text{if} \quad \tilde{u} < -1 \\ \tilde{u} & \text{if} \quad -1 \leq \tilde{u} \leq 1 \\ 1 & \text{if} \quad \tilde{u} > 1 \end{cases} \tag{6.3}$$

6.1.2 The null controllable region and the null reachable region

For a dynamical system with a single input we define

$$\mathcal{U}_a \subseteq \mathbb{R} \tag{6.4}$$

as the set of admissible input $u(t) \in \mathcal{U}_a \, \forall \, t \in \mathbb{R}$.

The null controllable region $\mathcal{C}$ of a system is the maximum region in state space for which there exists an admissible input that can steer the the system to the origin.

Definition 1
Let $\Phi(t, x_0, u(t))$ denote the state of a dynamical system at time $t > 0$, starting with the initial condition x_0 at $t = 0$ and subjected to the input $u(t)$. A state x is said to be null controllable if there exists an admissible control $u(t) \in \mathcal{U}_a$ that steers the trajectory $\Phi(\cdot, x, u(t))$ to the origin, i.e.

$$\lim_{t \to \infty} \Phi(t, x, u(t)) = 0.$$

All states being null controllable belong to the set of the null controllable region which is denoted by $\mathcal{C}$.

The null reachable region $\mathcal{R}$ of a system is the maximum region in state space to which the system can be steered from the origin with an admissible input.

Definition 2
Let $\Phi(t, x, u(t))$ denote the state of a dynamical system at time $t < 0$, starting with the initial condition at the origin at $t = 0$ and subjected to the input $u(t)$. A state x is said

to be null reachable if there exists an admissible control $u(t) \in \mathcal{U}_a$ in reverse time $(t < 0)$ that steers the trajectory $\Phi(\cdot, x, u(t))$ to the origin, i.e.

$$\lim_{t \to -\infty} \Phi(t, x, u(t)) = 0.$$

All states being null reachable belong to the set of the null reachable region which is denoted by $\mathcal{R}$.

From this it is obvious that the null reachable region of a system is the null controllable region of its time reversed system and vice-versa.

For a system with saturated input as defined by (6.3), the set of admissible control $u(t)$ is given by

$$\mathcal{U}_a = [-1, 1]. \tag{6.5}$$

Consider system (6.1) with the saturated input (6.3). Then its null controllable region is given by ([3, 27, 28, 49])

$$\mathcal{C} = \left\{ x \in \mathbb{R}^2 : |x_1| < 1 \right\} \tag{6.6}$$

and its boundaries are defined by

$$\partial\mathcal{C}_+ = \left\{ x \in \mathbb{R}^2 : x_1 = 1 \right\}, \quad \partial\mathcal{C}_- = \left\{ x \in \mathbb{R}^2 : x_1 = -1 \right\}. \tag{6.7}$$

The proof is given by considering the unstable part of system (6.1), which is $\dot{x}_1 = \lambda_1 x_1 + \lambda_1 u$. For all $x \geq 1$ we have

$$\dot{x}_1 = \lambda_1(x_1 + u) \geq 0 \quad \text{for } x_1 \geq 1 \text{ and } u \in \mathcal{U}_a = [-1, 1]$$

which means that the unstable state x_1 cannot be steered back to the origin. If we want to steer the unstable state to the origin from an initial condition $x \geq 1$ we need $\dot{x} < 0$. A similar approach can be given for all $x \leq -1$ where we have

$$\dot{x}_1 = \lambda_1(x_1 + u) \leq 0 \quad \text{for } x_1 \leq -1 \text{ and } u \in \mathcal{U}_a = [-1, 1].$$

This proves that the set $\mathbb{R}^2 \setminus \left\{ x \in \mathbb{R}^2 : |x_1| < 1 \right\}$ cannot belong to the null controllable region $\mathcal{C}$. To prove that every state $x \in \left\{ x \in \mathbb{R}^2 : |x_1| < 1 \right\}$ can be steered back to the origin we use the control law

$$u = -\operatorname{sgn}(x_1) \in \mathcal{U}_a.$$

For the unstable part of system (6.1) this leads to following relations

$$\begin{aligned}
\dot{x}_1 &= \lambda_1(x_1 - \operatorname{sgn}(x_1)) < 0 \quad \text{for } 0 < x_1 < 1 \\
\dot{x}_1 &= \lambda_1(x_1 - \operatorname{sgn}(x_1)) > 0 \quad \text{for } 0 > x_1 > -1 \\
\dot{x}_1 &= \lambda_1(x_1 - \operatorname{sgn}(x_1)) = 0 \quad \text{for } x_1 = 0.
\end{aligned}$$

Therefore, the unstable state reaches in finite time the state $x_1 = 0$ and it remains there for the remaining time. When the unstable state has reached $x_1 = 0$ then $u = 0$ and the stable state $x_2 \in \mathbb{R}$ of the stable part of system (6.1), given by $\dot{x}_2 = \lambda_2 x_2 + \lambda_2 u$, asymptotically reaches $x_2 = 0$, since $\lambda_2 < 0$. Thus, there exists at least one control $u(t) \in \mathcal{U}_a$, in our case given by the control law $u = -\operatorname{sgn}(x_1)$, for which all states $x \in \left\{ x \in \mathbb{R}^2 : |x_1| < 1 \right\}$ are

steered back to the origin. The set $\{x \in \mathbb{R}^2 : |x_1| < 1\}$ is therefore the null controllable region of system (6.1).

From the null controllable region (6.6) it can be deduced that the boundaries of the null controllable region are only due to fact that system (6.1) possesses the unstable state x_1. The null controllable region is therefore only bounded in one dimension of $\mathbb{R}^2$. Consider for example a planar stable linear system with saturated input. Then it is obvious that its null controllable region is equal to the whole state space $\mathbb{R}^2$. We can choose the control input $u = 0$ and since the poles of the system have both negative real parts the system reaches asymptotically the origin. On the other hand, if we consider a planar anti-stable system (no stable poles) with saturated input, then the boundaries are due to both unstable states and thus the closure of the null controllable region is a closed subset in $\mathbb{R}^2$. We can state that the null controllable region is bounded in both dimension of $\mathbb{R}^2$. The exact shape of the null controllable region of an anti-stable planar system with saturated input is given in [27].

The null reachable region of system (6.1) is given by

$$\mathcal{R} = \left\{ x \in \mathbb{R}^2 : |x_2| < 1 \right\} \tag{6.8}$$

and its boundaries are defined by

$$\partial \mathcal{R}_+ = \left\{ x \in \mathbb{R}^2 : x_2 = 1 \right\}, \quad \partial \mathcal{R}_- = \left\{ x \in \mathbb{R}^2 : x_2 = -1 \right\}. \tag{6.9}$$

Since the null reachable region is the null controllable region of the time reversed system the proof is similar to the proof for the null controllable region. The result of the null reachable region is derived from the fact that the stable state and unstable state are interchanged for the time reversed system of (6.1).

6.1.3   Linear state feedback

In what follows we consider the linear state feedback

$$\tilde{u} = fx = f_1 x_1 + f_2 x_2 \tag{6.10}$$

leading to the autonomous closed-loop system

$$\dot{x} = Ax + b \operatorname{sat}(fx), \tag{6.11}$$

where f is the feedback gain vector. The matrix $A + bf$ is assumed to be Hurwitz, i.e. the system is stable without saturation. Let $\tilde{\lambda}_1$ and $\tilde{\lambda}_2$ be the eigenvalues of $A + bf$. The two conditions that correspond to $A + bf$ being Hurwitz are:

1. $\lambda_1(1 + f_1) + \lambda_2(1 + f_2) < 0$ (6.12)
2. $\lambda_1\lambda_2(1 + f_1 + f_2) > 0$. Since $\lambda_1\lambda_2 < 0$,
   $(1 + f_1 + f_2) < 0$.   (6.13)

Also, it can be verified that $f_1 < 0$, though f_2 can take either sign.

The Hurwitz conditions are derived from the determination of the eigenvalues of $A + bf$

$$\left| A + bf - \tilde{\lambda} I \right| = \tilde{\lambda}^2 - \tilde{\lambda}(\lambda_1(1 + f_1) + \lambda_2(1 + f_2)) + \lambda_1\lambda_2(1 + f_1 + f_2) = 0.$$

By substituting $p = \lambda_1(1 + f_1) + \lambda_2(1 + f_2)$ and $q = \lambda_1\lambda_2(1 + f_1 + f_2)$ the eigenvalues are given by

$$\tilde{\lambda}_{1,2} = \frac{p}{2} \pm \sqrt{\frac{p^2}{4} - q}.$$

Since the closed-loop $A + bf$ has to be stable, both eigenvalues $\tilde{\lambda}_1$ and $\tilde{\lambda}_2$ have to be negative. This is only verified when $p < 0$ and $q > 0$ which leads to the results (6.12) and (6.13). To show that $f_1 < 0$ both inequalities (6.12) and (6.13) have to be combined. Multiplying (6.13) with $\lambda_2 < 0$ leads to

$$f_1\lambda_2 > -\lambda_2(1 + f_2)$$

and (6.12) can be expressed as

$$\lambda_1(1 + f_1) < -\lambda_2(1 + f_2).$$

This leads to the inequality

$$f_1\lambda_2 > \lambda_1(1 + f_1) \quad \implies \quad 0 > \lambda_1 + f_1(\lambda_1 - \lambda_2)$$

which is only satisfied when $f_1 < 0$ since $\lambda_1 > 0$ and $\lambda_1 - \lambda_2 > 0$.

6.1.4   The region of attraction

The region of attraction $\mathcal{A}$ is the maximum region in state space for which the state of the closed-loop system, i.e. (6.11), reaches asymptotically the origin.

Definition 3
Let $\Phi(t, x_0)$ denote the state of a closed-loop system at time t, starting with the initial condition x_0 at $t = 0$. The region of attraction of the stable equilibrium point is defined by:

$$\mathcal{A} = \left\{ x \in \mathbb{R}^2 : \lim_{t \to \infty} \Phi(t, x) = 0 \right\}. \tag{6.14}$$

The boundary of $\mathcal{A}$ is denoted by $\partial \mathcal{A}$.

Definitions 1 and 3 imply that the region of attraction is always smaller or equal to the null controllable region $\mathcal{A} \subseteq \mathcal{C}$.

   One of the goals of this section is to characterise the region of attraction of system (6.11).

6.1.5   Linear and saturated regions in state space

Since, for the closed loop system (6.11), the linear feedback $\tilde{u} = fx$ is subjected to saturation the state space can be subdivided in three different regions.

1. The linear region for which the control input is in the linear region of the saturation function, i.e. $u = fx$, is defined by

$$\mathcal{L} = \left\{ x \in \mathbb{R}^2 : |fx| \leq 1 \right\}, \tag{6.15}$$

where its boundaries are

$$\partial\mathcal{L}_+ = \left\{x \in \mathbb{R}^2 : fx = 1\right\}, \quad \partial\mathcal{L}_- = \left\{x \in \mathbb{R}^2 : fx = -1\right\}. \tag{6.16}$$

Moreover we define the hyperplane of zero control $u = fx = 0$

$$\partial\mathcal{L}_0 = \left\{x \in \mathbb{R}^2 : fx = 0\right\} \subset \mathcal{L}. \tag{6.17}$$

2. The positive saturated region for which $u = 1$ is defined by

$$\overline{\mathcal{L}_+} = \left\{x \in \mathbb{R}^2 : fx > 1\right\}. \tag{6.18}$$

3. The negative saturated region for which $u = -1$ is defined by

$$\overline{\mathcal{L}_-} = \left\{x \in \mathbb{R}^2 : fx < -1\right\}. \tag{6.19}$$

If the state of the system is inside the linear region $x \in \mathcal{L}$ then system (6.11) becomes the linear autonomous system

$$\dot{x} = (A + bf)x. \tag{6.20}$$

On the contrary, when the state is located in either the positive saturated region $x \in \overline{\mathcal{L}_+}$ or the negative saturated region $x \in \overline{\mathcal{L}_-}$, then the system becomes

$$\dot{x} = Ax + b\bar{u}, \tag{6.21}$$

where $\bar{u}$ is constant, either 1 or -1, respectively. Upon applying the state translation

$$x = \bar{x} - A^{-1}\bar{u} \tag{6.22}$$

it turns out that the system follows the same dynamics as the open-loop system (6.1)

$$\dot{\bar{x}} = A\bar{x}. \tag{6.23}$$

Remark that A^{-1} exists only if A has full rank, which is verified since λ_1 and λ_2 are both nonzero.

6.1.6 Equilibrium points

System (6.11) with one stable and one unstable open-loop pole has three equilibrium points, as opposed to all other open-loop pole configurations (both poles stable or unstable) where the origin is the unique equilibrium point (Theorem 2.3 in [3]).

Theorem 2
The closed-loop system (6.11) has three equilibrium points:

- $x_{e0} = 0$

- $x_{e+} = A^{-1}b = \begin{bmatrix} 1 & 1 \end{bmatrix}^T$

- $x_{e-} = -A^{-1}b = \begin{bmatrix} -1 & -1 \end{bmatrix}^T.$

Of these, x_{e0} is stable, while the other two are saddle points [3].

Proof:
The proof of this theorem might be taken from the proof of the more general theorem, which is valid for any linear or nonlinear saturated state feedback, presented in [3]. Its proof rests on knowledge of index theory and homotopy techniques which might not be evident to understand. Fortunately, in the case of pure linear saturated state feedback the proof is much easier to establish. For this we need to study the existence of equilibrium points in the linear region $\mathcal{L}$ and in the saturated region $\overline{\mathcal{L}_+} \cup \overline{\mathcal{L}_-}$. An equilibrium point is defined as a point in state space where the time derivative of the state variable $\dot{x}$ and thus the vector field $Ax + b\operatorname{sat}(fx)$ associated to the system vanish, i.e. $\dot{x} = Ax + b\operatorname{sat}(fx) = 0$.

- Consider the linear region where the vector field is $(A + bf)x$. Since $A + bf$ is required to be Hurwitz both eigenvalues of $A + bf$ have strictly negative real part and thus $A + bf$ has full rank. Therefore the vector field vanishes $(A + bf)x = 0$ only at the origin $x_{e0} = 0$. Since $A + bf$ is Hurwitz, x_{e0} is a stable equilibrium point.

- Consider the saturated region where the vector field is either $Ax + b$ in the positive saturated region or $Ax - b$ in the negative saturated region. Due to the state translation (6.22) the system dynamics is determined only by A (6.23). Thus the equilibrium point of $\dot{\bar{x}} = A\bar{x}$ is located at $\bar{x}_e = 0$. Moreover, since A has a negative and a positive eigenvalue ($\lambda_1 > 0$ and $\lambda_2 < 0$) this equilibrium point is a saddle point. By the state translation (6.23) there exists to different saddle equilibrium points

$$x_{e-} = -A^{-1}b = \begin{bmatrix} -1 & -1 \end{bmatrix}^T \quad \text{for } u = 1$$
$$x_{e+} = A^{-1}b = \begin{bmatrix} 1 & 1 \end{bmatrix}^T \quad \text{for } u = -1.$$

It remains to prove that both equilibrium point candidates are located in the saturated region where $|fx| > 1$. Since the system is symmetric it suffices to prove it for one point only, e.g. $x = \begin{bmatrix} 1 & 1 \end{bmatrix}^T$. For this point fx should verify

$$fx = f\begin{bmatrix} 1 & 1 \end{bmatrix}^T = f_1 + f_2 < -1 \quad \Longrightarrow \quad 1 + f_1 + f_2 < 0$$

which is the second Hurwitz condition (6.13). Thus, since $A + bf$ is Hurwitz the equilibrium points $\pm \begin{bmatrix} 1 & 1 \end{bmatrix}^T$ always exist.

■

6.2   The stable and unstable manifolds of equilibrium points

First, the definitions of the stable and unstable manifolds of the three equilibrium points are given. We then describe qualitatively the shape of the stable and unstable manifolds of the two saddle equilibrium points which consist the key for understanding the structure of the region of attraction of (6.11).

6.2.1 Definition of the stable and unstable manifolds of equilibrium points

The stable manifold $\mathcal{S}(x_e)$ of an equilibrium point x_e is the maximum region in state space for which the autonomous system, i.e. (6.11), asymptotically reaches this equilibrium point x_e.

Definition 4
Let $\Phi(t, x_0)$ denote the state of an autonomous system at time t, starting with the initial condition x_0 at $t = 0$. The stable manifold of an equilibrium point x_e is defined by:

$$\mathcal{S}(x_e) = \left\{ x \in \mathbb{R}^2 : \lim_{t \to \infty} \Phi(t, x) = x_e \right\}. \tag{6.24}$$

The unstable manifold $\mathcal{U}(x_e)$ of an equilibrium point x_e is the maximum region in state space for which the time reversed autonomous system, i.e. (6.11), asymptotically reaches this equilibrium point x_e.

Definition 5
Let $\Phi(t, x_0)$ denote the state of an autonomous system at time t, starting with the initial condition x_0 at $t = 0$. The unstable manifold of an equilibrium point x_e is defined by:

$$\mathcal{U}(x_e) = \left\{ x \in \mathbb{R}^2 : \lim_{t \to -\infty} \Phi(t, x) = x_e \right\}. \tag{6.25}$$

Remark:
Consider system (6.11) and its the equilibrium point at the origin $x_{e0} = 0$. Since the state space of (6.11) is of dimension 2 and since x_0 is stable ($A + bf$ is Hurwitz) the manifold of x_0 is obviously stable and of dimension 2. Moreover, for this equilibrium point the definition of its stable manifold coincides with the definition of the region of attraction (definition 3). Thus, the stable manifold $\mathcal{U}(x_0)$ is the region of attraction $\mathcal{A}$.

On the other hand, since the equilibrium points x_{e+} and x_{e-} are saddle points due to the dynamics given by $\dot{\bar{x}} = A\bar{x}$ (6.22-6.23) there exists one stable manifold $\mathcal{S}(x_{e\pm})$ and one unstable manifold $\mathcal{U}(x_{e\pm})$ for each equilibrium point. It is obvious from linear system analysis [32, 50] that both manifolds are of dimension 1. Therefore, since a trajectory of a dynamical system is a manifold of dimension 1 and because of the definitions of the stable and unstable manifolds (6.24) and (6.25) we can conclude that $\mathcal{S}(x_{e\pm})$ and $\mathcal{U}(x_{e\pm})$ are trajectories of the dynamical system.

6.2.2 Qualitative description of the stable and unstable manifolds of the saddle equilibrium points

For the description of the stable and unstable manifolds the following lemmas, theorem and definition are required:

- **Lemma 1** *Consider system (6.11), the stable manifolds $\mathcal{S}(x_{e\pm})$ and the unstable manifolds $\mathcal{U}(x_{e\pm})$ of its equilibrium points x_{e+} and x_{e-}. Then $\mathcal{S}(x_{e\pm})$ is located in the closure of the null controllable region*

$$\mathcal{S}(x_{e\pm}) \subset \overline{\mathcal{C}}, \tag{6.26}$$

and $\mathcal{U}(x_{e\pm})$ is located in the closure of the null reachable region

$$\mathcal{U}(x_{e\pm}) \subset \overline{\mathcal{R}}. \tag{6.27}$$

Proof:

Since for states x located outside of $\overline{\mathcal{C}}$ the unstable part of system (6.1) verifies the conditions

$$
\begin{aligned}
\dot{x}_1 &= \lambda_1(x_1 + u) > 0 \quad \text{for } x_1 > 1 \text{ and } u \in \mathcal{U}_a = [-1, 1] \\
\dot{x}_1 &= \lambda_1(x_1 + u) < 0 \quad \text{for } x_1 < -1 \text{ and } u \in \mathcal{U}_a = [-1, 1]
\end{aligned}
$$

there exists no admissible control $u \in \mathcal{U}_a$ that could steer the system to x_{e+} or x_{e-}. Thus, the stable manifolds $\mathcal{S}(x_{e\pm})$ are located in $\overline{\mathcal{C}}$.

The proof of $\mathcal{U}(x_{e\pm}) \subset \overline{\mathcal{R}}$ is similar by considering the time reversed system of (6.1).
∎

- A basic property of linear systems states:

  Lemma 2 *Consider a planar linear system with its equilibrium point located at the origin. Every trajectory crossing a ray $\mathrm{R}(r)$, defined by*

  $$\mathrm{R}(r) = \left\{ x \in \mathbb{R}^2 : x = \mu r, \ \mu \geq 0, \ r \in \mathbb{R}^2 \right\}, \tag{6.28}$$

  can cross the same ray $\mathrm{R}(r)$ if and only if it encircles the equilibrium point. Thus, every trajectory crosses the ray in the same direction.

  Proof: We consider an arbitrary second order autonomous linear system defined by $\dot{x} = Ax$ and a ray $\mathrm{R}(r)$, where $r = \begin{bmatrix} a & b \end{bmatrix}^T$. The vector $r' = \begin{bmatrix} -b & a \end{bmatrix}^T$ is parallel to the normal vector of the ray $\mathrm{R}(r)$ since $r'^T \cdot r = 0$. We verify the direction of the trajectory crossing the ray $\mathrm{R}(r)$ by testing if the scalar product of r' and the vector field $\dot{x}$ at each point of the ray $x \in \mathrm{R}(r)$ has the same sign

  $$r'^T \cdot \dot{x} = r'^T Ax = r'^T Ar\mu.$$

  Since $\mu \geq 0$ and since $r'^T Ar$ is a scalar, the scalar product $r'^T \cdot \dot{x} \ \forall \, x \in \mathrm{R}(r)$ possesses the same sign or is zero. Remark that if $r'^T \cdot \dot{x} = 0$ then the trajectory reaches $\mathrm{R}(r)$ or stays into $\mathrm{R}(r)$ but does not cross it.   ∎

- Since system (6.11) is Lipschitz it has a unique solution for any initial condition (the existence and unicity theorem of nonlinear systems [32]). Thus, no trajectory can cross another trajectory.

- We will need the notion of partial trajectories defined by

  Definition 6

  A part of a trajectory starting at a point $a \in \mathbb{R}^2$ and ending at a point $b \in \mathbb{R}^2$ is denoted as

  $$\mathrm{Trj}(a, b). \tag{6.29}$$

The qualitative description of the stable and unstable manifolds rests on the analysis of the evolution in time of these manifolds. For the stable manifolds, evolution in reverse time is considered. Since the system (6.11) is symmetric we restrict the analysis to the two manifolds $\mathcal{S}(x_{e-})$ and $\mathcal{U}(x_{e+})$.

We first consider the evolution of the manifolds inside the saturated regions since the equilibrium points of the stable and unstable manifolds $(x_{e\pm})$ are located there. In this case, we know from Section 6.1.5 that by the state translation

$$x = \bar{x} - A^{-1}\bar{u}, \quad \text{where } \bar{u} = 1 \text{ or } \bar{u} = -1 \tag{6.30}$$

the system follows the dynamics

$$\dot{\bar{x}} = A\bar{x}. \tag{6.31}$$

Figure 6.1 illustrates the qualitative behavior of the trajectories of the system 6.31. Since
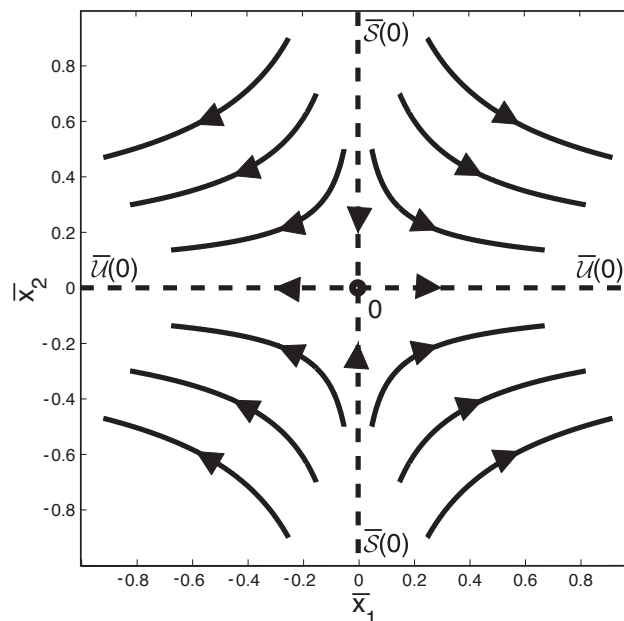
Figure 6.1: Qualitative behavior of the trajectories of system (6.31) (dashed line: stable and unstable manifolds).

A is diagonal the stable and unstable manifolds are given by $\bar{\mathcal{S}}(0) = \{\bar{x} \in \mathbb{R}^2 : \bar{x}_1 = 0\}$ and $\bar{\mathcal{U}}(0) = \{\bar{x} \in \mathbb{R}^2 : \bar{x}_2 = 0\}$, respectively. But since we consider the whole state space of the closed-loop system (6.11), the manifolds $\bar{\mathcal{S}}(0)$ and $\bar{\mathcal{U}}(0)$ are translated by x_{e+} in the positive saturated region and by x_{e-} in the negative saturated region. Therefore, from the saddle points $x_{e\pm}$, the branches of the manifolds $\mathcal{S}(x_{e-})$ and $\mathcal{U}(x_{e+})$ extend along $\partial\mathcal{R}$ and $\partial\mathcal{C}$, respectively, until they hit the linear region. The two points where the manifolds $\mathcal{S}(x_{e-})$ and $\mathcal{U}(x_{e+})$ intersect the boundaries of the linear region are given by:

$$c_+ = \partial\mathcal{C}_- \cap \partial\mathcal{L}_+ = \begin{bmatrix} -1 & \frac{(1+f_1)}{f_2} \end{bmatrix}^T \tag{6.32}$$

$$r_- = \partial\mathcal{R}_+ \cap \partial\mathcal{L}_- = \begin{bmatrix} -\frac{(1+f_2)}{f_1} & 1 \end{bmatrix}^T \tag{6.33}$$

For the following description we need additionally the intersection points

$$c_0 = \partial\mathcal{C}_- \cap \partial\mathcal{L}_0, \qquad c_- = \partial\mathcal{C}_- \cap \partial\mathcal{L}_-, \tag{6.34}$$

$$r_0 = \partial\mathcal{R}_- \cap \partial\mathcal{L}_0, \qquad r_+ = \partial\mathcal{R}_- \cap \partial\mathcal{L}_+. \tag{6.35}$$

The Figure 6.2 illustrates these points and the shape of the stable and unstable manifolds in the saturated regions.
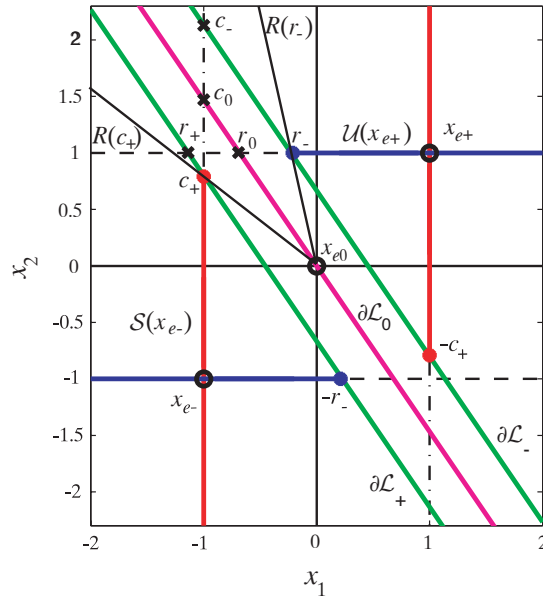
Figure 6.2: The points c_+, c_0, c_-, r_+, r_0 and r_- and the evolution of the stable and unstable manifolds of x_{e+} and x_{e-} in the saturated regions.

Since the remaining evolution of the manifolds evolves in the linear region $\mathcal{L}$ we have to distinguish 3 different cases depending on the sign of f_2.

1. $f_2 = 0$

   There is no intersection of the stable manifold $\mathcal{S}(x_{e-})$ with the linear region $\mathcal{L}$ since the point c_+ is not defined for $f_2 = 0$. Therefore $\mathcal{S}(x_{e-})$ stays in the positive saturated region $\overline{\mathcal{L}_+}$ and thus, $\mathcal{S}(x_{e-}) = \{x \in \mathbb{R}^2 : x_1 = -1\}$ and $\mathcal{S}(x_{e+}) = \{x \in \mathbb{R}^2 : x_1 = 1\}$ which are the boundaries of the null controllable region $\mathcal{C}$. This implies that one branch of $\mathcal{U}(x_{e+})$ stays inside the null controllable region $\mathcal{C}$ and the other branch is located in the negative saturated region $\overline{\mathcal{L}_-}$.

2. $f_2 < 0$

   Consider Figure 6.2. From Lemma 1 the stable manifold $\mathcal{S}(x_{e-})$ cannot cross the segment $\overline{c_+ c_0}$ and from Lemma 2 it cannot cross the ray $\mathrm{R}(c_+)$. Thus, it has to cross the segment set $\overline{x_{e0} c_0} \setminus x_{e0}$ of $\partial\mathcal{L}_0$, where we denote the intersection by $c^\star$. Remark that we omit the equilibrium point x_{e0} from the potential crossing segment set since we consider the stable manifold in reverse time, where in this case x_{e0} is unstable. Similarly, from Lemmas 1 and 2, the unstable manifold $\mathcal{U}(x_{e+})$ cannot cross the segment $\overline{r_- r_0}$ and the ray $\mathrm{R}(r_-)$, respectively. Thus, it has to cross the segment set $\overline{x_{e0} r_0}$ of $\partial\mathcal{L}_0$, where the intersection is denoted by $r^\star$. Since the intersection of both potential crossing segment sets is not empty three cases can occur (Figure 6.3).

   (a) $\|c^\star\| > \|r^\star\|$

      The stable manifold $\mathcal{S}(x_{e-})$ cannot cross: i) the segment $\overline{c_0 c_-}$ (Lemma 1), ii) the ray $\mathrm{R}(c^\star)$ (Lemma 2) and iii) the trajectory part $\mathrm{Trj}(r_-, r^\star)$ (existence and unicity theorem). Thus, it has to cross the segment set $\overline{r_- c_-} \setminus r_-$ of $\partial\mathcal{L}_-$,
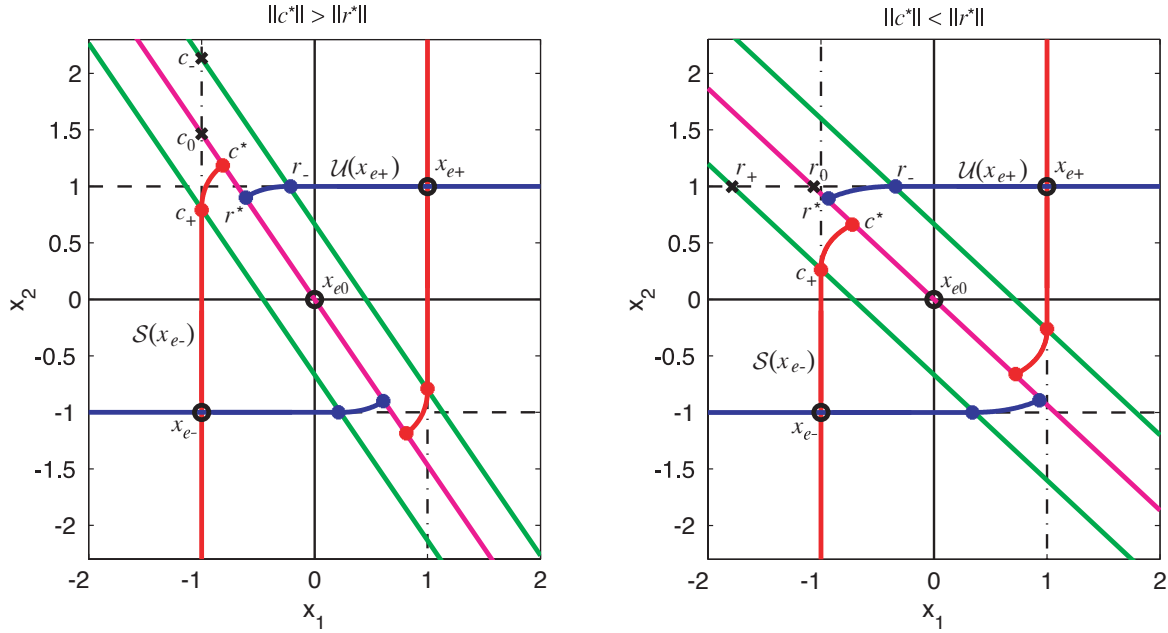
Figure 6.3: The points $c^\star$ and $r^\star$ and the evolution of the manifolds until $\mathcal{L}_0$ is reached for both cases $\|c^\star\| > \|r^\star\|$ and $\|c^\star\| < \|r^\star\|$.

where we denote the intersection by $c^{\star\star}$ (Figure 6.4). At $c^{\star\star}$ the stable manifold evolves hyperbolically inside the negative saturated region according to the dynamics of the linear system (6.31) with the state translation (6.30) (see Figure 6.1). Since Lemma 1 states that $\mathcal{U}(x_{e+}) \subset \overline{\mathcal{R}}$ the unstable manifold $\mathcal{U}(x_{e+})$ remains in the region bounded by both stable manifolds $\mathcal{S}(x_{e\pm})$. Moreover, it converges to x_{e0} (Figure 6.4). In fact, as we will see in Section 6.4.3, every trajectory in this region converges to the origin x_{e0}.

(b) $\|c^\star\| < \|r^\star\|$

The unstable manifold $\mathcal{U}(x_{e+})$ cannot cross: i) the segment $\overline{r_0 \, r_+}$ (Lemma 1), ii) the ray $\mathrm{R}(r^\star)$ (Lemma 2) and iii) the trajectory part $\mathrm{Trj}(c_+, c^\star)$ (existence and unicity theorem). Thus, it has to cross the segment set $\overline{c_+ \, r_+} \setminus c_+$ of $\partial\mathcal{L}_+$, where we denote the intersection by $r^{\star\star}$ (Figure 6.4). At $r^{\star\star}$ the unstable manifold evolves hyperbolically inside the negative saturated region according to the dynamics of the linear system (6.31) with the state translation (6.30) (see Figure 6.1). Since Lemma 1 states that $\mathcal{S}(x_{e-}) \subset \overline{\mathcal{C}}$ the stable manifold $\mathcal{S}(x_{e-})$ remains in the region bounded by both unstable manifolds $\mathcal{U}(x_{e\pm})$. Moreover, it converges to a limit cycle (Figure 6.4). In fact, as we will see in Section 6.4.3, in reverse time every trajectory in this region converges to this limit cycle.

(c) $\|c^\star\| = \|r^\star\|$

In this case the stable manifold $\mathcal{S}(x_{e-})$ converges to x_{e+} in reverse time and the unstable manifold $\mathcal{U}(x_{e+})$ converges to x_{e-} in forward time. Such trajectories which connect two different equilibrium points are called heteroclinic connections. We will see in Section 6.4.3 that every trajectory evolving in the region bounded by $\mathcal{S}(x_{e-}) = \mathcal{U}(x_{e+})$ and $\mathcal{S}(x_{e+}) = \mathcal{U}(x_{e-})$ converges to the origin x_{e0}.
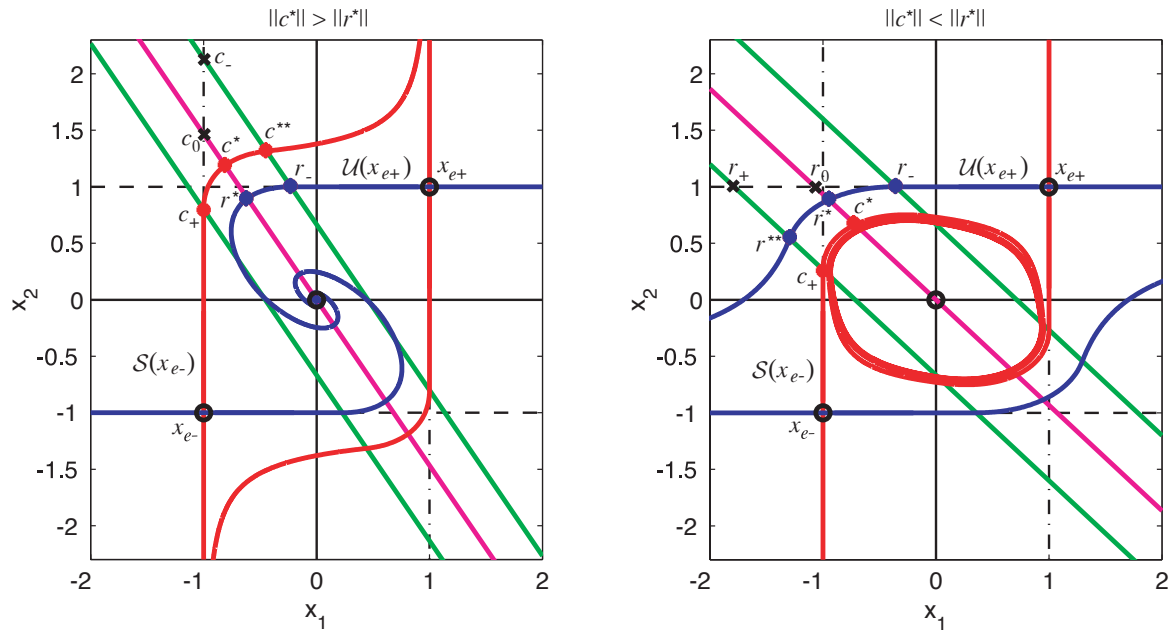
Figure 6.4: The points $c^{\star\star}$ and $r^{\star\star}$ and the evolution of the manifolds for both cases $\|c^\star\| > \|r^\star\|$ and $\|c^\star\| < \|r^\star\|$.

3. $f_2 > 0$

   By reformulating the second Hurwitz condition (6.13) we obtain

   $$\frac{1 + f_1}{f_2} < -1.$$

   Thus, the point c_+ lies always outside the null reachable region $\mathcal{R}$ in the state space $\overline{\mathcal{R}_-} = \{x \in \mathbb{R}^2 : x_2 < -1\}$. In $\overline{\mathcal{R}_-}$ the vector field $\dot{x}$ points always to $\mathcal{R}$ since

   $$\dot{x}_2 = \lambda_2(x_2 + u) > 0 \quad \text{for } x_2 < -1 \text{ and } u \in \mathcal{U}_a = [-1, 1].$$

   Moreover, Lemma 1 states $\mathcal{S}(x_{e-}) \subset \overline{\mathcal{C}}$. Therefore, the stable manifold $\mathcal{S}(x_{e-})$ inevitably crosses $\partial\mathcal{L}_0$ and $\partial\mathcal{L}_-$, where the intersection points are denoted by $c^\star \in \overline{\mathcal{R}_-}$ and $c^{\star\star} \in \overline{\mathcal{R}_-}$, respectively. At $c^{\star\star}$ the stable manifold evolves hyperbolically inside the negative saturated region according to the dynamics of the linear system (6.31) with the state translation (6.30) (see Figure 6.1). Since Lemma 1 states that $\mathcal{U}(x_{e+}) \subset \overline{\mathcal{R}}$ the unstable manifold $\mathcal{U}(x_{e+})$ crosses or reaches $\partial\mathcal{L}_0$ inside $\overline{\mathcal{R}}$, where the intersection is denoted by $r^\star$. Thus, the condition $\|c^\star\| > \|r^\star\|$ is always verified. Figure 6.5 illustrates the evolution of both manifolds.

We showed that the stable and unstable manifolds, $\mathcal{S}(x_{e\pm})$ and $\mathcal{U}(x_{e\pm})$, are not topologically equivalent for any system parameters λ_1 and λ_2 and controller parameters f_1 and f_2. In fact it depends on how the manifolds cross $\mathcal{L}_0$, where either the conditions $\|c^\star\| > \|r^\star\|$, $\|c^\star\| < \|r^\star\|$ or $\|c^\star\| = \|r^\star\|$ can occur. For the condition $\|c^\star\| > \|r^\star\|$ both branches of $\mathcal{S}(x_{e\pm})$ are unbound, where one branch of $\mathcal{U}(x_{e\pm})$ is bounded. The contrary happens when condition $\|c^\star\| < \|r^\star\|$ is satisfied. In the case where $\|c^\star\| = \|r^\star\|$ is verified all manifolds have one bounded branch creating two heteroclinic connections between x_{e+} and x_{e-}. This is the condition at which a topological bifurcation of the stable and unstable manifolds occurs. We will show in the following sections that this is the cause for the bifurcation of the region of attraction $\mathcal{A}$ of (6.11).
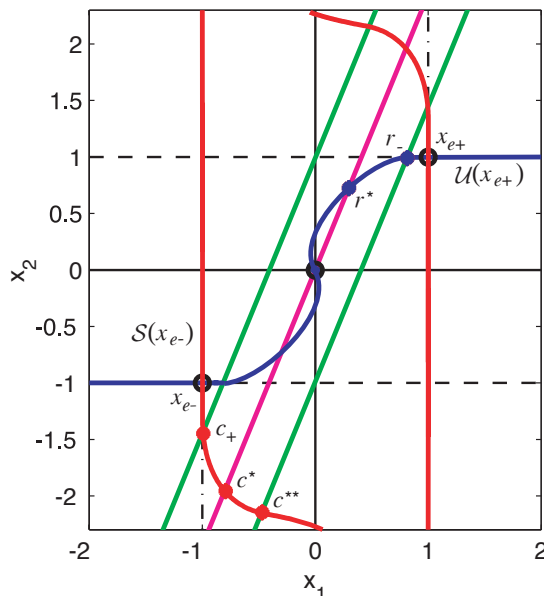
Figure 6.5: The points c_+, $c^\star$, $c^{\star\star}$, r_- and $r^\star$ and the evolution of the manifolds in the case where $f_2 > 0$. The condition $\|c^\star\| > \|r^\star\|$ is always verified.

6.3 The condition for bifurcation

For the class of systems considered, the boundary of the region of attraction can be either i) unbounded hyperbolically shaped or ii) a bounded limit cycle, depending on the parameters of the system and the controller. The limiting case between the two types of the region of attraction corresponds to a set bounded by two heteroclinic connections. In this section, a condition depending on the system and controller parameters will be defined, with which it will be possible to distinguish between the two categories and detect the limiting case. However, the link between this condition and the bifurcation of the region of attraction $\mathcal{A}$ is deferred to Section 6.4.

6.3.1 Intersection of system trajectory with $\partial\mathcal{L}_0$

The condition for bifurcation is based on how the trajectories from points c and r intersect $\partial\mathcal{L}_0$, where the intersection is denoted by $c^\star$ and $r^\star$ (these intersection points are defined and qualitatively described in Section 6.2.2), respectively. The first intersection of the trajectory from an arbitrary initial condition is considered. Let T_+ denote the first positive time for which the trajectory intersects $\partial\mathcal{L}_0$, and T_- the first negative time. The analytical expressions for T_+ and T_- depend on the nature of the closed-loop poles $\tilde{\lambda}_1$ and $\tilde{\lambda}_2$. Three cases have to be distinguished: (i) distinct and real poles, (ii) double poles, and (iii) complex conjugate poles.

6.3.1.1   Distinct real poles

Proposition 1 *Let the eigenvalues of $(A+bf)$ be distinct and real. Given $x_o = \begin{bmatrix} x_1 & x_2 \end{bmatrix}^T$ in $\mathcal{L} \setminus 0$, the intersection times T_+ and T_- are given by:*

$$T_+ = \begin{cases} \gamma & \text{if} \quad \gamma > 0 \text{ and } \alpha > 0 \\ \infty & \text{if} \quad \gamma \leq 0 \text{ or } \alpha \leq 0 \end{cases} \tag{6.36}$$

$$T_- = \begin{cases} \gamma & \text{if} \quad \gamma < 0 \text{ and } \alpha > 0 \\ \text{undefined} & \text{if} \quad \gamma \geq 0 \text{ or } \alpha \leq 0 \end{cases} \tag{6.37}$$

where

$$\gamma = \frac{\ln(\alpha)}{\tilde{\lambda}_2 - \tilde{\lambda}_1}, \quad \alpha = \frac{f_1 x_1(\tilde{\lambda}_1 - \lambda_2) + f_2 x_2(\tilde{\lambda}_1 - \lambda_1)}{f_1 x_1(\tilde{\lambda}_2 - \lambda_2) + f_2 x_2(\tilde{\lambda}_2 - \lambda_1)} \tag{6.38}$$

Proof:
The following transformation is used to diagonalise the system (6.11) without saturation:

$$\tilde{V} = \frac{1}{\tilde{\lambda}_2 - \tilde{\lambda}_1} \begin{bmatrix} f_1(\lambda_2 - \tilde{\lambda}_1) & f_2(\lambda_1 - \tilde{\lambda}_1) \\ f_1(\tilde{\lambda}_2 - \lambda_2) & f_2(\tilde{\lambda}_2 - \lambda_1) \end{bmatrix}$$

Then, the evolution of the states is given by

$$x(t) = e^{(A+bf)t} x_o = \tilde{V}^{-1} \begin{bmatrix} e^{\tilde{\lambda}_1 t} & 0 \\ 0 & e^{\tilde{\lambda}_2 t} \end{bmatrix} \tilde{V} x_o \tag{6.39}$$

The intersection time T satisfying $f e^{(A+bf)T} x_o = 0$ is sought. Since $\tilde{\lambda}_1 \neq \tilde{\lambda}_2$, the previous expression reads:

$$\begin{aligned} & e^{\tilde{\lambda}_1 T}(f_1 x_1(\lambda_2 - \tilde{\lambda}_1) + f_2 x_2(\lambda_1 - \tilde{\lambda}_1)) \\ & + e^{\tilde{\lambda}_2 T}(f_1 x_1(\tilde{\lambda}_2 - \lambda_2) + f_2 x_2(\tilde{\lambda}_2 - \lambda_1)) = 0 \end{aligned} \tag{6.40}$$

which always admits the solution $T = \infty$. The other solution is $T = \gamma = \frac{\ln(\alpha)}{\tilde{\lambda}_2 - \tilde{\lambda}_1}$, where

$$\alpha = e^{(\tilde{\lambda}_2 - \tilde{\lambda}_1)T} = \frac{f_1 x_1(\tilde{\lambda}_1 - \lambda_2) + f_2 x_2(\tilde{\lambda}_1 - \lambda_1)}{f_1 x_1(\tilde{\lambda}_2 - \lambda_2) + f_2 x_2(\tilde{\lambda}_2 - \lambda_1)} \tag{6.41}$$

α is well defined as long as both the numerator and the denominator do not vanish simultaneously. This will not happen due to the invertibility of $\tilde{V}$. However, α can be negative, in which case the solution of (6.41) is imaginary, and so $T = \infty$ is the only solution. Depending upon the sign of γ, the solution is either in forward time or in reverse time. ∎

Note that, when the closed-loop poles are real, in addition to reaching the origin asymptotically, there is at most one intersection with $\partial \mathcal{L}_0$. This intersection can either be in forward (positive) time or in reverse (negative) time. The positive intersection time is always defined since, in the worst case, the system reaches the origin asymptotically. However, there might be no intersection in negative time and T_- may be undefined.

Corollary 1 *T_- is defined from the point c.*

Proof:
Assume, without loss of generality, that $(\tilde{\lambda}_1 - \tilde{\lambda}_2) > 0$. Then from (6.37) and (6.38), $T_- = \gamma < 0$ exists only if $\alpha > 1$. Substituting $x_o = c$,

$$\alpha = 1 + \frac{(\tilde{\lambda}_1 - \tilde{\lambda}_2)}{f_1(\lambda_2 - \lambda_1) + (\tilde{\lambda}_2 - \lambda_1)}. \tag{6.42}$$

Since $(\tilde{\lambda}_1 - \tilde{\lambda}_2) > 0$, $\alpha > 1$ when the denominator of (6.42) is positive. Using the fact that $\tilde{\lambda}_1 + \tilde{\lambda}_2 = (1 + f_1)\lambda_1 + (1 + f_2)\lambda_2$, the denominator becomes:

$$f_1(\lambda_2 - \lambda_1) + (\tilde{\lambda}_2 - \lambda_1) = \lambda_2(1 + f_1 + f_2) - \tilde{\lambda}_1 \tag{6.43}$$

From $\lambda_2, \tilde{\lambda}_1 < 0$ and the second Hurwitz condition $(1 + f_1 + f_2) < 0$, the denominator is positive, so $\alpha > 1$, $\gamma < 0$, and thus T_- exists. ∎

6.3.1.2 Double poles

When $\tilde{\lambda}_1 = \tilde{\lambda}_2 = \tilde{\lambda}$, $\alpha = 1$ and γ is indeterminate. However, the limiting value can be easily found:

$$T_+ \;=\; \begin{cases} \gamma & \text{if} \quad \gamma > 0 \\ \infty & \text{if} \quad \gamma \leq 0 \end{cases} \tag{6.44}$$

$$T_- \;=\; \begin{cases} \gamma & \text{if} \quad \gamma < 0 \\ \text{undefined} & \text{if} \quad \gamma \geq 0 \end{cases} \tag{6.45}$$

where

$$\gamma = \frac{f_1 x_1 + f_2 x_2}{f_1 x_1(\lambda_2 - \tilde{\lambda}) + f_2 x_2(\lambda_1 - \tilde{\lambda})} \tag{6.46}$$

6.3.1.3 Complex conjugate poles

The expression (6.38) can also be used when the poles are complex. Note that the numerator and denominator of α are complex conjugates. So, $|\alpha| = 1$, the real part of $\ln(\alpha)$ is zero and so is $\text{Re}(\tilde{\lambda}_2 - \tilde{\lambda}_1)$. However, the important difference is that $\ln(\alpha)$ admits multiple solutions, and there are infinitely many intersections both in positive and negative times. Among the solutions of $\ln(\alpha)$, the first positive solution and the first negative solution are used for the computation of T_+ and T_-. So,

$$T_+ \;=\; \text{first positive solution of } \left(\frac{\ln(\alpha)}{\tilde{\lambda}_2 - \tilde{\lambda}_1} \right) \tag{6.47}$$

$$T_- \;=\; \text{first negative solution of } \left(\frac{\ln(\alpha)}{\tilde{\lambda}_2 - \tilde{\lambda}_1} \right) \tag{6.48}$$

with α given by (6.38).

6.3.2   Definition of the Condition on C

Definition 7

Let $r^* = \Phi(T_+, r) = e^{(A+bf)T_+} r$ be the first intersection of the trajectory starting from r and $\partial \mathcal{L}_0$ and, similarly, $c^* = \Phi(T_-, c) = e^{(A+bf)T_-} c$. Then, C is defined as

$$C = \|c^*\| - \|r^*\| = \|e^{(A+bf)T_-} c\| - \|e^{(A+bf)T_+} r\|. \tag{6.49}$$

It will be shown in the next section that the shape of the region of attraction depends on whether $C > 0$, $C < 0$, or $C = 0$. The condition on C can be interpreted as follows: In backward time, $\mathcal{R}$ forms the region to which a trajectory cannot return, once it has left. The sign of C indicates whether or not the trajectory from c leaves $\mathcal{R}$ in backward time. If $C < 0$, the trajectory $\Phi(t, c)$ does not leave $\mathcal{R}$ while when $C > 0$, it leaves $\mathcal{R}$. A similar argument can be made with $\mathcal{C}$ and r.

6.3.3   Simple checks for the Condition on C

Though C has to be computed using (6.49), there are easier sufficient conditions to check whether $C > 0$ or $C < 0$. From the interpretation of the condition on C, $C > 0$ if $c \notin \mathcal{R}$. Similarly, $C < 0$ if $r \notin \mathcal{C}$. This leads to the following proposition.

Proposition 2 $(1 - f_1 + f_2) < 0 \Longrightarrow C < 0$ *and* $(1 + f_1 - f_2) < 0 \Longrightarrow C > 0$.

Proof: If $(1 - f_1 + f_2) < 0$, $(1 + f_2) < f_1$. Since $f_1 < 0$, $\frac{1+f_2}{f_1} > 1$. So, the first component of r is smaller than -1, and $r \notin \mathcal{C}$ leads to $(1 - f_1 + f_2) < 0 \Rightarrow C < 0$. If $(1 + f_1 - f_2) < 0$, then $(1 + f_1) < f_2$. Since f_2 is not sign definite, two cases need to be considered. If $f_2 < 0$, $\frac{1+f_1}{f_2} > 1$. So, the second component of c is larger than 1, and $c \notin \mathcal{R}$. If $f_2 > 0$, the Hurwitz condition $(1 + f_1 + f_2) < 0$ itself indicates that $\frac{1+f_1}{f_2} < -1$. So, in either case, $c \notin \mathcal{R}$, and $(1 + f_1 - f_2) < 0 \Rightarrow C > 0$.   ∎

Although the conditions are easy to verify, there exists a gap between the two conditions. In this gap, it is necessary to compute C using (6.49).

Proposition 3 $(\lambda_1 + \lambda_2) \leq 0 \Longrightarrow C \geq 0$.

Proof: The proof of this proposition is quite detailed and thus only a sketch of proof is given here. It uses Bendixson's theorem and the results that will be presented in the proof of Theorem 3 of the next section. We will show in the proof of Theorem 3 that in the closure of the region of attraction, denoted by $\bar{\mathcal{A}}$, there exists no limit cycle if $C \geq 0$ is satisfied and that there exists always one limit cycle if $C < 0$ is verified. Moreover, it will be shown that, by applying Bendixson's theorem, there exists no limit cycle if $\lambda_1 + \lambda_2 \leq 0$ which leads to the result of $(\lambda_1 + \lambda_2) \leq 0 \Rightarrow C \geq 0$.   ∎

This proposition implies that, if the unstable open-loop pole is slower than the stable one, then no bifurcation can occur. Also, this shows why that not all systems with one stable and one unstable open-loop pole exhibit bifurcation as a function of the controller parameters.

6.4   The region of attraction and its bifurcation

In this section, we first present a result proving the existence of bifurcation of the region of attraction for the class of systems considered, i.e. (6.11). Then the link between the

condition on C and the shape of the region of attraction will be established. It will be shown that the bifurcation between a hyperbolic type region of attraction and a region of attraction bounded by a limit cycle occurs at $C = 0$.

6.4.1 Existence of bifurcation

For a system with one stable and one unstable open-loop pole and saturated linear or nonlinear state feedback, an existential result on bifurcation of the region of attraction was given in [3]:

1. If $\mathcal{U}(x_{e+}) \cap \mathcal{A} \neq \emptyset$ and $\mathcal{U}(x_{e-}) \cap \mathcal{A} \neq \emptyset$, then $\partial\mathcal{A} = \mathcal{S}(x_{e+}) \cup \mathcal{S}(x_{e-})$.

2. If $\mathcal{U}(x_{e+}) \cap \mathcal{A} \neq \emptyset$ and $x_{e-} \notin \partial\mathcal{A}$ then $\partial\mathcal{A} = \mathcal{S}(x_{e+})$

3. If $\mathcal{U}(x_{e-}) \cap \mathcal{A} \neq \emptyset$ and $x_{e+} \notin \partial\mathcal{A}$ then $\partial\mathcal{A} = \mathcal{S}(x_{e-})$.

4. If $\mathcal{U}(x_{e+}) \cap \mathcal{A} = \emptyset$ and $\mathcal{U}(x_{e-}) \cap \mathcal{A} = \emptyset$, then $\partial\mathcal{A}$ is either a closed orbit or a graph of homoclinic/heteroclinic connections.

This result calls for some remarks. Firstly, the result depends on the shape of $\mathcal{A}$ and $\partial\mathcal{A}$ that are unknown. In this chapter, an analytical condition for bifurcation is introduced that does not assume *a priori* the shape of $\mathcal{A}$. Secondly, since the considered system (6.11) is symmetric the Statements 2 and 3 cannot occur. Also, in Statement 4, homoclinic connections, i.e. manifolds starting from and ending at the same saddle point, do not exist for the system considered. In addition, it is possible to distinguish between the cases when heteroclinic connections occur (manifolds starting from one saddle point and ending at another) and when the boundary is a closed orbit.

6.4.2 Preliminaries

In the next section we will state the theorem which characterises the shape of the region of attraction $\mathcal{A}$ of system (6.11) as a function of the condition C. For the proof of this theorem some preliminary knowledge about the existence and characteristics of limit cycles for the considered system is required.

Consider the region

$$\mathcal{D} = \mathcal{C} \cap \mathcal{R} = \left\{ x \in \mathbb{R}^2 : |x_1| < 1 \text{ and } |x_2| < 1 \right\}. \tag{6.50}$$

The next lemma claims that if there exists limit cycles then they are located only in this region.

Lemma 3 *Consider system (6.1) with the admissible input $u \in \mathcal{U}_a = [-1, 1]$. A limit cycle can only occur in the region $\mathcal{D}$ around the equilibrium point $x_{e0} \in \mathcal{D}$.*

Proof:
According to Theorem 2 the system (6.1) with the input $u \in \mathcal{U}_a$ has three equilibrium points x_{e0}, x_{e+} and x_{e-}. Since from Section 6.2 the stable and unstable manifolds of $x_{e\pm}$ possess always at least one unbounded branch (the branch converge to infinity) no trajectory can encircle $x_{e\pm}$. Thus, from the Poincaré theorem (Theorem A.1) we know that if a limit cycle exists it has to encircle the stable equilibrium point x_{e0}.

In the region $\mathbb{R}^2 \setminus \mathcal{C} = \{x \in \mathbb{R}^2 : |x_1| \geq 1\}$ the unstable part of system (6.1) follows

$$\dot{x}_1 = \lambda_1(x_1 + u) \leq 0 \quad \text{for } x_1 \leq -1 \text{ and } u \in \mathcal{U}_a = [-1, 1]$$
$$\dot{x}_1 = \lambda_1(x_1 + u) \geq 0 \quad \text{for } x_1 \geq 1 \text{ and } u \in \mathcal{U}_a = [-1, 1]. \tag{6.51}$$

Therefore, a trajectory leaving the region $\mathcal{C}$ cannot reenter it. Similarly, in the region $\mathbb{R}^2 \setminus \mathcal{R} = \{x \in \mathbb{R}^2 : |x_2| \geq 1\}$ the stable part of system (6.1) follows

$$\dot{x}_2 = \lambda_2(x_2 + u) \geq 0 \quad \text{for } x_2 \leq -1 \text{ and } u \in \mathcal{U}_a = [-1, 1]$$
$$\dot{x}_2 = \lambda_2(x_2 + u) \leq 0 \quad \text{for } x_2 \geq 1 \text{ and } u \in \mathcal{U}_a = [-1, 1]. \tag{6.52}$$

It follows that a trajectory entering the region $\mathcal{R}$ stays in it. Therefore, there exists no limit cycle for which a part of its trajectory is located in $\mathbb{R}^2 \setminus \mathcal{D}$. ∎

For what follows we describe qualitatively where the limit cycle is located in $\mathcal{D}$. Since in the linear region the closed-loop system (6.11) is stable there cannot exist any limit cycle in it. Thus, a part of the limit cycle has to pass through the positive and negative saturated regions by crossing $\partial\mathcal{L}_+$ and $\partial\mathcal{L}_-$. We first study how a potential limit cycles crosses $\partial\mathcal{L}_+$ and $\partial\mathcal{L}_-$. Since system (6.11) is symmetric only $\partial\mathcal{L}_+$ is considered. To determine if a trajectory exists or enters the linear region we study the vector field $\dot{x}(x)$ of (6.1) for all $x \in \partial\mathcal{L}_+$ and $u = 1$. The sign of the scalar product $f\dot{x}(x \in \partial\mathcal{L}_+, 1)$ allows the following conclusion:

- if $f\dot{x}(x \in \partial\mathcal{L}_+) > 0$ then the trajectory exits the linear region $\mathcal{L}$

- if $f\dot{x}(x \in \partial\mathcal{L}_+) < 0$ then the trajectory enters the linear region $\mathcal{L}$

- if $f\dot{x}(x \in \partial\mathcal{L}_+) = 0$ then the vector field is parallel to $\partial\mathcal{L}_+$ and trajectory stays in $\partial\mathcal{L}_+$.

The scalar product

$$f\dot{x}(x \in \partial\mathcal{L}_+) = f_1\lambda_1(x_1 + 1) + f_2\lambda_2(x_2 + 1) \tag{6.53}$$

can be expressed as a function of only one state variable, i.e. x_2 if x_1 is substituted by means of equation $fx = f_1 x_1 + f_2 x_2 = 1$ defining $\partial\mathcal{L}_+$:

$$f\dot{x}(x \in \partial\mathcal{L}_+) = f_2(\lambda_2 - \lambda_1)(1 + x_2) + \lambda_1(1 + f_1 + f_2). \tag{6.54}$$

This equation is obviously linearly dependent on x_2 and thus there exists only one point for which it is zero. We define the point

$$p_0 \in \mathcal{L}_+ \text{ for which } f\dot{x}(p_0) = 0. \tag{6.55}$$

From point p_0 there exists two branches on $\partial\mathcal{L}_+$, where for one of them $f\dot{x} > 0$ and for the other one $f\dot{x} < 0$ since equation (6.54) is a linear expression of x_2. Denote the intersection of $\partial\mathcal{L}_+$ with $\partial\mathcal{C}_-$ and $\partial\mathcal{R}_-$ by

$$c_+ = \partial\mathcal{C}_- \cap \partial\mathcal{L}_+ = \begin{bmatrix} -1 & \frac{(1+f_1)}{f_2} \end{bmatrix}^T \quad \text{and} \quad -r_- = \partial\mathcal{R}_- \cap \partial\mathcal{L}_+ = \begin{bmatrix} \frac{(1+f_2)}{f_1} & -1 \end{bmatrix}^T. \tag{6.56}$$

This leads to following result

Lemma 4 *Consider the points p_0, c_+ and $-r_-$ and the closed-loop system (6.11). The point p_0 is always located on the segment bounded by c_+ and $-r_-$, $p_0 \in \overline{c_+ - r_-} \subset \partial\mathcal{L}_+$. Furthermore, for all $x \in \overline{p_0\,c_+} \setminus p_0$ the trajectory of (6.11) exits the linear region $\mathcal{L}$ since $f\dot{x}(x) > 0$ and enters $\mathcal{L}$ for all $x \in \overline{p_0 - r_-} \setminus p_0$ since $f\dot{x}(x) < 0$.*

Proof:
The points p_0, c_+ and $-r_-$ are elements of $\partial\mathcal{L}_+$. By considering the scalar product $f\dot{x}$ for these points we obtain

$$f\dot{x}(p_0) = 0$$
$$f\dot{x}(c_+) = \lambda_2(1 + f_1 + f_2) > 0$$
$$f\dot{x}(-r_-) = \lambda_1(1 + f_1 + f_2) < 0$$

since the second Hurwitz condition satisfies $1 + f_1 + f_2 < 0$. Therefore, the point p_0 is element of $\overline{c_+ - r_-} \subset \partial\mathcal{L}_+$ since for all $x \in \partial\mathcal{L}_+$ the scalar product $f\dot{x}(x)$ is a linearly depending function. Moreover, for the same reason $f\dot{x}(x) > 0, \forall\, x \in \overline{p_0\,c_+} \setminus p_0$ and $f\dot{x}(x) < 0, \forall\, x \in \overline{p_0 - r_-} \setminus p_0$. $\blacksquare$

The following lemma characterises qualitatively the existence and shape of one ore more limit cycles as a function of the sign of the controller parameter f_2 (Figure 6.6).
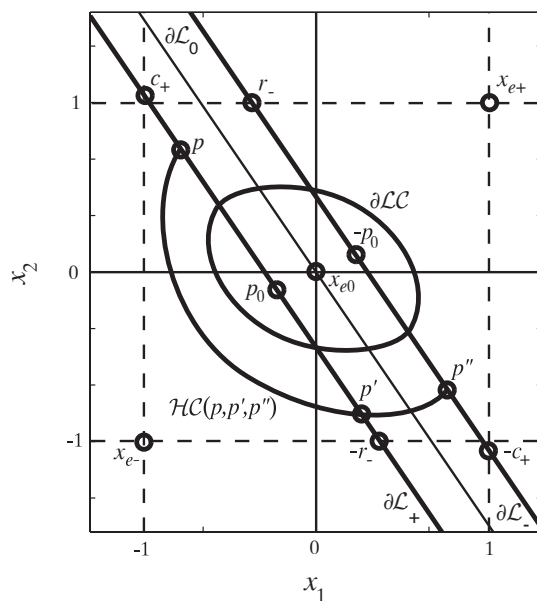
Figure 6.6: Qualitative characterisation of a limit cycle and illustration of a half cycle.

Lemma 5 *Consider the closed-loop system (6.11) and the controller parameter $f_2 \in \mathbb{R}$. Then*

- *for $f_2 \geq 0$ there exists no limit cycle*

- *for $f_2 < 0$ one or more limit cycles can occur. If one or more limit cycles exist then they are located in $\mathcal{D}$ and they encircle the points x_{e0}, p_0 and $-p_0$.*

Proof:

- $f_2 = 0$

  From equation (6.54) the cross product becomes

  $$f\dot{x}(x \in \partial\mathcal{L}_+) = \lambda_1(1 + f_1) < 0$$

  since the second Hurwitz condition satisfies $1 + f_1 + f_2 = 1 + f_1 < 0$. Thus, p_0 does not exist and all trajectories entering the linear region $\mathcal{L}$ can no more leave it. Since the linear region is stable there cannot exist any limit cycle.

- $f_2 > 0$

  We are seeking for the point p_0. From (6.54) and (6.55) we have

  $$f\dot{x}(p_0) = f_2(\lambda_2 - \lambda_1)(1 + x_2) + \lambda_1(1 + f_1 + f_2) = 0. \tag{6.57}$$

  Since from the second Hurwitz condition $\lambda_1(1 + f_1 + f_2) < 0$ the first term has to verify $f_2(\lambda_2 - \lambda_1)(1 + x_2) > 0$. Moreover, since $f_2(\lambda_2 - \lambda_1) < 0$ the expression $(1 + x_2)$ has to be negative which means that x_2 of p_0 has to satisfy $x_2 < -1$. Thus, p_0 is not located in $\mathcal{D}$ and we conclude from Lemma 3 that there cannot exist any limit cycle.

- $f_2 < 0$ (Figure 6.6)

  In this case we have $f_2(\lambda_2 - \lambda_1) > 0$ which implies that x_2 of p_0 is $x_2 > -1$. Thus, there exists points p_0 which are elements of $\mathcal{D}$ implying that one or more limit cycles can appear. Since a limit cycle cannot appear exclusively in the linear region it has to pass through the positive and negative saturated regions. Therefore, from Lemma 4 the trajectory of the limit cycle exits the linear region $\mathcal{L}$ on the open segment $\overline{p_0\,c_+} \setminus p_0 \subset \partial\mathcal{L}_+$ and reenters $\mathcal{L}$ on the open segment $\overline{p_0 - r_-} \setminus p_0 \subset \partial\mathcal{L}_+$. Since the considered system is symmetric the same consideration can be drawn for $\partial\mathcal{L}_-$ and $-p_0 \in \partial\mathcal{L}_-$. Thus, all limit cycle encircle p_0 and $-p_0$. The encirclement of the equilibrium point $xe0$ is due to the Poincaré theorem.

  ∎

Definition 8

Assume that there exists a limit cycle denoted by $\partial\mathcal{LC}$ and its interior by $\mathcal{LC}$. Then there exists trajectories encircling $p_0 \in \mathcal{LC}$, $-p_0 \in \mathcal{LC}$ and $x_{e0} \in \mathcal{LC}$ and converging to $\partial\mathcal{LC}$ in forward time if $\partial\mathcal{LC}$ is stable or in reversed time if $\partial\mathcal{LC}$ is unstable. We define a part of such a trajectory as a half cycle, denoted by

$$\mathcal{HC}(p, p', p''), \tag{6.58}$$

when, in forward time, it starts at $p \in \overline{p_0\,c_+} \setminus p_0 \subset \partial\mathcal{L}_+$ crosses $p' \in \overline{p_0 - r_-} \setminus p_0 \subset \partial\mathcal{L}_+$ and ends at $p'' \in \overline{-p_0 - c_+} \setminus -p_0 \subset \partial\mathcal{L}_-$.

Figure 6.6 illustrates a limit cycle $\partial\mathcal{LC}$ and a half cycle $\mathcal{HC}(p, p', p'')$. A half cycle $\mathcal{HC}(p, p', p'')$ for which $p'' = -p$ is a half limit cycle and by symmetry $\partial\mathcal{LC} = \mathcal{HC}(p, p', p'') \cup -\mathcal{HC}(p, p', p'')$.

6.4.3   Region of attraction as a function of condition C

Theorem 3

1. *If $C > 0$, (region bordered by hyperbolae)*

   - $\mathcal{S}(x_{e+})$ *and* $\mathcal{S}(x_{e-})$ *are disjoint and unbounded.*
   - *For both* $\mathcal{U}(x_{e+})$ *and* $\mathcal{U}(x_{e-})$*, one of the branches converges to the origin.*
   - *The boundary of the region of attraction is* $\partial\mathcal{A} = \mathcal{S}(x_{e+}) \cup \mathcal{S}(x_{e-})$.

2. *If $C < 0$, (region bounded by a limit cycle)*

   - $\mathcal{U}(x_{e+})$ *and* $\mathcal{U}(x_{e-})$ *are disjoint and unbounded.*
   - *For both* $\mathcal{S}(x_{e+})$ *and* $\mathcal{S}(x_{e-})$*, one of the branches converges to a limit cycle.*
   - *The boundary of the region of attraction is the unique time-reversed stable limit cycle*

   $$\partial\mathcal{A} = \lim_{t\to\infty} \Phi(-t, x_0) \; \forall\, x_0 \in \mathcal{U}$$

   where the boundary of $\mathcal{U}$ *is* $\partial\mathcal{U} = \mathcal{U}(x_{e+}) \cup \mathcal{U}(x_{e-})$.

3. *If $C = 0$, (region bounded by two heteroclinic connections)*

   - *One of the branches of* $\mathcal{U}(x_{e+})$ *is bounded and coincides with that of* $\mathcal{S}(x_{e-})$.
   - *One of the branches of* $\mathcal{U}(x_{e-})$ *is bounded and coincides with that of* $\mathcal{S}(x_{e+})$.
   - *The boundary of the region of attraction is a double heteroclinic connection,* $\partial\mathcal{A} = (\mathcal{U}(x_{e+}) \cap \mathcal{S}(x_{e-})) \cup (\mathcal{U}(x_{e-}) \cap \mathcal{S}(x_{e+}))$.

Proof:

1. $C > 0$

   From Section 6.2.2 we know that the stable manifolds $\mathcal{S}(x_{e\pm})$ have two unbounded branches evolving in opposite directions. Since from Lemma 1 $\mathcal{S}(x_{e\pm}) \subset \overline{\mathcal{C}}$ we define the connected set $\mathcal{S}_0 \subset \mathcal{C}$ for which its boundaries are $\partial\mathcal{S}_0 = \mathcal{S}(x_{e+}) \cup \mathcal{S}(x_{e-})$ and where $\partial\mathcal{S}_0 \not\subset \mathcal{S}_0$. Since $\partial\mathcal{S}_0$ are trajectories then, from the unicity theorem, a trajectory starting in $\mathcal{S}_0$ stays in it. Consider the bounded closed set $\overline{\mathcal{B}} = \overline{\mathcal{S}_0} \cap \overline{\mathcal{D}}$, where $\mathcal{B} = \overline{\mathcal{B}} \setminus \partial\mathcal{B}$. Then according to relations (6.52) and since there is no equilibrium point in $\overline{\mathcal{S}_0} \setminus \mathcal{B}$ all trajectories starting in $\overline{\mathcal{S}_0} \setminus \mathcal{B}$ enter and remain in $\overline{\mathcal{B}}$. Thus, $\overline{\mathcal{B}}$ is a closed bounded invariant set which contains the three equilibrium points x_{e+}, x_{e-} and the origin x_{e0}. According to Poincaré-Bendixson's theorem (Theorem A.2) and Lemma 3 all trajectories starting in $\overline{\mathcal{B}}$ will converge either to x_{e+}, x_{e-}, x_{e0} or to a limit cycle encircling x_{e0}. Since $x_{e\pm} \in \partial\mathcal{B} \cap \partial\mathcal{S}_0$ only the trajectory starting from the part of the stable manifolds $\partial\mathcal{B} \cap \partial\mathcal{S}_0$ converge to $x_{e\pm}$. Thus, all other points in $\overline{\mathcal{B}}$, denoted by $\overline{\mathcal{B}} \setminus \partial\mathcal{S}_0$, will converge to the origin x_{e0} or to a limit cycle encircling x_{e0}. From what follows we show that there exists no limit cycle which implies that $\mathcal{S}_0$ is the region of attraction $\mathcal{A}$, where $\partial\mathcal{A} = \partial\mathcal{S}_0 = \mathcal{S}(x_{e+}) \cup \mathcal{S}(x_{e-})$. Moreover, this implies that one of the branches of $\mathcal{U}(x_{e\pm})$ converges to x_{e0}.

   The proof of the nonexistence of limit cycles is divided into two cases i) $\lambda_1 + \lambda_2 \leq 0$ and ii) $\lambda_1 + \lambda_2 > 0$

- Case: $\lambda_1 + \lambda_2 \leq 0$

  From the proof of the Bendixson theorem (Theorem A.3) we claim that if there exists a limit cycle, where its closed curve is denoted by $\partial \mathcal{LC}$ and its interior by $\mathcal{LC}$, then the integral over the area $\mathcal{LC}$

  $$\int\!\!\!\int_{\mathcal{LC}} \nabla \cdot \dot{x} \, dx_1 dx_2 = 0,$$

  where $\nabla \cdot \dot{x}$ is the divergence of the vector field of the closed-loop system (6.11)

  $$\nabla \cdot \dot{x} = \frac{\partial \dot{x}_1}{\partial x_1} + \frac{\partial \dot{x}_2}{\partial x_2} = \begin{cases} D_L := \lambda_1(1 + f_1) + \lambda_2(1 + f_2) & \text{if } x \in \mathcal{L} \\ D_S := \lambda_1 + \lambda_2 & \text{if } x \in \mathbb{R}^2 \setminus \mathcal{L} \end{cases}.$$

  Since the system in $\mathcal{L}$ is Hurwitz the condition (6.12) $\lambda_1(1+f_1)+\lambda_2(1+f_2) < 0$ is verified and thus

  $$D_L < 0.$$

  Since we only investigate the case where $\lambda_1 + \lambda_2 \leq 0$ we obtain

  $$D_S \leq 0.$$

  Since the origin x_{e0} is in the stable region $\mathcal{L}$ the integral is always

  $$\int\!\!\!\int_{S} \nabla \cdot \dot{x} \, dx_1 dx_2 < 0, \tag{6.59}$$

  over any area $S \subset \mathbb{R}^2$ containing the origin. Assume that there exists a limit cycle. Then, since the limit cycle has to encircle the stable node located at the origin and since the integral (6.59) is not equal zero there cannot exist a limit cycle.

- Case: $\lambda_1 + \lambda_2 > 0$

  Assume that there exists at least one limit cycle in $\mathcal{B}$ and denote the closed curve of the biggest limit cycle by $\partial \mathcal{LC}_{max}$ and its interior by $\mathcal{LC}_{max}$. Then all trajectories starting in $\mathcal{B} \setminus \mathcal{LC}_{max}$ encircle $\partial \mathcal{LC}_{max}$ and converge to $\partial \mathcal{LC}_{max}$ at $t \to \infty$. According to Lemma 5 the limit cycle $\partial \mathcal{LC}_{max}$ encircles p_0, $-p_0$ and x_{e0}. From definition 8 we define two arbitrary half cycles $\mathcal{HC}_1(p_1, p_1', p_1'')$ and $\mathcal{HC}_2(p_2, p_2', p_2'')$ located in $\mathcal{B} \setminus \mathcal{LC}_{max}$. If $\partial \mathcal{LC}_{max}$ exists then the distance between both half cycles has to shorten

  $$\|p_1 - p_2\| > \|p_1'' - p_2''\|. \tag{6.60}$$

  From Lemma A.4 and A.2 it follows that since $\lambda_1 + \lambda_2 > 0$ is considered, $\|p_1' - p_2'\| < \|p_1'' - p_2''\|$ and $\|p_1 - p_2\| < \|p_1' - p_2'\|$. Therefore

  $$\|p_1 - p_2\| < \|p_1 - p_2\| < \|p_1'' - p_2''\|$$

  is verified in the whole region $\mathcal{B}$ which is a contradiction to (6.60). Therefore, there cannot exist any limit cycle in $\mathcal{B}$.

2. $C < 0$

   From Section 6.2.2 we know that the unstable manifolds $\mathcal{U}(x_{e\pm})$ have two unbounded branches evolving in opposite directions. Since from Lemma 1 $\mathcal{U}(x_{e\pm}) \subset \overline{\mathcal{R}}$ we define the connected set $\mathcal{U}_0 \subset \mathcal{R}$ for which its boundaries are $\partial \mathcal{U}_0 = \mathcal{U}(x_{e+}) \cup \mathcal{U}(x_{e-})$ and where $\partial \mathcal{U}_0 \not\subset \mathcal{U}_0$. Since $\partial \mathcal{U}_0$ are trajectories then from the unicity theorem a trajectory starting in $\mathcal{U}_0$ stays into it. Consider the bounded and closed set $\overline{\mathcal{B}} = \overline{\mathcal{U}_0} \cap \overline{\mathcal{D}}$, where $\mathcal{B} = \overline{\mathcal{B}} \setminus \partial \mathcal{B}$. Remark that from what follows we consider the system in reversed time. Similarly to point 1. and by considering the relations of (6.51), all trajectories starting in $\mathcal{U}_0 \setminus \mathcal{B}$ enter and remain into $\mathcal{B}$ and either converge to x_{e0} or to a limit cycle encircling x_{e0}. Since we consider the system in reversed time, the equilibrium point x_{e0} is unstable and thus at least one limit cycle exists. It remains to show that there exists only one limit cycle.

   We first show that if the condition $C < 0$ is verified then

   $$\lambda_1 + \lambda_2 > 0$$

   always holds. We have shown in the proof of point 1, where $C > 0$, with means of the Bendixson theorem that there cannot exist a limit cycle if $\lambda_1 + \lambda_2 \leq 0$. This proof holds also in the case where $C < 0$ is verified. Since there always exists a limit cycle if $C < 0$ the condition $\lambda_1 + \lambda_2 > 0$ always holds in the case where $C < 0$.

   Assume two arbitrary limit cycle $\partial \mathcal{LC}_1$ and $\partial \mathcal{LC}_1$ which according to Lemma 5 are located in $\mathcal{B}$ and encircle p_0, $-p_0$ and x_{e0}. By means of definition 8 we define the half cycles of this two limit cycles, denoted by $\mathcal{HC}_1(p_1, p_1', p_1'') \subset \partial \mathcal{LC}_1$ and $\mathcal{HC}_2(p_2, p_2', p_2'') \subset \partial \mathcal{LC}_2$, where $p_1 = -p_1''$ and $p_2 = -p_2''$. This leads to

   $$\|p_1 - p_2\| = \|p_1'' - p_2''\|. \tag{6.61}$$

   From Lemma A.4 and A.2 it follows that since $\lambda_1 + \lambda_2 > 0$ is considered, $\|p_1' - p_2'\| < \|p_1'' - p_2''\|$ and $\|p_1 - p_2\| < \|p_1' - p_2'\|$. Therefore

   $$\|p_1 - p_2\| < \|p_1 - p_2\| < \|p_1'' - p_2''\|$$

   is verified in the whole region $\mathcal{B}$ which is a contradiction to (6.61). Therefore, there exists only one limit cycle in $\mathcal{B}$. Moreover, all trajectories starting in $\mathcal{U}_0 \setminus x_{e0}$ converge to it in reversed time. Thus, since $\mathcal{S}(x_{e\pm}) \subset \mathcal{U}_0$ one branch of each stable manifold converge to the limit cycle. In forward time all trajectories starting inside the limit cycle converge to the origin x_{e0}. The limit cycle is therefore the boundary of the region of attraction $\mathcal{A}$

3. If $C = 0$

   We define the sets $\mathcal{S}_0 = \mathcal{B}$ bounded by the stable or unstable manifolds $\partial \mathcal{S}_0 = \partial \mathcal{B} = \mathcal{S}(x_{e+}) \cup \mathcal{S}(x_{e-}) = \mathcal{U}(x_{e+}) \cup \mathcal{U}(x_{e-})$. Thus, $\partial \mathcal{S}_0$ is bounded by trajectories and therefore no trajectory starting in $\mathbb{R}^2 \setminus \mathcal{S}_0$ can enter $\mathcal{S}_0$. Moreover, all trajectories starting in $\mathcal{S}_0$ remain into it. From what follows we show that there exists no limit cycle in $\mathcal{S}_0$ which implies that $\mathcal{S}_0$ is the region of attraction $\mathcal{A}$, where $\partial \mathcal{A} = \mathcal{S}(x_{e+}) \cup \mathcal{S}(x_{e-}) = \mathcal{U}(x_{e+}) \cup \mathcal{U}(x_{e-})$.

   The remainder of the proof is similar to the proof of point 1.

   ∎

The shapes of the regions in the three scenarios are illustrated in Figures 6.7, 6.8 and 6.9.
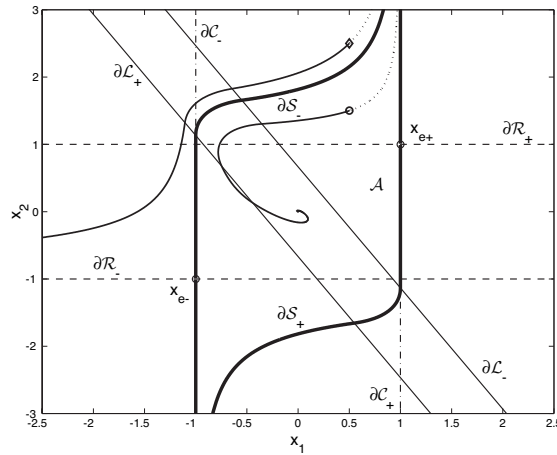
Figure 6.7: Example of the region of attraction for the condition $C > 0$ ($\circ = x_s$, $\diamond = x_u$) (solid line - forward time, dotted line - reverse time).
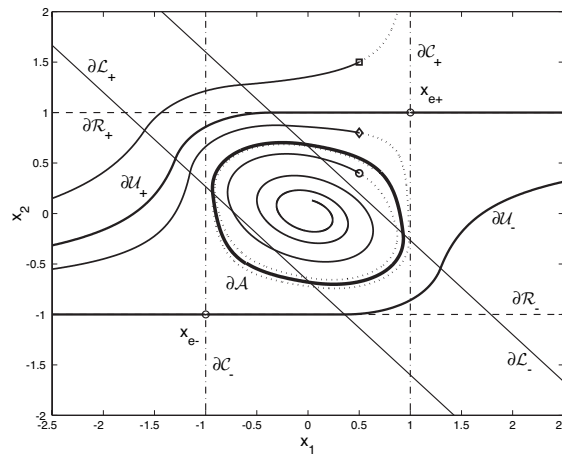
Figure 6.8: Example of the region of attraction for the condition $C < 0$ ($\circ = x_s$, $\diamond = x_{su}$, $\square = x_u$) (solid line - forward time, dotted line - reverse time).
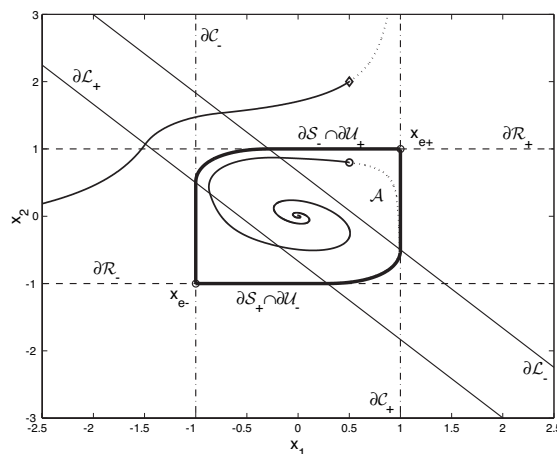
Figure 6.9: Example of the region of attraction for the condition $C = 0$ ($\circ = x_s$, $\diamond = x_u$) (solid line - forward time, dotted line - reverse time).

6.5 Conclusion

In this chapter, the bifurcations of the region of attraction are analysed. It is shown that a planar system with one stable and one unstable pole only exhibits a bifurcation when the unstable pole is faster than the stable one. An analytical condition is provided for which the region of attraction changes from an unbounded hyperbolic region to a bounded limit cycle.

Chapter 7

A globally stabilising controller under saturated input for systems with one unstable pole

In this chapter we present a new globally stabilising controller resulting from the incorporation of a simple continuous nonlinear function into a linear controller, referred to as the Continuous Nonlinear Globally Stabilising Controller (CNGSC). Linear systems with one unstable pole and a single input with saturated linear and nonlinear feedback will be considered. We first analyse the new controller by means of a second-order system and then extend the results to higher order systems ($n > 2$ order system).

Various standard controllers, linear controllers included, are compared against each other by considering five essential requirements which have to be taken into account for the design of a tokamak controller:

1. Global stability:
   Two important concepts pertaining to these systems have to be distinguished. First we have the *null controllable region* $\mathcal{C}$ and the second is the *region of attraction* $\mathcal{A}$ defined in Chapter 6. A controller is considered as globally stabilising when $\mathcal{A} = \mathcal{C}$.

   The following results have been proposed in the literature for planar systems (second order systems). For semi-stable planar systems (both poles have nonpositive real parts), $\mathcal{C} = \mathbb{R}^2$ and $\mathcal{A} = \mathcal{C} = \mathbb{R}^2$ for any linear state feedback which makes the origin globally asymptotically stable in the absence of saturation [51]. However, for systems with one stable and one unstable pole, $\mathcal{C} \subset \mathbb{R}^2$ and $\mathcal{A} = \mathcal{C}$ can be achieved either with an optimal or near optimal variable structure control (VSC) [43, 49] or using a linear state feedback controller where only the unstable state is fed back [3, 49]. For anti-stable systems (both poles have positive real parts), $\mathcal{C} \subset \mathbb{R}^2$ and the only way to obtain $\mathcal{A} = \mathcal{C}$ is with optimal or near optimal switching controllers (bang-bang controllers) [27, 28].

2. Local performance:
   The aim is to enforce the desired performance locally around the origin. For systems with one unstable pole, a simple way of obtaining global stability is to feed back solely the unstable state. However, such a controller will have poor local performance due to the absence of feedback on the stable modes. The proposed controller should guarantee, at least locally, the desired temporal performance.

3. Avoidance of large AC losses:
   The results concerning the AC losses reduction are presented in Chapter 5 of Part
   I. The main statement for avoiding large AC losses is to design controllers which
   generate control signals with i) least possible oscillations, ii) amplitudes as small as
   possible and iii) signal frequencies as low as possible. Therefore, we have to avoid
   chattering (discontinuous switching at very high frequencies) in the control signal
   which is due to the controller itself (e.g. sliding mode bang-bang controller) or which
   is induced in the presence of noise. In general, chattering is due to discontinuities
   in the control law, e.g. bang-bang controller. A discontinuity may also give rise to
   an oscillating transient phase appearing just after its occurrence. These oscillations
   increase the AC losses.

4. Application for higher order systems:
   The controller should be able to handle higher order systems. We define a higher
   order system as a dynamic system higher than second order.

5. Simple design and implementation:
   Experience shows that new controllers with complicated and complex structures are
   often not considered in practice, especially in the field of industrial applications. In
   general, there seems to be a fear of controllers for which considerable knowledge is
   required for design and implementation. We therefore have to focus on controllers
   for which the design and the implementation are simple and fairly intuitive.

In what follows various standard controllers proposed in the literature are analysed
from the perspective of control of linear planar or higher order systems with one unstable
pole.

i. **Standard linear state feedback controllers** where both states are fed back [18]:
   Requirement 1 is not satisfied.

ii. **Linear state feedback controllers** where only the unstable state is fed back
   [3, 49]: Requirement 2 is not satisfied since the stable states are left to follow their
   own dynamics.

iii. **Controller switching** from controller (ii) to controller (i) [27, 28]: When the state
   reaches an invariant non-saturated region, the controller switches from type (ii) to
   (i). The problem is that the invariant region could be very small, thus Require-
   ment 2 might not be satisfied. Furthermore, the switching from one controller to
   another implies a discontinuity which might give raise to an increase of AC losses,
   thus Requirement 3 might not be verified. The design and implementation requires
   knowledge of Lyapunov stability theory (for the invariant region) and thus Require-
   ment 5 is not satisfied.

iv. **Time optimal controller** [43]: Since chattering of the control signal is induced in
   the presence of noise and disturbances Requirement 3 is not satisfied. No solutions
   for higher order systems have been found in the literature, thus it is assumed that
   Requirement 4 is not satisfied.

v. **Near-time optimal VSC controller** [49]: Since the controller is chattering during
   sliding-mode Requirement 3 is not satisfied. There is no proposition for application
   to higher order system in [49]. Nevertheless, an extension to higher order system

seems possible but will considerably complicate the controller structure and thus the design and implementation, i.e. Requirement 5 is not satisfied.

Remark:

From the point of view of Requirements 1 and 2, the time optimal or near-time optimal switching strategies are the methods of choice. The controllers have the maximum region of attraction and provide excellent time performance, not only locally, but even globally. However, the main problem is that the control signal is chattering. Absence of chattering and therefore reduction of AC-losses is an important requirement for the controller we want.

The properties of these controllers are summarised in Table 7.1. The controllers available in the literature cannot satisfy one or more of the requirements stated above. Thus, a controller is proposed that meets all the aforementioned requirements. The idea is to obtain a controller of type (iii) with a continuous switching from controller type (ii) to controller type (i). This way, the problems linked to chattering and discontinuities (AC losses) are avoided and the region of attraction is the null controllable region $\mathcal{A} = \mathcal{C}$.

	Global stability	Local performance	Avoid large AC losses	Higher order systems	Simple design
Standard linear	−	√	√	√	√
Feedback unstable state	√	−	√	√	√
Switching controller	√	−	−	√	−
Time optimal controller	√	√	−	−	√
Near-time optimal VSC	√	√	−	√	−

Table 7.1: Properties of state of the art controllers.

This chapter is organised as follows. In Section 7.1, definitions and terms used in this chapter are introduced. Section 7.2 provides the main idea behind the structure of the proposed CNGSC controller. Then global stabilisation in the null controllable region is discussed and the CNGSC controller is compared against the standard controllers in terms of local performance and chattering by means of simulations. Section 7.3 provides an extension of the controller for the application to higher order systems. Conclusions are drawn in Section 7.4.

7.1 Preliminaries

7.1.1 Linear system with input saturation

We consider a single input linear system with a single unstable pole. Upon state transformation, the system can be written as

$$\dot{x} = Ax + bu \tag{7.1}$$

where, $x \in \mathbb{R}^n$ is the state vector and $u \in \mathbb{R}$ the input. Without loss of generality, A can be written as

$$
A = \begin{bmatrix}
\lambda_1 & 0 & \cdots & 0 & 0 & \cdots & 0 \\
0 & \lambda_2 & \cdots & 0 & 0 & \cdots & 0 \\
\vdots & \vdots & \ddots & \vdots & \vdots & \vdots & \vdots \\
0 & 0 & \cdots & \lambda_r & \mu_r \nu_r & \cdots & 0 \\
0 & 0 & \cdots & -\mu_r/\nu_r & \lambda_r & \cdots & 0 \\
\vdots & \vdots & \vdots & \vdots & \vdots & \ddots & \vdots \\
0 & 0 & \cdots & 0 & 0 & \cdots & \lambda_{n_c}
\end{bmatrix}
\tag{7.2}
$$

where $\lambda_1 > 0$ is the unstable pole and $0 > \lambda_2 \geq \lambda_3 \geq \ldots \geq \lambda_{n_c}$ are the real parts of the stable poles, where $n_c \leq n$. Conjugate complex pole pairs (i.e. $\lambda_r \pm j\mu_r$) are represented as square submatrices, where $\nu_r \in \mathbb{R}$ can by an arbitrary chosen value. Furthermore, upon state transformation,

$$
b = \begin{bmatrix} \lambda_1 & \lambda_2 & \cdots & b_{r_1} & b_{r_2} & \cdots & \lambda_{n_c} \end{bmatrix}^T,
\tag{7.3}
$$

where b_{r_1}, b_{r_2} and also ν_r are chosen so that $A^{-1}b = \begin{bmatrix} 1 & 1 & \ldots & 1 \end{bmatrix}$.

System (7.1) can be subdivided into a system composed of an anti-stable and a stable subsystem [27]

$$
\begin{bmatrix} \dot{x}_1 \\ \dot{x}_s \end{bmatrix} = \begin{bmatrix} \lambda_1 & 0 \\ 0 & A_s \end{bmatrix} \begin{bmatrix} x_1 \\ x_s \end{bmatrix} + \begin{bmatrix} \lambda_1 \\ b_s \end{bmatrix} u,
\tag{7.4}
$$

where $x_1 \in \mathbb{R}$ and λ_1 describe the anti-stable subsystem and $x_s = [x_2 \ x_3 \ \ldots \ x_n]^T \in \mathbb{R}^{n-1}$, A_s and b_s describe the stable subsystem.

We consider the symmetric saturation function with unity saturation level defined as

$$
\text{sat}(\tilde{u}) = \begin{cases} -1 & \text{if} \quad \tilde{u} < -1 \\ \tilde{u} & \text{if} \quad -1 \leq \tilde{u} \leq 1 \ . \\ 1 & \text{if} \quad \tilde{u} > 1 \end{cases}
\tag{7.5}
$$

With saturated state feedback, the closed-loop system becomes

$$
\dot{x} = Ax + b \, \text{sat}(\tilde{u}(x)),
\tag{7.6}
$$

where $\tilde{u}(x) : \mathbb{R}^n \to \mathbb{R}$ represents the nonlinear control law as a function of the states.

7.1.2 Equilibrium points, null controllable region, region of attraction, stable manifolds and non-saturated region

The general definitions of the equilibrium points $x_{e\pm}$, the null controllable region $\mathcal{C}$, the region of attraction $\mathcal{A}$, the stable manifolds $\mathcal{S}$ and the non-saturated region $\mathcal{L}$ are already provided in Chapter 6 for planar systems. We need to define these system characteristic properties for the considered system of order n.

Equilibrium points and null controllable region

Consider the upper (positive) saturation level σ_u and the lower (negative) saturation level

σ_l of a saturation. When the input u is equal to one of the two saturation levels then there exists, for any system for which A is invertible, an equilibrium ($\dot{x} = 0$) for each saturation level, given by

$$x_{e+} = -A^{-1}b\sigma_l \qquad \text{and} \qquad x_{e-} = -A^{-1}b\sigma_u. \tag{7.7}$$

When we consider the closed-loop system (7.6) where the feedback $\tilde{u}(x)$ is a global stabiliser for (7.1) then trivially there exists a stable equilibrium point at the origin, defined as $x_{e0} = 0$.

Let us denote the part of the equilibrium points $x_{e\pm}$ which corresponds to the subspace of the unstable state x_1 as $x_{e\pm_1} \in \mathbb{R}$. Then we can define the null controllable region of a single input saturated system as

$$\mathcal{C} = \{x \in \mathbb{R}^n : |x_1| < |x_{e\pm_1}|\}, \tag{7.8}$$

where its boundaries are given by

$$\partial\mathcal{C}_+ = \{x \in \mathbb{R}^n : x_1 = x_{e+_1}\} \qquad \text{and} \qquad \partial\mathcal{C}_- = \{x \in \mathbb{R}^n : x_1 = x_{e-_1}\}. \tag{7.9}$$

Note that in the case of the normalised system considered (System 7.1) the equilibrium points are

$$x_{e\pm} = \pm A^{-1}b = \pm \begin{bmatrix} 1 \\ 1 \\ \vdots \\ 1 \end{bmatrix} \tag{7.10}$$

and the null controllable region is therefore

$$\mathcal{C} = \{x \in \mathbb{R}^n : |x_1| < 1\}. \tag{7.11}$$

The proof of the null controllable region for nth order systems is similar to the proof given for second order systems (Chapter 6) when we consider the separation of the nth order system into a first order anti-stable system and into a $(n-1)$th order stable system (System 7.4).

By considering the closed-loop system (7.6) with a global stabilising feedback $\tilde{u}(x)$ we can prove the existence of the equilibrium points $x_{e\pm}$, i.e. x_{e+} has to be inside the negative saturated region $u = \sigma_l$, while x_{e+} has to be inside the positive saturated region $u = \sigma_+$. Since we are only interested in globally stabilising controllers for which the region of attraction is equivalent to the null controllable region, this proof is derived straightforwardly from the proof of the null controllable region.

We conclude that the closed-loop system (7.6) with a global stabilising feedback $\tilde{u}(x)$ possesses at least 3 equilibrium points, referred to as $x_{e\pm}$ and $x_{e0} = 0$. However, the following theorem (provided in [3]) claims that for planar systems there only exist these 3 equilibrium points.

Theorem 4
Let the feedback $\tilde{u}$ be a global stabiliser for a planar system (7.1) at the origin. Then, the closed-loop system (7.6) has three equilibrium points: $x_{e+} = A^{-1}b = \begin{bmatrix} 1 & 1 \end{bmatrix}^T$, $x_{e-} = -A^{-1}b = \begin{bmatrix} -1 & -1 \end{bmatrix}^T$, and $x_{e0} = 0$. Of these, x_{e0} is stable, while the other two are saddle points.

Proof: The proof of this theorem is presented in [3]. Its proof relies on knowledge of index theory and homotopy techniques which is not easily accessible. In the case of pure linear saturated state feedback the proof is provided in Chapter 6. ∎

Note that such a theorem does not exist for higher order systems ($n > 0$). Therefore, there may exist more than only these 3 equilibrium points.

Region of attraction

Definition 9
Let $\Phi(t, x_0)$ denote the state of (7.6) at time t, starting with the initial condition x_0 at $t = 0$. The region of attraction of the stable equilibrium point $x_{e0} = 0$ is defined as:

$$\mathcal{A} = \left\{ x \in \mathbb{R}^n : \lim_{t \to \infty} \Phi(t, x) = 0 \right\}. \tag{7.12}$$

The boundary of $\mathcal{A}$ is denoted by $\partial \mathcal{A}$.

Stable manifolds of the equilibrium points $x_{e\pm}$
The stable manifolds of the equilibrium points $x_{e\pm}$ are defined as

$$\mathcal{S}(x_{e+}) = \left\{ x \in \mathbb{R}^n : \lim_{t \to \infty} \Phi(t, x) = x_{e+} \right\} \tag{7.13}$$

$$\mathcal{S}(x_{e-}) = \left\{ x \in \mathbb{R}^n : \lim_{t \to \infty} \Phi(t, x) = x_{e-} \right\}. \tag{7.14}$$

Non-saturating region
The non-saturating region is defined as

$$\mathcal{L} = \left\{ x \in \mathbb{R}^n : |\tilde{u}(x)| \leq 1 \right\}. \tag{7.15}$$

The hypersurfaces

$$\partial \mathcal{L}_+ = \{ x \in \mathbb{R}^n : \tilde{u}(x) = 1 \} \quad \text{and} \quad \partial \mathcal{L}_- = \{ x \in \mathbb{R}^n : \tilde{u}(x) = -1 \} \tag{7.16}$$

are the boundaries of the region $\mathcal{L}$ and

$$\partial \mathcal{L}_0 = \{ x \in \mathbb{R}^n : \tilde{u}(x) = 0 \} \tag{7.17}$$

is the hypersurface of zero control.

7.1.3 Globally stabilising linear state feedback controller

In this section we present a review of an important result pertaining to saturated linear state feedback. We show that there exists a linear controller for which the region of attraction is equal to the null controllable region ($\mathcal{A} = \mathcal{C}$) [3]. Consider the linear state feedback control

$$\tilde{u}(x) = f_1 x_1 + f_2 x_2 + f_3 x_3 + \ldots + f_n x_n \tag{7.18}$$

which is a stabiliser for System (7.1). Then it can be shown that $\mathcal{A} = \mathcal{C}$, if and only if $f_2 = f_3 = \ldots = f_n = 0$. With such a choice of control parameters the anti-stable subsystem becomes

$$\dot{x}_1 = \lambda_1 (x_1 + \text{sat}(f_1 x_1)). \tag{7.19}$$

Since the Hurwitz condition calls for $1 + f_1 < 0$, then

$$\dot{x}_1 < 0 \quad \forall \, x_1 > 0$$
$$\dot{x}_1 > 0 \quad \forall \, x_1 < 0 \quad \text{and}$$
$$\dot{x}_1 = 0 \quad \text{for } x_1 = 0$$

is satisfied for $x \in \mathcal{C}$ leading the unstable state x_1 to converge to zero independently of the other states. Since $x_1 \to 0$, this implies that $\tilde{u} \to 0$ and the stable subsystem becomes $\dot{x}_s = A_s x_s$. Therefore, since A_s is stable, $x_s \to 0$.

For all other linear controllers where at least one of the parameters $f_2, f_3 \ldots f_n$ is nonzero, the region of attraction is always smaller than the null controllable region ($\mathcal{A} \subset \mathcal{C}$). This can be explained as follows. On the boundaries of the null controllable region $\partial \mathcal{C}_\pm$ for which $x_1 = \pm 1$ and on the zero control hypersurface $\partial \mathcal{L}_0$ for which $\tilde{u}(x) = 0$ the linear state feedback (Equation 7.18) becomes

$$\tilde{u}(x) = 0 = \pm f_1 + f_2 x_2 + f_3 x_3 + \ldots + f_n x_n.$$

By solving this equation for x there is always at least one solution when at least one of the parameters $f_2, f_3 \ldots f_n$ is nonzero. In this case there exists always an intersection of the zero control hypersurface $\partial \mathcal{L}_0$ with the boundaries of the null controllable region $\partial \mathcal{C}_\pm$. Thus, there exists a zero control $\tilde{u}(x) = 0$ on the boundaries of the null controllable region. Let us denote the intersection of $\partial \mathcal{L}_0$ with $\partial \mathcal{C}_+$ as V_+ and with $\partial \mathcal{C}_-$ as V_-. Since the linear state feedback $\tilde{u}(x)$ is a continuous function of the state x there exists a small neighborhood of $V_\pm$, denoted as $W_\pm$, for which $\tilde{u}(x) \approx 0$ and for which $W_\pm \subset \mathcal{C}$. Thus, for the anti-stable subsystem

$$\dot{x}_1 > 0 \quad \forall x \in W_+ \text{ (where } x_1 \approx 1) \quad \text{and}$$
$$\dot{x}_1 < 0 \quad \forall x \in W_- \text{ (where } x_1 \approx -1)$$

is satisfied. Therefore, the trajectories starting in $W_\pm \subset \mathcal{C}$ inevitably leave the null controllable region and thus $\mathcal{A} \subset \mathcal{C}$.

7.2 CNGSC controller for planar systems

In this section we present the CNGSC controller by only considering planar systems (System (7.1) with n=2) defined as

$$\dot{x} = Ax + bu = \begin{bmatrix} \lambda_1 & 0 \\ 0 & \lambda_2 \end{bmatrix} x + \begin{bmatrix} \lambda_1 \\ \lambda_2 \end{bmatrix} u \tag{7.20}$$

where, $x \in \mathbb{R}^2$ is the state vector, u the input, A and b appropriate matrices, and λ_1, λ_2 the eigenvalues of the open-loop system. Assume that $\lambda_1 > 0$ and $\lambda_2 < 0$.

Consider the controller

$$\tilde{u}(x) = f_1 x_1 + k(x) f_2 x_2 \qquad u = \text{sat}(\tilde{u}), \tag{7.21}$$

where $f = \begin{bmatrix} f_1 & f_2 \end{bmatrix} \in \mathbb{R}^2$ and $k(x) : \mathbb{R}^2 \to \mathbb{R}$. Assume that f has been chosen to deliver the desired performance (Requirement 2) of the closed-loop system near the origin. If we set $k(x) = 1$, then (7.21) corresponds to a linear state feedback controller with the desired

performance. If $k(x) = 0$, then the stable state is not fed back leading to $\mathcal{A} = \mathcal{C}$ (Section 7.1.3). Continuous switching is introduced by choosing:

$$k(x) = 1 - |x_1| \tag{7.22}$$

or

$$k(x) = 1 - x_1^2, \tag{7.23}$$

where $0 < k(x) \leq 1$ since within the null controllable region $|x_1| < 1$.

The idea behind this nonlinear controller is as follows. If $x_1 \approx 0$, then $k(x) \approx 1$ which implies that the controller is approximately the linear state feedback $\tilde{u} \approx f_1 x_1 + f_2 x_2$. In this case, the controller concentrates on local performance (Requirement 2). On the contrary, if the unstable state approaches the boundary of the null controllable region $\mathcal{C}$, $x_1 \approx \pm 1$ and $k(x) \approx 0$. This implies that the controller is approximately the linear state feedback $\tilde{u} \approx f_1 x_1$, where it focuses on the stabilisation of the unstable state and global stability (Requirement 1). Since the controller (7.21)-(7.22) is a continuous one, chattering is avoided and Requirement 3 is also fulfilled.

Since f stabilises the system locally, it satisfies the Hurwitz stability conditions:

1. $\lambda_1(1 + f_1) + \lambda_2(1 + f_2) < 0$

2. $\lambda_1 \lambda_2(1 + f_1 + f_2) > 0$, $(1 + f_1 + f_2) < 0$

Furthermore, the condition that the system has to be stable at $k(x) = 0$ implies that $(1 + f_1) < 0$ has to be satisfied.

To described the regions where the control is saturated and where it is not, consider the function $g_{\tilde{u}} : (-1, 1) \to \mathbb{R}$ that describes x_2 as a function of x_1 for a given $\tilde{u} \in [-1, 1]$:

$$x_2 = g_{\tilde{u}}(x_1) = \frac{\tilde{u} - f_1 x_1}{f_2(1 - |x_1|)}. \tag{7.24}$$

With this function, it is possible to express $\partial \mathcal{L}_0$, $\partial \mathcal{L}_+$ and $\partial \mathcal{L}_-$ by setting $\tilde{u} = 0$, $\tilde{u} = 1$ and $\tilde{u} = -1$, respectively:

$$\partial \mathcal{L}_0 = \{x \in (-1, 1) \times \mathbb{R} : x_2 = g_{\tilde{u}}(x_1) \text{ with } \tilde{u} = 0\}$$
$$\partial \mathcal{L}_+ = \{x \in (-1, 1) \times \mathbb{R} : x_2 = g_{\tilde{u}}(x_1) \text{ with } \tilde{u} = 1\}$$
$$\partial \mathcal{L}_- = \{x \in (-1, 1) \times \mathbb{R} : x_2 = g_{\tilde{u}}(x_1) \text{ with } \tilde{u} = -1\}$$

Figure 7.1 illustrates $\partial \mathcal{L}_0$, $\partial \mathcal{L}_+$, $\partial \mathcal{L}_-$, the boundary of the null controllable region $\partial \mathcal{C}_+$ and $\partial \mathcal{C}_-$, and the equilibrium saddle nodes x_{e+} and x_{e-}.

7.2.1   Analysis of the proposed controller

In what follows we analyse the controller with $k(x) = 1 - |x_1|$ since there exists a formal conservative proof for $\mathcal{A} = \mathcal{C}$. Although the behaviour of the controller with $k(x) = 1 - x_1^2$ is similar to that with $k(x) = 1 - |x_1|$ a formal proof has not yet been derived.

Consider the closed-loop system with (7.6), (7.21) and (7.22) :

$$\dot{x} = Ax + b \operatorname{sat}(f_1 x_1 + f_2 x_2(1 - |x_1|)) \tag{7.25}$$

It was shown in Chapter 6 that the stable manifolds are the boundaries of the region of attraction $\mathcal{A}$. In what follows, it will be shown that, with controller (7.21) the stable manifolds are in fact the boundaries of the null controllable region $\mathcal{C}$.
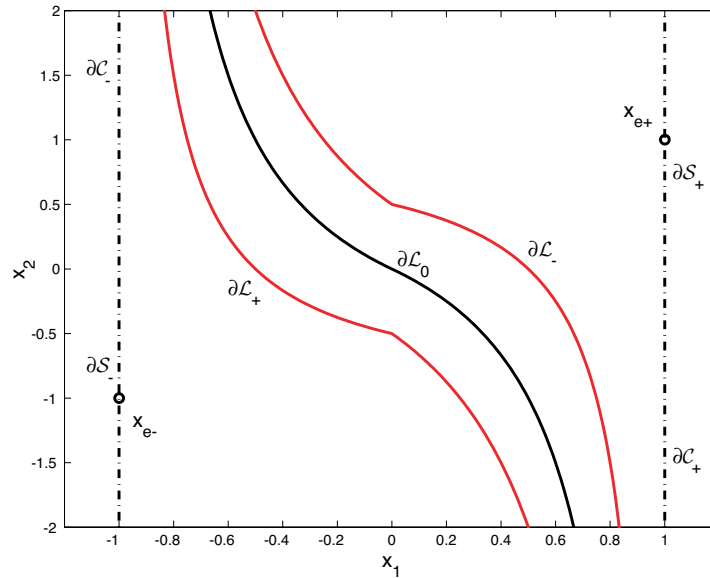
Figure 7.1: Illustration of $\partial\mathcal{L}_0$, $\partial\mathcal{L}_+$, $\partial\mathcal{L}_-$, the boundary of the null controllable region $\partial\mathcal{C}_+$ and $\partial\mathcal{C}_-$, the stable manifolds $\partial\mathcal{S}_+$ and $\partial\mathcal{S}_-$, and the equilibrium saddle nodes x_{e+} and x_{e-}.

Proposition 4 *Consider system (7.25). If $(1 + f_1) < 0$, then*

$$\partial\mathcal{S}_+ = \partial\mathcal{C}_+ \ \text{and} \ \partial\mathcal{S}_- = \partial\mathcal{C}_-.$$

Proof: Consider the input (7.21) along the manifold $\partial\mathcal{C}_+$ (for which $x_1 = 1$): $u = \text{sat}(f_1) = -1$, since $f_1 < -1$. Then, (7.25) along $\partial\mathcal{C}_+$ reads:

$$\dot{x}_1 = \lambda_1(x_1 - 1) = 0 \tag{7.26}$$
$$\dot{x}_2 = \lambda_2(x_2 - 1) \tag{7.27}$$

Thus, x_1 stays at 1, and since $\lambda_2 < 0$, x_2 converges to 1 as well. Thus, $\partial\mathcal{C}_+$ forms the set of all points that converge to the equilibrium point x_{e+}. So, $\partial\mathcal{S}_+ = \partial\mathcal{C}_+$. A similar proof can be written for $\partial\mathcal{S}_- = \partial\mathcal{C}_-$. ■

Lemma 6 *Let $X = (-1, 1) \times [-1, 1]$ and $D = [-1 + \epsilon, 1 - \epsilon] \times [-1, 1]$, with $\epsilon > 0$ chosen such that $|u(x)| = 1$ for all $x \in (X \setminus D)$. Then, all trajectories starting in $\mathcal{C}$ will enter the compact invariant set D.*

Proof: Consider the subset $X_+ = (-1, 1) \times (1, \infty]$. Within this set,

$$\dot{x}_2 = \lambda_2(x_2 + u) < 0$$

since $\lambda_2 < 0$, $x_2 > 1$, and $|u| \leq 1$ due to saturation. So, all trajectories starting in X_+ will leave X_+. A similar argument can be provided for $X_+ = (-1, 1) \times [-\infty, -1)$. So, since $\mathcal{C}$ is invariant, all trajectories starting in $\mathcal{C}$ will reach $X = \mathcal{C} \setminus (X_+ \cup X_-) = (-1, 1) \times [-1, 1]$.

Consider the subset $Y_- = (-1, -1 + \epsilon) \times [-1, 1]$, with $\epsilon > 0$ chosen such that $u(x) = 1$ for all $x \in Y_-$. So, within this set

$$\dot{x}_1 = \lambda_1(x_1 + u) > 0$$

since $\lambda_1 > 0$, $x_1 > -1$, and $u = 1$. Thus, eliminating Y_- and its counterpart $Y_+ = (1, 1-\epsilon) \times [-1, 1]$ gives the compact invariant set $D = X \setminus (Y_+ \cup Y_-)$. So, every trajectory starting in X reaches D.

The proof is complete since every trajectory starting in $\mathcal{C}$ reaches X and every trajectory starting in X reaches D. Thus, D is invariant. ∎

Lemma 7 *If $\lambda_1 + \lambda_2 > 0$ or $(f_2 - f_1) \le 0$, then the non-saturated region $\mathcal{L}$ is an invariant set for (7.25).*

Proof: The lemma is proved by showing that the vector field of (7.25) points into the non-saturated region $\mathcal{L}$ for every point along the manifolds $\partial \mathcal{L}_+$ and $\partial \mathcal{L}_-$. Since $\partial \mathcal{L}_+$ and $\partial \mathcal{L}_-$ are symmetric it is sufficient to prove it only for one manifold ($\partial \mathcal{L}_+$, $\tilde{u} = 1$).

The slope of the tangent of $\partial \mathcal{L}_+$, s_1, is given by:

$$s_1 = \frac{dx_2}{dx_1} = \frac{dg_{\tilde{u}}(x_1)}{dx_1} = \frac{-f_1 + \text{sgn}(x_1)}{f_2(1 - |x_1|)^2}, \tag{7.28}$$

Note that $s_1 < 0$ for $f_2 < 0$ and $s_1 > 0$ for $f_2 > 0$.

Noting that $x_2 = g_{\tilde{u}}(x_1)$ along $\partial \mathcal{L}_+$, the slope of the vector field s_2 is given by:

$$s_2 = \frac{\dot{x}_2}{\dot{x}_1} = \frac{\lambda_2(x_2 + 1)}{\lambda_1(x_1 + 1)} = \frac{\lambda_2}{\lambda_1} \frac{1 - f_1 x_1 + f_2(1 - |x_1|)}{f_2(1 - |x_1|)(1 + x_1)} \tag{7.29}$$

The vector field points into the non-saturated region $\mathcal{L}$ if $s_2 > s_1$ for $s_1 < 0$ ($f_2 < 0$) and $s_2 < s_1$ for $s_1 > 0$ ($f_2 > 0$). Since both s_1 and s_2 have f_2 in the denominator, the two cases with $f_2 > 0$ and $f_2 < 0$ can be unified to give the following condition:

$$\frac{\lambda_2}{\lambda_1} \frac{1 - f_1 x_1 + f_2(1 - |x_1|)}{(1 - |x_1|)(1 + x_1)} < \frac{-f_1 + \text{sgn}(x_1)}{(1 - |x_1|)^2}.$$

Since $(1 + x_1) \ge (1 - |x_1|) > 0$ and $(-f_1 + \text{sgn}(x_1)) > (-f_1 - 1)$, the condition can be rearranged to give:

$$\lambda_1(1 + f_1) + \lambda_2(1 + f_2(1 - |x_1|)) - \lambda_2 f_1 x_1 < 0 \tag{7.30}$$

So, the lemma is proved if it can be shown that (7.30) is verified.
Case 1: $x_1 \ge 0$
From the Hurwitz stability condition, $\lambda_1(1 + f_1) + \lambda_2(1 + f_2(1 - |x_1|)) < 0$. Since $\lambda_2 < 0$ and $f_1 < 0$ the last term of (7.30), $-\lambda_2 f_1 x_1 \le 0$. So, the inequality (7.30) holds.
Case 2: $x_1 < 0$
Substituting $|x_1| = -x_1$ in (7.30) reads:

$$\phi(x_1) = \lambda_1(1 + f_1) + \lambda_2(1 + f_2) + \lambda_2 x_1(f_2 - f_1) < 0 \tag{7.31}$$

Due to linearity, the maximum of $\phi(x_1)$ $\forall -1 \le x_1 \le 0$ occurs either at $x_1 = -1$ or $x_1 = 0$ depending on the sign of $(f_2 - f_1)$. If $(f_2 - f_1) \le 0$, the maximum is at $x_1 = 0$. Thus, it is required to prove $\lambda_1(1 + f_1) + \lambda_2(1 + f_2) < 0$, which is verified since it is the Hurwitz stability condition. If $(f_2 - f_1) > 0$, the maximum is at $x_1 = -1$, and the inequality (7.31) becomes:

$$(\lambda_1 + \lambda_2)(1 + f_1) < 0.$$

Due to the Hurwitz stability condition, $(1+f_1) < 0$, and due to the hypothesis, $(\lambda_1+\lambda_2) > 0$, this condition is verified. ∎

The next theorem is the main result where the global asymptotic stability in $\mathcal{C}$ is guaranteed under the condition

$$\lambda_1(2 + f_1) + \lambda_2(1 + f_2) < 0. \tag{7.32}$$

Since $\lambda_1 > 0$, this is a slightly more restrictive condition than the Hurwitz condition $\lambda_1(1 + f_1) + \lambda_2(1 + f_2) < 0$.

Theorem 5
If f satisfies the conditions

$$(1 + f_1 + f_2) < 0, \quad \lambda_1(2 + f_1) + \lambda_2(1 + f_2) < 0, \tag{7.33}$$

then, the closed loop system

$$\dot{x} = h(x) = Ax + b\,\mathrm{sat}(f_1 x_1 + f_2 x_2(1 - |x_1|)) \tag{7.34}$$

is asymptotically stable for all initial conditions in $\mathcal{C}$.

Proof: First it is shown, using an extension of Bendixson's theorem [13], that no limit cycle exists. The extension of the Bendixson's theorem claims that if on a compact invariant set F, the divergence $\nabla \cdot h$ defined by:

$$\nabla \cdot h(x) = \begin{bmatrix} \frac{\partial}{\partial x_1} & \frac{\partial}{\partial x_1} \end{bmatrix} \cdot \begin{bmatrix} h_1(x_1, x_2) \\ h_2(x_1, x_2) \end{bmatrix} = \frac{\partial \dot{x}_1}{\partial x_1} + \frac{\partial \dot{x}_2}{\partial x_2} \tag{7.35}$$

exists and has the same sign almost everywhere in F, then F contains no closed trajectories.

For the non-saturated region without the boundaries $(\mathcal{L} \setminus (\partial\mathcal{L}_+ \cup \partial\mathcal{L}_-))$, using the condition (7.33), it can be seen that

$$\begin{aligned}
\nabla \cdot h(x) &= \lambda_1(1 + f_1) + \lambda_2(1 + f_2(1 - |x_1|)) \\
&\quad -\lambda_1 f_2 x_2 \mathrm{sgn}(x_1) < 0
\end{aligned} \tag{7.36}$$

For the compact saturated region $(D \setminus \mathcal{L})$

$$\nabla \cdot h(x) = \lambda_1 + \lambda_2 \tag{7.37}$$

Case 1: $\lambda_1 + \lambda_2 > 0$
In this case, the non-saturated region $\mathcal{L}$ is invariant (Lemma 7). Since $\nabla \cdot h < 0$ in the invariant region there are no limit cycles.
Case 2: $\lambda_1 + \lambda_2 \leq 0$
In this case, $\nabla \cdot h$ is non-positive in both the saturated and non-saturated regions, and so there are no limit cycles either.

The proof of the theorem is now based on the application of the Poincare-Bendixson's theorem within the compact invariant set D. So, every trajectory of (7.34) starting at $x_0 \in \mathcal{C}$ will either i) go to the equilibrium point at the origin, ii) tend to a limit cycle or iii) be a limit cycle itself. In the first part of the proof, it has been shown that there are no limit cycles. So, all trajectories in $\mathcal{C}$ converge asymptotically to the origin. Thus, the region of attraction is in fact $\mathcal{A} = \mathcal{C}$. ∎

7.2.2 Comparison of controllers via simulations

System (7.20) is considered with the parameters $\lambda_1 = 1$ and $\lambda_2 = -0.5$, i.e.

$$\dot{x}_1 = x_1 + u$$
$$\dot{x}_2 = -0.5\,(x_2 + u)$$

The following 4 controllers are compared:

- C1: Linear saturated controller:
  $u = \text{sat}(f_1 x_1 + f_2 x_2)$, $f_1 = -6$ and $f_2 = -3$

- C2: Linear saturated controller with only x_1 fed back:
  $u = \text{sat}(f_1 x_1)$, $f_1 = -3$

- C3: Time optimal controller [43] (it is assumed that the results for the near-time optimal VSC controller [49] are similar):
  Switching between $u = -1$ and $u = 1$

- C4: Continuous nonlinear controller (CNGSC):
  $u = \text{sat}(f_1 x_1 + f_2 x_2(1 - |x_1|))$, $f_1 = -6$
  and $f_2 = -3$

The controllers C1 and C4 are tuned such that both closed-loop poles of the linear system are placed at -2. As far as C2 is concerned, only the pole corresponding to the unstable mode can be influenced by the controller and this pole is placed at -2. The switching control law for C3 is given by the following set of equations:

$$u_s = \text{sgn}\left(\begin{bmatrix} -1 & 1 \end{bmatrix} x\right)$$

$$\tilde{x}_0 = x + u_s x_{e+} = \begin{bmatrix} \tilde{x}_{0_1} \\ \tilde{x}_{0_2} \end{bmatrix}$$

$$\tilde{x} = \begin{bmatrix} \left(\frac{\tilde{x}_{0_1}}{\tilde{x}_{0_2}}\right)^{\frac{\lambda_1}{\lambda_2 - \lambda_1}} & 0 \\ 0 & \left(\frac{\tilde{x}_{0_1}}{\tilde{x}_{0_2}}\right)^{\frac{\lambda_2}{\lambda_2 - \lambda_1}} \end{bmatrix} \tilde{x}_0$$

$$\delta = \text{sgn}(\|x_{e+}\| - \|\tilde{x}\|)$$

$$u = \begin{cases} u_s & \text{if } \delta = 0 \\ u_s\,\delta & \text{if } \delta \neq 0 \end{cases} \tag{7.38}$$

Three of the five properties mentioned in the introduction, i.e. 1) global stability, 2) local performance, and 3) chattering behavior (avoiding large AC losses) are analysed for these four controllers.

7.2.2.1 Global stability

In Figure 7.2, the evolution of the closed-loop trajectories for the initial condition $x_0 = \begin{bmatrix} -0.8 & 2.8 \end{bmatrix}^T$ is illustrated. This initial condition is not in the region of attraction $\mathcal{A}$ of C1 and therefore the corresponding trajectory leaves the null controllable region $\mathcal{C}$ and escapes to infinity. However, all the other controllers are globally stable with $\mathcal{A} = \mathcal{C}$ and thus the corresponding trajectories converge to the origin.

Figure 7.2: Phase diagram. The lines $\partial\mathcal{L}_+$ and $\partial\mathcal{L}_-$ are the borders of the non-saturated region of controller C4.

7.2.2.2 Local performance

In Figure 7.3, the evolution of the trajectories of all controllers for the initial condition $x_0 = \begin{bmatrix} 0.7 & 2.8 \end{bmatrix}^T \in \mathcal{C}$ is shown. It is seen that the trajectory of controller C2 first goes towards the x_2 axis since only the unstable state x_1 is fed back. Then, convergence to the origin is ensured via the open-loop dynamics of the stable state.

The time evolution of the two states is shown in Figure 7.4. For controller C2, the unstable state is damped quickly. However, the damping of the stable state takes a long time. The best time performance for both states is given by the time-optimal controller C3. The controller C4 needs more time to damp the states but does better than C1. For initial conditions that are located nearer the origin, the performance of C4 and C1 is similar.

7.2.2.3 Chattering in the control signal

For this example, pseudo-random white noise disturbance is added to the measurements of the state variables. Figure 7.5 shows the control signal u for all controllers. It is seen that the control signals of C1, C2 and C4 show no chattering behavior since they are generated by continuous controllers. However, the control signal of C3 shows chattering when the state is near the origin (after $t = 3.9[s]$). Chattering is also present during the switching from $u = -1$ to $u = 1$ at $t = 1.826 \ldots 1.833$ [s] (Figure 7.6).
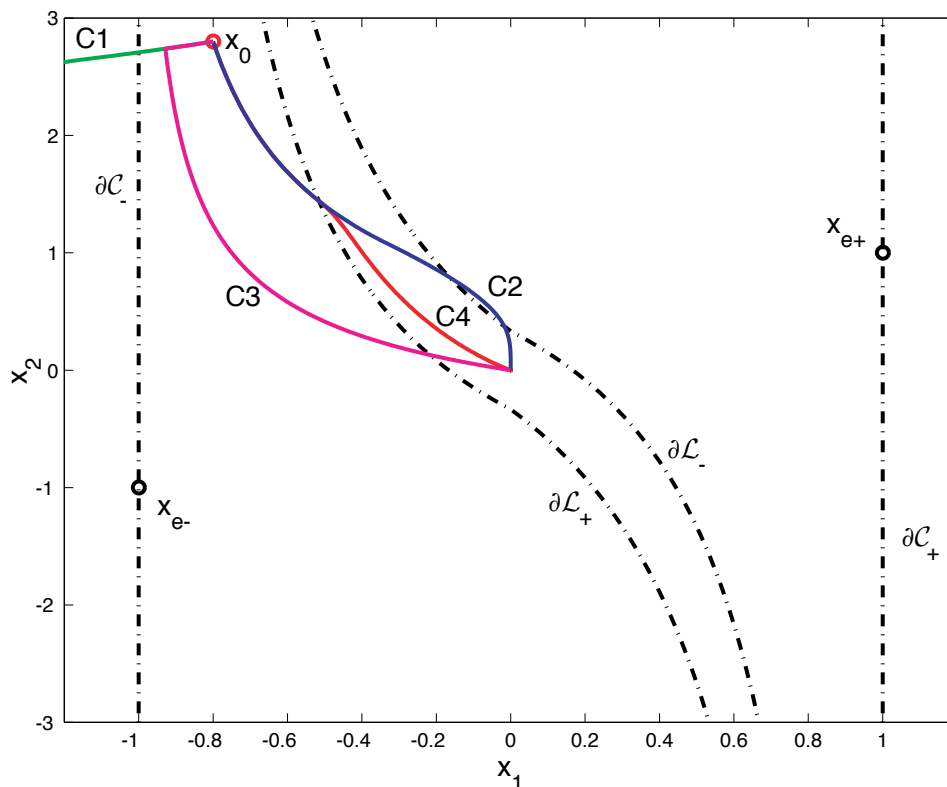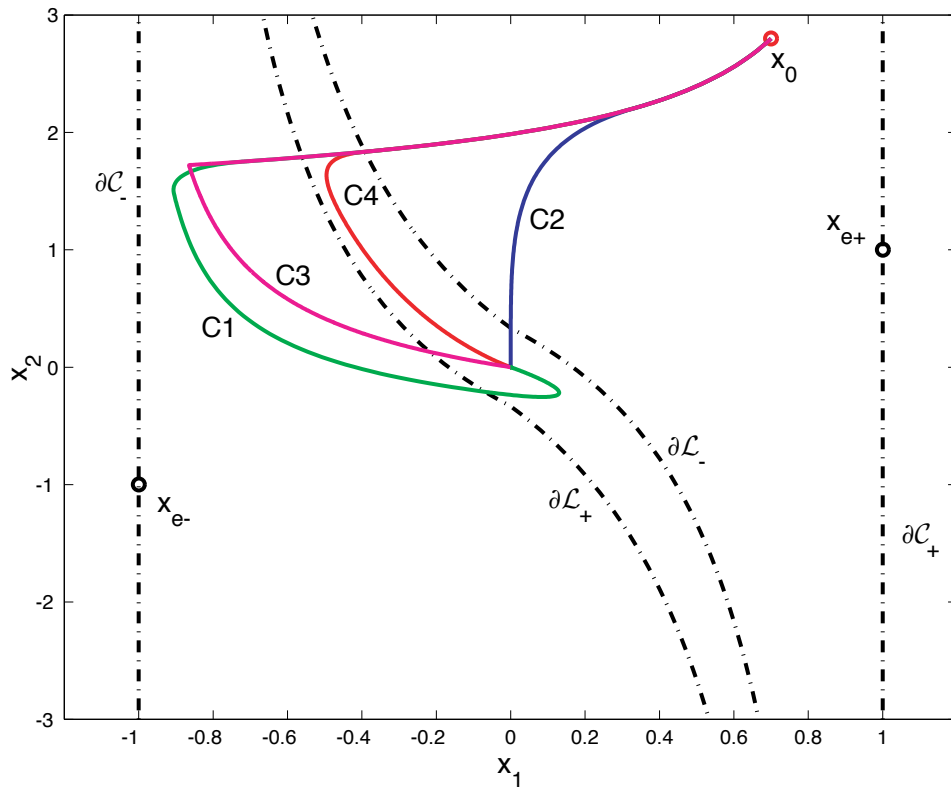
Figure 7.3: Phase diagram. The lines $\partial\mathcal{L}_+$ and $\partial\mathcal{L}_-$ are the borders of the non-saturated region of controller C4.
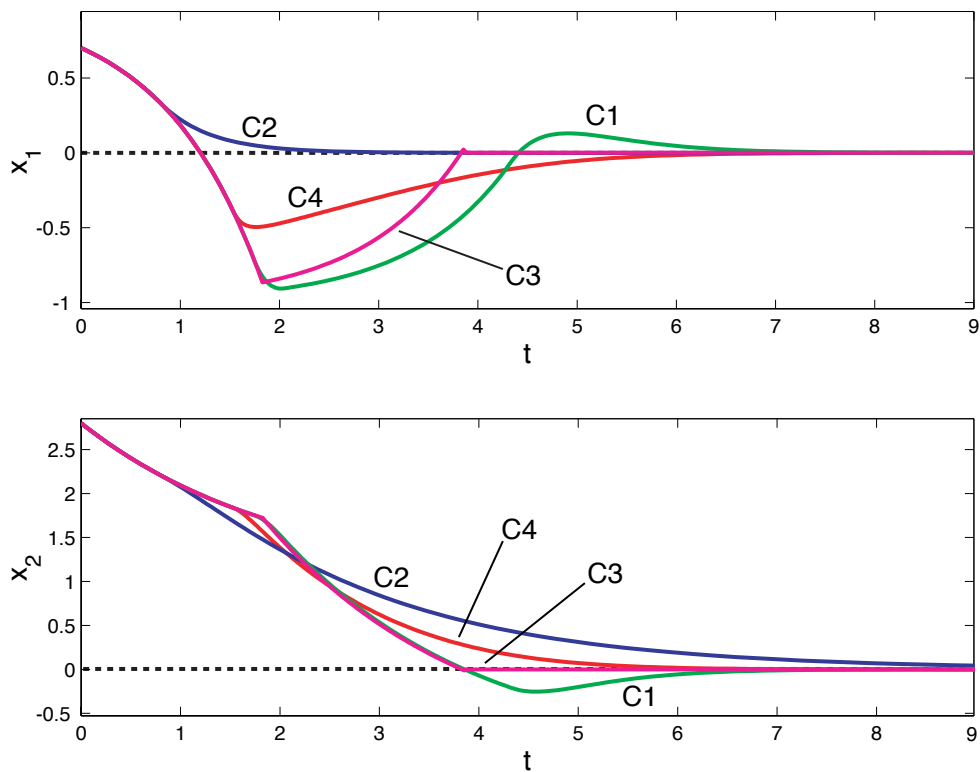
Figure 7.4: Time evolution of x_1 and x_2.
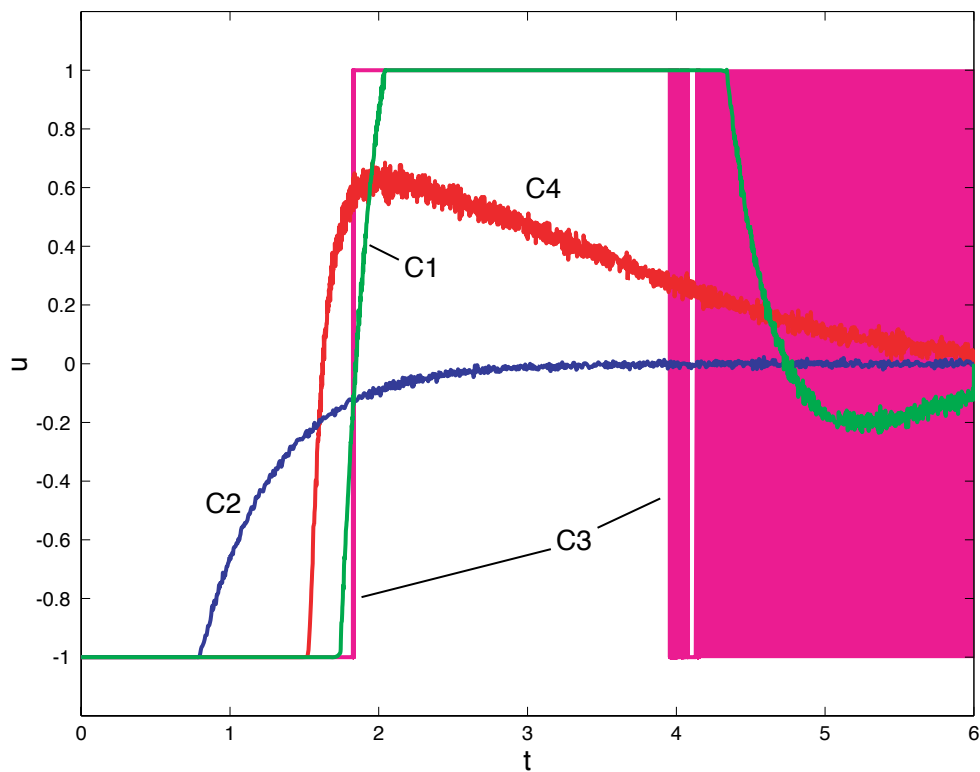
Figure 7.5: Time evolution of the input u.
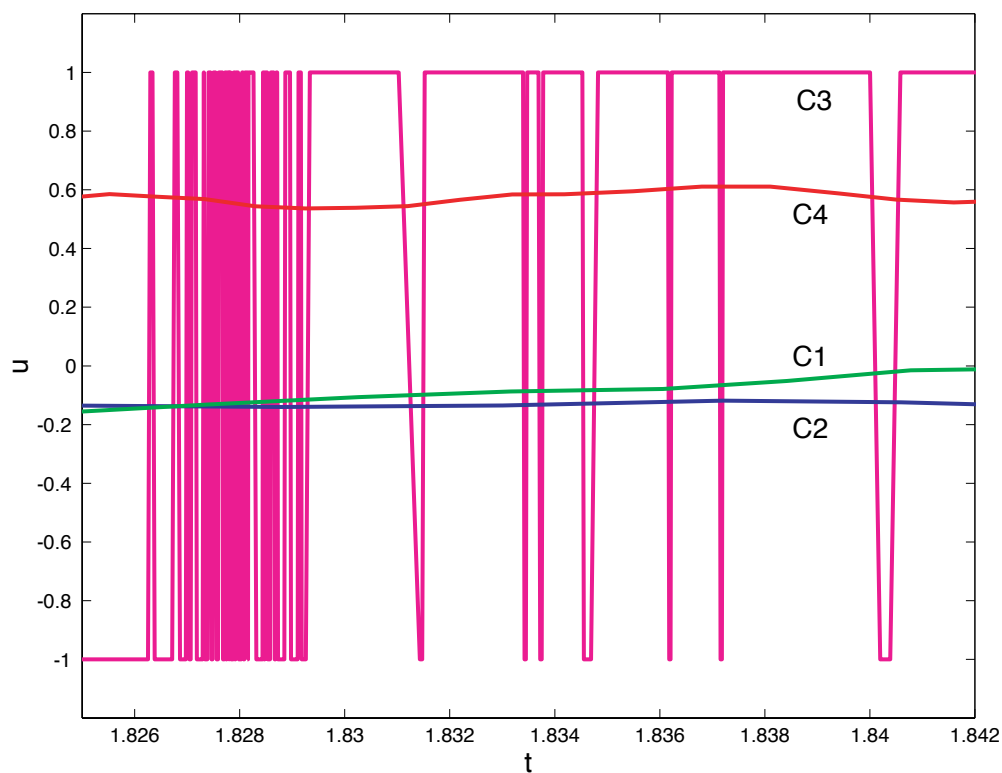
Figure 7.6: Time evolution of the input u (zoomed: $t = 1.826 \ldots 1.833$ [s]).

7.3   CNGSC controller for higher order systems

In the extension of the nonlinear controller (7.21) to higher order systems (System 7.1), the idea is to push all the terms except $f_1 x_1$ to zero as $|x_1| \to 1$. This is done by the following modification:

$$\tilde{u}(x) = f_1 x_1 + k(x)(f_2 x_2 + f_3 x_3 + \ldots + f_n x_n) \tag{7.39}$$

and

$$k(x) = 1 - |x_1| \tag{7.40}$$

or

$$k(x) = 1 - x_1^2 \tag{7.41}$$

The reason for using the same $k(x)$ to push each of the terms $f_2 x_2, f_3 x_3, \ldots, f_n x_n$ to zero is due to the fact that the system without saturation ($u = \tilde{u}$) and with a constant $k \in [0, 1]$ can be proven to be stable.

Proposition 5 *Consider (7.4) along (7.39)*

$$u(x) = f_1 x_1 + \bar{k}(f_2 x_2 + f_3 x_3 + \ldots + f_n x_n) \tag{7.42}$$

where $\bar{k} \in [0, 1]$ is fixed. If $1 + f_1 < 0$ and $A + bf$ is Hurwitz then the feedback system is stable for any $0 \le \bar{k} \le 1$.

Proof: Consider only the feedback $u = f_1 x_1$. This leads to the closed loop state matrix

$$\bar{A} = A + bf_1 x_1 = \begin{bmatrix} \lambda_1(1 + f_1) & 0 \\ b_s f_1 & A_s \end{bmatrix}. \tag{7.43}$$

By construction $\bar{A}$ is stable.
Now, consider the input-output system

$$\dot{x} = \bar{A}x + b\bar{u} \tag{7.44}$$
$$\bar{y} = -\bar{f}x$$

where $\bar{f} = \begin{bmatrix} 0 & f_2 & f_3 & \ldots & f_n \end{bmatrix}$. This system is open loop stable since $\bar{A}$ is stable. Let the open-loop transfer function of (7.44) be denoted by

$$\frac{\bar{Y}(s)}{\bar{U}(s)} = L(s). \tag{7.45}$$

Consider the closed-loop system

$$\dot{x} = \bar{A}x + b\bar{f}\bar{k}x = Ax + bu(x) \tag{7.46}$$

which can be considered as the closed loop system with $L(s)$ and $\bar{k}$ in the loop. Since $L(s)$ is stable and the closed-loop system is stable with $\bar{k} = 1$ (this is due to $A + bf$ being Hurwitz) the Nyquist plot of $L(s)$ does not encircle $(-1, 0)$ in the complex plane. Thus, there exists **no** $\omega \in \mathbb{R}$ for which the following two conditions are satisfied

$$|L(j\omega)| > 1 \quad \text{and} \quad \angle L(j\omega) = \pm\pi. \tag{7.47}$$

It can be seen that for $0 \leq \bar{k} \leq 1$ we have $|\bar{k}L(j\omega)| \leq \bar{k}|L(j\omega)| \leq |L(j\omega)|$ and $\angle(\bar{k}L(j\omega)) = \angle L(j\omega)$. Thus, from (7.47) there exists **no** $\omega \in \mathbb{R}$ for which both conditions

$$|\bar{k}L(j\omega)| > 1 \quad \text{and} \quad \angle(\bar{k}L(j\omega)) = \pm\pi \tag{7.48}$$

are satisfied implying that the Nyquist plot of $\bar{k}L(s)$ does not encircle $(-1, 0)$. Therefore, since $\bar{k}L(s)$ is stable the closed-loop system (7.46) is stable for every $0 \leq \bar{k} \leq 1$. ∎

Of course this proposition does not constitute a proof of the global stability of the closed loop system with saturation. But it is an interesting property encouraging the search for a formal stability proof. Another promising fact is that all simulations done until now have revealed themselves to be stable. Simulation results with linear systems (linear tokamak models) are given in Chapter 9.

7.4 Conclusion

In this chapter, a simple continuous nonlinear globally stabilising controller, referred to as CNGSC, for the stabilisation of linear planar systems with one unstable pole and a single saturated input was proposed. The main idea was to modify an existing linear controller by incorporating a nonlinear term into the control law. A formal proof that the controller is globally stabilising, i.e. the region of attraction is equivalent to the null controllable region, was provided for slightly more conservative conditions. It was shown that the controller satisfies the desired performance locally around the origin. Furthermore, since this controller is a continuous function of the state, chattering and oscillations in the control signal are avoided which diminishes the AC losses.

We showed that the extension of the CNGSC controller to higher order systems is straightforward. But the quest for a formal proof of the global closed-loop stability is highly complicated in this case. Therefore, the global stability of higher order closed-loop systems is illustrated by means of simulations (provided in Chapter 9). Nevertheless, we have provided an interesting property encouraging the search for a formal stability proof in the future.

Chapter 8

Tokamak control

8.1 Introduction

This chapter is devoted to the problem of applying the CNGSC (provided in Chapter 7) to tokamaks. In general, we assume, for the controller design phase, a tokamak closed-loop system consisting of a linearised tokamak model with several saturated inputs and two input-output controllers. There are a slow controller which is responsible for the plasma shape control (SC controller) and a fast controller which is responsible for the vertical plasma position stabilisation control (VC controller) and which ensures the so-called "vertical plasma position" stability. Although the terminology varies from one tokamak to another, this property is common to ITER, JET, MAST and TCV.

The goal of this thesis is to improve the stability properties of the tokamak closed-loop system in the sense of increasing its region of attraction to the null controllable region (Chapter 7). Since in general only the VC controller is responsible for the stability of the closed-loop system we focus only on the improvement of this controller. Therefore, we limit the application of the CNGSC controller to the VC control part.

Section 8.2 provides a survey of the main ideas discussed in this chapter. Section 8.3 deals with the structure of the tokamak closed-loop system and shows on which points particular attention has to be paid when the input-output controllers are designed. Furthermore, since the CNGSC controller is a state feedback controller we discuss the problems and the modifications that have to be taken into consideration when migrating from an input-output controller to a state feedback controller. We provide a scheme which describes a way to transform any tokamak closed-loop system into a normalised closed-loop system. This transformation will allow us to apply the results of Chapter 7 straightforwardly for the design of the CNGSC controller. Section 8.4 is devoted to the state reconstruction procedure which represents a crucial step if we are seeking a well conditioned state feedback controller. Furthermore, we show that for the CNGSC controller it is sufficient to provide an accurate reconstruction of solely the unstable state, while a reconstruction of all stable states is not required. In Section 8.5 we discuss the problems and provide solutions linked to the output tracking of reference signals with a nonlinear state feedback controller. An elementary study of the effect of disturbances on the tokamak closed-loop system is provided in Section 8.6. We will show that during a disturbance it is practically impossible to predict whether the closed-loop system is still stable or if the control has been lost. Nevertheless, we will suggest possibilities to improve stability during disturbances by slightly modifying the CNGSC controller. Section 8.7 is devoted to resulting detrimental effects on stability when a pure delay or a limited bandwith are

added to the closed-loop system. Pragmatic solutions to avoid these detrimental effects on the CNGSC controller will therefore be suggested.

8.2 Survey of concepts for the application of a state feedback controller

The analysis of the tokamak closed-loop system and the application of a nonlinear state feedback controller can become complex if we want to take into account simultaneously the analysis of both controllers, the reference signal problem and the link between the nonlinear tokamak plant and the linearised tokamak model. This complexity can lead to a loss of the overall view of the general ideas discussed in this chapter. Therefore we start with a simple survey which summarises the important concepts for this chapter.

For what follows we will deal with i) the nonlinear tokamak plant (tokamak in operation) or model and with ii) the linear tokamak model which is derived from the nonlinear tokamak plant or model at an equilibrium point. The equilibrium point at which the linear tokamak model is derived is referred to as the linearisation equilibrium. Figure 8.1 a) illustrates the considered closed-loop system containing the nonlinear tokamak plant (tokamak in operation) or model while Figure 8.1 b) shows the considered closed-loop systemt containing the linear tokamak model.
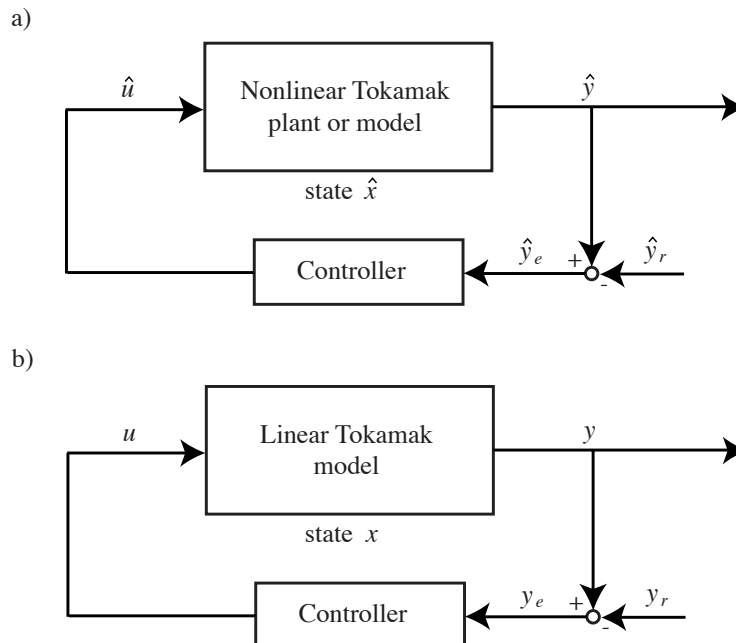
Figure 8.1: Illustration of the nonlinear tokamak plant or model closed-loop system a) and the linear tokamak model closed-loop system b) with its signals and states.

We define in a generalised manner the link between the closed-loop system containing the nonlinear tokamak plant or model and the closed-loop system containing the linear tokamak model by defining the generalising variable s which stands for any signal (e.g. y, u, y_r or y_e) or state (e.g. x). The notation $\hat{s}$ represents the signals and states corresponding to the closed-loop system with the nonlinear tokamak plant or model, while the notation s represents the signals and states corresponding to the closed-loop system with the

linearised tokamak model. The relation between both closed-loop systems is given by

$$\hat{s} = s_0 + s + \epsilon_s(s), \tag{8.1}$$

where s_0 denotes the signals and states at the linearisation equilibrium and $\epsilon_s(s)$ the error due to the linearisation, referred to as the linearisation error. If the nonlinear tokamak plant is at the linearisation equilibrium then we have $\hat{s} = s_0$, $s = 0$ and $\epsilon_s(s) = \epsilon_s(0) = 0$. This means that in the closed-loop system with the linear tokamak model all states and signal are at zero when the closed-loop system with the nonlinear tokamak plant is at the linearisation equilibrium s_0. Furthermore, the error $\epsilon_s(s)$ due to the linearisation is evidently zero at the linearisation equilibrium s_0. Since in general a linear model is only valid at the linearisation equilibrium s_0 the correspondence of the linear tokamak model to the nonlinear tokamak plant is more and more degraded as $\hat{s}$ moves away from the linearisation equilibrium s_0. This implies that the error $\epsilon_s(s)$ is increased as a function of the distance $\parallel \hat{s} - s_0 \parallel$. When nothing is specified we consider that $\hat{s}$ is in the neighborhood of s_0 such as the error $\epsilon_s(s)$ is small. In this case we assume that the error is negligible and consider $\epsilon_s(s) = 0$.

The notation $\bar{\hat{s}}$ is used to denote an equilibrium of the closed-loop system containing the nonlinear tokamak plant or model, while the notation $\bar{s}$ is used to denote an equilibrium of the closed-loop system containing the linear tokamak model.

A survey of the generalised notation is given in Table 8.1

	Closed-loop system with nonlinear tokamak model	Closed-loop system with linear tokamak model
Signals and states	$\hat{s}$	s
Equilibrium	$\bar{\hat{s}}$	$\bar{s}$
Linearisation equilibrium	s_0	$-$

Table 8.1: Generalised signal and state notation.

Consider a tokamak closed-loop system with a simplified nonlinear tokamak plant and a sole simplified linear controller (Figure 8.2 a)). It is assumed that the nonlinear tokamak plant can be modelled by means of the nonlinear system

$$\dot{\hat{x}} = a(\hat{x}) + b(\hat{u}) \tag{8.2}$$
$$\hat{y} = c(\hat{x}),$$

where $\hat{x} \in \mathbb{R}^n$ denotes the states, $\hat{u} \in \mathbb{R}^k$ the tokamak inputs and $\hat{y} \in \mathbb{R}^m$ the tokamak outputs and where we consider the nonlinear functions $a : \mathbb{R}^n \rightarrow \mathbb{R}^n$, $b : \mathbb{R}^k \rightarrow \mathbb{R}^n$ and $c : \mathbb{R}^n \rightarrow \mathbb{R}^m$.

Note that nonlinear codes for tokamaks like the DINA code (Chapter 2) cannot be formulated with the structure specified in System (8.2). There exists a simplified nonlinear model, referred to as CREATE, which is expressed as System (8.2). But due to the simplification it does not possess the ability to reproduce accurately every nonlinearity of a tokamak in operation or of the DINA code. We therefore assume that an ideal (perfect) model could exist for the purpose of demonstrating rigorously which problems linked to the control of nonlinear systems can be encountered.

For this section we consider a simplified stabilising linear input-output controller consisting of a $k \times m$ static gain matrix K, i.e.

$$\hat{u} = K\hat{y}_e = K(\hat{y} - \hat{y}_r),\tag{8.3}$$

where $\hat{y}_r \in \mathbb{R}^m$ denotes the reference signal and $\hat{y}_e$ the error between the outputs and the references. If we consider the closed-loop system

$$\dot{\hat{x}} = a(\hat{x}) + b\left(K(c(\hat{x}) - \hat{y}_r)\right),\tag{8.4}$$

then $\hat{y}_r$ constitutes the input of the closed-loop system.
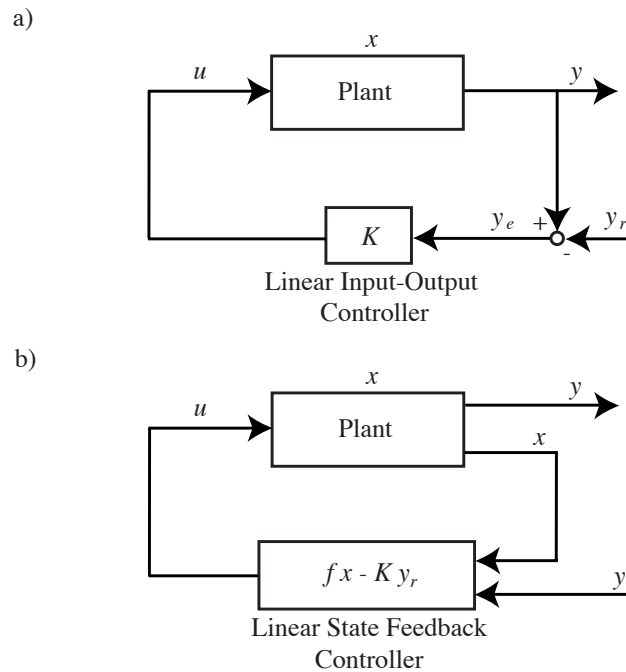
Figure 8.2: Illustration of the difference between a closed-loop system with a linear input-output controller a) and a closed-loop system with a linear state feedback controller b).

For what follows we assume that due to the controller K the closed-loop system is stable. Thus, when $\hat{y}_r$ is varying then we assume that the output $\hat{y}$ approximately follows the reference in the sense that only a small error $\hat{y}_e$ remains. Furthermore, we assume that for any constant reference $\hat{y}_r = \bar{\hat{y}}_r = $ const the system converges to an equilibrium. An equilibrium point, denoted as $\bar{\hat{x}} = $ const, is reached when $\dot{\hat{x}}$ of the closed-loop system (System (8.4)) is zero. The equilibrium point $\hat{x} = \bar{\hat{x}}$ is therefore deduced by solving the equation

$$\dot{\hat{x}} = 0 = a(\bar{\hat{x}}) + b\left(K(c(\bar{\hat{x}}) - \hat{y}_r)\right)\tag{8.5}$$

for $\bar{\hat{x}}$ as a function of $\hat{y}_r = \bar{\hat{y}}_r = $ const. Straightforwardly, we can deduce from System (8.2) the output corresponding to this equilibrium, defined as $\bar{\hat{y}} = c(\bar{\hat{x}})$. Of course, strictly speaking these assumptions are not valid for any nonlinear system. But practice has shown that for tokamak control purposes these assumptions are always satisfied. Note that if the reference is changed, for example by means of a step variation, then the state does not transit instantaneously to the new equilibrium, but there is a transitory phase of

which the duration depends on the closed-loop system dynamics. Theoretically, the state converges to the equilibrium when the time converges to infinity

$$\lim_{t \to \infty} \hat{x}(t) = \bar{\hat{x}}.$$

In practice we consider that the state has reached the new equilibrium when the error $\hat{y}_e$ is small enough for the control purpose or smaller then the noise amplitude.

Once an equilibrium is reached we can derive a linearised tokamak model. We define such an equilibrium as the linearisation equilibrium for which its corresponding state is denoted as x_0, its input as u_0, its output as y_0 and its reference as y_{r_0}. The resulting linear model is described by the system

$$\dot{x} = Ax + Bu \tag{8.6}$$
$$y = Cx.$$

There exists several linearised tokamak models, e.g. RZIP and CREATE-L (see Section 4). The RZIP model is derived from experimental data of tokamak discharges, while CREATE-L is derived from the nonlinear CREATE model described as System (8.2).

Since the considered controller is linear the control law for the closed-loop system with the linear model is the same

$$u = Ky_e = K(y - y_r), \tag{8.7}$$

where the closed-loop system is given by

$$\dot{x} = (A + BKC)x - BKy_r. \tag{8.8}$$

In general, controllers are designed by means of the linear model. Thus, the desired stability and performance of the closed-loop system with the full nonlinear tokamak is only valid when $\hat{s}$ is located in the neighborhood of s_0. In practice, it turns out that input-output controllers are robust enough to ensure stability and acceptable performance even if the tokamak plant follows nonlinear dynamics, i.e the ramp-up and ramp-down phases of a discharge. Thus, if we design the controllers at a linearisation equilibrium during the flat-top phase, they usually work well for the whole discharge. This handling is simple and may work well for input-output controllers, but for state feedback controllers, especially when nonlinearities are introduced as for the CNGSC controller, we are faced with new problems. These problems are discussed in the next section.

8.2.1 State feedback controller for the nonlinear tokamak model

8.2.1.1 Linear approximation to the output function

The substitution of the output equation $\hat{y} = c(\hat{x})$ of System (8.2) in the input-output controller law described by Equation (8.3) leads to

$$\hat{u} = K\hat{y}_e = Kc(\hat{x}) - K\hat{y}_r. \tag{8.9}$$

The nonlinear function $Kc(\hat{x})$ can be interpreted as the nonlinear state feedback part. But since there is no nonlinear model available, $c(\hat{x})$ is not known. We therefore have

to derive the state feedback controller by using $y = Cx$ of the linear tokamak model described by System (8.6) which leads to

$$\hat{u} = KC\hat{x} - K\hat{y}_r = f\hat{x} - K\hat{y}_r, \tag{8.10}$$

where $f = KC$ represents the linear state feedback gain matrix. The resulting closed-loop system (Figure 8.2 b)) is given by

$$\dot{\hat{x}} = a(\hat{x}) + b\left(f\hat{x} - K\hat{y}_r\right) \tag{8.11}$$

and the equilibrium $\hat{x} = \bar{\hat{x}}$ is therefore deduced by solving the equation

$$\dot{\hat{x}} = 0 = a(\bar{\hat{x}}) + b\left(f\bar{\hat{x}} - K\hat{y}_r\right) \tag{8.12}$$

for $\bar{\hat{x}}$.

The use of the linear $C\hat{x}$ instead of the nonlinear $c(\hat{x})$ might be considered as an approximation. But since the feedback gain K is designed by means of the linear model at its linear equilibrium $\hat{s}_0$, we can say that we do the same for the design of the state feedback controller. Thus, similarly to the linear input-output controller, the linear state feedback controller (8.10) might work well for the whole discharge.

8.2.1.2   State reconstruction

A more serious problem is due to the fact that in general, as opposed to the output $\hat{y}$, the state $\hat{x}$ is not directly measurable. Thus, a state reconstruction is required. For this purpose we might implement classic dynamic observers like the Luenberger observer [58] and the Kalman filter observer [15, 41]. But, for the tokamak plant a state reconstruction relying on a static observer seems to be more convenient (see Section 8.4). In the nonlinear model case this can be achieved by seeking for an approximated inverse function of the output equation $\hat{y} = c(\hat{x})$. This can represent a difficult duty to solve when the model possesses more than 50 state variables. It is therefore preferable to use the output equation of the linear model $y = Cx$ and approximate the inverse function by the least square error method with the pseudo-inverse matrix of C for the tokamak (see Section 8.4). This leads to the state reconstruction

$$\breve{x} = C^\dagger y \tag{8.13}$$

for the linear model and to

$$\breve{\hat{x}} = C^\dagger \hat{y} \tag{8.14}$$

for the nonlinear model or plant. In Section 8.4 we will show, by applying the proposed state reconstruction to experimental data from TCV, that the reconstruction is surprisingly accurate for the whole discharge, even during the ramp-up and the ramp-down. This might be interpreted as though $c(\hat{x})$ contains only weak nonlinearities. Thus, for what follows we assume that the state reconstruction is ideal (perfect) by imposing the equivalences

$$\hat{x} = \breve{\hat{x}} \qquad \text{and} \qquad x = \breve{x}. \tag{8.15}$$

Therefore, by assuming an accurate state reconstruction, we might again assume that the linear state feedback given by Equation (8.10) works well for the whole discharge, i.e. for any equilibrium $\bar{\hat{s}}$.

8.2.1.3 The state error

In general, when a linear state feedback controller is designed we assume that the equilibrium of the closed-loop system is at the origin, i.e. $\bar{\hat{x}} = 0$. For the cases where the equilibrium is not at the origin $\bar{\hat{x}} \neq 0$ (which is always the case for tokamaks) we introduce a state error $\hat{x}_e$ between the instantaneous state $\hat{x}$ and the equilibrium $\bar{\hat{x}}$, i.e.

$$\hat{x}_e = \hat{x} - \bar{\hat{x}}. \tag{8.16}$$

Thus, the linear state feedback control law (Equation 8.10)) can be expressed as a linear function of $\hat{x}_e$ which is given by

$$\hat{u} = f\hat{x}_e + f\bar{\hat{x}} - K\hat{y}_r, \tag{8.17}$$

where $f\bar{\hat{x}}$ denotes the offset induced by the equilibrium $\bar{\hat{x}}$. Note that formulating the state feedback control law by means of the state error $\hat{x}_e$ represents a mathematical artifact which permits us to state that when the state $\hat{x}$ converges to the closed-loop equilibrium $\bar{\hat{x}}$ then the state error $\hat{x}_e$ converges to zero. In other words, we can state that the linear state feedback controller works around the equilibrium $\bar{\hat{x}}$. This formulation has not much significance for linear state feedback controllers since it is equivalent to the initial formulation (Equation (8.10)).

Let us turn our attention to nonlinear feedback controllers and denote any general pure continuous nonlinear state feedback controller as

$$u_c = \varphi(x_c), \tag{8.18}$$

where x_c denotes the fed back state and u_c the controller output. The proposed CNGSC controller presented in Chapter 7 possesses two particularities:

1. When the fed back state is at the origin $x_c = 0$ then the controller is equivalent to a linear state feedback controller.

2. When the closed-loop system containing $\varphi(x_c)$ is at an equilibrium $\hat{x} = \bar{\hat{x}}$ then we have to satisfy $x_c = 0$ and $\varphi(0) = 0$. This permits us to obtain the same conceived properties and performances (for example the rejection of disturbances) of the CNGSC controller at any equilibrium $\bar{\hat{x}}$.

We therefore define a class of continuous nonlinear state feedback controllers, denoted as $\mathcal{K}_c$, for which all controllers pertaining to this class possess these particularities. We define the class $\mathcal{K}_c$ as a set of continuous nonlinear state feedback controllers for which each element $\varphi(x_c)$ corresponds to a linear state feedback fx_c at the origin $x_c = 0$, i.e.

$$\lim_{x_c \to 0} \varphi(x_c) = fx_c. \tag{8.19}$$

Thus, any nonlinear state feedback controller $\varphi(x_c)$ belonging to the class $\mathcal{K}_c$ behaves approximately like its corresponding linear controller fx_c in the neighborhood of the origin. Furthermore, to meet the second particularity we state that if $\lim_{t \to 0} \hat{x}(t) = \bar{\hat{x}}$ then $\lim_{t \to 0} x_c(t) = 0$ and $\lim_{t \to 0} \varphi(x_c(t)) = 0$.

The substitution of the linear state controller $f\hat{x}$ by the nonlinear state controller $\varphi(\hat{x})$ in the the control law given by Equation (8.10) leads to the nonlinear control law

$$\hat{u} = \varphi(\hat{x}) - K\hat{y}_r. \tag{8.20}$$

By considering the second particularity we deduce that this control law is only applicable to the closed-loop system equilibrium located at the origin $\bar{\hat{x}} = 0$. Thus, to permit the application of the nonlinear state feedback controller for any equilibrium we have to introduce the state error $\hat{x}_e = \hat{x} - \bar{\hat{x}}$ and substitute $f\hat{x}_e$ by $\varphi(\hat{x}_e)$ in the the control law given by Equation (8.17) which leads to

$$\hat{u} = \varphi(\hat{x}_e) + f\bar{\hat{x}} - K\hat{y}_r. \tag{8.21}$$

We see that, in contrast to linear state feedback controllers, for nonlinear state feedback controllers of the class $\mathcal{K}_c$ the concept of considering the state error $\hat{x}_e$ becomes indispensable.

8.2.1.4 The closed-loop system with nonlinear state feedback

The resulting closed-loop system is given by

$$\dot{\hat{x}} = a(\hat{x}) + b\left(\varphi(\hat{x}_e) + f\bar{\hat{x}} - K\hat{y}_r\right) = a(\hat{x}) + b\left(\varphi(\hat{x} - \bar{\hat{x}}) + f\bar{\hat{x}} - K\hat{y}_r\right). \tag{8.22}$$

Since $\lim_{\hat{x} \to \bar{\hat{x}}} \varphi(\hat{x} - \bar{\hat{x}}) = 0$, the equilibrium $\hat{x} = \bar{\hat{x}}$ is deduced by solving the equation

$$\dot{\hat{x}} = 0 = a(\bar{\hat{x}}) + b\left(f\bar{\hat{x}} - K\hat{y}_r\right) \tag{8.23}$$

for $\bar{\hat{x}}$.

This equilibrium equation is equivalent to the equilibrium equation for the pure linear state feedback controller (Equation 8.12). Thus the equilibrium $\bar{\hat{x}}$ expressed as a function of $\hat{y}_r$ depends on the linear state feedback $f\hat{x}$ and not on the nonlinear state feedback $\varphi(\hat{x})$. Moreover, the reference tracking and the disturbance rejection can be separated in the sense that reference tracking follows the closed-loop dynamics characterised by the linear state feedback $f\hat{x}$ and the rejection of a disturbance follows the dynamics characterised by the nonlinear state feedback $\varphi(\hat{x})$. Of course, this is only valid when the reference $\hat{y}_r$ is varied slowly compared to the reaction velocity of the closed-loop system dynamics.

Consider, as an illustration for this purpose, a variation of the reference from a constant signal $\hat{y}_{r_1} = \bar{\hat{y}}_{r_1}$ to another constant signal $\hat{y}_{r_2} = \bar{\hat{y}}_{r_2}$ by means of a slow varying ramp. Thus, if the closed-loop dynamics is fast compared to the velocity of the varying reference then we can assume that $\|\hat{x}_e\|$ is small so that, due to Condition (8.19), the approximation $\varphi(\hat{x}_e) \approx f\hat{x}_e$ is valid. Thus, the reference tracking follows the closed-loop system dynamics characterised by the linear state feedback, while since $\|\hat{x}_e\|$ is small ($\|\hat{x}_e\| \approx 0$), the performance of the disturbance rejection specified by the nonlinear state feedback $\varphi(\hat{x}_e)$ remains similar even during reference tracking.

The main problem of the control law (8.21) is linked to the fact that we have to derive the equilibrium $\bar{\hat{x}}$ as a function of the reference $\hat{y}_r$. Therefore, the nonlinear Equation (8.23) has to be solved for $\bar{\hat{x}}$ which may not be evident to manage. We show in the next section that this problem does not persist when we constrain the application of the control law (8.21) to a linear tokamak model.

We may summarise the important results of this section as follows:

- The state reconstruction is given by

$$\check{\hat{x}} = C^\dagger \hat{y}.$$

- The control law constituted of the nonlinear state feedback controller is given by

$$\hat{u} = \varphi(\hat{x}_e) + f\bar{\hat{x}} - K\hat{y}_r = \varphi(\hat{x} - \bar{\hat{x}}) + f\bar{\hat{x}} - K\hat{y}_r.$$

- This leads to the closed-loop system

$$\dot{\hat{x}} = a(\hat{x}) + b\left(\varphi(\hat{x}_e) + f\bar{\hat{x}} - K\hat{y}_r\right) = a(\hat{x}) + b\left(\varphi(\hat{x} - \bar{\hat{x}}) + f\bar{\hat{x}} - K\hat{y}_r\right).$$

- Since $\lim_{\hat{x} \to \bar{\hat{x}}} \varphi(\hat{x} - \bar{\hat{x}}) = 0$, we deduce the equilibrium $\hat{x} = \bar{\hat{x}}$ of the closed-loop system by solving the equation

$$\dot{\hat{x}} = 0 = a(\bar{\hat{x}}) + b\left(f\bar{\hat{x}} - K\hat{y}_r\right)$$

  for $\bar{\hat{x}}$.

8.2.2   State feedback controller for the linear tokamak model

All principles developed and discussed in the last section for the nonlinear tokamak model are similar for the linear model (System 8.6). We therefore only summarise the important results which are as follows:

- The state reconstruction is given by

$$\breve{x} = C^\dagger y. \tag{8.24}$$

- The control law constituted of the nonlinear state feedback controller is given by

$$u = \varphi(x_e) + f\bar{x} - Ky_r = \varphi(x - \bar{x}) + f\bar{x} - Ky_r. \tag{8.25}$$

- This leads to the closed-loop system

$$\dot{x} = Ax + B\left(\varphi(x_e) + f\bar{x} - Ky_r\right) = Ax + B\left(\varphi(x - \bar{x}) + f\bar{x} - Ky_r\right). \tag{8.26}$$

- Since $\lim_{x \to \bar{x}} \varphi(x - \bar{x}) = 0$, we deduce the equilibrium $x = \bar{x}$ of the closed-loop system by solving the equation

$$\dot{\bar{x}} = 0 = (A + Bf)\bar{x} - BKy_r \tag{8.27}$$

  for $\bar{x}$.

Since the closed-loop system is stable the eigenvalues of $A + Bf$ are all negative and thus $A + Bf$ is invertible. Therefore, from Equation (8.27), the equilibrium becomes explicitly

$$\bar{x} = (A + Bf)^{-1}BKy_r. \tag{8.28}$$

In practice the reconstruction of the state is exclusively accomplished by means of the nonlinear tokamak plant outputs $\hat{y}$, since there exists no other (e.g. linear model) output data. Thus, if we assume an ideal (perfect) reconstruction, referred to as $\hat{x} = \bar{\hat{x}}$, the reconstruction corresponding to the linear model, referred to as $\breve{x}$, is calculated by

means of Relation (8.1). Since the error $\epsilon_{\breve{x}}(\breve{x})$ is not known we set $\epsilon_{\breve{x}}(\breve{x}) = 0$ which leads to

$$\breve{x} = \hat{x} - x_0 = \hat{\breve{x}} - x_0. \tag{8.29}$$

By means of Relation (8.1) we substitute $\hat{x}$ with $x + x_0 + \epsilon_x(x)$ leading to

$$\breve{x} = x + \epsilon_x(x). \tag{8.30}$$

Thus, an ideal (perfect) reconstruction of the linear tokamak model state $\breve{x} = x$ can only be achieved when the linearisation error $\epsilon_x(x)$ is negligible. Furthermore, from Equation (8.30) the state error becomes

$$x_e = \breve{x} - \bar{x} = x - \bar{x} + \epsilon_x(x) \tag{8.31}$$

and again we may consider $x_e = x - \bar{x}$ only when the linearisation error $\epsilon_x(x)$ is negligible.

From this we conclude that the nonlinear state feedback control law (8.25) usually only works in the neighborhood of the linearisation equilibrium x_0 for which $\epsilon_x(x)$ is negligible. In this case the linear model is valid and we can derive from it an explicit relation (Equation (8.28)) between the state equilibrium $\bar{x}$ signal and the reference signal y_r. Thus, a tracking of the reference signals $\hat{y}_r$ can still be considered, even with a nonlinear state feedback controller. Of course, by considering the nonlinear plant, since a variation of the reference signals $\hat{y}_r = y_0 + y_r$ displaces the linearisation equilibrium x_0 to a new equilibrium $\hat{\bar{x}} = x_0 + \bar{x}$, tracking can only be considered if for the resulting new equilibrium the linear tokamak model is still accurate enough, i.e. the linearisation error $\epsilon_x(x)$ is small. Therefore, tracking works only accurately for small changes of the reference signals $\hat{y}_r$.

For large reference signal changes which result in large equilibrium displacements, e.g. during the ramp-up and ramp-down phases, the linearisation error $\epsilon_x(x)$ might no more be negligible. Thus, when the state is at the equilibrium, i.e $x = \bar{x}$, the state error is no more at the origin but is equal to linearisation error $x_e = \epsilon_x(x)$. In this case, the nonlinear state feedback control $\varphi(x_e)$ possesses, due to the nonlinearities, not the same stability properties as at the equilibrium for which it was designed and the stabilisation of the closed-loop system could fail during a disturbance. Therefore, the use of a linear input-output controller during large equilibrium displacements seems to be indispensable. Subsequently, the control system can be switched into the nonlinear state feedback control law (8.25) once the linearisation equilibrium x_0 is reached (which is usually during the flat-top).

We can also take into consideration the design of control systems with several state feedback controllers, where each controller possesses a different linearisation equilibrium. This permits us to switch between different controllers as a function of the actual value of the closed-loop system state (gain scheduling). In this work we do not focus on such switching control systems. We reduce the analysis to a single state feedback controller with a single linearisation equilibrium.

When a state feedback controller is implemented the adaptation from the closed-loop system with the nonlinear plant to the closed-loop system with the linear model and vice-versa is crucial and is realised by means of Relation (8.1). Figure 8.3 illustrates the implementation scheme of the nonlinear state feedback controller. In general, the adaptation is carried out by removing the values of the linearisation equilibrium to get the controller inputs and by adding the values of the linearisation equilibrium to get the

controller outputs. The input $y = \hat{y} - y_0$ is needed for the state reconstruction and the input $y_r = \hat{y}_r - y_{r_0}$ is needed for reference tracking. The output is obtained by adding the controller output value of the linearisation equilibrium $\hat{u} = u_0 + u$.
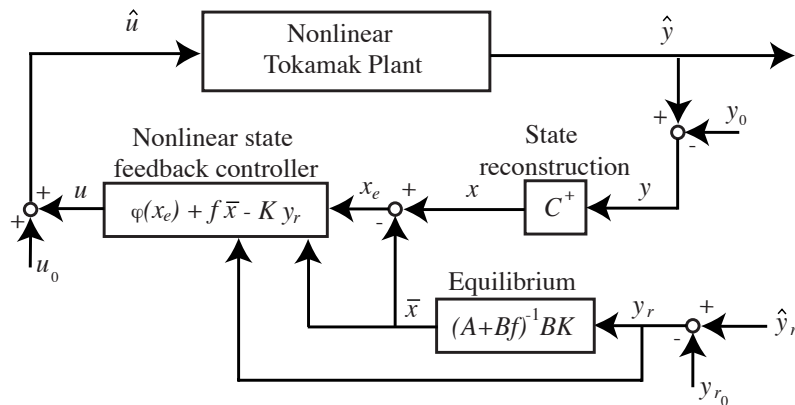
Figure 8.3: Illustration of the closed-loop tokamak system with the implementation scheme.

8.3 Application of the proposed CNGSC controller to the tokamak

The control strategy we propose, relies on the fact that the controller is split into two parts: i) the vertical stabilisation controller (VC), also called the fast controller and ii) the plasma shape controller (SC), also called the slow controller. Figure 8.4 a) shows how the controllers and the tokamak plant are connected together. We assume that only one power supply is devoted to the vertical stabilising control part (VC) since our studies on system stability with saturated inputs is limited, so far, to single saturated input systems. Note that many tokamaks, e.g. ITER, JET, MAST and TCV meet these requirements. For other tokamaks where no particular power supply but several power supplies are devoted for the vertical plasma position stabilisation, the power supplies have to be connected together in such a way that the resulting system becomes equivalent to a single saturated input system.

The following section describes the closed-loop system of a tokamak plant. Note that this description remains valid for each tokamak meeting the requirements mentioned above.

8.3.1 The tokamak closed-loop system

We have to differentiate between two closed-loop systems.

- There is one closed-loop system where the tokamak is represented as a nonlinear dynamic system (Figure 8.4 a)). In general, this nonlinear system can correspond to for 3 different items implying 3 different purposes:

  1. Tokamak in operation (Physical tokamak plant):
     The closed-loop system represents the implementation scheme of the tokamak in operation.
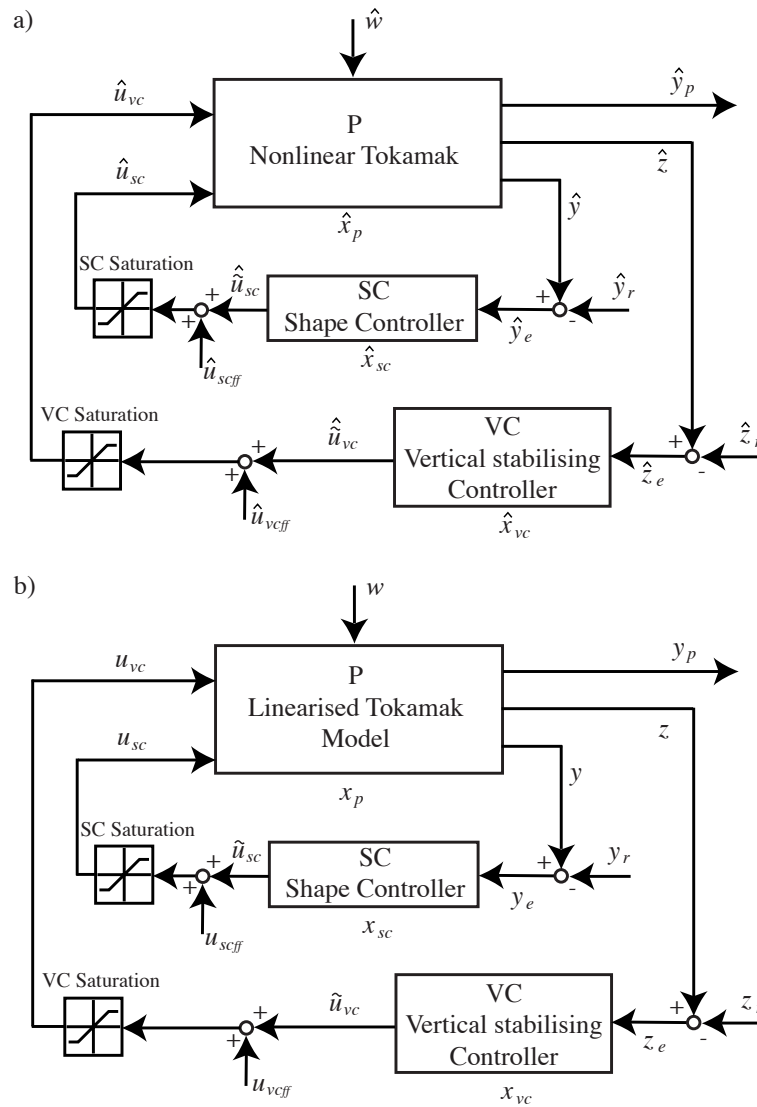
Figure 8.4: Illustration of the closed-loop tokamak system containing the nonlinear toka-mak plant (nonlinear tokamak closed-loop system) a) and containing the linearised toka-mak model (linear tokamak closed-loop system) b).

2. Nonlinear tokamak code, like DINA:
   Such a code permits us to carry out nonlinear simulations. When all relevant properties of a tokamak are well modeled such a nonlinear tokamak simulation should provide results which are close to reality (tokamak in operation). Since such a code possesses a quite complicated structure (see Chapter 2 for the DINA code) it usually is unsuitable for controller design purposes.

3. Nonlinear tokamak model, like CREATE:
   Compared to a tokamak code, such a model possesses a more convenient struc-ture, like the state space model given in System (8.2), and is therefore more appropriated for the analysis of the dynamical nonlinearities of a tokamak and for controller design.

The closed-loop system containing a nonlinear tokamak system is referred to as the **nonlinear tokamak closed-loop system**.

- On the other hand, there is a closed-loop system where the tokamak is represented as a linear dynamical system (Figure 8.4 b)). This linear system represents a linear tokamak model derived at an equilibrium point from experimental data. For tokamaks there exist several linear models, i.e. RZIP and CREATE-L, which are extensively used for the design of controllers.

  The closed-loop system containing a linear tokamak system is referred to as the **linear tokamak closed-loop system**.

All input and output signals of both closed-loop systems are listed in Table 8.2. We may consider the signals and states of the nonlinear tokamak closed-loop system, referred to as $\hat{s}$, as the absolute or real signal and state values since for a tokamak in operation they correspond to the real-time measurements. As already mentioned in Section 8.2 the equilibrium point at which the linear model is derived is defined as the linearisation equilibrium. The signals and states at the linearisation equilibrium are denoted as s_0, while the signals and states for the linear tokamak closed-loop system are denoted as s. This definition permits us to make the link between the nonlinear tokamak system and the linear tokamak system which is given by Relation (8.1), i.e.

$$\hat{s} = s_0 + s + \epsilon_s(s).$$

x_p	Tokamak state variables
x_{sc}	Shape controller state variables
x_{vc}	Vertical stabilising controller state variables
u_{sc}	Tokamak inputs for shape control
u_{vc}	Tokamak input for vertical stabilising control
$\tilde{u}_{sc}$	Shape controller output
$\tilde{u}_{vc}$	Vertical stabilising controller output
$u_{sc_{ff}}$	Feedforward inputs for shape control
$u_{vc_{ff}}$	Feedforward input vertical stabilising control
y_p	Tokamak outputs
y	Tokamak outputs used for shape control
z	Tokamak output used vertical stabilising control
y_r	Reference signal for shape control
z_r	Reference signal for vertical stabilising control
y_e	Error signal for shape control
z_e	Error signal for vertical stabilising control
w	Disturbance input

Table 8.2: Tokamak closed-loop signals.

8.3.1.1 Inputs and outputs of the closed-loop system

In Figures 8.4 a) and b) we consider 5 signals which constitute the inputs and 1 signal constituting the output of the closed-loop system.

There are two feedforward input signals $u_{sc_{ff}}$ and $u_{vc_{ff}}$ and two reference signals y_r and z_r which are solely required for reference tracking purposes, presented in Section 8.5.

As we have shown in Section 8.2, a variation of a closed-loop system input, i.e. for example $u_{sc_{ff}} = \bar{u}_{sc_{ff}} = \text{const} \neq 0$, implies a variation of the closed-loop system equilibrium.

On the other hand, there is the plasma disturbance input, denoted as w. We assume that its mean value or its equilibrium value is fixed to zero $\hat{\bar{w}} = w_0 = \bar{w} = 0$. There is only a variation of this signal during a disturbance, where the variation is equivalent for the nonlinear and the linear tokamak system $\hat{w} = w$. After a disturbance the signal goes back to zero $\hat{w} = w = 0$.

The output of the closed-loop system is referred to as y_p and includes both, the magnetic diagnostic measurements and the plasma parameters. Note that the tokamak outputs y and z are output subsets of y_p. Furthermore, z can be, but has not imperatively to be an output subset of y.

8.3.2   Link between the nonlinear tokamak and the linear tokamak closed-loop systems

In this section we provide rules to which we have to pay attention when we make the link between the nonlinear tokamak closed-loop system and the linear tokamak closed-loop system. Figure 8.4 a) illustrates schematically how the nonlinear tokamak plant and both linear input-output controllers are connected together in operation. Since for the design of both controllers a linear tokamak model is required, we have to choose the time point during the discharge at which we want to derive the linearised model. The state of the tokamak plant and the whole closed-loop at this time point is referred to as the linearisation equilibrium s_0 (definition of the linearisation equilibrium in Section 8.2). The resulting linear tokamak model and its resulting closed-loop is illustrated in Figure 8.4 b).

If at the linearisation equilibrium s_0 the sums of the controller outputs and the feedforward signals $\tilde{u}_{sc_0} + u_{sc_{ff0}}$ and $\tilde{u}_{vc_0} + u_{vc_{ff0}}$ are not zero then there is an offset at the corresponding saturation inputs and thus the saturations are not driven symmetrically. This means that we have to consider asymmetric saturations for the linear tokamak closed-loop system (Figure 8.4 b)). In this case, the upper saturation level is given by $\sigma_{a_u} = \sigma_a - (\tilde{u}_{a_0} + u_{a_{ff0}})$ and the lower saturation level is given by $\sigma_{a_l} = -\sigma_a - (\tilde{u}_{a_0} + u_{a_{ff0}})$ for both, the SC saturation (a=sc) and the VC saturation (a=vc), where with $\sigma_a > 0$ we denote the symmetric upper σ_a and lower $-\sigma_a$ saturation levels. Nevertheless, as we will see in Section 8.3.5, to permit the application of the CNGSC controller (presented in Chapter 7) we assume that the SC power supplies never reach their saturation levels σ_{sc}. Thus, only have to solve the asymmetric saturation problem of the VC power supply. In fact, since the theory presented in Chapter 7 relies on a symmetric input saturation we have to avoid an eventual asymmetric saturation. Usually, we omit any feedforward input voltage by imposing $u_{vc_{ff0}} = 0$. Thus, we only have to cancel the VC controller output voltage $\tilde{u}_{vc_0}$. In general, due to the small coil resistance, particularly if superconducting coils are used, $\tilde{u}_{vc_0}$ is small (a few percent) compared to the saturation level σ_{vc} and the asymmetric component can therefore be neglected. But we can also completely cancel $\tilde{u}_{vc_0}$ either i) by using a pure derivative VC controller (D controller) since the mean output value is zero for such controllers or ii) by adding into the SC controller a supplementary integral controller (I controller) for the controlled tokamak output z. The last proposition will be discussed in Section 8.5.

In general, if we design controllers at the linearisation equilibrium then the desired stability and performance of the closed-loop system is only valid when $\hat{s}$ are located in

the neighborhood of s_0. In practice, it turns out that input-output controllers are robust enough to ensure stability and acceptable performance even if the tokamak plant follows highly nonlinear dynamics, such as during ramp-up and ramp-down phases of a discharge. Thus, if we for example design the controllers at a linearisation equilibrium during the flat-top phase, they usually work well for the whole discharge. This handling may work well for **linear** input-output controllers but we cannot exclude that it might fail for **nonlinear** state feedback controllers. The explanation for this conjecture is discussed in Section 8.2.

We conclude that nonlinear state feedback controllers usually work only in the neighborhood of the linearisation equilibrium s_0. In this case the linearised model is valid and we can derive from the linear model an explicit relation between the state reference signal and the output reference signal. Thus, a tracking of the reference signals $\hat{y}_r$ and $\hat{z}_r$ (Figure 8.4 a)) can still be considered, even with a state feedback controller (detailed discussion in Section 8.5). Of course, since a change of the reference signals displaces the linearisation equilibrium to a new equilibrium, tracking can only be considered if for the resulting new equilibrium the linear tokamak model is still accurate enough. Therefore, tracking works only for small changes of the reference signals. For large reference signals changes which result in large equilibrium displacements, i.e. during the ramp-up and ramp-down phases, tracking with state feedback is probably not possible. Therefore, the use of an input-output controller during such phases seems to be indispensable. Subsequently, the control system can be commuted into the state feedback controller once its corresponding linearisation equilibrium is reached (usually during the flat-top).

We can also take into consideration the design of control systems with several state feedback controllers, where each controller possesses a different linearisation equilibrium. This permits to switch between different controllers as a function of the actual value of the closed-loop system state. In this work we do not focus on such switching control systems. We restrict the analysis to a single state feedback controller with a single linearisation equilibrium.

When a state feedback controller is implemented the adaptation from the closed-loop system with the nonlinear plant to the closed-loop system with the linear model and vice-versa is crucial and is realised by means of Relation (8.1). Figure 8.5 illustrates the implementation scheme of the VC state feedback controller, while the SC controller is assumed to remain an input-output controller. In general, the adaptation is carried out by removing the values of the linearisation equilibrium to get the controller inputs and by adding the values of the linearisation equilibrium to get the controller outputs. In the case of the VC state feedback controller the inputs $y_p = \hat{y}_p - y_{p_0}$ and $z = \hat{z} - z_0$ are needed for the state reconstruction (Section 8.4) and the inputs $y_r = \hat{y}_r - y_{r_0}$ and $z_r = \hat{z}_r - z_{r_0}$ are needed for reference tracking purposes (Section 8.5). The output is obtained by adding the controller output and feedforward input values of the linearisation equilibrium $\tilde{u}_{vc_0}$ and $u_{vc_{ff_0}}$, respectively.

8.3.3 The tokamak closed-loop system for the controller design

For the controller design purpose we consider a tokamak closed-loop system composed of following 3 parts (Figure 8.4 b)).

1. The linear tokamak model:
   The typical tokamak linear model (RZIP or CREATE-L) consists of $50 \ldots 100$ state variables $x_p \in \mathbb{R}^{n_p}$, several Poloidal Field coils and their voltage inputs and several
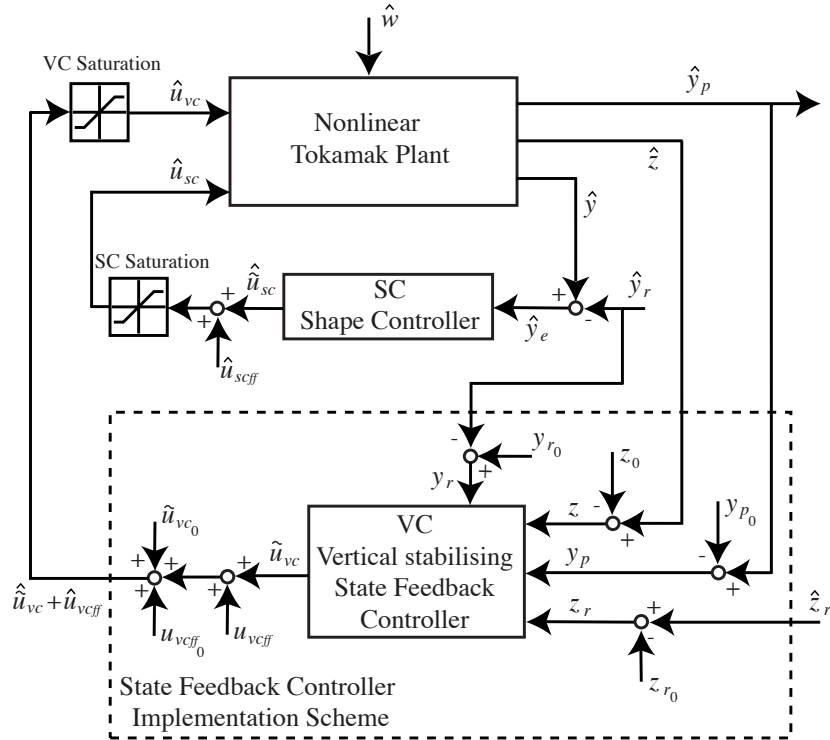
Figure 8.5: Illustration of the closed-loop tokamak system with the implementation scheme for a state feedback controller (dashed box).

outputs $y_p \in \mathbb{R}^{m_p}$. As mentioned before, the inputs are divided into two parts: i) the vertical stabilisation control input $u_{vc} \in \mathbb{R}$ and ii) the plasma shape control input $u_{sc} \in \mathbb{R}^{k_p}$. The physical outputs of a tokamak are the magnetic diagnostic measurements (about 100 sensors). Linear combinations of these magnetic diagnostic measurement outputs represent physical plasma parameters like: the vertical position z and the radial position R of the plasma, some plasma shape parameters like the gaps g between the edge of the plasma and the surrounding plasma facing components (Figure 8.6) and the plasma current I_p. The input $w \in \mathbb{R}^{l_p}$ is the disturbance input for minor disruption, ELM and sawteeth like disturbance simulations. The linear tokamak model is discussed in Chapter 4 and is give by

$$
\begin{aligned}
\dot{x}_p &= A_p x_p + B_{p_{sc}} u_{sc} + B_{p_{vc}} u_{vc} + E_p \dot{w} \\
y_p &= C_p x_p + F_p w \\
y &= C_{p_y} x_p + F_{p_y} w \\
z &= C_{p_z} x_p + F_{p_z} w.
\end{aligned}
\tag{8.32}
$$

Note that the output y_p includes both, the magnetic diagnostic measurements and the plasma parameters. The outputs $y \in \mathbb{R}^{m_{sc}}$ and $z \in \mathbb{R}^{m_{vc}}$ are output subsets of y_p. The outputs y (i.e. z, R, g and I_p) are needed for the plasma shape control, while z is needed for the vertical stabilising control. Usually y and z are referred to as the plasma control parameters. For the stabilising controller usually the vertical position of the plasma z is used and that is why we denote this output as z. But note that we could also use a different output than the vertical plasma position for the vertical stabilisation control. The important thing is that z has to be a single output $z \in \mathbb{R}$. Note that z can be, but has not imperatively to be an output subset
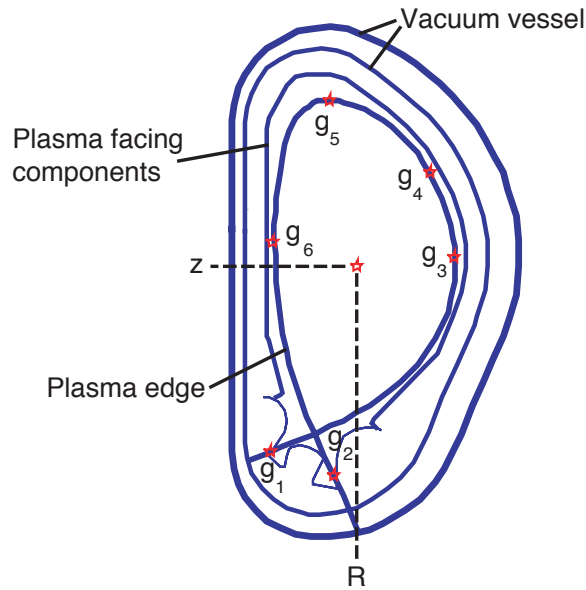
of y.

Figure 8.6: Illustration of the plasma control parameters like the vertical z and radial R positions and the gaps g_1, g_2, ..., g_6.

2. The plasma shape controller and power supplies (SC):
   In general, the plasma shape controller is a low order controller which only controls the slow movement of the plasma equilibrium. There are several inputs $y_e \in \mathbb{R}^{k_{sc}}$ and outputs $\tilde{u}_{sc} \in \mathbb{R}^{m_{sc}}$. Each output drives a single power supply and each power supply possesses a saturation with a saturation level denoted as σ_{sc_i}, where each $i \in 1 \ldots m_{sc}$ corresponds to a power supply. The controller can be any stable and proper system which is described by

$$\dot{x}_{sc} = A_{sc}x_{sc} + B_{sc}y_e \tag{8.33}$$
$$\tilde{u}_{sc} = C_{sc}x_{sc} + D_{sc}y_e.$$

   Note that if we want to implement a PID controller then we have to add a low-pass filter into the derivative part D to satisfy the condition of a proper system.

3. The vertical stabilising controller and power supply (VC):
   Similar to the plasma shape controller the vertical stabilising controller can be any stable and proper system with a single input $y_e \in \mathbb{R}$ and a single output $\tilde{u}_{vc} \in \mathbb{R}$ which is described by

$$\dot{x}_{vc} = A_{vc}x_{vc} + B_{vc}z_e \tag{8.34}$$
$$\tilde{u}_{vc} = C_{vc}x_{vc} + D_{vc}z_e.$$

   In practice, the vertical stabilising controllers are often simple PD or pure D controllers. The single power supply possesses a saturation with a saturation level denoted by σ_{vc}.

Additionally, there are two feedforward input signals $u_{sc_{ff}}$ and $u_{vc_{ff}}$ and two reference signals y_r and z_r in Figure 8.4 a) and b). These signals are solely required for reference tracking purposes, presented in Section 8.5.

8.3.4   SC and VC controller design

The common approach for the design of the SC and VC controllers is as follows. Usually the nonlinearities, i.e. mainly saturation for our purposes, are not considered for the first design since most controller design techniques rest on linear approaches. Moreover, this permits us to analyse the stability of the closed-loop system by means of its eigenvalues. As a first step of the controller design we only consider and elaborate the VC controller. Since it has the property of stabilising the tokamak the eigenvalues of the closed-loop system, mainly composed of the tokamak and the VC controller, have to be without exceptions negative. The next step consists of adding the SC controller with the objective of enhancing the response of the plasma shape movement to a reference demand signal or disturbance. It is obvious that the resulting linear tokamak closed-loop system composed of the tokamak and both controllers (Figure 8.4 b)) has to be stable. But what happens if the VC controller is omitted, i.e. if the closed-loop system is composed of the tokamak and the SC controller only? For this closed-loop system we distinguish three cases depending on the number and the values of occurring unstable eigenvalues (positive eigenvalues). Let us therefore define the unstable eigenvalue(s) of this closed-loop system as $\gamma_{1_{sc}}$, $\gamma_{2_{sc}}, \ldots$ and the single unstable eigenvalue of the tokamak open-loop system as γ_{ol}. The three cases can be described as follows:

1. No unstable eigenvalues or a reduced single unstable value $\gamma_{1_{sc}} < \gamma_{ol}$:
   This means that the SC controller takes fully (no unstable eigenvalue) or partly ($\gamma_{1_{sc}} < \gamma_{ol}$) over the stabilising function. Thus, the separation between vertical stabilising control and the plasma shape control is not complete. The problem that could occur is that saturation could appear on both the SC controller power supplies and the VC controller power supply. Thus, since the SC controller takes fully or partly over the stabilising function we would have to analyse the stability of a closed-loop system with several saturated inputs. But since in this thesis we only consider systems with a single saturated input (e.g. VC controller power supply) we have to avoid that the SC controller stabilises the system. Thus, the SC control design has to be reviewed and modified.

2. More than a single unstable eigenvalue:
   The SC controller adds supplementary unstable modes. This could appear as a benign fact since the integral closed-loop system is stable. But, by considering the input saturation, it has been shown in [27, 28] that the the null controllable region is reduced for each supplementary unstable mode. To be more explicit, it turns out that with input saturation the null controllable region is equal $\mathbb{R}^n$ for a stable system, where n denotes the number of state variables of the closed-loop system. This means that each state variable can evolve in $\mathbb{R}$ implying that there is no control loss possible for a stable system. If the system possesses one unstable eigenvalue then, by adequate state transformation, the null controllable region is limited in one dimension $\mathbb{R}^{n-1} \times (-l_1, l_1)$, where the interval limit $0 < l_1$ depends on the eigenvalue of the unstable pole and on the saturation level. If the state is located outside the null controllable region the control is definitely lost and cannot be restored anymore. For a system with a second unstable eigenvalue the maximal stability region is limited in a supplementary dimension $\mathbb{R}^{n-2} \times (-l_1, l_1) \times (-l_2, l_2)$ and so on. Therefore, since our aim is to improve the vertical stabilising control in the sense of increasing its region of attraction to the null controllable region, the

SC controller has to be again reviewed and modified until supplementary unstable modes are canceled.

3. A single unstable eigenvalue for which $\gamma_{1_{sc}} \approx \gamma_{ol}$:
In this case the SC controller is well conditioned. This is the aim that has to be achieved during the linear controller design phase. Nevertheless, it should be taken care that this apparently well conditioned controller does not result from a combination of both cases 1. and 2., i.e. the SC controller eliminates the original unstable mode of the tokamak but simultaneously introduces a new unstable mode. Therefore, a certain knowledge of how to decouple the vertical stabilising control part from the plasma shape control part is indispensable.

For the purposes of what follows we impose that the SC and VC controllers are well conditioned, i.e. solely the VC controller has an impact on the stabilisation of the closed-loop system.

8.3.5 Transformation of the tokamak closed-loop system

Before the application of the CNGSC controller can be considered we first have to transform the closed-loop system with both input-output controllers to a closed-loop system for which its VC controller is a state feedback controller.

Figure 8.7 a) illustrates the initial tokamak closed-loop system composed of the linearised tokamak model, the input-output SC and VC controllers and their corresponding saturations (identical scheme to Figure 8.4 b)). The linearised tokamak model, the SC controller and the VC controller are described by Equations (8.32) - (8.34), respectively.

8.3.5.1 First transformation step leading to the PSC system

The first transformation step consists of unifying the linearised tokamak model P and the SC controller (blocks enclosed by the dashed frame in Figure 8.7 a)) into a linear system to be controlled by the VC controller, referred to as the PSC system (P model and SC controller unified). For this purpose we assume that the SC controller never saturates its power supplies and thus we remove the SC saturation. Note that in practice the SC power supplies are never or rarely in saturation. Furthermore, even if a SC power supplies saturation occurs then no detrimental consequences on the closed-loop stability have to be feared since we assume that the SC controller is not designed for stabilising purposes.

The linearised tokamak model and the SC controller are connected in a feedback loop structure. Section A.3.1 of the Appendix shows in detail how to calculate the resulting system. By applying these results the PSC system becomes

$$
\begin{bmatrix} \dot{x}_p \\ \dot{x}_{sc} \end{bmatrix} = \begin{bmatrix} A_p + B_{p_{sc}} D_{sc} C_{p_y} & B_{p_{sc}} C_{sc} \\ B_{sc} C_{p_y} & A_{sc} \end{bmatrix} \begin{bmatrix} x_p \\ x_{sc} \end{bmatrix} + \begin{bmatrix} B_{p_{vc}} \\ 0 \end{bmatrix} u_{vc}
$$

$$
+ \begin{bmatrix} E_p + B_{p_{sc}} D_{sc} F_{p_y} \\ B_{sc} F_{p_y} \end{bmatrix} \dot{w} + \begin{bmatrix} B_{p_{sc}} & -B_{p_{sc}} D_{sc} \\ 0 & -B_{sc} \end{bmatrix} \begin{bmatrix} u_{sc_{ff}} \\ y_r \end{bmatrix} \qquad (8.35)
$$

$$
y_p = \begin{bmatrix} C_p & 0 \end{bmatrix} \begin{bmatrix} x_p \\ x_{sc} \end{bmatrix} + F_p w
$$

$$
z = \begin{bmatrix} C_{p_z} & 0 \end{bmatrix} \begin{bmatrix} x_p \\ x_{sc} \end{bmatrix} + F_{p_z} w,
$$
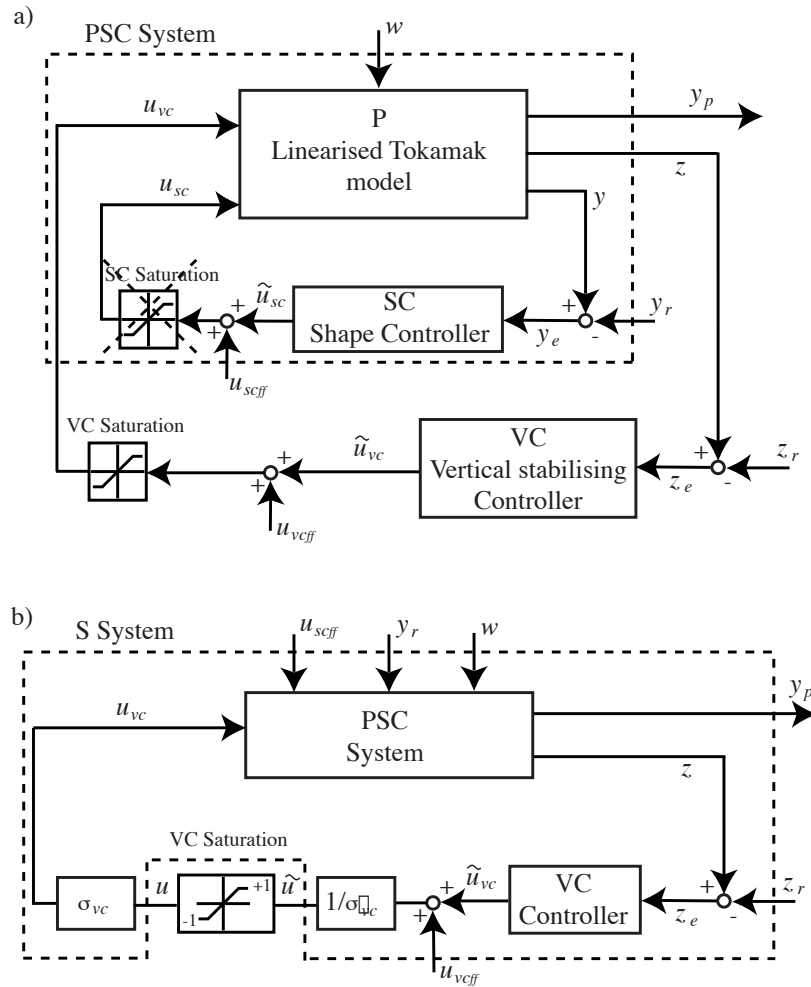
Figure 8.7: Transformation of the tokamak closed-loop system: i) unification of the linearised tokamak model and the SC controller into the PSC system and ii) substitution of the VC saturation by the normalised saturation with a saturation level of 1.

where the resulting tokamak closed-loop system is illustrated in Figure 8.7 b). Furthermore, since the design of the CNGSC controller relies on the normalised saturation function with unity saturation level (Equation 7.5), the saturation of the VC power supplies, for which the saturation level is denoted as σ_{vc}, has to be substituted by the normalised saturation function. The equivalence to the SC saturation is simply achieved by dividing the input and multiplying the output of the normalised saturation with σ_{vc} (Figure 8.7 b)).

8.3.5.2 Second transformation step leading to the S system with state feedback controller

The second major transformation step consists of substituting the input-output VC controller into a state feedback controller. We therefore calculate the transfer function from the normalised saturation output u to its input $\tilde{u}$. The connection of two systems in series is described in detail in Section A.3.2 of the Appendix. The serial connection of the PSC

system and the VC controller results into the S system given by

$$
\begin{bmatrix} \dot{x}_p \\ \dot{x}_{sc} \\ \dot{x}_{vc} \end{bmatrix} = \begin{bmatrix} A_p + B_{p_{sc}} D_{sc} C_{p_y} & B_{p_{sc}} C_{sc} & 0 \\ B_{sc} C_{p_y} & A_{sc} & 0 \\ B_{vc} C_{p_z} & 0 & A_{vc} \end{bmatrix} \begin{bmatrix} x_p \\ x_{sc} \\ x_{vc} \end{bmatrix} + \begin{bmatrix} B_{p_{vc}} \\ 0 \\ 0 \end{bmatrix} \sigma_{vc} u
$$
$$
+ \begin{bmatrix} E_p + B_{p_{sc}} D_{sc} F_{p_y} \\ B_{sc} F_{p_y} \\ B_{vc} F_{p_z} \end{bmatrix} \dot{w} + \begin{bmatrix} B_{p_{sc}} & -B_{p_{sc}} D_{sc} & 0 \\ 0 & -B_{sc} & 0 \\ 0 & 0 & -B_{vc} \end{bmatrix} \begin{bmatrix} u_{sc_{ff}} \\ y_r \\ z_r \end{bmatrix}
$$
$$
y_p = \begin{bmatrix} C_p & 0 & 0 \end{bmatrix} \begin{bmatrix} x_p \\ x_{sc} \\ x_{vc} \end{bmatrix} + F_p w \tag{8.36}
$$
$$
\tilde{u} = \frac{1}{\sigma_{vc}} \begin{bmatrix} D_{vc} C_{p_z} & 0 & C_{vc} \end{bmatrix} \begin{bmatrix} x_p \\ x_{sc} \\ x_{vc} \end{bmatrix} + \frac{1}{\sigma_{vc}} D_{vc} F_{p_z} w + \begin{bmatrix} \frac{1}{\sigma_{vc}} & -\frac{1}{\sigma_{vc}} D_{vc} \end{bmatrix} \begin{bmatrix} u_{vc_{ff}} \\ z_r \end{bmatrix}.
$$

We substitute

$$
x_s = \begin{bmatrix} x_p \\ x_{sc} \\ x_{vc} \end{bmatrix} \qquad \text{and} \qquad q = \begin{bmatrix} u_{sc_{ff}} \\ u_{vc_{ff}} \\ y_r \\ z_r \end{bmatrix} \tag{8.37}
$$

which permits us to reformulate System (8.36) more conveniently as

$$
\begin{aligned}
\dot{x}_s &= A_s x_s + b_s u + E_s \dot{w} + B_{s_{ff,r}} q \\
y_p &= C_s x_s + F_s w \\
\tilde{u} &= \tilde{C}_s x_s + \tilde{F}_s w + \tilde{D}_{s_{ff,r}} q,
\end{aligned} \tag{8.38}
$$

where $x_s \in \mathbb{R}^n$.

The resulting tokamak closed-loop system is illustrated in Figure 8.8 a). The state output matrix $\tilde{C}_s$ can be interpreted as a state feedback controller. Because of the disturbance w and the matrix F_p we have to add a disturbance feedback part denoted as $\tilde{F}_s$. Note that the disturbance w can be interpreted as a state of the system as we will see in Section 8.4 in which the state reconstruction is discussed. We therefore define the state feedback gain as $f_s = \begin{bmatrix} \tilde{C}_s & \tilde{F}_s \end{bmatrix}$ and the state feedback results in

$$
\tilde{u} = \begin{bmatrix} \tilde{C}_s & \tilde{F}_s \end{bmatrix} \begin{bmatrix} x_s \\ w \end{bmatrix} + \tilde{D}_{s_{ff,r}} q = f_s \begin{bmatrix} x_s \\ w \end{bmatrix} + \tilde{D}_{s_{ff,r}} q. \tag{8.39}
$$

Note that when the equilibrium of the closed-loop system is located at the origin, all feedforward inputs and references are cancelled, i.e. $u_{vc_{ff}} = 0$ and $z_r = 0$ (see Section 8.5 for the detailed reference tracking discussion). In this case we can express the resulting control law as a pure state feedback controller without the additionally inputs $u_{vc_{ff}}$ and z_r

$$
\tilde{u} = \begin{bmatrix} \tilde{C}_s & \tilde{F}_s \end{bmatrix} \begin{bmatrix} x_s \\ w \end{bmatrix} = f_s \begin{bmatrix} x_s \\ w \end{bmatrix}. \tag{8.40}
$$
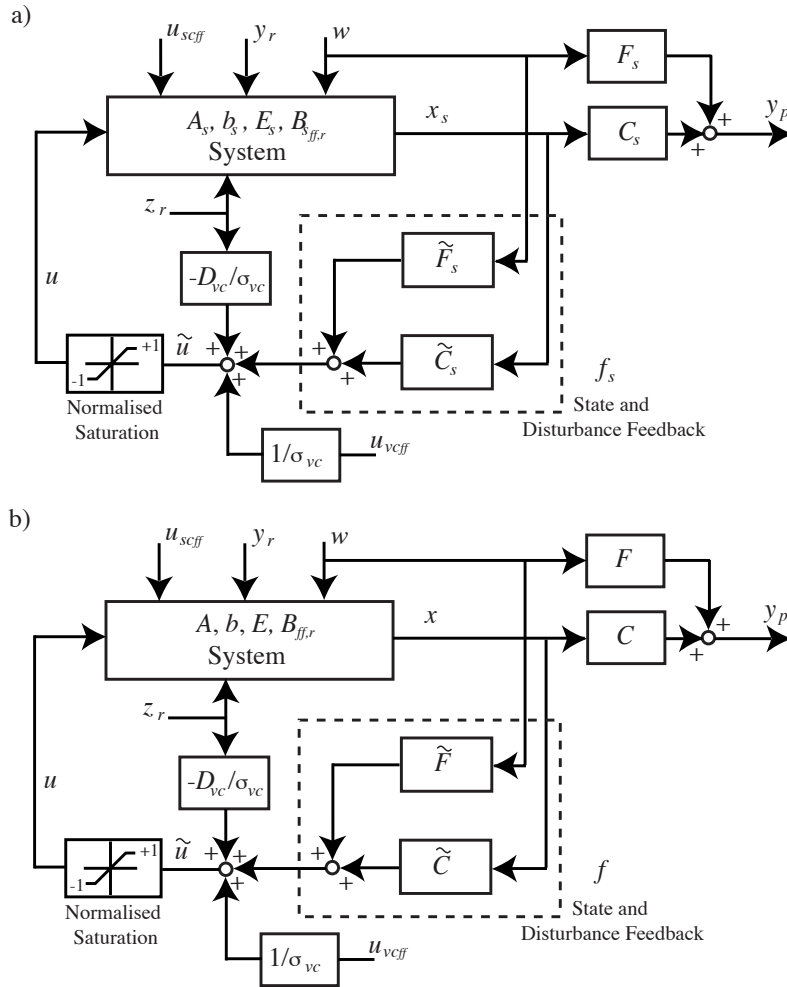
Figure 8.8: Transformation of the tokamak closed-loop system into a closed loop system with state feedback controller.

8.3.6 Application of the proposed CNGSC controller

For the application of the CNGSC controller presented in Chapter 7 we still have to transform the S system described by Equation (8.38) into the normalised system given by Equations (7.1)-(7.3). This is achieved by the linear state transformation

$$x = T^{-1}x_s. \tag{8.41}$$

The resulting normalised system is defined as

$$
\begin{aligned}
\dot{x} &= Ax + bu + E\dot{w} + B_{ff,r}q \\
y_p &= Cx + Fw \\
\tilde{u} &= \tilde{C}x + \tilde{F}w + \tilde{D}_{ff,r}q,
\end{aligned}
\tag{8.42}
$$

where

$$
\begin{aligned}
A &= T^{-1}A_sT, \quad b = T^{-1}b_s, \quad E = T^{-1}E_s, \quad B_{ff,r} = T^{-1}B_{s_{ff,r}} \\
C &= C_sT, \quad F = F_s, \quad \tilde{C} = \tilde{C}_sT, \quad \tilde{F} = \tilde{F}_s \quad \text{and} \quad \tilde{D}_{ff,r} = \tilde{D}_{s_{ff,r}}.
\end{aligned}
$$

Figure 8.8 b) illustrates the resulting normalised closed-loop system.

The linear transformation matrix T is derived by means of a modified eigenvalue and eigenvector decomposition where we impose that the diagonal elements of matrix A are the real parts of the eigenvalues of A_s (and thus A) such that

$$
A = T^{-1} A_s T = \begin{bmatrix}
\lambda_1 & 0 & 0 & \cdots & 0 & 0 & \cdots & 0 \\
0 & \lambda_2 & 0 & \cdots & 0 & 0 & \cdots & 0 \\
0 & 0 & \lambda_3 & \cdots & 0 & 0 & \cdots & 0 \\
\vdots & \vdots & \vdots & \ddots & \vdots & \vdots & \vdots & \vdots \\
0 & 0 & 0 & \cdots & \lambda_r & \mu_r \nu_r & \cdots & 0 \\
0 & 0 & 0 & \cdots & -\mu_r/\nu_r & \lambda_r & \cdots & 0 \\
\vdots & \vdots & \vdots & \vdots & \vdots & \vdots & \ddots & \vdots \\
0 & 0 & 0 & \cdots & 0 & 0 & \cdots & \lambda_{n_c}
\end{bmatrix}, \tag{8.43}
$$

where $\lambda_1 > 0$ is the unstable pole and $0 > \lambda_2 \geq \lambda_3 \geq \ldots \geq \lambda_{n_c}$ are the real parts of the stable poles, where $n_c \leq n$. Conjugate complex pole pairs (i.e. $\lambda_r \pm j\mu_r$) are represented as square submatrices, where $\nu_r \in \mathbb{R}$ can be an arbitrary chosen value. Furthermore,

$$
b = T^{-1} b_s = \begin{bmatrix} \lambda_1 & \lambda_2 & \lambda_3 & \cdots & b_{r_1} & b_{r_2} & \cdots & \lambda_{n_c} \end{bmatrix}^T, \tag{8.44}
$$

where b_{r_1}, b_{r_2} and also ν_r are given by imposing $A^{-1}b = \begin{bmatrix} 1 & 1 & \ldots & 1 \end{bmatrix}$. Note that this imposition cannot be accomplished when there are elements of b_s which are zero. In this case the corresponding elements of b can be kept to zero. In fact, to allow the application of the proposed CNGSC controller, the normalisation is only important for the first element of b_s describing the input linked to the unstable state. If we want to stabilise the S system then this element inevitably has to be nonzero and thus imposing $A^{-1}b = \begin{bmatrix} 1 & e_2 & e_3 & \ldots & e_n \end{bmatrix}$, where $e_2, e_3, \ldots, e_n \in \mathbb{R}$ is always realisable and sufficient for our purpose.

Similarly to the S system (Equation 8.38) the state output matrix $\tilde{C}$ is interpreted as a state feedback controller. Again we have to add the part due to the disturbance input w and for which $\tilde{F}$ represents the disturbance feedback and we therefore again interpret the disturbance w as a state of the system (see Section 8.4). We define the state feedback gain as

$$
f_x = \begin{bmatrix} f_1 & f_2 & \ldots & f_n \end{bmatrix} = \tilde{C}
$$

and the disturbance feedback gain as

$$
f_w = \begin{bmatrix} f_{w_1} & f_{w_2} & \ldots & f_{w_{l_p}} \end{bmatrix} = \tilde{F}.
$$

Since the disturbance input has to be added to the feedback we define an extended state feedback controller given by

$$
\tilde{u} = \begin{bmatrix} \tilde{C} & \tilde{F} \end{bmatrix} \begin{bmatrix} x \\ w \end{bmatrix} + \tilde{D}_{ff,r} q = \varrho \left(\begin{bmatrix} x \\ w \end{bmatrix} \right) + \tilde{D}_{ff,r} q, \tag{8.45}
$$

where

$$
\varrho \left(\begin{bmatrix} x \\ w \end{bmatrix} \right) = \begin{bmatrix} f_x & f_w \end{bmatrix} \begin{bmatrix} x \\ w \end{bmatrix} = f_1 x_1 + f_2 x_2 + f_3 x_3 + \ldots + f_n x_n + f_w w \tag{8.46}
$$

denotes the linear state feedback control. We might also design the state feedback controller without the disturbance part $f_w w$. But this evidently results in a closed-loop

system which is no longer equivalent to the initial tokamak closed-loop system with the input-output VC controller (Figure 8.7 a)).

Similarly to what was discussed in Section 8.2 we introduce the state error

$$\begin{bmatrix} x_e \\ w_e \end{bmatrix} = \begin{bmatrix} x \\ w \end{bmatrix} - \begin{bmatrix} \bar{x} \\ \bar{w} \end{bmatrix}, \tag{8.47}$$

where $\begin{bmatrix} \bar{x} & \bar{w} \end{bmatrix}^T$ denotes the equilibrium of the linear closed-loop system. By substituting $\begin{bmatrix} x & w \end{bmatrix}^T = \begin{bmatrix} x_e & w_e \end{bmatrix}^T + \begin{bmatrix} \bar{x} & \bar{w} \end{bmatrix}^T$ in Equation (8.45) the linear extended state feedback control law becomes

$$\tilde{u} = \varrho \left(\begin{bmatrix} x \\ w \end{bmatrix} \right) + \tilde{D}_{ff,r} q \tag{8.48}$$

$$= \varrho \left(\begin{bmatrix} x_e \\ w_e \end{bmatrix} \right) + \begin{bmatrix} f_x & f_w \end{bmatrix} \begin{bmatrix} \bar{x} \\ \bar{w} \end{bmatrix} + \tilde{D}_{ff,r} q.$$

By considering the results provided in Section 8.2 we migrate from the linear control law given by Equation (8.48) to a control law containing the nonlinear state feedback $\varphi(x)$ pertaining to the class $\mathcal{K}_c$. We therefore apply the nonlinear control law given by Equation (8.25) straightforwardly which leads to

$$\tilde{u} = \varphi \left(\begin{bmatrix} x_e \\ w_e \end{bmatrix} \right) + \begin{bmatrix} f_x & f_w \end{bmatrix} \begin{bmatrix} \bar{x} \\ \bar{w} \end{bmatrix} + \tilde{D}_{ff,r} q. \tag{8.49}$$

The nonlinear state feedback $\varphi(x)$ represents the CNGSC controller (Chapter 7) which is given by

$$\varphi \left(\begin{bmatrix} x \\ w \end{bmatrix} \right) = f_1 x_1 + k(x)(f_2 x_2 + f_3 x_3 + \ldots + f_n x_n + f_w w), \tag{8.50}$$

with the nonlinear function

$$k(x) = 1 - x_1^2 \qquad \text{or} \qquad k(x) = 1 - |x_1|. \tag{8.51}$$

Since

$$\lim_{x_1 \to 0} k(x) = 1 \tag{8.52}$$

we obtain

$$\lim_{x_1 \to 0} \varphi \left(\begin{bmatrix} x \\ w \end{bmatrix} \right) = \begin{bmatrix} f_x & f_w \end{bmatrix} \begin{bmatrix} x \\ w \end{bmatrix}, \tag{8.53}$$

which confirms that $\varphi(x)$ belongs to the class $\mathcal{K}_c$.

It is left for us to derive the equilibrium point

$$\begin{bmatrix} \bar{x} \\ \bar{w} \end{bmatrix},$$

where we only have to worry about $\bar{x}$ since we assume that $\bar{w} = 0$ (Section 8.3.1.1). Furthermore, the concept of considering the error $\begin{bmatrix} \bar{x}_e & \bar{w}_e \end{bmatrix}^T$ and the equilbrium $\begin{bmatrix} \bar{x} & \bar{w} \end{bmatrix}^T$

has only been introduced to permit variations of the feedforward inputs and the reference signals, denoted as q, without deteriorating the rejection of disturbances. Thus, the equilibrium $\bar{x}$ has to be completely decoupled from w and therefore has to be uniquely derived as a function of q, and not as a function of the disturbance, i.e. $w = 0$. Moreover, we assume that the variation of q does not drive the output of the controller $\tilde{u}$ into saturation. With these assumptions, we consider the closed-loop System (8.42) by substituting $u = \tilde{u}$ and $w = 0$ which leads to

$$\dot{x} = (A + b\tilde{C})x + (B_{ff,r} + b\tilde{D}_{ff,r})q. \tag{8.54}$$

The equilibrium $\bar{x}$ is reached when the condition $\dot{x} = 0$ is satisfied. Thus, by solving for x the equilibrium is given by

$$\bar{x} = -(A + b\tilde{C})^{-1}(B_{ff,r} + b\tilde{D}_{ff,r})q. \tag{8.55}$$

Remarks:
The controller results given in Chapter 7 claim that for stability purposes the condition

$$f_1 + 1 < 0 \tag{8.56}$$

has to be satisfied. If this condition is not verified then we have to increase either the gain of the control parameter f_1 or the gain of the VC input-output controller, implying an increase of the f_1 gain.

If we implement the controller given by Equations (8.49)-(8.51) then the physical controller output fed to the tokamak input is $\tilde{u}_{vc}$ and not $\tilde{u}$. Thus, we have to multiply $\tilde{u}$ with the VC saturation level σ_{vc} to get the physical control signal $\tilde{u}_{vc}$.

Up to now, we assumed that the values of the state variables x and the disturbance input w are directly accessible, i.e. the state variables and the disturbance input are measurable. But in practice this is never the case for tokamaks. Therefore, we have to reconstruct the state x and the disturbance w by means of the measurable outputs which are the magnetic diagnostic measurements. We discuss the state and disturbance reconstruction procedure in the next section.

For the implementation of the state feedback controller the reconstructed state $\breve{x}$ and disturbance $\breve{w}$ will be used. Nevertheless, for controller analysis and design purposes we consider an ideal reconstruction procedure for which we assume that the reconstructed state $\breve{x}$ and disturbance $\breve{w}$ are equivalent to the actual state x and disturbance w, i.e.

$$\begin{bmatrix} \breve{x} \\ \breve{w} \end{bmatrix} \equiv \begin{bmatrix} x \\ w \end{bmatrix}. \tag{8.57}$$

8.4   State and disturbance reconstruction

There are 3 different state vectors in the tokamak closed-loop system considered (depicted in Figure 8.4 b)) which are

$$x_s = \begin{bmatrix} x_p \\ x_{sc} \\ x_{vc} \end{bmatrix},$$

where x_p denotes the physical state variables of the linearised tokamak model, x_{sc} the state of the SC controller and x_{vc} the state of the VC controller. Since the SC controller is

implemented explicitly, its state x_{sc} is directly accessible. From this, we have to implement the input-output VC controller in such a way as to provide direct access to its internal state x_{vc}. What remains is to reconstruct the linearised tokamak model state x_p. This can be achieved by means of the standard dynamic observers like Leuenberger and Kalman filter observers as mentioned. For these reconstruction methods the whole linear tokamak model with the $50 \ldots 100$ state variables has to be implemented, increasing considerably the real-time computing time. To avoid this drawback we propose in this section a static reconstruction which rests on the least square error method.

Once all states are reconstructed, referred to as

$$\breve{x}_s = \begin{bmatrix} \breve{x}_p \\ \breve{x}_{sc} \\ \breve{x}_{vc} \end{bmatrix},$$

the reconstructed normalised state is obtained by means of the linear state transformation (Equation (8.41))

$$\breve{x} = T^{-1} \breve{x}_s.$$

Additionally, as discussed in Section 8.3, we have to reconstruct the disturbance input w. By considering the linear tokamak model we can show that the disturbance input w can be handled as a state. We therefore add a disturbance state $x_w = w$ and pure integrator dynamics into System (8.32) (the feedforward inputs and references are not considered here) resulting in the equivalent system

$$\begin{bmatrix} \dot{x}_p \\ \dot{x}_w \end{bmatrix} = \begin{bmatrix} A_p & 0 \\ 0 & 0 \end{bmatrix} \begin{bmatrix} x_p \\ x_w \end{bmatrix} + \begin{bmatrix} B_{psc} \\ 0 \end{bmatrix} u_{sc} + \begin{bmatrix} B_{pvc} \\ 0 \end{bmatrix} u_{vc} + \begin{bmatrix} E_p \\ 0 \end{bmatrix} \dot{w}$$

$$+ \begin{bmatrix} 0 \\ I \end{bmatrix} \dot{w} \qquad\qquad (8.58)$$

$$y_p = \begin{bmatrix} C_p & F_p \end{bmatrix} \begin{bmatrix} x_p \\ x_w \end{bmatrix},$$

where $\dot{w}$ is the time derivative of the disturbance input. With this mathematical artifact we do not have to make a distinction between a state and a disturbance reconstruction. On the contrary, it clearly shows that for the reconstruction the state and the disturbance can be treated equivalently. For what follows we prefer to use the notation

$$\begin{bmatrix} x_p \\ w \end{bmatrix} \qquad \text{instead of} \qquad \begin{bmatrix} x_p \\ x_w \end{bmatrix}.$$

For any state reconstruction, measurable plant outputs have to be available. In the case of the linear tokamak model the output y_p contains two different parts: i) the physical outputs which are the magnetic diagnostic measurements and ii) physical plasma parameters like the vertical position z and the radial position R of the plasma, the gaps g and the plasma current I_p. The plasma parameters are linear combination of the magnetic diagnostic measurements since it is not possible to measure directly the plasma parameters in real-time. Therefore only the magnetic diagnostic measurements are available for the state reconstruction. For what follows we define the magnetic diagnostic output as

$$y_{md} = \begin{bmatrix} B_{pol} \\ \Psi \\ I_{pol} \end{bmatrix} = \begin{bmatrix} C_{md} & F_{md} \end{bmatrix} \begin{bmatrix} x_p \\ w \end{bmatrix} = \begin{bmatrix} C_{B_{pol}} & F_{B_{pol}} \\ C_{\Psi} & F_{\Psi} \\ C_{I_{pol}} & F_{I_{pol}} \end{bmatrix} \begin{bmatrix} x_p \\ w \end{bmatrix}, \qquad (8.59)$$

where B_{pol} denotes the measure of the poloidal magnetic field probes, Ψ denotes the measure of the poloidal flux loops and I_{pol} denotes the currents in the PF coils.

8.4.1 Reconstruction with the least square error method

We consider the linear problem (8.59) for which we seek to solve for $\begin{bmatrix} x_p & w \end{bmatrix}^T$. If we consider the output $y_{md} \in \mathbb{R}^{m_{md}}$, the state $x_p \in \mathbb{R}^{n_p}$ and the disturbance input $w \in \mathbb{R}^{l_p}$ then the least square method can be applied if the condition $m_{md} > n_p + l_p$ is satisfied, i.e. the number of outputs has to be superior to the number of state variables and disturbance inputs together. This condition fits in general since there are about 100 of different magnetic diagnostic measurements, while the linear tokamak model possesses about 50 state variables and the disturbance input is modeled with 2 different inputs. Thus, by applying the least square error method described in Section A.4 of the Appendix the state reconstruction is given by taking the pseudo-inverse of the output matrix of Equation (8.59)

$$\begin{bmatrix} \breve{x}_p \\ \breve{w} \end{bmatrix} = \begin{bmatrix} C_{md} & F_{md} \end{bmatrix}^\dagger y_{md}. \tag{8.60}$$

8.4.1.1 Normalised reconstruction

Since the outputs B_{pol} and Ψ have values which are about 10^5 times smaller than I_{pol} the problem is not well conditioned and the computation of the pseudo-inverse matrix can lead to severe errors in the state reconstruction estimation. We therefore try to normalise the matrix $\begin{bmatrix} C_{md} & F_{md} \end{bmatrix}$ and the output y_{md} with a factor g_n as follows

$$y_{md_n} = \begin{bmatrix} g_n B_{pol} \\ g_n \Psi \\ I_{pol} \end{bmatrix} = \begin{bmatrix} C_{md_n} & F_{md_n} \end{bmatrix} \begin{bmatrix} x_p \\ w \end{bmatrix} = \begin{bmatrix} g_n C_{B_{pol}} & g_n F_{B_{pol}} \\ g_n C_\Psi & g_n F_\Psi \\ C_{I_{pol}} & F_{I_{pol}} \end{bmatrix} \begin{bmatrix} x_p \\ w \end{bmatrix}. \tag{8.61}$$

The objective is to find a g_n which minimises the ratio between the minimal and the maximal value of the elements of C_{md_n} denoted by $C_{md_{n_{ij}}}$

$$\min_{g_n} \left(\frac{\min\limits_{i,j} |C_{md_{n_{ij}}}|}{\max\limits_{i,j} |C_{md_{n_{ij}}}|} \right). \tag{8.62}$$

It is enough to use just the matrix C_{md} for solving the minimisation problem since it is assumed that the structure of F_{md} is similar to that of C_{md}.

8.4.2 Robustness of the reconstruction

Since the proposed least square reconstruction method rests on the pseudo-inverse of both output matrices of the linear tokamak model, we in general assume that the reconstruction is only accurate in the neighborhood of the linear model's linearisation equilibrium (see Section 8.3.2 for the definition of the linearisation equilibrium). In this section we present an elementary study of the robustness of this reconstruction method by analysing the accuracy of the reconstruction when the state of the tokamak plant is steered away from the linearisation equilibrium.

We cannot provide an extensive analysis but we rather focus on a few important plasma parameter variations occurring during a discharge. We therefore restrict the study to the analysis of a varying elongation κ, of a varying vertical plasma position z and during the ramp-up and ramp-down. We additionally consider two similar discharges, where we derive the linear tokamak model by means of one discharge and apply the reconstruction to the other discharge. This allows us to analyse whether the reconstruction method based on one linear tokamak model is robust for similar discharges.

This study was carried out by analysing experimental TCV discharges. The linearised tokamak model was obtained with RZIP. The time at which the linear model was derived from the discharge is defined as the linearisation equilibrium time, denoted as t_0. To avoid the reconstruction of the disturbance input w we assume that no important disturbances occur during the discharges considered. The state reconstruction was done with the normalisation reconstruction, where the normalised pseudo-inverse matrix at t_0 is denoted as $C_0^\dagger$. With this, we obtain a simplified state reconstruction given by

$$\breve{x}_p = C_0^\dagger \, y_{md_n}. \tag{8.63}$$

In Section 8.4.3 we will show that for the CNGSC controller it is sufficient to provide an accurate reconstruction of solely the unstable state, while a reconstruction of all stable states is not required. Therefore, the robustness study is focused on the reconstruction of the unstable state x_1, while the stable states are not taken into consideration.

As mentioned in Section 8.3.4, we assume that in general the SC controller plays only a minor role concerning the stabilisation of the tokamak. In other words, this means that the SC controller has only a limited influence on the unstable state. We therefore neglect the effect of the SC controller on the unstable state, i.e. we assume that the VC controller is totally decoupled from the unstable state. Thus, the transformation of System (8.36) into the normalised system by means of the linear transformation given by Equations (8.41), (8.43) and (8.44) can be solely applied to the linear tokamak model, resulting in

$$x = T^{-1}x_p, \qquad A = T^{-1}A_pT \qquad \text{and} \qquad b = T^{-1}B_{p_{vc}}\sigma_{vc}.$$

With this, the reconstructed value of the unstable state $\breve{x}_1$ can be derived from

$$\breve{x} = T^{-1}\breve{x}_p = T^{-1}C_0^\dagger \, y_{md_n}, \tag{8.64}$$

in which $\breve{x}_1$ is the first state variable of the state vector $\breve{x}$.

For the robustness study the following 3 TCV discharges were considered:

- ♯12868
  With this discharge we analyse the influence of a variation of the elongation κ in the presence of a variation of the plasma current I_p on the state reconstruction. These variations are illustrated in Figure 8.9 where the evolution of following plasma parameters are depicted: the plasma current I_p, the vertical and radial plasma positions z and R, the safety factor q, the elongation κ, the triangularity δ, the ratio between the averaged plasma kinetic pressure and the pressure of the poloidal magnetic field β_p, the ratio between the averaged plasma kinetic pressure and the pressure of the toroidal magnetic field β_t and the internal self inductance l_i. All plasma parameters are derived using the LIUQE reconstruction code [26]. Additionally, the plasma current I_p is computed by means of a trapezoidal integration of the magnetic field measurements B_{pol}, denoted as 'Trapeze' in the figure. This allows us to obtain the plasma current at the beginning and at the end of a discharge when LIUQE is not able to compute any reconstruction.
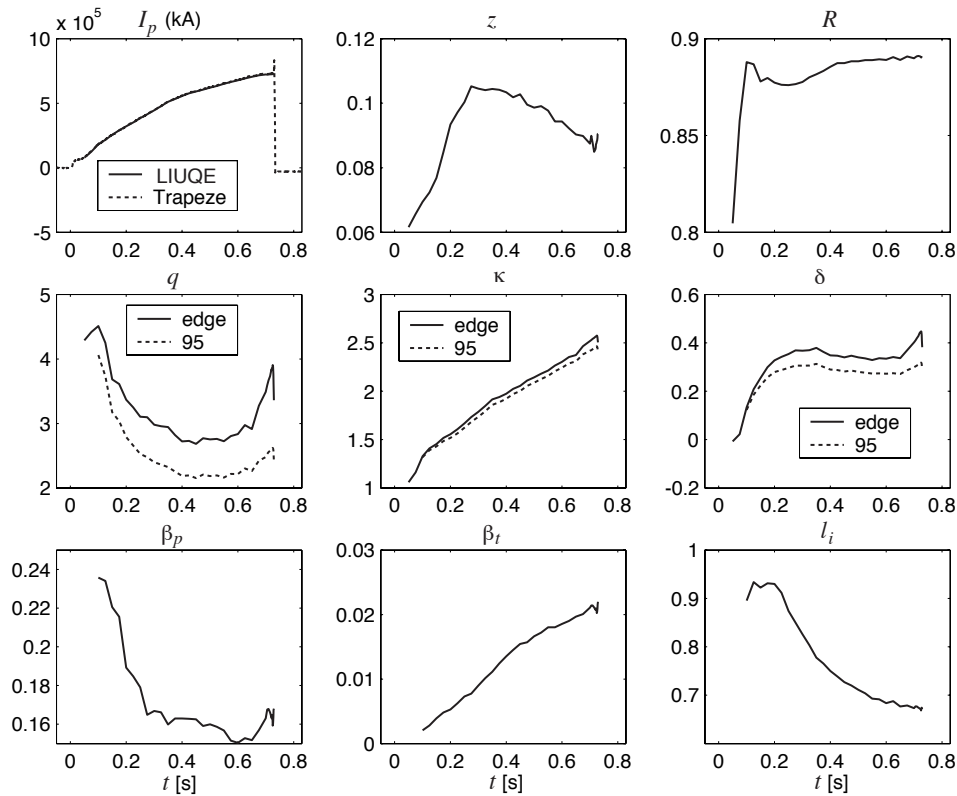
Figure 8.9: The evolution of the plasma parameters of discharge ♯12868

- ♯24377

  By means of this discharge we analyse the influence of a variation of the plasma vertical position z on the state reconstruction. Figure 8.10 depicts the evolution of the same plasma parameters for this discharge.

- ♯24375

  This discharge is similar to the discharge ♯24377 excepted that the plasma vertical position z does not vary. Figure 8.11 depicts the evolution of the plasma parameters for this discharge.

  This discharge is used to obtain the linear tokamak model and the resulting state reconstruction matrix $C_0^\dagger$. The state reconstruction is then applied to the similar discharge ♯24377. This permits us to analyse whether the reconstruction method computed by means of discharge ♯24375 is accurate enough for the similar discharge ♯24377.

  Furthermore, this discharge is used to analyse the robustness of the state reconstruction method during the plasma current ramp-up and the ramp-down.

The analysis of the state reconstruction robustness is done by comparison. Thus, the evolution of the reconstructed states has to be compared to the evolution of states which
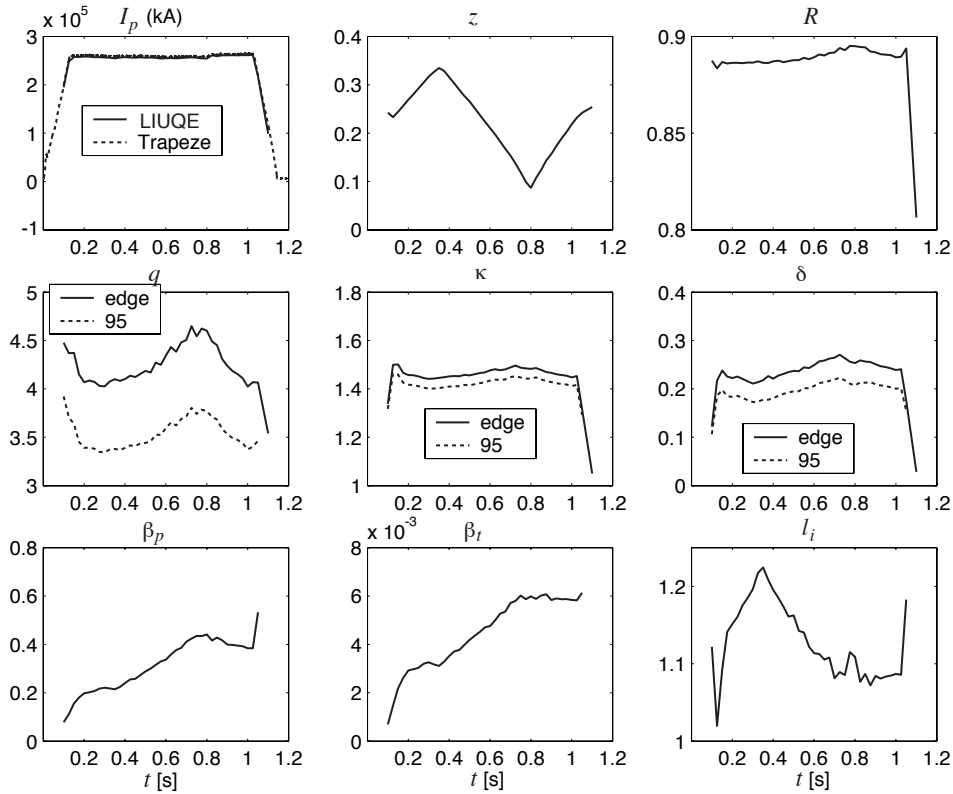
Figure 8.10: The evolution of the plasma parameters of discharge ♯24377

can be considered as a reference. We consider two different state references:

- The LIUQE plasma parameter reconstruction reference:
  We will use the LIUQE reconstruction of the plasma current I_p and of the plasma vertical and radial position z and R, respectively. The linear tokamak model provides the same plasma parameters as outputs, contained in y_p. Since the output of the linear tokamak model is a linear combination of its state x_p (or of the normalised state x be linear transformation) the comparison of these parameters gives a first impression of the state reconstruction accuracy. Moreover, due to the linear combination, it is possible by applying an appropriate linear state transformation to express the plasma parameters I_p, z and R as state variables. This allows us to claim that we can analyse the reconstruction accuracy of 3 state variables. The major problem of LIUQE is that it does not provide the evolution of the unstable state. We therefore have to provide the unstable state reference evolution in another way which is presented next.

- Nonlinear time dependent state reconstruction (NTDSR) reference:
  For the construction of this state reference we apply a piecewise linearisation of the discharge by means of the linear RZIP tokamak model. For this purpose we subdivide the duration of a discharge into discrete time intervals, using t_k with $k \in \mathbb{Z}$, where

$$t_k > t_{k-1} \quad \text{and} \quad \Delta t = t_k - t_{k-1} = \text{const.}$$

The time defining the start of the discharge is denoted as t_{k_s} with $k_s < 0$ and the time defining the end of the discharge is denoted as t_{k_e} with $k_e > 0$. We derive at each
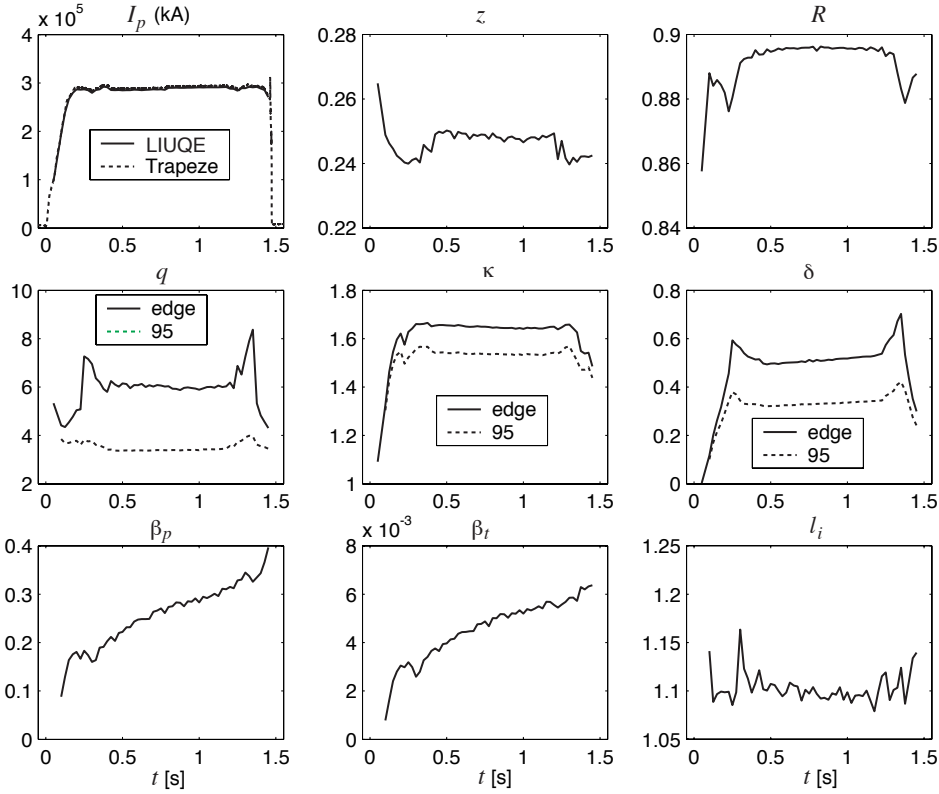
Figure 8.11: The evolution of the plasma parameters of discharge ♯ 24375

time step t_k an RZIP model with which we compute the corresponding normalised pseudo-inverse matrix $C_k^\dagger$. Furthermore, for each time step there corresponds a normalised output

$$y_{p_k} = y_{md_n}(t_k).$$

With y_{p_k} we define the variation of y_{md_n} during Δt by

$$\Delta y_{p_k} = y_{p_k} - y_{p_{k-1}}.$$

Thus, we can reconstruct the variation of the state, denoted as $\Delta \check{x}_{p_k}$, as a linear function of the variation Δy_{p_k}

$$\Delta \check{x}_{p_k} = \check{x}_{p_k} - \check{x}_{p_{k-1}} = C_k^\dagger \, \Delta y_{p_k} = C_k^\dagger \, (y_{p_k} - y_{p_{k-1}}).$$

We assume that the variation Δy_{p_k} is small enough so that the linear model derived at t_k is valid for this variation. In this case the corresponding $C_k^\dagger$ is accurate for the variation Δy_{p_k} implying an accurate state reconstructed variation $\Delta \check{x}_{p_k}$. From this the state reconstructed $\check{x}_{p_k} = \check{x}_p(t_k)$ is obtained by the sum

$$\check{x}_p(t_k) = \check{x}_{p_k} = \sum_{i=k_s+1}^{k} \Delta \check{x}_{p_i} + \check{x}_{p_{k_s}} = \sum_{i=k_s+1}^{k} \left(C_i^\dagger \, (y_{p_i} - y_{p_{i-1}}) \right) + \check{x}_{p_{k_s}}. \qquad (8.65)$$

Since this piecewise linearisation principle follows the time dependent nonlinearities ($C_k^\dagger$ is a function of time) during the discharge, a more accurate state reconstruction is achieved compared to the state reconstruction given by Equation (8.63), i.e.

$$\breve{x}_p(t_k) = C_0^\dagger \, y_{md_n}(t_k). \qquad (8.66)$$

We therefore use this nonlinear time dependent state reconstruction (NTDSR) as a state reference.

By means of these two state references we analyse by comparing the state reconstruction robustness of the following 4 cases:

1. Variation of the elongation κ (discharge $\sharp 12868$)

   The $C_0^\dagger$ matrix is taken at $t_0 = 0.4$ s.

   The comparison of the plasma parameters $\hat{z}$, $\hat{R}$ and $\hat{I}_p$ against the LIUQE and the NTDSR references is depicted in Figure 8.12.
   The reconstruction is very accurate near the linearisation equilibrium at t_0.
   In general the state reconstruction fits well the NTDSR reference during the whole discharge. The maximum error is about 0.5 cm for both z and R. This appears to be acceptable.
   There is a pronounced discrepancy between the LIUQE and the NTDSR references for z and R. Nevertheless, the maximum error between the two references is about 2 cm for z and about 1 cm for R which again appears to be acceptable.
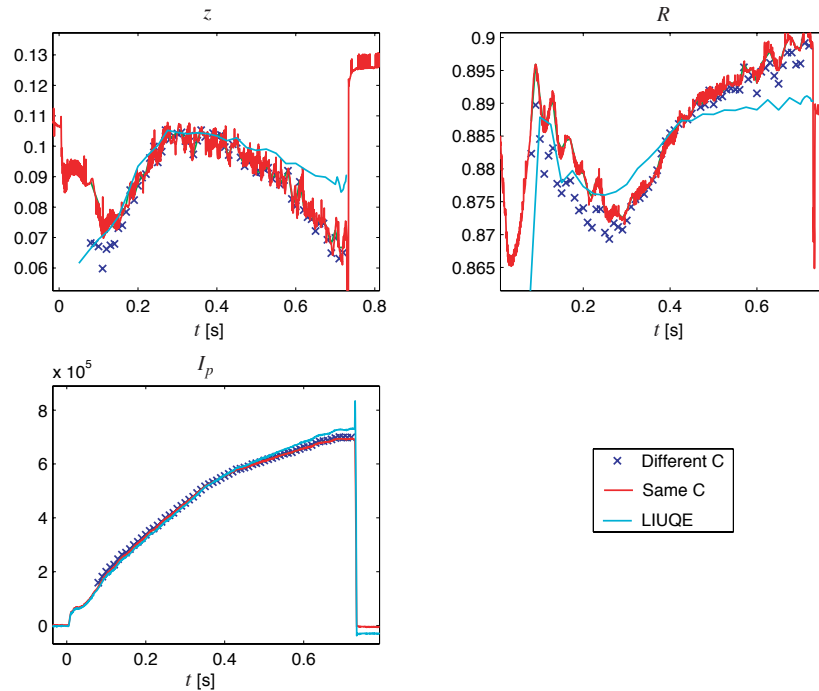

Figure 8.12: Reconstruction of $\hat{z}$, $\hat{R}$ and $\hat{I}_p$. red solid: state reconstruction; blue x: NTDSR reference; cyan solid: LIUQE reference

The comparison of the unstable state reconstruction $\hat{x}_1$ against the LIUQE and the NTDSR references is depicted in Figure 8.13.
As already seen the state reconstruction perfectly fits the reference in the neighborhood of the linearisation equilibrium at t_0. The accuracy gets slightly worse when the elongation κ and the plasma current I_p differ too much from the corresponding values at the linearisation equilibrium (times between $0.1 - 0.2$ s and around 0.7 s). Nevertheless, the state reconstruction can be assessed as astonishingly accurate for the whole discharge.
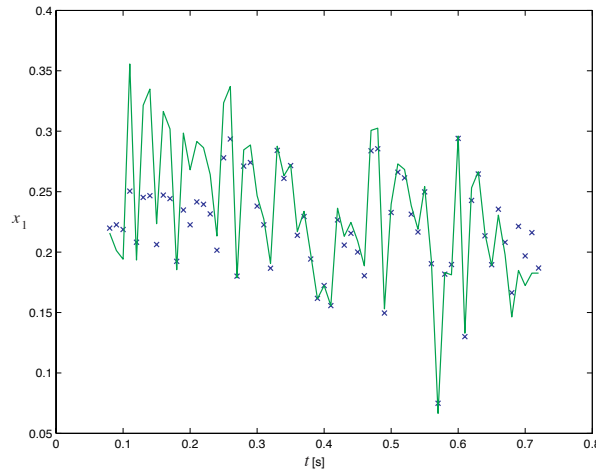
Figure 8.13: Reconstruction of the unstable state $\hat{x}_1$. green solid: state reconstruction; blue x: NTDSR reference

2. Variation of the vertical plasma position z (discharge $\sharp 24377$)

   The $C_0^\dagger$ matrix is taken at $t_0 = 0.55$ s.

   The comparison of the plasma parameters $\hat{z}$, $\hat{R}$ and $\hat{I}_p$ against the LIUQE and the NTDSR references is depicted in Figure 8.14.
   As in the first case, the reconstruction is very accurate near the linearisation equilibrium at t_0.
   In general the state reconstruction fits both references well during the whole discharge, excepted a slight disagreement for all parameters during the lower knee of the z evolution. Nevertheless, the errors, about 2 cm for z and less than 0.5 cm for R, are acceptable.

   The comparison of the unstable state reconstruction $\hat{x}_1$ against the LIUQE and the NTDSR references is depicted in Figure 8.15.
   Again, the state reconstruction fits the reference perfectly in the neighborhood of the linearisation equilibrium at t_0. The accuracy gets slightly worse during the upper and the lower knees of the z evolution, where in both cases the state reconstruction is slightly underestimated compared to the reference.

3. Variation of the vertical plasma position z ($\sharp 24377$) with a state reconstruction matrix $C_0^\dagger$ derived from a similar discharge (discharge $\sharp$ 24375) without any variation of the plasma parameters

   The $C_0^\dagger$ matrix is taken from discharge $\sharp 24375$ at $t = 0.55$ s, while the NTDSR reference is derived from discharge $\sharp 24377$.

   The comparison of the plasma parameters $\hat{z}$, $\hat{R}$ and $\hat{I}_p$ against the LIUQE and the NTDSR references is depicted in Figure 8.16.
   The state reconstruction accuracy is similar to the second case.

   The comparison of the unstable state reconstruction $\hat{x}_1$ against the LIUQE and the NTDSR references is depicted in Figure 8.17.
   This time there is a pronounced discrepancy between the slopes of the state reconstruction and the NTDSR reference. This is due to a static gain error of the C matrices (and thus of the $C^\dagger$ matrices) between the linear model derived from
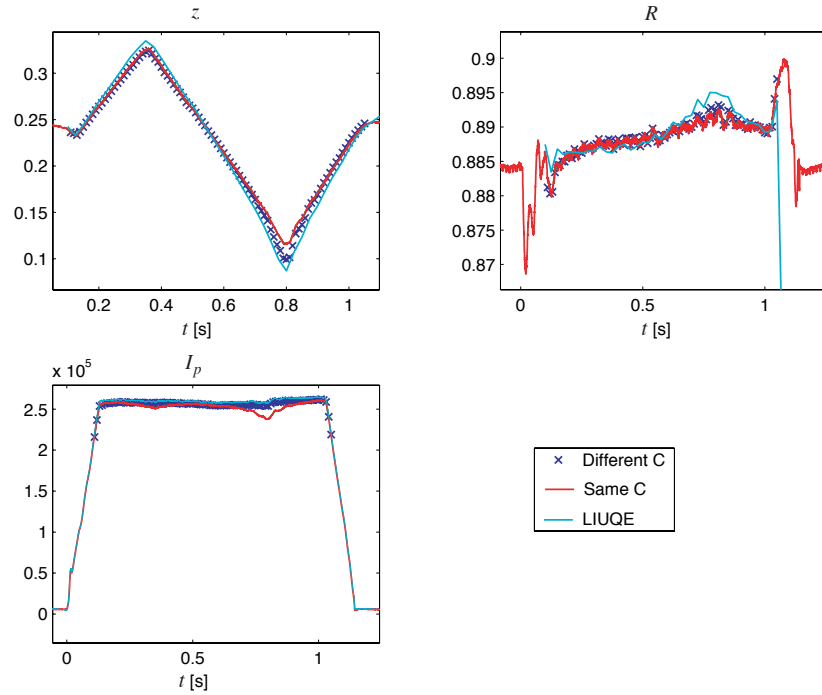
Figure 8.14: Reconstruction of $\hat{z}$, $\hat{R}$ and $\hat{I}_p$. red solid: state reconstruction; blue x: NTDSR reference; cyan solid: LIUQE reference

Figure 8.15: Reconstruction of the unstable state $\hat{x}_1$. green solid: state reconstruction; blue x: NTDSR reference

discharge ♯24375 and the model derived from discharge ♯24377. In this particular case, this leads to an overestimation of the unstable state compared to the reference. But in general, we have to consider that such a reconstruction can lead to an underestimation, too.

4. Ramp-up and ramp-down of the plasma current I_p (discharge ♯24375)

The $C_0^\dagger$ matrix is taken at $t_0 = 0.55$ sec.

The comparison of the plasma parameters $\hat{z}$, $\hat{R}$ and $\hat{I}_p$ against the LIUQE and the NTDSR references is depicted in Figure 8.18.

Figure 8.16: Reconstruction of $\hat{z}$, $\hat{R}$ and $\hat{I}_p$. red solid: state reconstruction; blue x: NTDSR reference; cyan solid: LIUQE reference
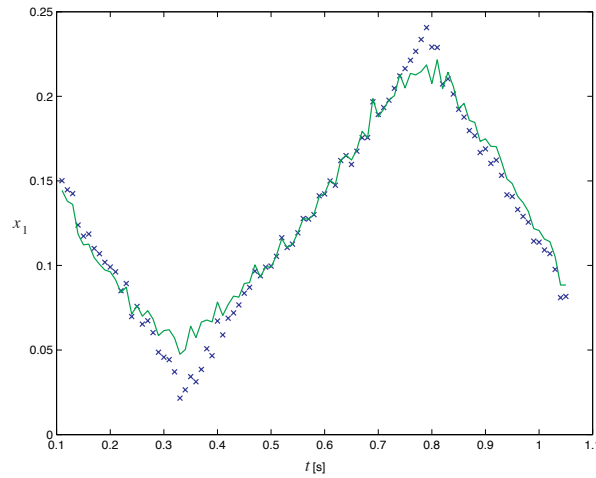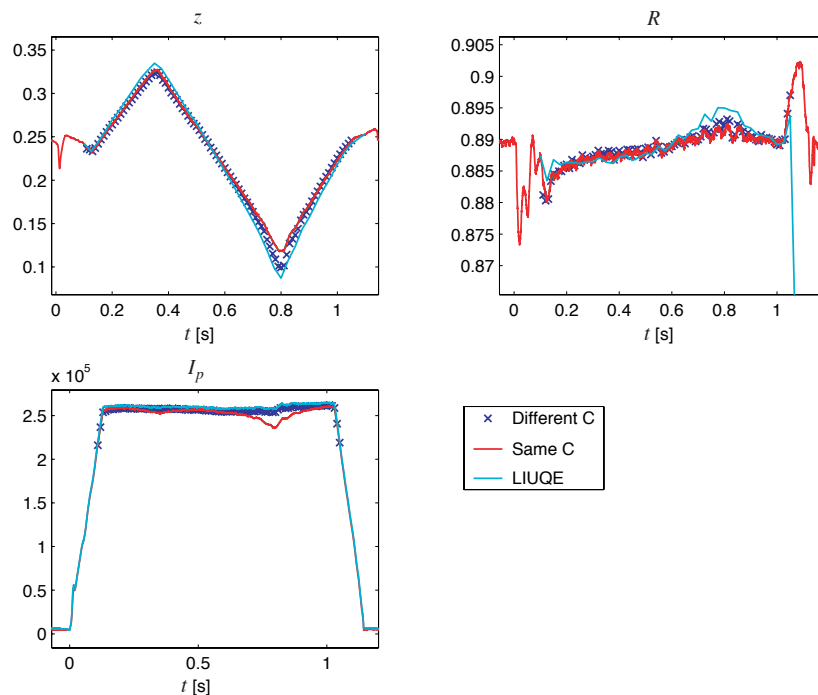

Figure 8.17: Reconstruction of the unstable state $\hat{x}_1$. green solid: state reconstruction; blue x: NTDSR reference

The reconstruction is very accurate for the whole discharge for R and I_p. There is a discrepancy for z at the end of the discharge. But again, the maximal error is about 1 cm which seems acceptable.

The comparison of the unstable state reconstruction $\hat{x}_1$ against the LIUQE and the NTDSR references is depicted in Figure 8.19.
The state reconstruction is astonishingly accurate for the whole discharge.

For the analysis of the ramp-up and the ramp-down of a discharge, LIUQE reconstructions and RZIP models have to be derived during the ramps. However, LIUQE is not able to provide a reconstruction at the very start of a discharge (during the
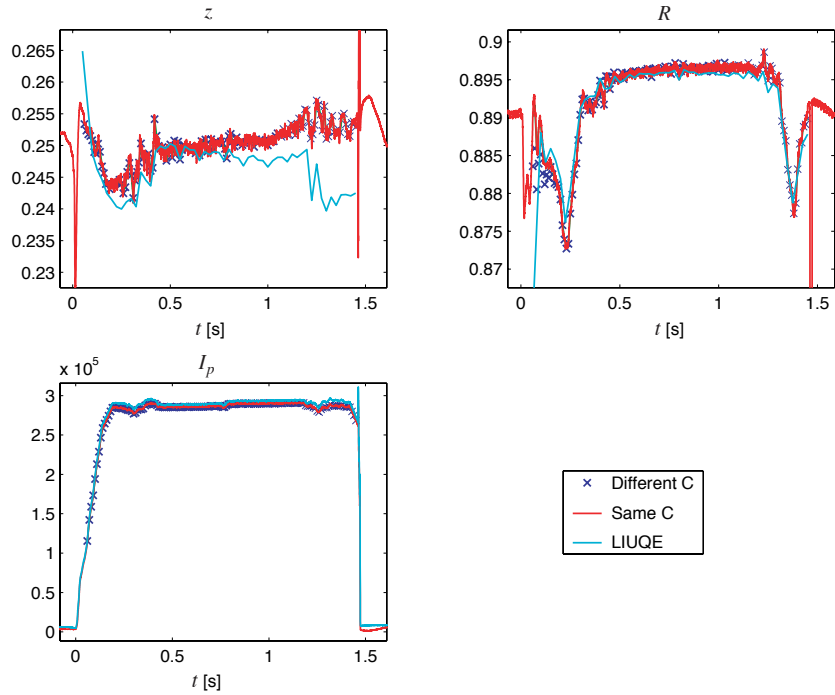
Figure 8.18: Reconstruction of $\hat{z}$, $\hat{R}$ and $\hat{I}_p$. red solid: state reconstruction; blue x: NTDSR reference; cyan solid: LIUQE reference
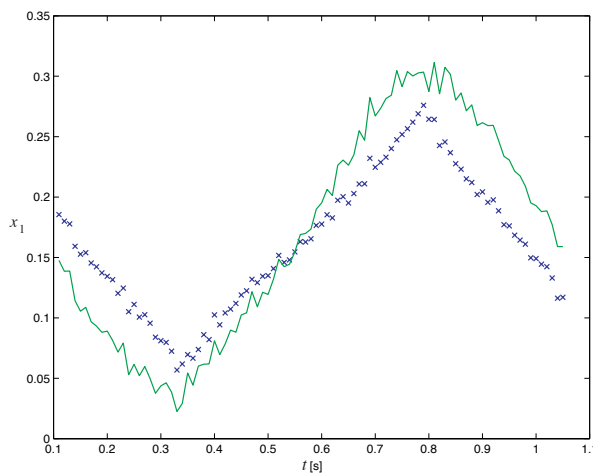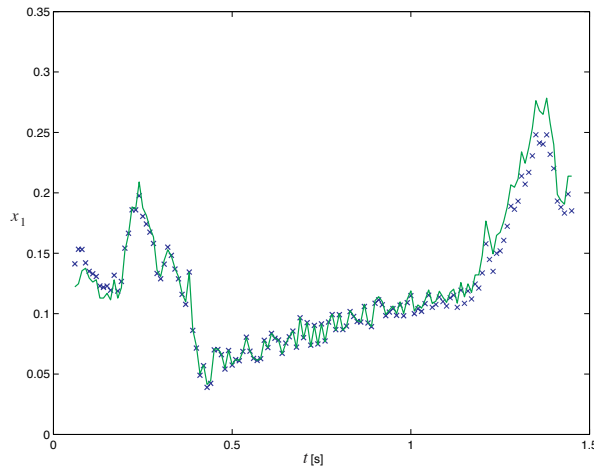

Figure 8.19: Reconstruction of the unstable state $\hat{x}_1$. green solid: state reconstruction; blue x: NTDSR reference

ramp-up) and at the very end of a discharge (during the ramp-down). Since RZIP uses LIUQE results to provide a linear model, there is no linear tokamak model available for a certain time lapse during the initial ramp-up and the final ramp-down. As mentioned earlier, there is a possibility to estimate the plasma current I_p during an entire discharge by means of a trapezoidal integration of the magnetic field measurements B_{pol}, denoted as 'Trapeze'. Thus, we are forced to restrict the study of the state reconstruction robustness during the ramp-up and the ramp-down by solely analysing the evolution of I_p.

Figures 8.20 and 8.21 illustrate the I_p reconstruction for the ramp-up and ramp-

down, respectively.

Since the fit is almost perfect we had to add a slight offset on the Trapeze reference permitting to distinguish between the evolution of state reconstruction (solid red) and of the Trapeze reference (solid cyan).
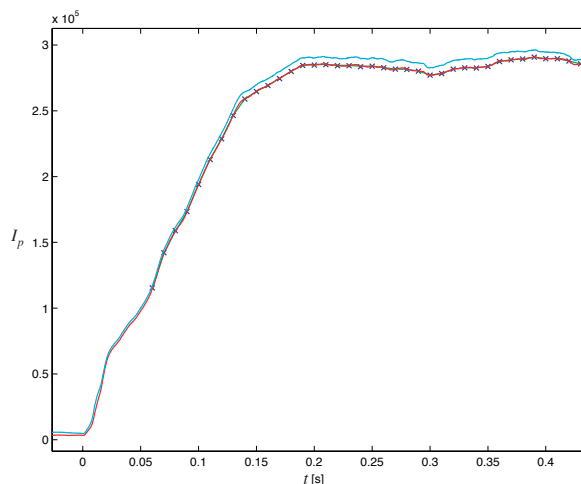
Figure 8.20: Reconstruction of the ramp up of I_p. red solid: state reconstruction; blue x: NTDSR reference; cyan solid: Trapeze reference (with an artificial offset)
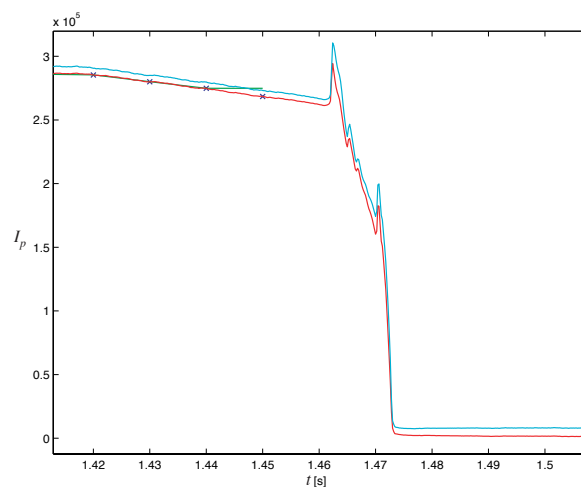
Figure 8.21: Reconstruction of the ramp down of I_p. red solid: state reconstruction; blue x: NTDSR reference; cyan solid: Trapeze reference(with an artificial offset)

The robustness study of the state reconstruction can by summarised by the following statements. We have seen that the reconstruction with the proposed static least square error method works well for TCV. Somewhat surprisingly, it seems that it works accurately for a whole discharge, i.e. including ramp-up and ramp-down. If we want to apply the reconstructed states to the CNGSC controller then the sole problem that can arise is due to an eventual underestimation of the unstable state x_1, while the overestimation is benign. Over- or underestimation can occur when the reconstruction matrix $C_0^\dagger$ is taken from one discharge and applied to another similar discharge (see case 3.).

The consequence due to an underestimation of the unstable state is as follows. We denote the real actual unstable state as x_1 and its reconstruction as $\breve{x}_1$ and consider that they are located in the proximity of the boundaries of the null controllable region, i.e. $x_1 \approx 1$ and $\breve{x}_1 \approx 1$ (Chapter 7). This allows us to to approximate the nonlinear state feedback controller (Equations (8.50) and (8.51)) by

$$\varphi(x_1) \approx f_1 x_1. \tag{8.67}$$

When there is an underestimation $x_1 > \breve{x}_1$ then the control action due to the reconstructed state $\breve{x}_1$ is smaller than the control action which theoretically should be applied for the actual state x_1, i.e. $|\varphi(x_1)| > |\varphi(\breve{x}_1)|$. Therefore, when the unstable state is in the proximity of the boundaries of the null controllable region the applied control $\varphi(\breve{x}_1)$ is no longer able to stabilise the closed-loop system. The underestimation of the unstable state can be interpreted as a reduction of the region of attraction. On the contrary, when we consider an overestimation $x_1 > \breve{x}_1$ then the applied control $|\varphi(\breve{x}_1)|$ is larger than the needed control $|\varphi(x_1)|$ for the real actual unstable state x_1. Thus, the overestimation does not induce a drawback in the sense of the closed-loop stability.

To avoid an eventual underestimation of the unstable state we may correct the reconstruction by increasing the estimation by

$$\breve{x}_{1_{corr}} = c_{x_1} \breve{x}_1, \tag{8.68}$$

where $c_{x_1} \geq 1$ denotes the correction factor and $\breve{x}_{1_{corr}}$ the corrected reconstruction of x_1.

Reconstruction errors on the other (stable) states are certainly more benign on the stability of the closed-loop system. A detailed study of the consequences due to such errors is not necessary, since, as we will see in the next section, the reconstruction of the other states is not required when we consider the nonlinear state feedback $\varphi(x)$.

The work during this robustness study revealed that the accuracy of the reconstruction of some states can be increased when only a subset of the magnetic diagnostic measurements (B_{pol}, Ψ and I_{pol}) is used. For example, the reconstruction of I_p is more accurate if only the B_{pol} and I_{pol} measurements are used. Therefore, an improvement could be achieved by analysing with which subset of magnetic diagnostic measurements the accuracy of the unstable state reconstruction can be enhanced.

8.4.3   Reconstruction improvement linked to the structure of the controller

In this section we show that when we consider the structure of the CNGSC controller φ, it is sufficient to solely reconstruct the unstable state $\breve{x}_1$. Of course, by applying the least square error reconstruction method the estimation of all states is automatically provided. But when solely the unstable state is required then we can improve the reconstruction accuracy of this sole state, while there is no effort needed for the improvement of the reconstruction accuracy of the other states.

Let us consider the nonlinear state feedback structure given by Equation (8.50), i.e.

$$\varphi \left(\begin{bmatrix} x \\ w \end{bmatrix} \right) = f_1 x_1 + k(x_1)(f_2 x_2 + f_3 x_3 + \ldots + f_n x_n + f_w w),$$

with the nonlinear function $k(x_1)$ (Equation (8.51)) which depends only on the unstable state x_1. By means of the substitution

$$x_q = f_2 x_2 + f_3 x_3 + \ldots + f_n x_n + f_w w \tag{8.69}$$

we obtain

$$\varphi\left(\begin{bmatrix} x \\ w \end{bmatrix}\right) = f_1 x_1 + k(x_1)x_q.$$

By means of a linear state transformation, System (8.42) can be transformed into a system containing the unstable state x_1, the new state x_q and all the remaining states. Therefore, the improvement of the reconstruction accuracy can be focused on x_1 and x_q. This represents the first simple improvement of the reconstruction quality which is due to the structure of the nonlinear state feedback controller.

A supplementary improvement can be achieved when we consider the input-output VC controller (8.34), i.e.

$$\dot{x}_{vc} = A_{vc}x_{vc} + B_{vc}z_e \tag{8.70}$$
$$\tilde{u}_{io} = \frac{1}{\sigma_{vc}}C_{vc}x_{vc} + \frac{1}{\sigma_{vc}}D_{vc}z_e.$$

with the error $z_e = z - z_r$. Note that we have to divide the output of the input-output VC controller by the VC saturation level σ_{vc} since we consider the normalised saturation function with a saturation level of 1 (Figure 8.7 b)). Furthermore we consider the linear state feedback controller (8.45), i.e.

$$\tilde{u}_{fb} = \begin{bmatrix} f_x & f_w \end{bmatrix} \begin{bmatrix} x \\ w \end{bmatrix} + \tilde{D}_{ff,r}q \tag{8.71}$$

and the resulting closed-loop system depicted in Figure 8.8 b). By considering Substitution (8.69) and $f = \begin{bmatrix} f_1 & f_2 & \dots & f_n \end{bmatrix}$, the state feedback controller (8.71) can be reformulated as

$$\tilde{u}_{fb} = f_1 x_1 + x_q + \tilde{D}_{ff,r}q. \tag{8.72}$$

Since the system with the input-output VC controller depicted in Figure 8.7 b), where $\tilde{u}_{io} = \tilde{u}$, is equivalent to the system with the state feedback controller depicted in Figure 8.8 b), where $\tilde{u}_{fb} = \tilde{u}$, we can state that the outputs of both controllers are equivalent, i.e. $\tilde{u}_{io} = \tilde{u}_{fb}$. Solving Equation (8.72) for x_q and substituting $\tilde{u}_{fb} = \tilde{u}_{io}$ leads to

$$x_q = \tilde{u}_{io} - \tilde{D}_{ff,r}q - f_1 x_1. \tag{8.73}$$

Thus, since the input-output VC controller (8.70) provides $\tilde{u}_{io}$ and since the input q containing the feedoward inputs and the references are known we obtain a reconstruction of x_q just by reconstructing the unstable state x_1, i.e.

$$\breve{x}_q = \tilde{u}_{io} - \tilde{D}_{ff,r}q - f_1 \breve{x}_1. \tag{8.74}$$

We can ever state that the input-output VC controller (8.70) works as an observer for the estimation of x_q under the condition that an accurate unstable state reconstruction $\breve{x}_1$ can be provided.

8.5　Reference tracking

As mentioned in Sections 8.2 and 8.3.6 we can separate the reference tracking problem from the disturbance rejection by neglecting the disturbance input $w = 0$. Furthermore, we assume reference and feedforward signals, denoted as

$$
q = \begin{bmatrix} u_{sc_{ff}} \\ u_{vc_{ff}} \\ y_r \\ z_r \end{bmatrix},
$$

which are either constant or which vary slowly such that the state x_e is kept small, i.e. $\|x_e\| \approx 0$. Therefore due to the characteristics of the nonlinear state feedback control (Condition (8.19)), the approximation $\varphi(\hat{x}_e) \approx f\hat{x}_e$ is valid which implies that the reference tracking follows the closed-loop system dynamics characterised by the linear state feedback. Moreover, we assume that the variation of q does not drive the output of the controller $\tilde{u}$ into saturation.

For this analysis we consider the S system (8.36) where its state vector is given by

$$
x_s = \begin{bmatrix} x_p \\ x_{sc} \\ x_{vc} \end{bmatrix}.
$$

Remember that, if required, the results obtained in this section can be applied straightforwardly to the normalised system (8.42) by simply applying the linear state transformation given by Equation (8.41), i.e

$$
x = T^{-1}x_s.
$$

By considering the assumptions mentioned above, the S system in closed-loop ($u = \tilde{u}$) leads to the linear tokamak closed-loop system (Figure 8.22) expressed as

$$
\begin{bmatrix} \dot{x}_p \\ \dot{x}_{sc} \\ \dot{x}_{vc} \end{bmatrix} = \begin{bmatrix} A_p + B_{p_{sc}}D_{sc}C_{p_y} + B_{p_{vc}}D_{vc}C_{p_z} & B_{p_{sc}}C_{sc} & B_{p_{vc}}C_{vc} \\ B_{sc}C_{p_y} & A_{sc} & 0 \\ B_{vc}C_{p_z} & 0 & A_{vc} \end{bmatrix} \begin{bmatrix} x_p \\ x_{sc} \\ x_{vc} \end{bmatrix}
$$
$$
+ \begin{bmatrix} B_{p_{sc}} & B_{p_{vc}} & -B_{p_{sc}}D_{sc} & -B_{p_{vc}}D_{vc} \\ 0 & 0 & -B_{sc} & 0 \\ 0 & 0 & 0 & -B_{vc} \end{bmatrix} \begin{bmatrix} u_{sc_{ff}} \\ u_{vc_{ff}} \\ y_r \\ z_r \end{bmatrix} \tag{8.75}
$$

$$
y = \begin{bmatrix} C_{p_y} & 0 & 0 \end{bmatrix} \begin{bmatrix} x_p \\ x_{sc} \\ x_{vc} \end{bmatrix}
$$

$$
z = \begin{bmatrix} C_{p_z} & 0 & 0 \end{bmatrix} \begin{bmatrix} x_p \\ x_{sc} \\ x_{vc} \end{bmatrix},
$$

where the outputs y and z are defined in System (8.32).

The equilibrium of the closed-loop system, denoted as $\bar{x}_s$, is defined as the solution of System (8.75) by imposing $\dot{x}_s = 0$. If the matrix

$$
\begin{bmatrix} A_p + B_{p_{sc}}D_{sc}C_{p_y} + B_{p_{vc}}D_{vc}C_{p_z} & B_{p_{sc}}C_{sc} & B_{p_{vc}}C_{vc} \\ B_{sc}C_{p_y} & A_{sc} & 0 \\ B_{vc}C_{p_z} & 0 & A_{vc} \end{bmatrix}
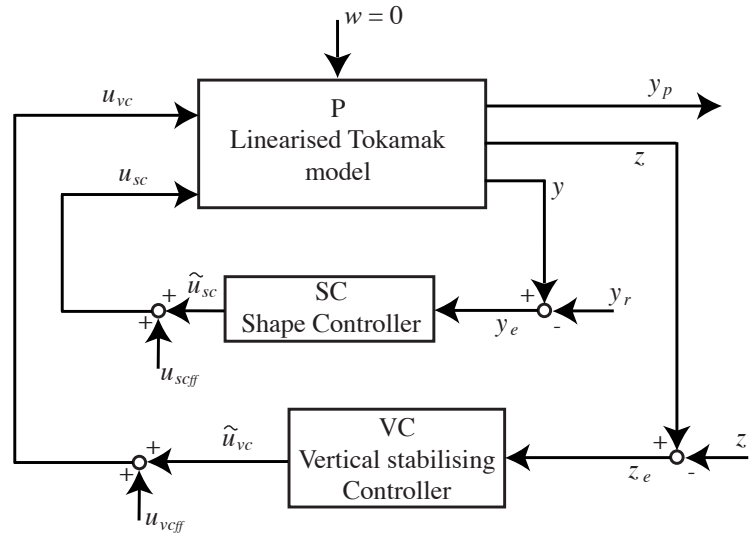$$

Figure 8.22: Illustration of the linear closed-loop system considered for reference tracking.

is invertible then there exists a solution and the equilibrium can be expressed as a function of the closed-loop system input q given by

$$
\bar{x}_s = - \left[\begin{array}{ccc} A_p + B_{p_{sc}} D_{sc} C_{p_y} + B_{p_{vc}} D_{vc} C_{p_z} & B_{p_{sc}} C_{sc} & B_{p_{vc}} C_{vc} \\ B_{sc} C_{p_y} & A_{sc} & 0 \\ B_{vc} C_{p_z} & 0 & A_{vc} \end{array} \right]^{-1} . \tag{8.76}
$$

$$
\cdot \left[\begin{array}{cccc} B_{p_{sc}} & B_{p_{vc}} & -B_{p_{sc}} D_{sc} & -B_{p_{vc}} D_{vc} \\ 0 & 0 & -B_{sc} & 0 \\ 0 & 0 & 0 & -B_{vc} \end{array} \right] \left[\begin{array}{c} u_{sc_{ff}} \\ u_{vc_{ff}} \\ y_r \\ z_r \end{array} \right] .
$$

Note that by applying the linear state transformation T this equilibrium is equivalent to the equilibrium given by (8.55).

When we consider a constant closed-loop system input $q = $ const then the state x_s converges asymptotically to the equilibrium $\bar{x}_s$, i.e.

$$
\lim_{t \to \infty} x_s(t) = \bar{x}_s. \tag{8.77}
$$

As for the initial assumption made in this section, if we vary q slowly then we can assume that the error between the actual state x_s and the equilibrium $\bar{x}_s$ is small and thus we assume $x_{s_e} = x_s - \bar{x}_s \approx 0$. Therefore we can state that the actual state x_s tracks approximately the equilibrium $\bar{x}_s$.

If we consider a constant reference $y_r = $ const ($z_r = $ const) then there remains a static error $y_e = y - y_r$ ($z_e = z - z_r$) when the transfer function from y_r (z_r) to the output y (z) possesses no integration effect (pure integrator). This fact is well known from control theory [42, 14]. Thus, since the tokamak linear model possesses no pure integrator there remains always an output error y_e (z_e) when no integral control is introduced in the SC and VC controllers. In such a case we have the possibility of removing output errors by adding a feedforward input $u_{sc_{ff}}$ ($u_{vc_{ff}}$). This feedforward input can be expressed as a function of the reference signals y_r (z_r). We therefore substitute $y_r = y$ and $z_r = z$ in

System (8.75) which leads to the closed-loop system

$$
\begin{bmatrix} \dot{x}_p \\ \dot{x}_{sc} \\ \dot{x}_{vc} \end{bmatrix} = \begin{bmatrix} A_p & B_{p_{sc}}C_{sc} & B_{p_{vc}}C_{vc} \\ 0 & A_{sc} & 0 \\ 0 & 0 & A_{vc} \end{bmatrix} \begin{bmatrix} x_p \\ x_{sc} \\ x_{vc} \end{bmatrix} + \begin{bmatrix} B_{p_{sc}} & B_{p_{vc}} \\ 0 & 0 \\ 0 & 0 \end{bmatrix} \begin{bmatrix} u_{sc_{ff}} \\ u_{vc_{ff}} \end{bmatrix} \quad (8.78)
$$

$$
y = \begin{bmatrix} C_{p_y} & 0 & 0 \end{bmatrix} \begin{bmatrix} x_p \\ x_{sc} \\ x_{vc} \end{bmatrix}
$$

$$
z = \begin{bmatrix} C_{p_z} & 0 & 0 \end{bmatrix} \begin{bmatrix} x_p \\ x_{sc} \\ x_{vc} \end{bmatrix}.
$$

Thus, for this closed-loop system the equilibrium for the controllers is trivially $\bar{x}_{sc} = 0$ and $\bar{x}_{vc} = 0$, while the equilibrium for the linear tokamak model is

$$
\bar{x}_p = -A_p^{-1} \begin{bmatrix} B_{p_{sc}} & B_{p_{vc}} \end{bmatrix} \begin{bmatrix} u_{sc_{ff}} \\ u_{vc_{ff}} \end{bmatrix}. \quad (8.79)
$$

Straightforwardly, since we imposed $y_r = y$ and $z_r = z$ the outputs y and z at the equilibrium $\bar{x}_p$ are given by

$$
\begin{bmatrix} y_r \\ z_r \end{bmatrix} = \begin{bmatrix} y \\ z \end{bmatrix} = Q \begin{bmatrix} u_{sc_{ff}} \\ u_{vc_{ff}} \end{bmatrix} = - \begin{bmatrix} C_{p_y} \\ C_{p_z} \end{bmatrix} A_p^{-1} \begin{bmatrix} B_{p_{sc}} & B_{p_{vc}} \end{bmatrix} \begin{bmatrix} u_{sc_{ff}} \\ u_{vc_{ff}} \end{bmatrix}. \quad (8.80)
$$

Therefore, if the number of feedforward inputs is equal to the number of outputs, the feedforward inputs can be calculated by inverting the matrix Q, i.e.

$$
\begin{bmatrix} u_{sc_{ff}} \\ u_{vc_{ff}} \end{bmatrix} = Q^{-1} \begin{bmatrix} y_r \\ z_r \end{bmatrix} = - \left(\begin{bmatrix} C_{p_y} \\ C_{p_z} \end{bmatrix} A_p^{-1} \begin{bmatrix} B_{p_{sc}} & B_{p_{vc}} \end{bmatrix} \right)^{-1} \begin{bmatrix} y_r \\ z_r \end{bmatrix}. \quad (8.81)
$$

In the case where there are more feedforward inputs than outputs we may get a square matrix Q by canceling some outputs, while for fewer feedforward inputs we may get a least square error approximation by using the pseudo-inverse matrix $Q^\dagger$ (see Section A.4 of the Appendix for the least square error method).

In general, it is more convenient to put integral control into the controllers instead of calculating the feedforward inputs. With integral control the feedforward input given by Equation (8.81) is intrinsically provided by the controller (see basic control theory [42, 14]).

For the VC controller there is a problem linked to the reference error z_e and the input of the VC saturation u_{vcs} (Figure 8.23). The theory of the CNGSC controller relies on the fact that at the equilibrium (when no disturbance occurs) the input of the saturation is zero, i.e. $u_{vcs} = 0$. Thus, the saturation is driven symmetrically during a rejection of a disturbance. For the tokamak closed-loop system considered (Figure 8.23) this condition is only satisfied when the equilibrium is at zero $\bar{x}_s = 0$, which implies also that $y_r = y = 0$ and $z_r = z = 0$, while a non-zero reference $z_r \neq 0$ always implies a non-zero saturation input $u_{vcs} \neq 0$. If we consider that there is no integral control in the VC controller implying a non-zero output error $z_e \neq 0$, then at the equilibrium the controller output is non-zero $\tilde{u}_{vc} \neq 0$, thus $u_{vcs} \neq 0$. On the other hand, when we introduce a feedforward signal (or equivalently an integral control, but we only consider the feedforward input here) then the output error vanishes $z_e = 0$ implying $\tilde{u}_{vc} = 0$. But since there is a

feedforward input $u_{vc_{ff}} \neq 0$ the saturation input is still not zero $u_{vcs} \neq 0$. This problem can be solved by introducing a feedforward input into the SC controller, instead of the VC controller. This can be done by imposing $u_{vc_{ff}} = 0$ and solving Equation (8.80) for $u_{sc_{ff}}$ as a function of z_r. Another solution consists of introducing an integral control into the SC controller for the output z by imposing that one of the outputs y contains an identical output z. With this solution the error z_e vanishes which implies that $\tilde{u}_{vc} = 0$ and since we imposed $u_{vc_{ff}} = 0$ there is no residual offset at the saturation input $\tilde{u}_{vcs} = 0$ when the closed-loop system is in equilibrium.
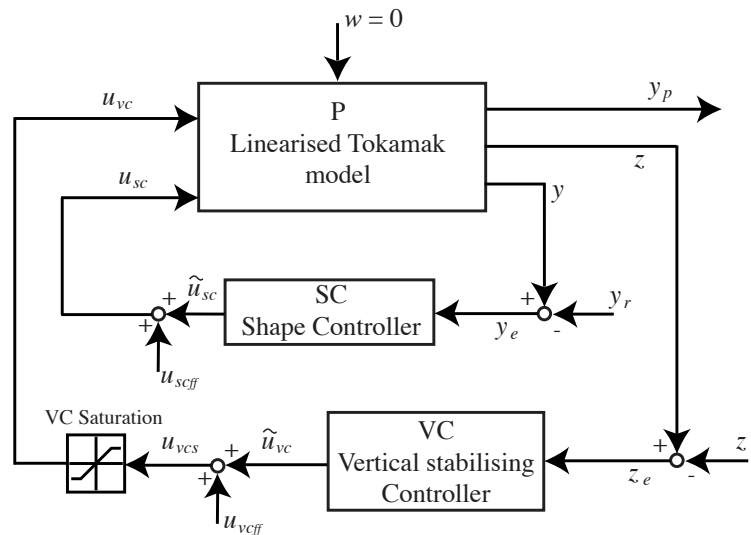

Figure 8.23: Illustration of the linear closed-loop system with VC saturation.

8.6   Disturbances

In this section we provide an elementary analysis on the effect of the disturbances on the stability of the closed-loop system. We restrict the analysis to a qualitative description of the behavior of the closed-loop system during a disturbance and the implied consequences for the closed-loop system stability. We will see that in general it is not possible to determine whether or not stability has been lost during a disturbance.

In the analysis of Chapter 7 concerning the CNGSC controller we derived the null controllable region and the region of attraction. The concept linked to these two regions makes only sense for autonomous closed-loop systems, i.e **time-invariant** closed-loop systems [50]. Recall that when, in absence of **time-varying** disturbance inputs, the initial condition is in the region of attraction then the controller brings the state back to the origin of the closed-loop system, while on the other hand, when the initial condition is outside the region of attraction the controller can not bring back the state to the origin and the stability is lost. The initial condition may be interpreted as a displacement of the state away from the equilibrium due to a disturbance. In general, a disturbance is introduced into a system by a **time-varying** external input, denoted as w. When no disturbance is occurring then the disturbance input is zero $w = 0$. Thus, the closed-loop system behaves like an autonomous system. During a disturbance, i.e. $w \neq 0$, the closed-loop system can no longer be considered to be an autonomous system and the concept linked to the region of attraction is no more valid. This concept becomes valid again just

after that the disturbance has disappeared, i.e. $w = 0$. During the disturbance the state has been displaced away from the equilibrium and the actual state just at the time at which the disturbance disappears can be taken as a new initial condition. Then by means of the region of attraction it is possible to determine whether or not the stability has been lost due to the disturbance.

The assumptions made in Section 8.5 state that the reference tracking mechanism has only a minor impact on the state error and we therefore assume that $x_e = x - \bar{x} = 0$. Thus, the disturbance rejection due to the nonlinear control (Equation (8.49)) (or linear control, Equation (8.48))

$$\varphi\left(\begin{bmatrix} x_e \\ w_e \end{bmatrix}\right) \qquad \left(\text{or} \quad \begin{bmatrix} f_x & f_w \end{bmatrix} \begin{bmatrix} x_e \\ w_e \end{bmatrix}\right)$$

is equivalent for any equilibrium $\bar{x}$. We therefore set the feedforward and reference signals at zero $q = 0$ which implies an equilibrium $\bar{x} = 0$ and a state error $x_e = x$. This permits us to consider solely x instead of x_e. With this assumption the normalised system (8.42) with an arbitrary linear or nonlinear state feedback, defined as

$$\vartheta\left(\begin{bmatrix} x \\ w \end{bmatrix}\right), \tag{8.82}$$

becomes

$$\dot{x} = Ax + bu + E\dot{w} \tag{8.83}$$

$$\tilde{u} = \vartheta\left(\begin{bmatrix} x \\ w \end{bmatrix}\right).$$

8.6.1   The ELM-like disturbance model

Two plasma parameters determine an effective internal disturbance to the plasma equilibrium: i) the internal inductance l_i and ii) the ratio of the kinetic plasma pressure energy to the poloidal magnetic field energy, referred to as β_p. Thus, the disturbance input w consists of a variation of both β_p and l_i, i.e.

$$w = \begin{bmatrix} \Delta\beta_p \\ \Delta l_i \end{bmatrix}. \tag{8.84}$$

The three most important disturbance types are [21]:

- A minor plasma current disruption (MD):
  This is a drop followed by a recovery of both β_p and l_i during a long time lapse.

- Compound edge localised modes (CELM):
  This is similar to the MD but with a smaller amplitude and a shorter time lapse.

- Type I edge localised modes (ELM1)
  This is a drop followed by a recovery of solely β_p. The amplitude is similar to that of the CELM, while the time lapse is shorter than for the CELM.

For the analysis we model a simplified ELM-like disturbance, where the drop and the recovery are represented as ramps. Figures 8.24 a) and b) illustrate the shape of an

ELM-like disturbance w and its time derivative $\dot{w}$, respectively. The disturbance starts at t_0, reaches its maximum at t_1 and vanishes at t_2. In practice, the amplitude, the duration of a disturbances and the time lapses between two disturbances vary strongly from discharge to discharge. Furthermore, the representation of the disturbance by ramps is an approximation compared to real ELM disturbances. But the advantage is that it considerably simplifies the analysis as we will see later.
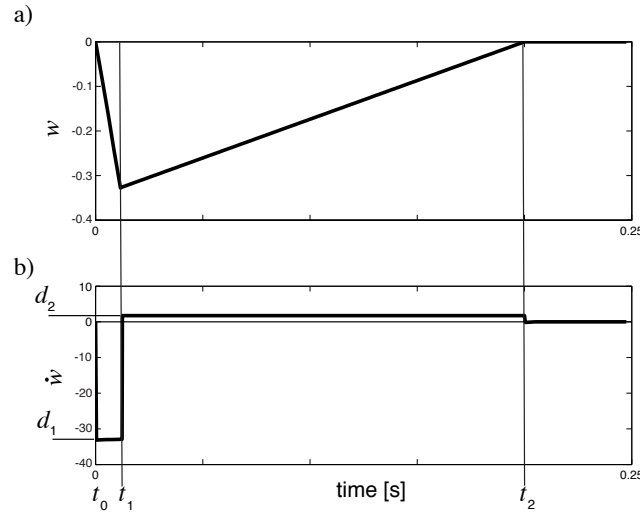

Figure 8.24: Evolution of an ELM like perturbation w a) and its derivative $\dot{w}$ b).

Since w is modeled by means of two ramps its derivative $\dot{w}$ comprises a negative constant value during the drop and a positive constant value during the recovery. Since for these disturbances $\Delta\beta_p$ and Δl_i vary simultaneously (same t_0, t_1 and t_2 for both) we can simplify the disturbance input by

$$E_1\dot{w} = \begin{cases} d_1 < 0 & \text{if} \quad t_0 < t \le t_1 \\ d_2 > 0 & \text{if} \quad t_1 < t \le t_2 \end{cases}. \tag{8.85}$$

The definition of $d_1 < 0$ and $d_2 > 0$ is arbitrary since it depends on the matrix E_1 and thus the contrary could also be taken into consideration. But since the closed-loop system is symmetric the sign of the disturbance is irrelevant.

8.6.2 Analysis of the effect on the closed-loop system stability induced by the disturbance

Since for the CNGSC controller the region of attraction $\mathcal{A}$ is equal to the null controllable region $\mathcal{C}$ we only consider the last one defined as

$$\mathcal{C} = \{x \in \mathbb{R}^n : |x_1| < 1\} \tag{8.86}$$

As we have seen in Chapter 7, the boundaries of $\mathcal{C}$ are solely located in the subspace of the unstable state x_1, while the subspace of the stable states is unbounded, i.e. $\mathbb{R}^{n-1}$. Thus, only the impact of the disturbance on the unstable state x_1 is relevant for the stability analysis. We therefore only consider the unstable subsystem of System (8.83) which is given by

$$\dot{x}_1 = \lambda_1 x_1 + \lambda_1 u + E_1\dot{w}, \tag{8.87}$$

where $\lambda_1 > 0$. Note that from the proof of the null controllable region (see Chapters 7) it can be deduced that the boundaries of the null controllable region in the unstable state subspace are deduced from the unstable state equilibrium when the input u is in saturation ($u = +1$ or $u = -1$). Thus, it derives from the equilibrium ($\dot{x}_1 = 0$) of System (8.87) that we may define a null controllable region, referred to as the varying null controllable region, since it varies as a function of the disturbance input $E_1\dot{w}$. The boundaries of this varying null controllable region are given by

$$x_{e+_1} = +1 - \frac{1}{\lambda_1}E_1\dot{w} \quad \text{for negative saturation } u = -1 \tag{8.88}$$

$$x_{e-_1} = -1 - \frac{1}{\lambda_1}E_1\dot{w} \quad \text{for positive saturation } u = +1.$$

Let us for the purposes of the analysis consider the controller (bang-bang controller)

$$u = \tilde{u} = \varsigma\left(\begin{bmatrix} x_d \\ w \end{bmatrix}\right) = -\text{sgn}(x_1) = \lim_{f_1 \to -\infty} \text{sat}(f_1 x_1). \tag{8.89}$$

We can deduce from Chapter 7 that this controller is stabilising the closed-loop system since $f_1 < -1$ is satisfied and since its region of attraction is equal to the null controllable region $\mathcal{C}$.

Before a disturbance occurs it is assumed that the system is in equilibrium, i.e. $x_1 = 0$. During the drop phase of the disturbance we consider the disturbance input $d_1 < 0$ and Equation (8.87) becomes

$$\dot{x}_1 = \lambda_1 x_1 + \lambda_1 u + d_1. \tag{8.90}$$

When there is no control $u = 0$ then the system becomes instantly unstable $\dot{x}_1 < 0$ since $d_1 < 0$ which implies that $x_1 < 0$. We therefore have to react by means of the control input u to reduce the impact of the destabilising effect of the disturbance. The most effective solution is to instantaneously counteract with a positive saturation $u = +1$. Thus, the most effective controller for counteracting a disturbance is the controller ς given by Equation (8.89). If we counteract with an input $u < +1$ then the resulting action is less effective. In any case the disturbance d_1 implies a displacement of the state away from the equilibrium. If the amplitude of the disturbance is too large or the control signal is too small then the trajectory can leave the null controllable region $x_1 \leq -1$ implying that at the end of the drop phase the state is located outside the null controllable region $x_1(t_1) \leq -1$. If we impose a positive saturation $\tilde{u} = u = +1$ when $x_1 \leq -1$ then we can consider the varying null controllable region. During the recovery $t_1 < t < t_2$ for which $d_2 > 0$ the boundary x_{e-_1} of the varying null controllable region is also located outside the null controllable region $x_{e-_1} = -1 - \frac{1}{\lambda_1}d_2 < -1$. Thus, if $x_{e-_1} < x_1(t_1) < 0$ then

$$\dot{x}_1 = \lambda_1 x_1 + \lambda_1 u + d_2 > 0 \tag{8.91}$$

is satisfied. In this case, the trajectory may reenter the null controllable region if the recovery time is long enough. Therefore, the state may be located in the null controllable region after the disturbance even when it has left the null controllable region during the disturbance. After the disturbance, at time $t \geq t_2$, the disturbance has vanished $w = 0$ and the closed-loop system again behaves like an autonomous system for which the concept of the region of attraction is valid. Therefore, since the region of attraction is

equivalent to the null controllable region the trajectory is steered back to the equilibrium. Figure 8.25 shows an example of a trajectory leaving and reentering the null controllable region during the disturbance and steering to the equilibrium after the disturbance. Since only the effect on the unstable state x_1 is important it is sufficient to show the evolution of the trajectory in a subspace composed of the unstable state x_1 and any arbitrary chosen stable state, referred to as x_s.
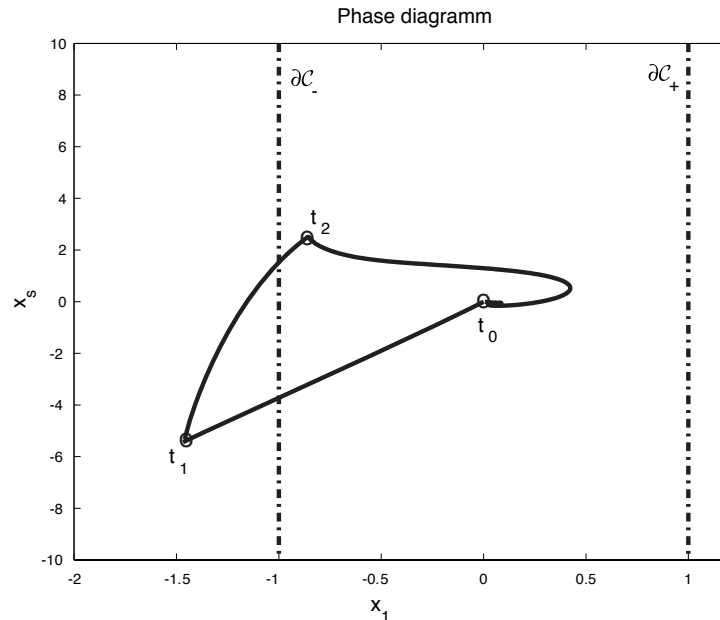

Figure 8.25: Trajectory of the tokamak closed-loop system during a disturbance.

As mentioned above, when the state is located outside the region of attraction we have to ensure that $u = +1$ for $x_1 \leq -1$ (or $u = -1$ for $x_1 \geq 1$). But the CNGSC controller given by Equations (8.50) and (8.51), i.e.

$$\varphi\left(\begin{bmatrix} x \\ w \end{bmatrix}\right) = f_1 x_1 + k(x)(f_2 x_2 + f_3 x_3 + \ldots + f_n x_n + f_w w),$$

and

$$k(x) = 1 - x_1^2 \qquad \text{or} \qquad k(x) = 1 - |x_1|$$

is only defined for the interval $x_1 \in [-1, 1]$. Therefore, we have to extend the CNGSC controller by considering an extended nonlinear function defined as

$$k(x) = \begin{cases} 1 - x_1^2 & \text{if} \quad |x_1| \leq 1 \\ 0 & \text{if} \quad |x_1| > 1 \end{cases} \qquad \text{or} \qquad k(x) = \begin{cases} 1 - |x_1| & \text{if} \quad |x_1| \leq 1 \\ 0 & \text{if} \quad |x_1| > 1 \end{cases}. \qquad (8.92)$$

Thus, since $f_1 < -1$, the controller guarantees to saturate the input $u = +1$ when $x_1 \leq -1$ (and $u = -1$ when $x_1 \geq 1$).

During a disturbance there is a second effect which has to be considered. It is due to the disturbance w in the state feedback control

$$\tilde{u} = \vartheta\left(\begin{bmatrix} x \\ w \end{bmatrix}\right).$$

In the case studied above, where $x_1 < 0$, the reaction to the disturbance w is accomplished with a positive control signal $u > 0$ and thus $\tilde{u} > 0$. If we compare the control $\vartheta\left(\begin{bmatrix} x & w \end{bmatrix}^T\right)$ with a disturbance $(w \neq 0)$ to the control without a disturbance $(w = 0)$ then two different cases can occur:

- A reinforced reaction, due to

$$\vartheta\left(\begin{bmatrix} x \\ w \end{bmatrix}\right) > \vartheta\left(\begin{bmatrix} x \\ 0 \end{bmatrix}\right).$$

  The feedback of the disturbance w has an advantageous impact on the stability of the closed-loop system during the disturbance.

- A weakened reaction, due to

$$\vartheta\left(\begin{bmatrix} x \\ w \end{bmatrix}\right) < \vartheta\left(\begin{bmatrix} x \\ 0 \end{bmatrix}\right).$$

  The feedback of the disturbance w has a disadvantageous impact on the stability of the closed-loop system during the disturbance. In this case we may improve the reaction by considering a state feedback without the disturbance w, as for example the controller given by Equation (8.89).

Note that for the case where $x_1 > 0$ the explanation is similar since the considered system is symmetric.

8.6.3 Propositions of controller modifications to increase stability during a disturbance

From this elementary study we conclude that it is important to obtain a large counteracting control output for an effective disturbance rejection. In general, this is achieved by means of a high controller gain. The optimal controller for the most effective disturbance rejection is the ς controller (bang-bang controller). The drawback of this controller is that it does not meet all requirements stated in Chapter 7, i.e. the local performance may not be met and the AC-losses are increased due to the induced control signal switching and chattering. For other controllers like the linear state feedback controller given by Equation(8.46),

$$\varrho\left(\begin{bmatrix} x \\ w \end{bmatrix}\right) = \begin{bmatrix} f_x & f_w \end{bmatrix}\begin{bmatrix} x \\ w \end{bmatrix} = f_1 x_1 + f_2 x_2 + f_3 x_3 + \ldots + f_n x_n + f_w w$$

or the CNGSC controller φ the rejection of disturbances is less effective. This is due to the fact that both controllers are expressed as continuous functions of the states and thus the induced control outputs are not instantly in saturation at the beginning of a disturbance. Therefore, the counteraction to the disturbance is smaller and the loss of control can occur for smaller disturbances than with the ς controller.

If we compare the CNGSC controller φ against the linear state feedback controller ϱ then the condition

$$\left|\varphi\left(\begin{bmatrix} x \\ w \end{bmatrix}\right)\right| < \left|\begin{bmatrix} f_x & f_w \end{bmatrix}\begin{bmatrix} x \\ w \end{bmatrix}\right| \tag{8.93}$$

might be satisfied. Since during a disturbance x_1 leaves the equilibrium and approaches the boundaries of the null controllable region the gain $k(x)$ is decreased which reduces the impact of the terms

$$f_2 x_2 + f_3 x_3 + \ldots + f_n x_n + f_w w$$

on the control. Thus, if the sum of these terms is large and has the same sign as $f_1 x_1$ then Condition (8.93) is inevitably satisfied. In this case the disturbance reaction of the CNGSC controller is less effective than the counteraction of the linear state feedback. Even though the CNGSC controller φ possesses a larger region of attraction than the linear state feedback controller ϱ, the stability may be lost with φ but not with ϱ during a disturbance. As mentioned above, this is due to the fact that the concept linked to the region of attraction and the null controllable region is no longer valid during a disturbance.

We can correct this weakness of the CNGSC controller by amplifying the effect of the main term $f_1 x_1$. Consider for this a modified φ controller, defined as

$$\varphi_m \left(\begin{bmatrix} x \\ w \end{bmatrix} \right) = g(x) f_1 x_1 + k(x)(f_2 x_2 + f_3 x_3 + \ldots + f_n x_n + f_w w), \qquad (8.94)$$

where $g(x)$ is a linear or nonlinear function. We may consider a correction by just increasing the gain of the unstable state feedback by defining

$$g(x) = c = \text{const.} \qquad (8.95)$$

In this case φ_m no longer belongs to the class $\mathcal{K}_c$ (Section 8.2) since at the equilibrium it is no more equivalent to the linear state feedback controller ϱ. Moreover, this type of correction intrinsically implies a modification of the closed-loop system dynamics. These two drawbacks can be avoided by introducing a nonlinearity of the type of

$$g(x) = 1 + x_1^2 c, \qquad (8.96)$$

where $c > 0$ is a constant. Since $1 + x_1^2 c \geq 1$ and thus $f_1 g(x) \leq f_1$ (from the Hurwitz condition $f_1 < -1$) we may state by intuition that this modified controller φ_m would probably work well and that its region of attraction would be the same as for φ. But, due to the introduction of the nonlinearity $g(x) = 1 + x_1^2 c$, a formal proof of the closed-loop system stability and the region of attraction is considerably harder to provide. It is therefore a challenging work for future investigations in the field of nonlinear control.

8.6.4 Asymmetric saturation

Figure 8.25 shows that for the considered disturbance the trajectory evolves asymmetrically in the unstable subspace, i.e. the amplitude of the deflection is higher in the $x_1 < 0$ direction. Since all considered plasma disturbances show a similar behavior (drop of β_p and l_i) its induced evolution of the trajectory is similarly asymmetric, too. Therefore, the stability properties during the considered disturbances could be improved by moving the null controllable region in the $x_1 < 0$ direction. This can be achieved by driving the normalised saturation asymmetrically. As discussed in Section 8.3.2 an asymmetric saturation is obtained by imposing a constant non-zero feedforward input, referred to as $u_{vc_{ff}} = \text{const} \neq 0$.

Consider for an asymmetric normalised saturation the upper saturation level $\sigma_u > 0$ and the lower level $\sigma_l < 0$ for which we assume that $\sigma_u - \sigma_l = 2$. Therefore, from the

results given in Chapter 7 we derive the implying asymmetric null controllable region, defined as

$$\mathcal{C}_{as} = \{x \in \mathbb{R}^n : -\sigma_u < x_1 < -\sigma_l\} \tag{8.97}$$

and its boundaries

$$\mathcal{C}_{as_+} = \{x \in \mathbb{R}^n : x_1 = -\sigma_l\} \quad \text{and} \quad \mathcal{C}_{as_-} = \{x \in \mathbb{R}^n : x_1 = -\sigma_u\}. \tag{8.98}$$

Figure 8.26 illustrates the boundaries of the asymmetric null controllable region. By considering the upper saturation level $\sigma_u = 1.5$ and the lower level $\sigma_l = -0.5$ the trajectory remains in the asymmetric null controllable region. Thus, the closed-loop system with an asymmetrically driven saturation should be able to handle larger disturbances than with a symmetric saturation. Note that this proposition is a new consideration for tokamaks and it has therefore to be verified rigorously in a future work.
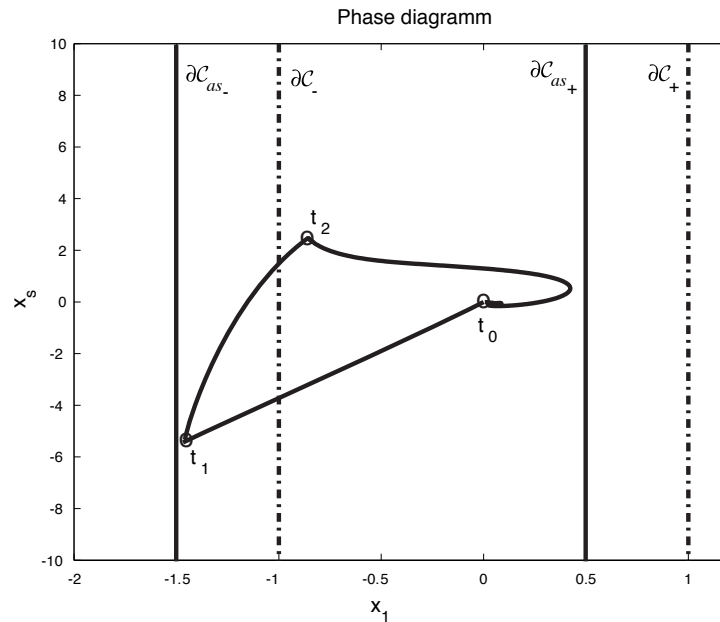

Figure 8.26: Trajectory of the tokamak closed-loop system during a disturbance and the boundaries of the asymmetric null controllable region.

8.7   Bandwidth limitation and time delay

In practice there is a bandwidth limitation of the control signal due to the power supplies. Furthermore, there is a pure time delay in the control signal due to the time needed by the implemented controller to compute the control signal and due to any pure delay in the power supplies. In this section we provide an elementary analysis of the deleterious effects that a bandwidth limitation and a pure delay can induce on the closed-loop system stability. Furthermore, we give solutions to reduce or even avoid these deleterious effects.

Since the bandwidth limitation can be modeled by a linear model, which in general is a first order low-pass filter, it can straightforwardly be incorporated into the linear normalised system. Thus we can analyse the pure delay problem by means of the linear

normalised system which either has incorporated the bandwidth limitation or not. This permits us to consider either both problems separately or to consider the accumulative deleterious effect of both problems together.

For the same reason mentioned in Section 8.6 we assume that the reference tracking has no impact on the behaviour of the system with bandwidth limitation and pure delay. We therefore set the feedforward and reference signals at zero ($q = 0$) which implies an equilibrium $\bar{x} = 0$ and a state error $x_e = x$. Since it is an elementary analysis we restrict the study to the deleterious effects on the region of attraction and the null controllable region. Thus, since the concept linked to both regions is only valid for autonomous systems (Section 8.6) we consider the disturbance input as $w = 0$. With this assumption the normalised system (8.42) becomes

$$\dot{x} = Ax + bu \tag{8.99}$$
$$\tilde{u} = \tilde{C}x = fx.$$

8.7.1 Bandwidth limitation

The bandwidth limitations of the power supplies are represented by means of linear low-pass filters. Figure 8.27 shows the linear tokamak closed-loop system with filters for the SC controller and for the VC controller. If we want to apply the results provided in Sections 8.3.5 and 8.3.6 then we simply add the filters into the tokamak system described by System (8.32). Since we do not yet consider the SC saturation, we may also incorporate the SC filters into the SC controller (System (8.32)).

Figure 8.27: The tokamak closed-loop system with bandwidth limitation of the control signals modeled with low-pass filters.

Since the incorporation of filters introduces new states we have to reconstruct these states. This reconstruction is simple if we consider a first order low-pass filter given by

$$Y_f(s) = \frac{1}{1 + s\tau} U_f(s), \tag{8.100}$$

where $Y_f(s)$ denotes the output, $U_f(s)$ the input and τ the time constant of the filter defining the bandwidth limitation. Thus, since the state space representation of this

low-pass filter can be given by

$$\dot{x}_f = -\frac{1}{\tau}x_f + \frac{1}{\tau}u_f \tag{8.101}$$

$$y_f = x_f,$$

the output of the filter y_f is equal to the state of the filter x_f. This permits us to reconstruct the state of the filter by measuring the output of the power supply. If this is not practicable due to noise or if we have to deal with a higher order filter then we can try to reconstruct the state or states

- by means of the tokamak outputs with the method proposed in Section 8.4,

- by standard dynamic observers like the Luenberger observer [58] and the Kalman filter observer [15, 41]

- by simply integrating numerically in real-time the filter output as a function of the filter input by means of a filter model (System (8.101) for a first order filter) .

The aim of the section is to show that the null controllable region is reduced by the bandwidth limitation which intrinsically implies a reduction of the region of attraction. Since the SC controller has no or only a negligible stabilisation effect on the closed-loop system (Section 8.3.4) we only consider the effect of the VC filter. Furthermore, it is more convenient to make the demonstration by considering a first order low-pass filter (System 8.101) and a second order normalised system (Equation 8.102) given by

$$\begin{bmatrix} \dot{x}_1 \\ \dot{x}_2 \end{bmatrix} = \begin{bmatrix} \lambda_1 & 0 \\ 0 & \lambda_2 \end{bmatrix} \begin{bmatrix} x_1 \\ x_2 \end{bmatrix} + \begin{bmatrix} \lambda_1 \\ \lambda_2 \end{bmatrix} u \tag{8.102}$$

$$\tilde{u} = f_1 x_1 + f_2 x_2.$$

The case of an $n > 2$ order normalised system the demonstration is similar and straightforward. Figure 8.28 illustrates the normalised closed-loop system with a VC filter.
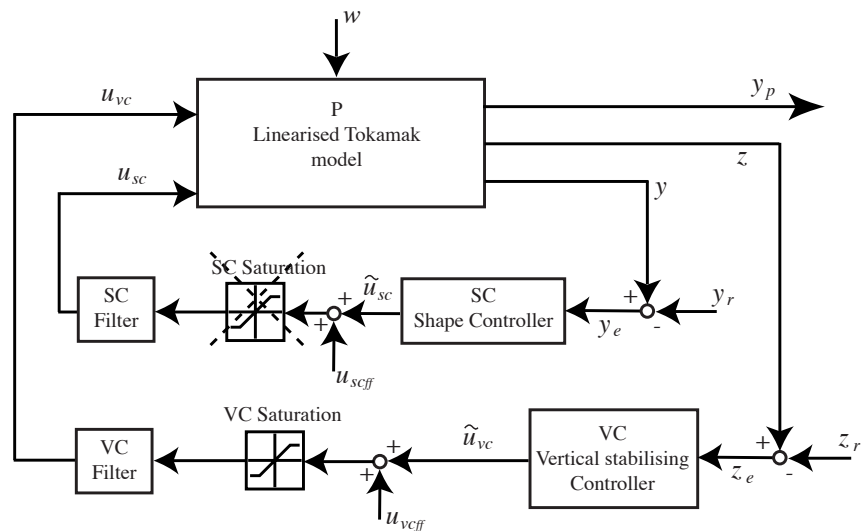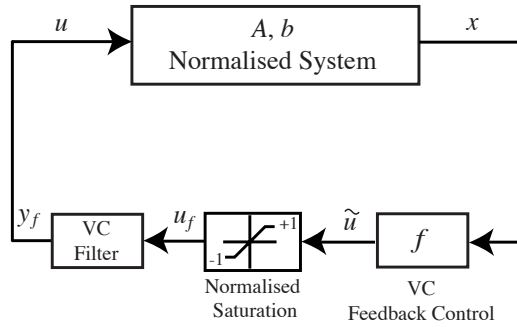

Figure 8.28: The tokamak closed-loop system with bandwidth limitation of the control signal modeled with a low-pass filter.

The serial connection of the filter and the normalised system ($u = y_f$) leads to the system

$$\begin{bmatrix} \dot{x}_1 \\ \dot{x}_2 \\ \dot{x}_f \end{bmatrix} = A_c x + b_c u_f = \begin{bmatrix} \lambda_1 & 0 & \lambda_1 \\ 0 & \lambda_2 & \lambda_2 \\ 0 & 0 & -\frac{1}{\tau} \end{bmatrix} \begin{bmatrix} x_1 \\ x_2 \\ x_f \end{bmatrix} + \begin{bmatrix} 0 \\ 0 \\ \frac{1}{\tau} \end{bmatrix} u_f \tag{8.103}$$

$$\tilde{u} = f_1 x_1 + f_2 x_2.$$

Since A_c is no longer diagonal, x_1 no longer represents the unstable state. Thus, we have to normalise this system by means of the linear state transformation

$$x = T\grave{x},$$

where

$$T = T^{-1} = \begin{bmatrix} 1 & 0 & \frac{\lambda_1\tau}{1+\lambda_1\tau} \\ 0 & 1 & \frac{\lambda_2\tau}{1+\lambda_2\tau} \\ 0 & 0 & -1 \end{bmatrix}. \tag{8.104}$$

This leads to the system

$$\dot{\grave{x}} = \begin{bmatrix} \dot{\grave{x}}_1 \\ \dot{\grave{x}}_2 \\ \dot{\grave{x}}_f \end{bmatrix} = T^{-1}A_cT\grave{x} + T^{-1}b_cu_f \tag{8.105}$$

$$= \begin{bmatrix} \lambda_1 & 0 & 0 \\ 0 & \lambda_2 & 0 \\ 0 & 0 & -\frac{1}{\tau} \end{bmatrix} \begin{bmatrix} \grave{x}_1 \\ \grave{x}_2 \\ \grave{x}_f \end{bmatrix} + \begin{bmatrix} \frac{\lambda_1}{1+\lambda_1\tau} \\ \frac{\lambda_2}{1+\lambda_2\tau} \\ -\frac{1}{\tau} \end{bmatrix} u_f,$$

where $\grave{x}_1$ represents the unstable state. We observe that when there is no bandwidth limitation $\tau = 0$ then this system corresponds exactly to the initially considered system (System 8.102). Note that for this observation we do not consider the state of the filter $\grave{x}_f$ since for $\tau = 0$ it does not exist. The equilibrium points corresponding to a saturated input $u_f = +1$ or $u_f = -1$, referred to as $\grave{x}_{e\pm}$ in Chapter 7, are given by

$$\grave{x}_{e\pm} = T^{-1}A_cb_c = \pm \begin{bmatrix} \frac{1}{1+\lambda_1\tau} \\ \frac{1}{1+\lambda_2\tau} \\ 1 \end{bmatrix}. \tag{8.106}$$

As discussed in Chapter 7, the boundaries of the null controllable region are equal to the equilibrium in the unstable state subspace $\grave{x}_{e\pm1} = \frac{1}{1+\lambda_1\tau}$. Thus, the null controllable region is given by

$$\mathcal{C} = \{\grave{x} \in \mathbb{R}^n : \grave{x}_1 < \frac{1}{1+\lambda_1\tau}\}. \tag{8.107}$$

We conclude that if the bandwidth of the power supply is reduced $\tau > 0$ then the null controllable region becomes smaller. Thus, the region of attraction for the CNGSC controller is equivalently reduced since it is equivalent to the null controllable region.

Theoretically, as far as pure linear systems are concerned, such a low-pass filter can be compensated by incorporating a compensator, such as

$$Y_c(s) = G_c(s)\tilde{U}(s) = \frac{1+s\tau}{1+s\tau_c}\tilde{U}(s), \tag{8.108}$$

into the VC controller (Figure 8.29). An ideal compensation is given for $\tau_c = 0$. We introduce a low-pass filter with a smaller time constant $\tau_c < \tau$ (larger bandwidth) since in practice there is always a bandwidth limitation due to other controller equipment components. The compensator works perfectly under linear conditions for which we can

connect the filter and the compensator directly in series by imposing $U_f(s) = Y_c(s)$, which leads to

$$Y_f(s) = \frac{1}{1 + s\tau_c}\tilde{U}(s). \tag{8.109}$$

But since there is the saturation between both components (Figure 8.29) the effect of the compensator is considerably reduced during saturation. If we consider a step signal at the compensator input $\tilde{u}$, referred to as $\tilde{U}(s) = \frac{A_{\tilde{u}}}{s}$, then at the beginning of the step response ($t = 0$) this signal is amplified by the factor $\frac{\tau}{\tau_c} > 1$ (since $\tau_c < \tau$). Note that this factor is due to the elementary Laplace transform rule (initial-value theorem)

$$\lim_{t \to 0} y_c(t) = \lim_{s \to \infty} s\, Y_c(s) = \lim_{s \to \infty} s\, G_c(s)\tilde{U}(s) = \lim_{s \to \infty} s\frac{1 + s\tau}{1 + s\tau_c}\frac{A_{\tilde{u}}}{s} = \frac{\tau}{\tau_c}A_{\tilde{u}}.$$

Thus, if this factor is large then the resulting induced large output signal y_c is saturating the power supply which considerably reduces the effect of the compensation. We conclude that due to the saturation the bandwidth of the power supply cannot be efficiently increased by a compensation. Therefore, the only way to augment the bandwidth is to implement a faster power supply.
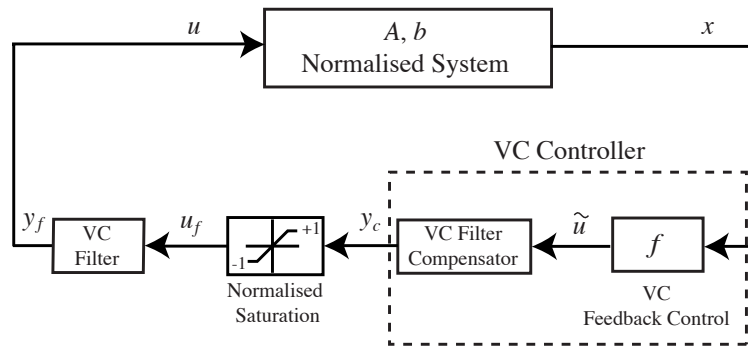
Figure 8.29: The tokamak closed-loop system with bandwidth limitation and compensator.

8.7.2   Pure time delay

There are two major pure time delays in the tokamak closed-loop system. One delay is due to the power supplies, referred to as t_{ps} and the other delay is due to the computing time of the controllers, referred to as t_c. The total delay is given by

$$t_d = t_{ps} + t_c. \tag{8.110}$$

Note that the delays in the VC control loop and in the SC control loop may differ from each other. Figure 8.30 illustrates the tokamak closed-loop system with the SC and VC delays.

Since we are generally assuming that the SC controller has no or only a negligible stabilisation effect on the closed-loop system (Section 8.3.4) we only consider the effect of the VC delay. The resulting normalised system is illustrated in Figure 8.31.

Figure 8.30: The tokamak closed-loop system with time delays due the controller computing time and due to the power supplies.
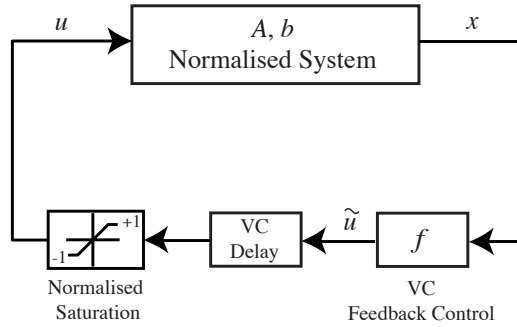
Figure 8.31: The normalised closed-loop system with solely the VC time delay.

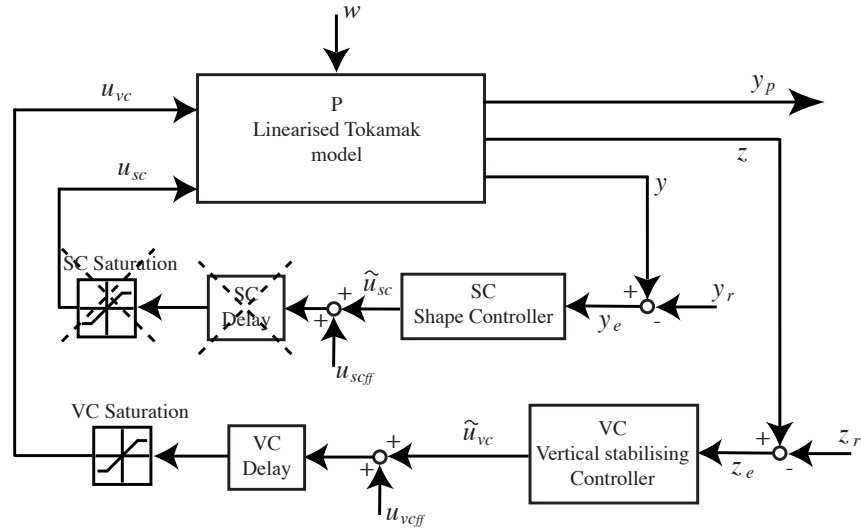Since the null controllable region is solely bounded in the subspace of the unstable state x_1 (Chapter 7) again only the effect on the unstable state has to be analysed. Thus, we consider the part of System (8.99) linked to the unstable state which is

$$\dot{x}_1 = \lambda_1 x_1 + \lambda_1 u. \tag{8.111}$$

Furthermore, we consider an arbitrary stabilising linear or nonlinear state feedback, defined as

$$\tilde{u} = \vartheta(x). \tag{8.112}$$

The deleterious effect of the delay on the stability of the closed-loop system is demonstrated by considering a trajectory in the state space (Figure 8.32). Since only the effect on the unstable state x_1 is important it is sufficient to show the evolution of the trajectory in a subspace composed of the unstable state x_1 and any arbitrary chosen stable state, referred to as x_s. Moreover, we discuss the problem solely for $x_1 < 0$ because since the system is symmetric the demonstration for $x_1 > 0$ is similar.

In Figure 8.32 the states $x(t_{s_i})$ represent the states which are acquired from the control system at the times t_{s_i}, where the sampling time of the acquisition is defined as

$$h = t_{i+1} - t_i > 0, \quad \text{for } i = 1, 2, 3, \ldots. \tag{8.113}$$

The time $t_{o_i} = t_{s_i} + t_d$ is the time at which the control $\vartheta(x(t_{s_i}))$ corresponding to the state $x(t_{s_i})$ is available at the output of the power supply. Thus, due to the delay t_d the control signal at the state $x(t_{o_i})$ is not $\vartheta(x(t_{o_i}))$ but $\vartheta(x(t_{s_i}))$. The distances d_i denote the distances in the unstable state subspace covered by the trajectory during the delay t_d. When the trajectory is approaching the negative boundary $x_{e-1} = -1$ of the null controllable region then the control u has to approach the positive saturation $+1$ to be able to stabilise System (8.111). On the other hand, for the states which are more distant to the boundary of the null controllable, referred to as $x(t_{s_i})$, the control amplitude is often smaller, especially for continuous controllers like the linear state feedback controller $\varrho(x)$ (Equation (8.46)) and the CNGSC controller $\varphi(x)$ (Equations (8.50) and (8.51)). In this case the relation

$$\vartheta(x(t_{o_i})) > \vartheta(x(t_{s_i})) \tag{8.114}$$

is satisfied. Since at the states $x(t_{o_i})$ a smaller control amplitude $\vartheta(x(t_{s_i}))$ is available, the control action might be too weak to stabilise the System (8.111) and the trajectory might leave the null controllable region $(\vartheta(x(t_{o_3})))$. Thus, the region of attraction is reduced. But since the delay represents a nonlinear function it is not trivial to derive the region of attraction.
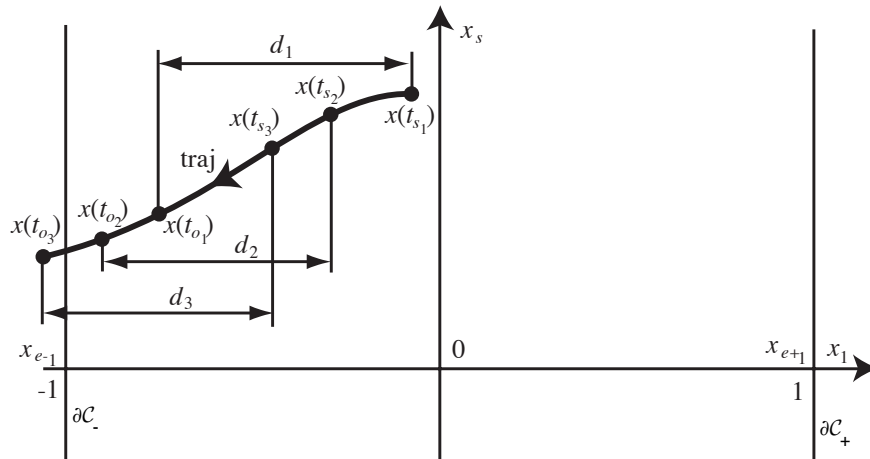
Figure 8.32: The normalised closed-loop system with solely the VC time delay.

Nevertheless, there exists a way to maintain the region of attraction equal to the null controllable region even with a delay. We have to impose two regions for which the control is in saturation. In Figure 8.33 these two saturating regions are giving by

- $\tilde{u} = u = +1$ for all $x_1 = [x_{e-1}, \Sigma_-] = [-1, \Sigma_-] < 0$ and

- $\tilde{u} = u = -1$ for all $x_1 = [\Sigma_+, x_{e+1}] = [\Sigma_+, 1] > 0$,

where $\Sigma_- = -\Sigma_+$ since the system is symmetric. These two regions ensure that the trajectories of the considered closed-loop system do not leave the null controllable region since $\dot{x}_1 < 0$ for $0 < x_1 \in [\Sigma_+, x_{e+1})$ and $\dot{x}_1 > 0$ for $0 > x_1 \in (x_{e-1}, \Sigma_-]$ is guaranteed. Let us assume for the remaining demonstration that the following distances in the unstable state subspace are known:

- d representing the distance covered by the trajectory during the delay t_d

- d_h representing the distance covered by the trajectory during the sampling time h.

The distance d_h ensures that a sampling, referred to the time t_s, occurs during the covering of the region $0 > x_1 \in (\Sigma_- - d_h, \Sigma_-]$ (Figure 8.33). This ensures that the control $\tilde{u} = u = -1$ is available at the state $x(t_o)$. Furthermore, since $|x_{e\pm_1}| - |\Sigma_\pm|| = d + d_h$ the state $x(t_o)$ is guaranteed to be located inside the null controllable region. Thus, $\dot{x}_1 > 0$ is guaranteed for $x_1 < 0$ and the trajectory cannot leave the null controllable region. Figure 8.33 illustrates three trajectories, where the two trajectories 'traj$_1$' and 'traj$_3$' represent the limiting cases. Note that for the third trajectory 'traj$_3$' the state $x(t_0)$ is on the boundary of the null controllable region for which $\dot{x}_1 = 0$ is satisfied. Thus, the third trajectory cannot be steered back to the origin. But it represents the limiting case and therefore all trajectories for which the sampling occurs in the interval $0 > x_1 \in (\Sigma_- - d_h, \Sigma_-]$ will remain in the null controllable region.
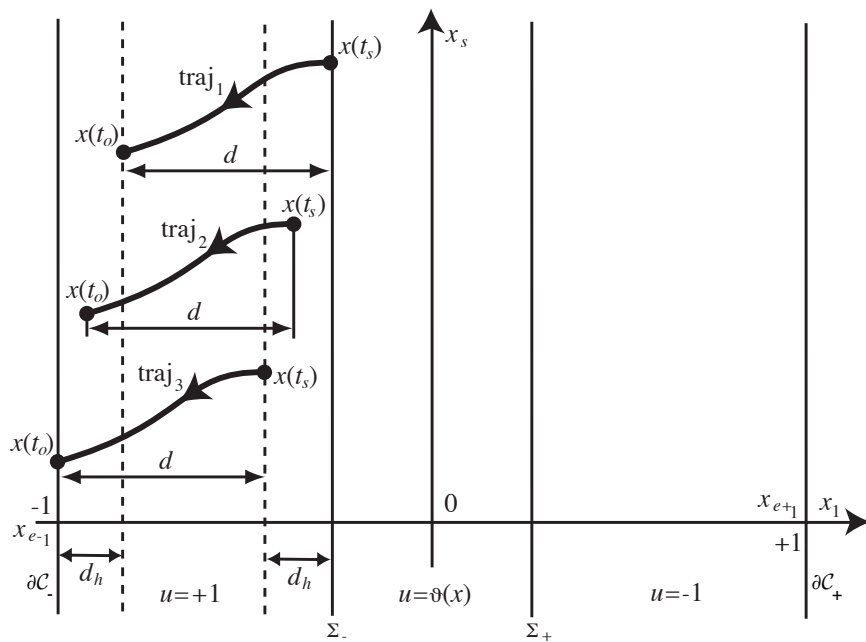
Figure 8.33: The normalised closed-loop system with solely the VC time delay.

We need to compute the distance $d + d_h = |x_{e\pm_1}| - |\Sigma_\pm||$ to be able to determine the boundary $\Sigma_\pm$ of the saturating regions. It is evident that the input u of System (8.111) varies as a function of the control law $\tilde{u} = \vartheta(x)$ and therefore it is difficult to solve the differential equation of System (8.111) to get this distance. But by considering the worst case which is represented by the largest distance $d + d_h$ which can be achieved with a control $u(t) \in [-1, 1]$ a solution exists. When we consider the boundary $\Sigma_- < 0$ and $x_1 < 0$ then the largest distance is given for the constant input $u(t) = -1$ since for this control input the velocity amplitude, referred to as $|\dot{x}_1|$, of System (8.111) is the highest. Therefore, System (8.111) with the constant input $u = -1$ resulting in

$$\dot{x}_1 = \lambda_1 x_1 - \lambda_1 \tag{8.115}$$

can be solved. Its solution is given by

$$x_1(t) = e^{\lambda_1 t} C + 1, \tag{8.116}$$

where C represents the integration constant. We define the initial condition as $x_1(0) = \Sigma_-$ resulting in

$$C = x_1(0) - 1 = \Sigma_- - 1. \tag{8.117}$$

Therefore, the final condition has to be

$$x(t) = x(t_d + h) = x_1(0) - (d + d_h) = \Sigma_- - (d + d_h) = x_{e-1} = -1 \tag{8.118}$$

which from Equation (8.116) leads to

$$x_{e-1} = -1 = e^{\lambda_1 t}(\Sigma_- - 1) + 1. \tag{8.119}$$

This leads to the saturating regions boundaries

$$\Sigma_- = \frac{-2}{e^{\lambda_1(t_d+h)}} + 1 \tag{8.120}$$

$$\Sigma_+ = -\Sigma_- = \frac{2}{e^{\lambda_1(t_d+h)}} - 1.$$

The proposed solution with the saturating regions works only for relative short delays for which the condition

$$e^{\lambda_1(t_d+h)} \leq 2 \tag{8.121}$$

is satisfied. Note that at the limit $e^{\lambda_1(t_d+h)} = 2$ the resulting control law corresponds to controller $\varsigma(x)$ given by Equation (8.89).

When we consider the arbitrary controller ϑ then in the presence of a delay its control law has to be modified to become

$$\tilde{u} = \vartheta_d(x) = \begin{cases} \vartheta(x) & \text{if} \quad |x_1| < |\Sigma_\pm| \\ -\text{sgn}(x_1) & \text{if} \quad |x_1| \geq |\Sigma_\pm| \end{cases}. \tag{8.122}$$

By considering the CNGSC controller $\varphi(x)$ (Equations (8.50) and (8.51)) it is evident that this modification induces a discontinuity of the control signal $\tilde{u}$ at the boundaries $\Sigma_\pm$. To eliminate these discontinuities we can modify the CNGSC controller as follows

$$\varphi_d\left(\begin{bmatrix} x \\ w \end{bmatrix}\right) = f_1 x_1 + k_d(x)(f_2 x_2 + f_3 x_3 + \ldots + f_n x_n + f_w w), \tag{8.123}$$

with

$$k_d(x) = \begin{cases} \Sigma_\pm^2 - x_1^2 & \text{if} \quad |x_1| < |\Sigma_\pm| \\ 0 & \text{if} \quad |x_1| \geq |\Sigma_\pm| \end{cases} \quad \text{or} \tag{8.124}$$

$$k_d(x) = \begin{cases} |\Sigma_\pm| - |x_1| & \text{if} \quad |x_1| \leq 1 \\ 0 & \text{if} \quad |x_1| \geq |\Sigma_\pm| \end{cases}.$$

Furthermore, we have to ensure that the controller is saturating the power supply $|\tilde{u}| \geq 1$ for $|x_1| \geq |\Sigma_\pm|$. Thus, since for $|x_1| \geq |\Sigma_\pm|$ the controller is equivalent to $\varphi_d\left(\begin{bmatrix} x & w \end{bmatrix}\right)^T = f_1 x_1$, the condition

$$|f_1 x_1| \geq 1 \tag{8.125}$$

has to be satisfied. If this condition is not satisfied then we either have to increase the gain of the control parameter f_1 or the gain of the VC input-output controller, implying an increase of the f_1 gain. The right gain increase is intrinsically provided when we consider a slightly different controller given by

$$\varphi_d \left(\begin{bmatrix} x \\ w \end{bmatrix} \right) = f_1 \frac{x_1}{|\Sigma_{\pm}|} + k_d(x)(f_2 x_2 + f_3 x_3 + \ldots + f_n x_n + f_w w), \qquad (8.126)$$

with

$$k_d(x) = \begin{cases} 1 - \frac{x_1^2}{\Sigma_{\pm}^2} & \text{if} \quad |x_1| < |\Sigma_{\pm}| \\ 0 & \text{if} \quad |x_1| \geq |\Sigma_{\pm}| \end{cases} \qquad \text{or} \qquad (8.127)$$

$$k_d(x) = \begin{cases} 1 - \frac{|x_1|}{|\Sigma_{\pm}|} & \text{if} \quad |x_1| \leq 1 \\ 0 & \text{if} \quad |x_1| \geq |\Sigma_{\pm}| \end{cases} .$$

Part III

Validation

Chapter 9

Validation via simulation

9.1 Simulation by means of linear models

9.1.1 Validation on ITER-FEAT with the linear CREATE-L model

In this section the validation is carried out on ITER-FEAT by means of its linear CREATE-L model [31], including the SC and VC input-output controllers proposed by [6]. The aim is to compare via simulation the reference VC controller against the proposed CNGSC controller. The reference VC controller expressed as a state feedback controller is given by Equation (8.46), i.e.

$$\varrho\left(\begin{bmatrix} x \\ w \end{bmatrix}\right) = \begin{bmatrix} f_x & f_w \end{bmatrix} \begin{bmatrix} x \\ w \end{bmatrix} = f_1 x_1 + f_2 x_2 + f_3 x_3 + \ldots + f_n x_n + f_w w,$$

while the CNGSC controller is given by Equation (8.50) with the extended nonlinear Function (8.92), i.e.

$$\varphi\left(\begin{bmatrix} x \\ w \end{bmatrix}\right) = f_1 x_1 + k(x)(f_2 x_2 + f_3 x_3 + \ldots + f_n x_n + f_w w),$$

and

$$k(x) = \begin{cases} 1 - x_1^2 & \text{if} \quad |x_1| \le 1 \\ 0 & \text{if} \quad |x_1| > 1 \end{cases}.$$

Note that the CREATE-L model for ITER-FEAT provides no magnetic diagnostic outputs so far. Thus, we cannot apply the state reconstruction as proposed in Section 8.4. We therefore use the state information directly from the linear model.

The comparison is illustrated in phase diagrams. Since we deal with a high order system (50 .. 100 states) we cannot show the evolution of all states. Thus, the phase diagrams show the evolution of only two states: i) the unstable state, referred to as x_1 and ii) one of the most disturbed stable states, referred to as x_s. For what follows, the region of attraction of the reference controller is referred to as $\mathcal{A}_r$ and the region of attraction of the CNGSC controller is referred to as $\mathcal{A}_c$. We show via simulation that for the reference controller the region of attraction is strictly a subset of the null controllable region $\mathcal{A}_r \subset \mathcal{C}$. Furthermore, we show that the trajectories of the closed-loop system with the CNGSC controller converge to the origin if the initial conditions are inside $\mathcal{A}_c = \mathcal{C}$.

9.1.1.1   Initial conditions

For the first example we do not disturb the system, thus $\dot{w} = 0$. Instead, we set non-zero initial conditions. The phase diagram (Figure 9.1) shows the evolution of the unstable state, denoted by x_1 and one of the most disturbed stable states, denoted by x_s. The starting point x_{init} denotes the initial conditions which are located inside the null control-lable region $x_{init} \in \mathcal{C}$. Since for the CNGSC controller the initial conditions are located within the region of attraction $x_{init} \in \mathcal{A}_c = \mathcal{C}$ the trajectory converges to the origin. For the reference controller the trajectory diverges, thus confirming by simulation that $\mathcal{A}_r \subset \mathcal{C}$.
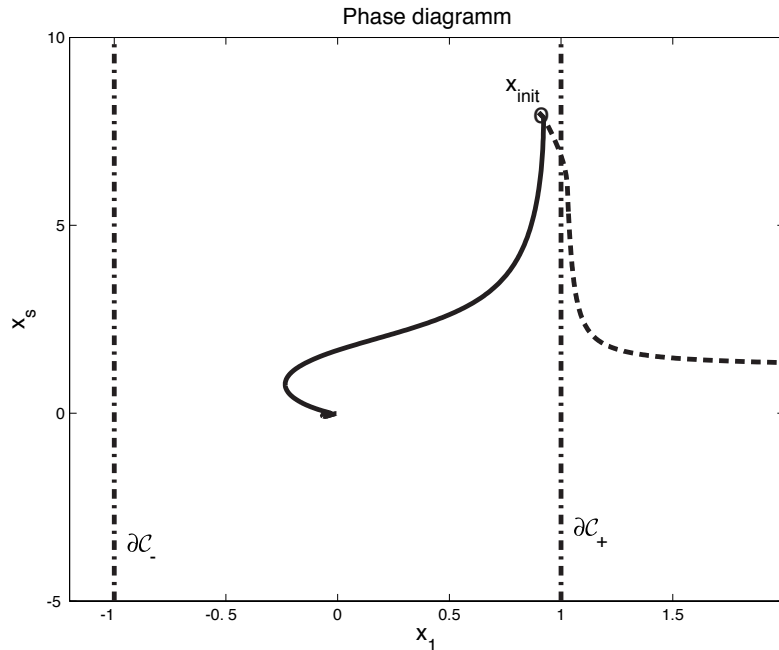
Figure 9.1: Example with non-zero initial conditions (x_{init}) and without disturbance, dashed: reference controller, solid: CNGSC controller. The model is CREATE-L.

9.1.1.2   Large disturbance

To disturb the system away from the equilibrium we apply an ELM disturbance as illustrated in Figure 8.24 (Section 8.6.1). The disturbance starts at t_0, reaches its maximum at t_1 and vanishes at t_2. Since it is difficult to know whether the state remains in the region of attraction during the disturbance (Section 8.6), we have to wait until the disturbance vanishes at $t = t_2$ to determine if the controller has been able to stabilise the system.

The evolution of the trajectories for both controllers during and after a large disturbance is illustrated in Figure 9.2. At t_2 the states of the systems with both controllers are in $\mathcal{C}$. Since for the CNGSC controller $\mathcal{A}_c = \mathcal{C}$, the trajectory converges to the origin. For the reference controller the trajectory diverges and thus, the state is not in $\mathcal{A}_r$.

9.1.1.3   Huge disturbance

The third example shows the trajectory evolutions for a much larger disturbance amplitude (Figure 9.3). Both trajectories leave the null controllable region $\mathcal{C}$ and only the
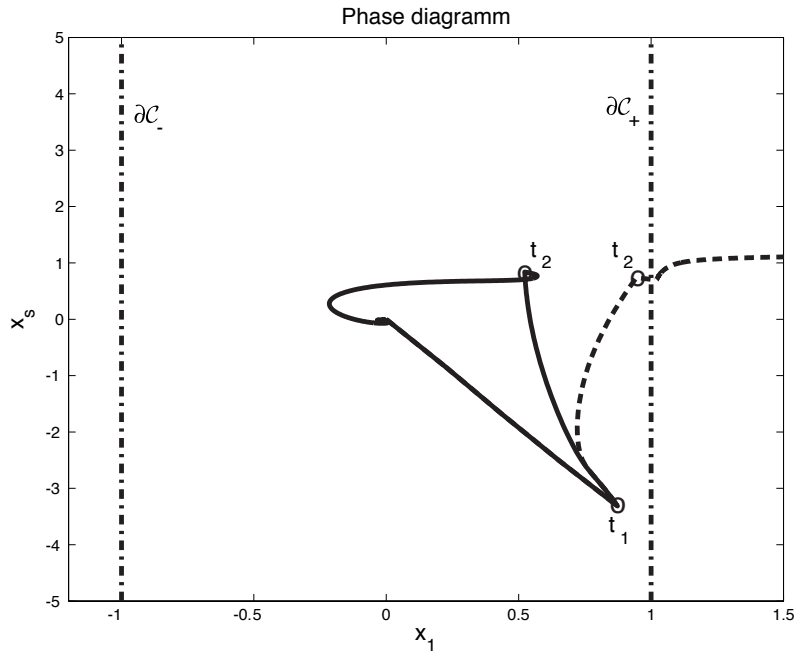
Figure 9.2: Example with a large disturbance, dashed: reference controller, solid: CNGSC controller. The model is CREATE-L.

trajectory for the system with the CNGSC controller reenters $\mathcal{C}$. Therefore, this trajectory converges to the origin and the trajectory of the system with the reference controller diverges.

For all these examples, the unstable state x_1 is brought back to the origin faster when the CNGSC controller is used. This is the benefit of the nonlinear function $k(x)$ which helps the controller concentrate on the unstable state in the proximity of the boundaries of $\mathcal{C}$ and beyond it.

9.1.2 Validation on JET with the linear CREATE-L model

We implement the same technique on the CREATE-L model for JET [1], including the reference controller. Since for JET the magnetic diagnostic outputs are available, the unstable state is reconstructed as proposed in Section 8.4. We increase the amplitude of the disturbance until the closed-loop system with the reference controller loses control due to saturation of the FRFA (Fast Radial Field Amplifier) supply. The simulation is repeated with the CNGSC controller and control is no longer lost.

Figure 9.4 shows an example of the evolution of the vertical plasma position z and the FRFA control voltage for a very large ELM disturbance in JET. The disturbance starts at t_0, reaches a maximum at t_1 and vanishes at t_2 (vertical dashed lines). The reference controller loses stability just after t_1.
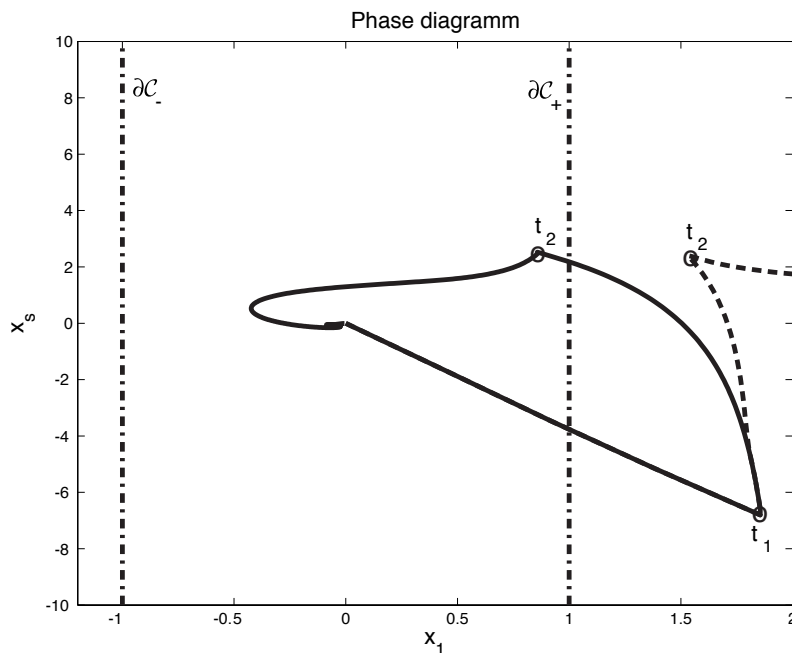
Figure 9.3: Example with a huge disturbance, dashed: reference controller, solid: CNGSC controller. The model is CREATE-L.
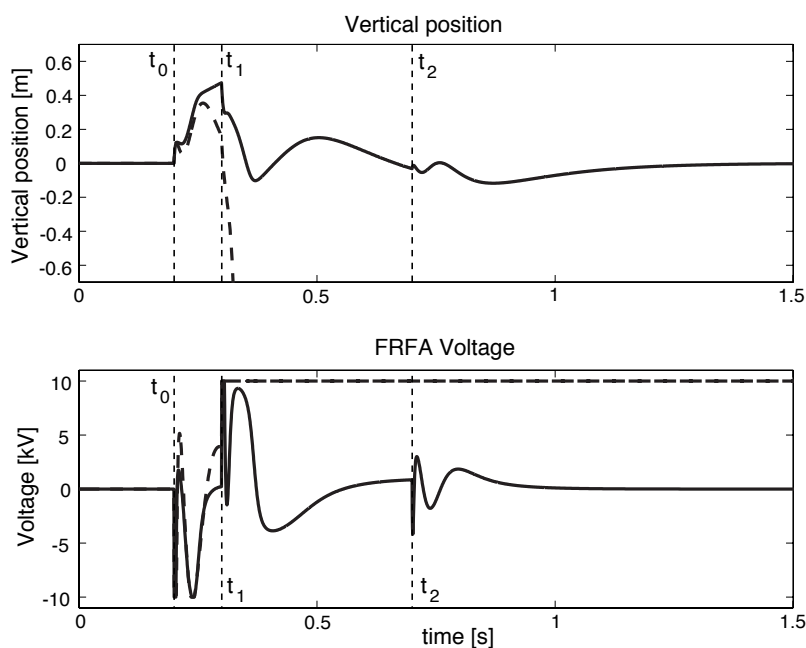
Figure 9.4: The CNGSC controller (solid) on a JET simulation. The reference controller (dashed) loses control.

9.2 Simulation by means of the DINA-CH code

9.2.1 Validation on TCV with the nonlinear DINA-CH code

Experimental validations on the TCV tokamak in operation cannot be carried out so far since the TCV control system does not permit the possibility of implementing nonlin-

ear control laws as required for the CNGSC controller. Therefore, we provide validation results which are carried out on TCV by means of the DINA-CH code a recent implementation of the original code. For the purpose of the controller design and the state reconstruction the linear RZIP model is used.

9.2.1.1 Modification of the standard VC controller due to the TCV specific characteristics

The TCV control system possesses two different vertical position stabilising controllers (VC controllers). The first controller supplies a combination of several F-coils, while the second controller supplies a single coil, referred to as the G-coil, located inside the vacuum vessel (Figure 3.1). For discharges with low vertical instability growth rates ($\gamma < 1000$) it is sufficient to only use the F-coil combination. But the F-coils are not able to stabilise discharges with higher growth rates ($\gamma > 1000$) and thus the G-coil has to be added for such discharges. By inspecting the closed-loop system consisting of the TCV, the VC controllers and the SC controller two major problems arise, which are linked to the fact that we only consider systems with a single unstable pole and a single saturated input:

1. When we consider discharges with low growth rates then in general only the F-coil combination is used. The problem is that every F-coil has its own power supply. Moreover, the controller gains associated to each F-coil differs from coil to coil. This leads to a VC controller system which has to supply several power supplies and thus to a stabilising control problem which has to deal with several saturated inputs.

2. When we consider discharges with high growth rates then both the F-coil combination and the G-coil are used. Since the G-coil is supplied by a single power supply (single saturated input) the first intention was to only consider the stabilising problem linked to the G-coil. But it turns out that the closed-loop system consisting of the linear TCV model, the SC controller and the VC controller with only the F-coil combination (without the G-coil) possesses not just a single unstable pole but two unstable poles.

For these reasons we modify the VC controller by removing the VC controller part suppling the F-coil combination and by only considering the VC controller part linked to the single power supply of the G-coil. This results in a problem consisting of a system with a single unstable pole and a single saturated input, while the new modified reference VC control is a simple PD controller.

9.2.1.2 Simulation setup

For the purposes of the validation we exploit discharge #20333 possessing a vertical instability growth rate of $\gamma \approx 230$ [rad/s]. The RZIP model and the initial conditions for the DINA-CH code are derived at the time 0.5 s.

For what follows we will use a succession of test disturbances which are occurring every 0.02 s as a result of pulsed anomalous transport. Figure 9.5 illustrates the derivative of the considered disturbances, referred to as $\dot{w}$. The amplitude of the disturbances is either increased (Figure 9.5 a)) or constant (Figure 9.5 b)) as a function of time.

The aim of the validation is to compare the stability of the closed-loop system with different VC controllers when the system is disturbed by the considered succession of test disturbances mentioned above. We consider following three different VC controllers:
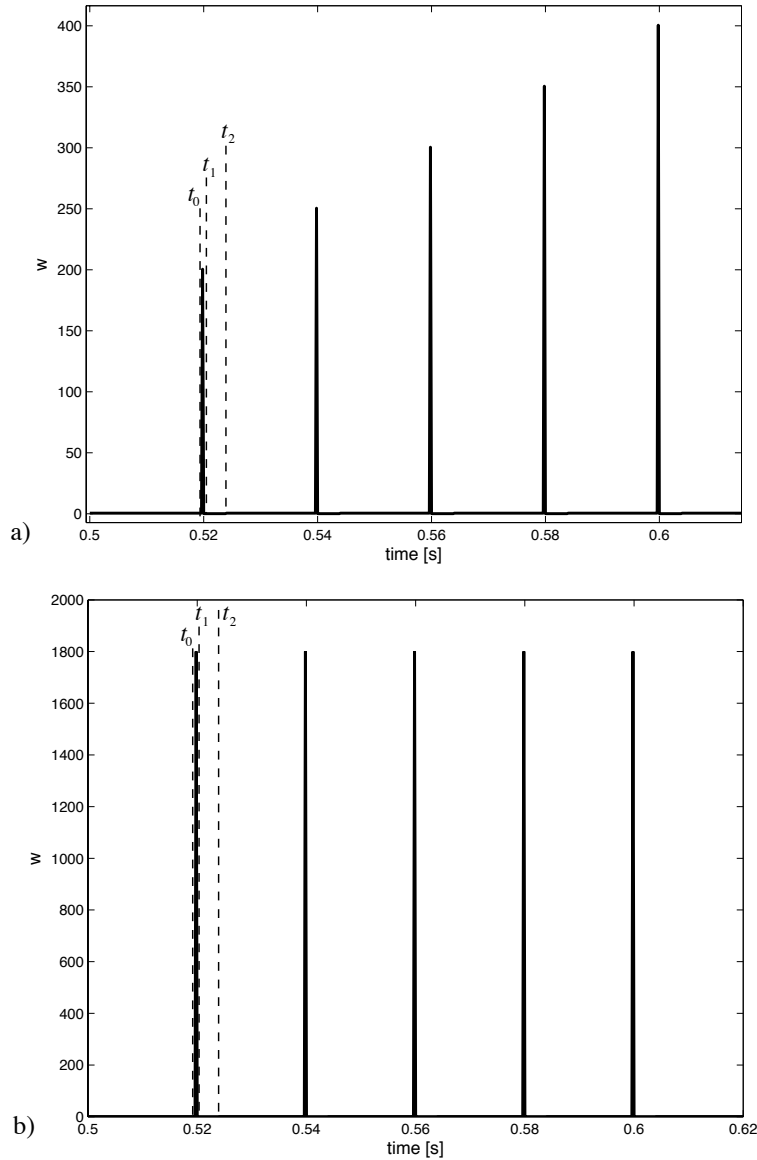
Figure 9.5: The succession of test disturbances w with a) increasing amplitude and b) constant amplitude. The y-axis is an arbitrary scale indicating the strength of a brief increase in conductivity to reduce β_p suddenly.

1. The reference controller which is a linear input-output PD controller.

2. The bang-bang controller presented in Section 8.6 given by Equation (8.89), i.e.

$$\varsigma\left(\left[\begin{array}{c} x_d \\ w \end{array}\right]\right) = -\mathrm{sgn}(x_1) = \lim_{f_1 \to -\infty} \mathrm{sat}(f_1 x_1).$$

As mentioned in Section 8.6 this is the best possible controller in terms of stability.

3. The proposed new CNGSC controller given by Equation (8.50) with the extended nonlinear Function (8.92), i.e.

$$\varphi\left(\left[\begin{array}{c} x \\ w \end{array}\right]\right) = f_1 x_1 + k(x)(f_2 x_2 + f_3 x_3 + \ldots + f_n x_n + f_w w),$$

and

$$k(x) = \begin{cases} 1 - x_1^2 & \text{if} \quad |x_1| \leq 1 \\ 0 & \text{if} \quad |x_1| > 1 \end{cases}.$$

For the bang-bang and the CNGSC controllers a state reconstruction is required. We apply the state reconstruction presented in Section 8.4.3 for which only the reconstruction of the unstable state x_1 is required. This is necessary since it turns out that the full state reconstruction is not accurate enough to permit a pure state feedback. The comparison of the generated control signal of the input-output reference controller against the generated control signal of the reference controller used as a state feedback controller given by Equation (8.46), i.e.

$$\varrho\left(\begin{bmatrix} x \\ w \end{bmatrix}\right) = \begin{bmatrix} f_x & f_w \end{bmatrix} \begin{bmatrix} x \\ w \end{bmatrix} = f_1 x_1 + f_2 x_2 + f_3 x_3 + \ldots + f_n x_n + f_w w$$

shows severe differences. Moreover, the simulation with the state feedback reference controller shows that the closed-loop system cannot be stabilised. The state reconstruction seems to be the major problem when the simulations are carried out with the nonlinear DINA-CH code. This observation is probably also valid for tokamaks in operation. On the other hand, simulations carried out with linear models (Section 9.1) do not show this problem since we used identical models for both the simulation and the state reconstruction. Thus, the state reconstruction is ideal (perfect).

Note that with the RZIP model, used for the state reconstruction, the matrix f_w cannot be derived. Thus, the reconstruction of the disturbance w cannot be carried out. This could be another reason for the inaccurate state reconstruction. Later, we will see that there is yet another major reason for the inaccuracy of the state reconstruction.

9.2.1.3 Intrinsic nonlinearities of the TCV tokamak simulation

We first show that besides the power supply saturation the tokamak simulation itself possesses intrinsic nonlinearities which can also lead to a loss of control. Since we demonstrate this fact by means of a DINA-CH simulation we assume that the DINA code accurately reproduces these intrinsic nonlinearities. The simulation setup for this demonstration is as follows:

- We do not consider any power supply saturation and thus we allow arbitrarily large control signal amplitudes.

- The closed-loop system is disturbed by means of the test disturbances scenario with increasing amplitudes as illustrated in Figure 9.5 a).

- We consider only the linear input-output reference controller.

Figure 9.6 illustrates the evolution of the vertical plasma position z and the G-coil voltage. The control is lost after the fourth disturbance at 0.58 s. Such a loss of control cannot be simulated with linear models since without power supply saturation the closed-loop system is a pure linear system and thus it is obviously stable or unstable for the whole simulation. This shows that it is important to validate a new controller like the proposed new CNGSC controller with a nonlinear code like DINA since the stability analysis of the CNGSC controller derived in the Control Theory part relies on a pure linear system with the input saturation as the sole nonlinearity.
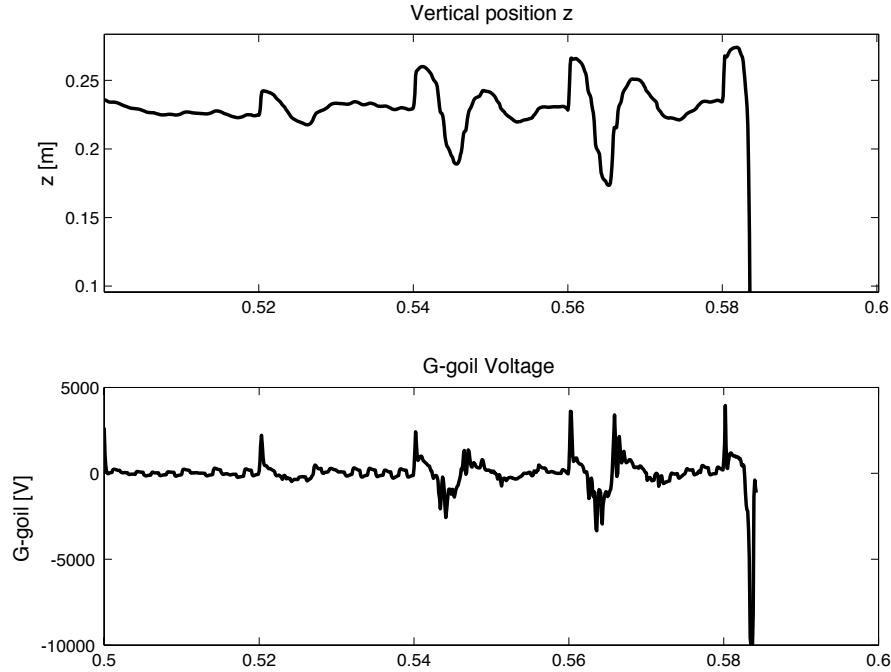
Figure 9.6: The loss of control due to intrinsic nonlinearities of the tokamak simulation.

9.2.1.4   Low saturation level and small disturbances

The first validation and comparison simulations are carried out with a low power supply voltage saturation level (160 V). The closed-loop system is disturbed by means of the test disturbances scenario with small increasing amplitudes.

1. **The reference controller**:
   Figure 9.7 illustrates the evolution of the vertical plasma position z, the G-coil voltage and the reconstructed unstable state $\breve{x}_1$. The control is lost after the fifth disturbance occurring at 0.6 s.

   The evolution of the vertical plasma position z and the reconstructed unstable state $\breve{x}_1$ varies strongly during periods without test disturbances, e.g. between two disturbances and at the beginning of the simulation $(0.5 - 0.52$ s) where no disturbance occurs. This is due to the badly understood "wandering" of the DINA-CH code simulation which can be interpreted as additional disturbances. These additional disturbances also lead to a saturation of the power supply since the saturation level is small.

2. **The bang-bang controller**:
   Figure 9.8 illustrates the evolution of the vertical plasma position z, the G-coil voltage and the reconstructed unstable state $\breve{x}_1$. The control is not lost. This confirms that with the bang-bang controller the closed-loop stability is increased. Furthermore, the rejection of the additional intrinsic disturbances is enhanced since the amplitude variations of z and $\breve{x}_1$ are less important during time lapses without the test disturbances.

3. **The CNGSC controller**:
   The first test with the CNGSC controller revealed that the control is lost similarly

Figure 9.7: DINA-CH simulation with a low saturation level and the **reference controller**. Illustration of the evolution of the vertical plasma position z, the G-coil voltage and the reconstructed unstable state x_1. The control is lost after the fifth disturbance occurring at 0.6 s.

Figure 9.8: DINA-CH simulation with a low saturation level and the **bang-bang controller**. Illustration of the evolution of the vertical plasma position z, the G-coil voltage and the reconstructed unstable state x_1. The control is not lost.

as for the reference controller. It turns out that this is due to an underestimation of the reconstructed unstable state $\breve{x}_1$. Several simulations with different disturbance amplitudes show that the control is always lost when the amplitude of the reconstructed unstable state $|\breve{x}_1|$ is larger than approximately $0.2 - 0.25$. In Figure 9.7 the closed-loop system remains stable when $\breve{x}_1$ reaches the value -0.25 (at time $t \approx 0.53$ s), while stability is lost when this value is exceeded (at time $t \approx 0.61$ s, dashed line). Since x_1 is the normalised unstable state and since the boundaries of the null controllable region of the normalised system are at $x_1 = 1$ and $x_1 = -1$ the stability of the closed-loop system with the bang-bang and the CNGSC controllers can theoretically only be lost when $|x_1| > 1$. But since the stability is already lost for $|\breve{x}_1| > 0.2 \ldots 0.25$ the stabilising enhancement effect due to the introduced nonlinearity in the CNGSC controller is strongly weakened and thus the evolution of the unstable state is similar to the reference controller leading to a loss of control. The deleterious consequence of such unstable state underestimations is discussed in Section 8.4.2. As suggested in the same section, the only way to avoid an underestimation is to increase the estimation by

$$\breve{x}_{1_{corr}} = c_{x_1} \breve{x}_1,$$

where $c_{x_1} \geq 1$ denotes the correction factor. For our case we have to choose a correction factor of $c_{x_1} = 5$, which remains to be explained.

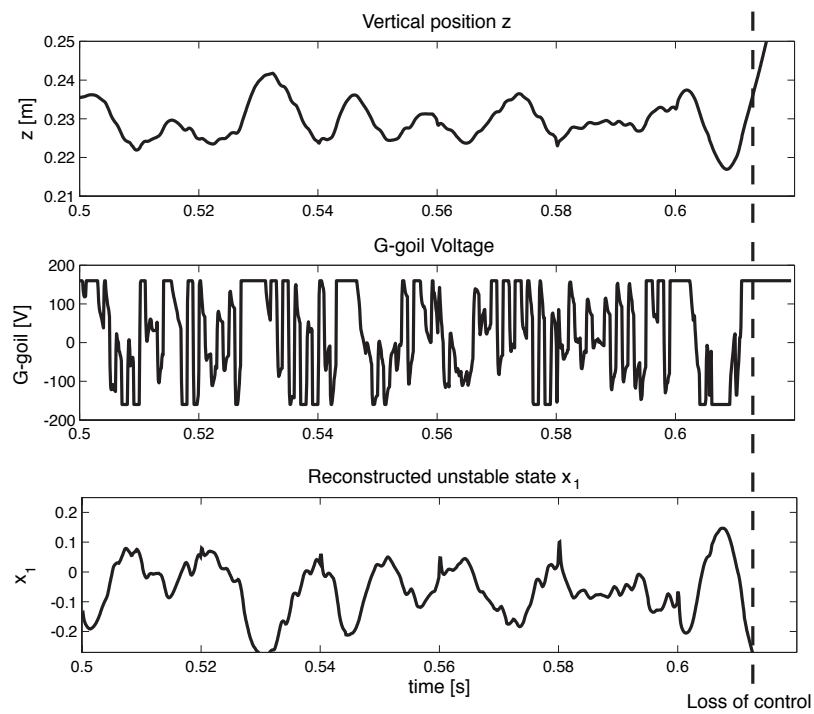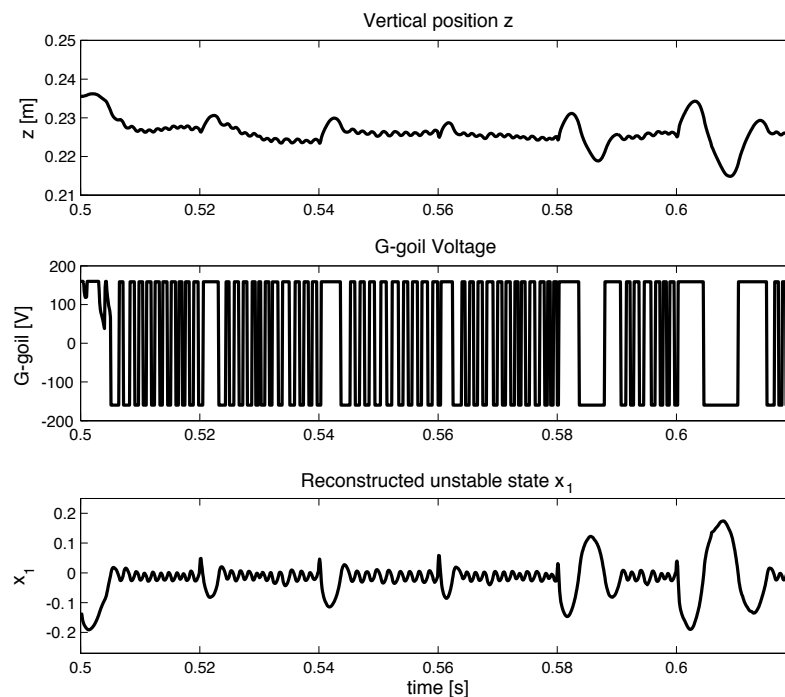Figure 9.9: DINA-CH simulation with a low saturation level and the **CNGSC controller**. Illustration of the evolution of the vertical plasma position z, the G-coil voltage and the reconstructed unstable state x_1. The control is not lost.

Note that this underestimate can be explained by the fact that there is a stability difference between the closed-loop systems with the linear RZIP model and the closed-loop system with the nonlinear DINA-CH code. It turns out that when the

parameters of the reference VC controller (PD controller) are tuned so that the closed-loop system with the RZIP model is at the limit of stability, the closed-loop system with DINA-CH is not stable. To obtain a stable closed-loop system with DINA-CH the gain of the reference controller has to be increased by factor 2. This illustrates very well that there is a discrepancy between the RZIP model and the DINA-CH code in the sense that the vertical instability growth rate of DINA-CH is larger than the growth rate of the RZIP model. Thus, the underestimate of the unstable state no longer seems surprising.

Figure 9.9 illustrates the evolution of the vertical plasma position z, the G-coil voltage and the reconstructed unstable state $\breve{x}_1$ for the CNGSC controller with a corrected unstable state reconstruction. The control is no longer lost. This confirms us that with the CNGSC controller the closed-loop stability is increased.

9.2.1.5   Higher saturation level and larger disturbances

In the previous section we showed that additional disturbances due to intrinsic noise of the DINA-CH code simulation give rise to saturation of the power supply. We therefore tried to avoid such saturations by carrying out similar simulations with a higher power supply voltage saturation level (750 V).

It turns out that in general for higher saturation levels the loss of stability occurs under similar conditions, i.e. similar amplitude of the test disturbance, for both the reference controller and the CNGSC controller. Therefore, an enhancement of the closed-loop system stability due to the CNGSC controller is no longer distinguishable. For what follows we demonstrate that this is again due to the inaccurate reconstruction of the unstable state x_1. For the demonstration we consider that the closed-loop system is disturbed by means of the test disturbances scenario with large and constant amplitudes as illustrated in Figure 9.5 b).

1. **The reference controller and the CNGSC controller**:
   Figures 9.10 and 9.11 illustrate the evolution of the vertical plasma position z, the G-coil voltage and the reconstructed unstable state $\breve{x}_1$ for the closed-loop system with the reference controller and for the closed-loop system with the CNGSC controller, respectively. Since the power supply is only saturated during marginal time lapses the closed-loop system remains stable with both controllers. Furthermore, the amplitude of the reconstructed unstable state $\breve{x}_1$ is distinctly below the limit of approximately $0.2 \ldots 0.25$ for which the control is lost.

2. **The bang-bang controller**:
   We know from Section 8.6 that the considered bang-bang controller is the best controller in terms of stability. Thus, since the closed-loop system with the reference and the CNGSC controllers are stable we naturally may assume that the closed-loop system with the bang-bang controller is stable, too. But, as illustrated in Figure 9.12, this is clearly not the case since the control is lost after the fourth disturbance occurring at 0.58 s. Furthermore, despite the fact that every test disturbance is equivalent, i.e. constant amplitude, the disturbing effect, i.e. the amplitude of the variation of z and $\breve{x}_1$, is increased with every following disturbance. This accumulating disturbing effect is surprising since before every occurring disturbance the state of the tokamak seems to be approximately at the same equilibrium, at least as far as z and x_1 are concerned.

Figure 9.10: DINA-CH simulation with a higher saturation level and the **reference controller**. Illustration of the evolution of the vertical plasma position z, the G-coil voltage and the reconstructed unstable state x_1. The control is not lost.
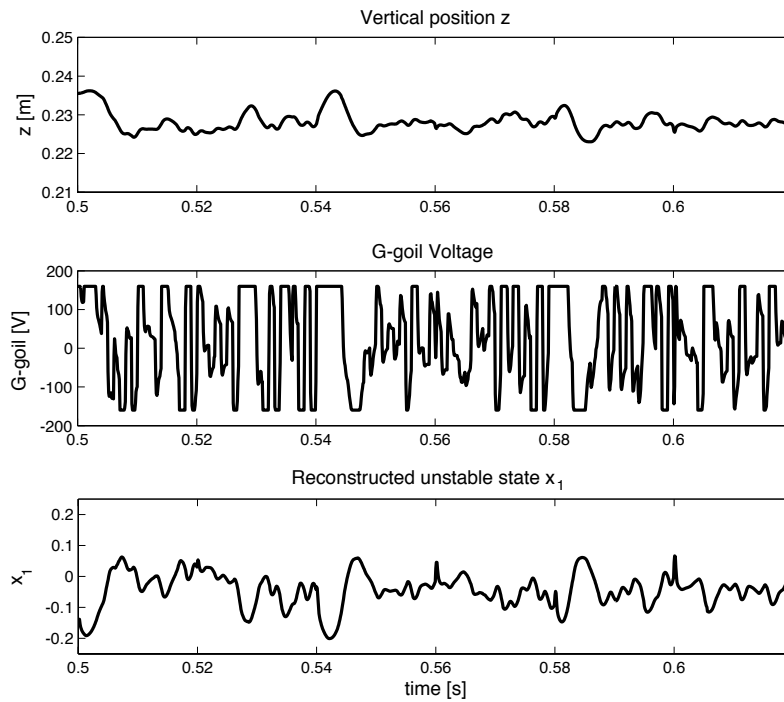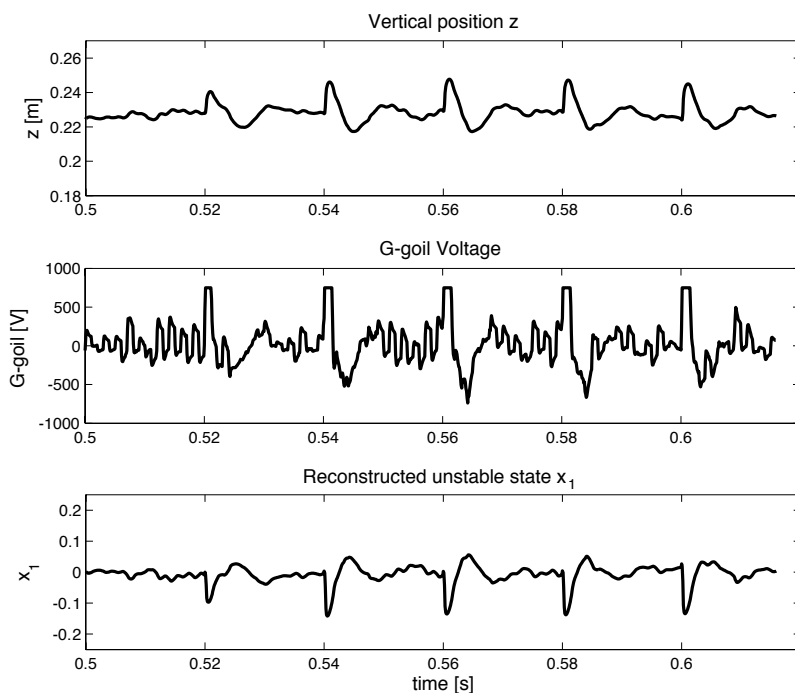

Figure 9.11: DINA-CH simulation with a higher saturation level and the **CNGSC controller**. Illustration of the evolution of the vertical plasma position z, the G-coil voltage and the reconstructed unstable state x_1. The control is not lost.

Since for the bang-bang controller only the unstable state x_1 is fed back it is evident that the problem has to be linked to the unstable state reconstruction. In the previous
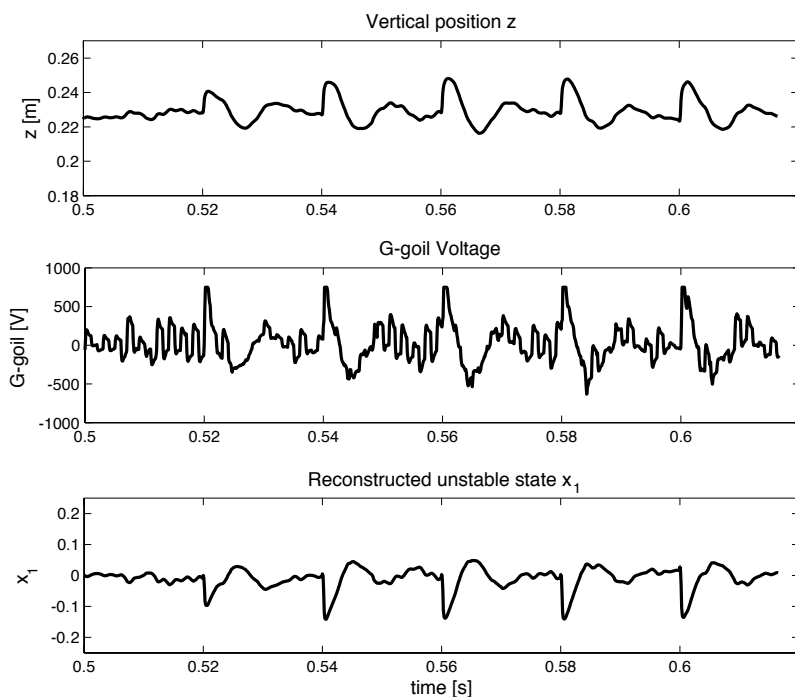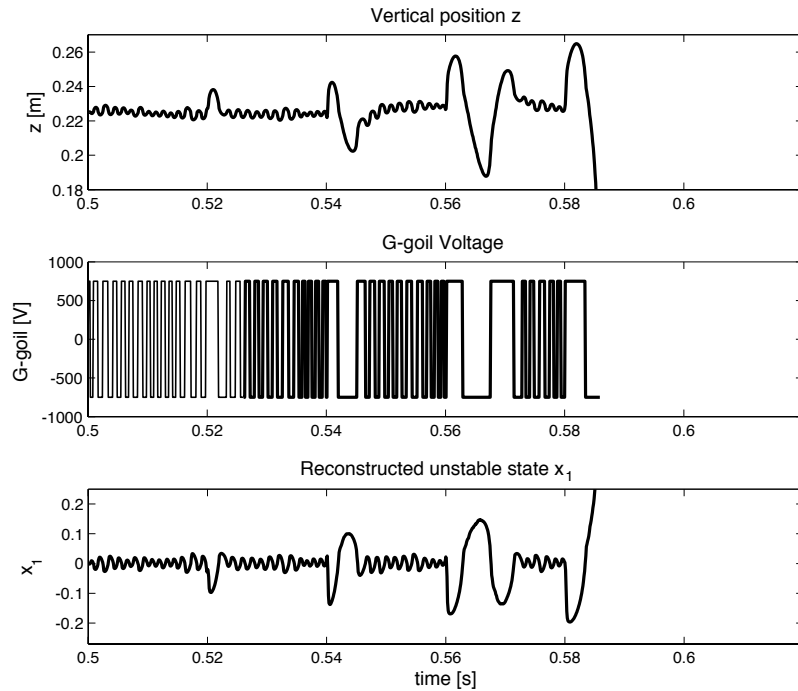
Figure 9.12: DINA-CH simulation with a higher saturation level and the **bang-bang controller**. Illustration of the evolution of the vertical plasma position z, the G-coil voltage and the reconstructed unstable state x_1. The control is lost after the fourth disturbance occurring at 0.58 s.

section we already discussed the problem of an underestimation of the unstable state. Since in this present case we have a bang-bang controller which has an infinite controller gain ($f_1 \to -\infty$) we clearly demonstrate that the inaccurate reconstruction of the unstable state is not solely due to an underestimation but is also due to an error in the estimation of the state subspace linked to the unstable state. In other words, the reconstructed unstable state $\breve{x}_1$ contains not only the informations of the unstable state but is probably rather a combination of the unstable state and other stable states. Of course, a more rigorous analysis will be necessary to confirm this hypothesis. Moreover, it will be important to determine if this reconstruction inaccuracy is either solely due to the discrepancy between the RZIP model and the DINA-CH code or simply due to the intrinsic nonlinearities contained in the DINA-CH code or in a tokamak in operation.

Chapter 10

Conclusions

10.1 Summary

The major contributions of this thesis can be traced in the following directions:

- **Tokamak physics and engineering**

  - **The DINA code**

    In order to be able to validate the proposed CNGSC controller under operational tokamak conditions we have presented a full nonlinear tokamak evolution code referred to as the DINA code. We give a detailed description of the principal plasma physics implemented in this code.

    Furthermore, validation of DINA was provided by comparing TCV experimental VDE responses with DINA code simulations. It turns out that we have only had to make minor adjustments to the initial conditions of fully nonlinear DINA simulations of VDEs in TCV in order to obtain convincing agreement between the experimental and modelled data. The highly elongated TCV vacuum vessel has allowed us to follow VDEs over a large distance before a disruption ensues. The vacuum field curvature varies significantly over these large distances, implying a large modification of the vertical instability growth rate during the VDE. This feature is correctly modelled by DINA and the underlying reasons are brought out by inspecting the growth rate estimated by the RZIP rigid current displacement model which is accurate for the equilibria investigated. The evolution of the elongation and triangularity in DINA does not agree perfectly with the LIUQE reconstructions and the multiple potential reasons are presented. Given these differences, it is impressive that the comparison shows such similar features and indeed, the inevitable differences illustrate the potential dangers of assuming absolute precision in nonlinear simulations of such a complex system.

  - **The AC loss reduction**

    AC losses are due to the reactions of the control system to disturbances to the plasma and noise in the plasma and in the measurement system. Disturbances are almost instantaneous events that move the state of the tokamak away from the equilibrium position. Most of the AC losses occur during and immediately after the disturbance, leading to sharp peaks in the AC loss evolution. Therefore, a significant reduction has to target these peaks, which are essentially due to the fast stabilising control system.

The need for stability of the plasma position imposes a strong and rapid re-action to strong disturbances. Present control system designs also apply the same strong reactions to weaker disturbances and noise. While this does not influence traditional performance and stability criteria, it causes unnecessary AC losses in the superconducting coils. Weaker controllers allow reductions of the AC losses during weaker disturbances to a fifth of their original value.

While the losses due to disturbances can be influenced, the losses due to the ramp-up and ramp-down of the scenario currents cannot be reduced, since they are due to the overall magnetic field changes, which are defined by the operating scenario.

The price of the AC loss reduction is a smaller stability margin, but only a slightly reduced performance. Establishing the optimal tradeoff between reducing the AC losses and maximising the stability margin will be made when the true disturbance and noise spectra have been measured.

From the point of view of controller design in general, the main result of the AC losses analysis reveals that for reducing the AC losses we need to design a con-troller which generates a weakly oscillating, low amplitude and low frequency control voltage signal.

Using existing models of the ITER tokamak and its control system, it has been shown that the AC losses in the superconducting coils can be reduced by adapting this control strategy.

- **Control theory**

  – **The region of attraction of planar systems with a single unstable pole and saturated feedback**
  We demonstrate that the characterisation of the region of attraction is possible for a second order linear system with one unstable and one stable pole. For such systems the region of attraction possesses a topological bifurcation for which the region of attraction changes from an unbounded hyperbolic region to a bounded limit cycle. We provide an analytical condition under which this bifurcation occurs. Furthermore, it is shown that bifurcation is only exhibited when the unstable pole is faster than the stable one.

  Since the analysis rests on methodologies like Poincaré and Bendixson's theo-rems which are unfortunately only valid for second order systems it is evident that there is no way to apply the results for second order systems to higher order systems. It turned out that the search for characterising the region of attraction for higher order systems was illusory and thus this research direction had to be abandoned.

  – **A globally stabilising controller under saturated input for systems with one unstable pole**
  A simple continuous nonlinear globally stabilising controller, referred to as CNGSC, is proposed for the stabilisation of linear planar systems with one unstable pole and a single saturated input. The main idea is to modify an existing linear controller by incorporating a nonlinear term into the control law. A formal proof that the controller is globally stabilising, i.e. the region of attraction is equivalent to the null controllable region, was provided for slightly more conservative conditions.

There are several advantages linked to this new controller: i) the stability properties are enhanced in the sense that the controller is globally stabilising, ii) the performance, AC loss reduction and fast disturbance rejection, can be taken into account, iii) the controller can be applied to any arbitrary high order system and iv) the controller possesses a simple structure which simplifies the design procedure.

We showed that the extension of the CNGSC controller to higher order systems is straightforward. But the quest for an analytic proof of the closed-loop system global stability is highly complicated in this case. Therefore, the global stability of the higher order closed-loop systems is illustrated by means of simulations. Nevertheless, we have provided an interesting property encouraging the search for a formal stability proof in the future.

– **Tokamak control**
We discuss the structure of the tokamak closed-loop system and show to which points particular attention has to be paid when the input-output controllers are designed. Furthermore, since the CNGSC controller is a state feedback controller we discuss the problems and the modifications that have to be taken into consideration when migrating from an input-output controller to a state feedback controller. We provide a scheme which describes a way to transform any tokamak closed-loop system into a normalised closed-loop system. This transformation will allow us to apply the CNGSC controller straightforwardly
.

Since the CNGSC controller is a state feedback controller, one of the major problems is linked to the state reconstruction procedure which represents a crucial step if we are seeking a well conditioned state feedback controller. We show that for the CNGSC controller it is sufficient to provide an accurate reconstruction of solely the unstable state, while a reconstruction of all stable states is not required.

Another pertinent topic is the study of the effect of the disturbances on the closed-loop system. We show that the determination of the closed-loop system stability by means of the region of attraction is only valid during intervals during which the system is not disturbed. This is due to the fact that the concept linked to the region of attraction is only applicable to autonomous (time-invariant) closed-loop systems. However, in system theory a disturbance is interpreted as time-varying external input to the closed-loop system. Another problem is due to the unknown evolution of the shape, the amplitude and the time duration of a disturbance. Thus, the evolution of the states is not predictable during a disturbance and we have to wait until the disturbance has vanished to determine whether the states are still in the region of attraction or not. Nevertheless, possibilities to improve the stability during disturbances by slightly modifying the CNGSC controller are provided.

A further problem lies in the nature of the state feedback controller when we want an output of the system to track a reference signal. For input-output systems, this is usually obtained by simply taking the error between the output and the reference. The resulting error signal is fed to the input-output controller which tries to cancel the error. We show that this is not as simple for nonlinear state feedback controllers, since such controllers work for a well

defined equilibrium point. Thus, if we want to track a reference signal then we have to move the equilibrium point as a function of the reference signal.

The tokamak closed-loop system inevitably has a limited bandwidth and a pure time delay due to the power supply and the controller computing time, which are in general not negligible. We demonstrate that both the limited bandwidth and the pure time delay reduce the region of attraction and thus diminish the closed-loop system stability. It turns out that due to the saturation it is not possible to efficiently compensate the effect of the limited bandwidth. Nevertheless, the detrimental effect of a short time delay can completely be suppressed by slightly modifying the CNGSC controller.

- **Validation**
  The simulations using linear models confirm that the global stability of the CNGSC controller is ensured when it is applied to higher order systems with a single unstable pole. Since for the purpose of the state reconstruction the same linear models are used as for the simulations, no problems due to an inaccurate unstable state reconstruction can be observed. The linear model simulations show clearly that the proposed CNGSC controller is able to maintain stability for larger ELM-like disturbances compared to a standard linear controller.

  The simulations using the nonlinear DINA-CH code demonstrate that the tokamak possesses intrinsic nonlinearities. For very large disturbances these nonlinearities can lead to a loss of control even without power supply saturation. We conclude that nonlinear codes like DINA are indispensable for the validation of new controllers, e.g. the proposed CNGSC controller.

  The enhancement of the closed-loop system stability could only be confirmed for a low saturation level and small test disturbances. For a higher saturation level and larger disturbances no stability enhancement could be distinguished. Even worse, for the best controller in terms of stability (unstable state bang-bang controller) the control is lost for smaller disturbances than with a standard linear controller (reference controller). We have demonstrated that this disagreement is linked to an inaccurate reconstruction of the unstable state. This problem has not been resolved so far but it could be attributable to following two items:

  1. **The discrepancy between the linear RZIP model and the DINA-CH code**
     We demonstrated that there is a discrepancy between the RZIP model and the DINA-CH code. As mentioned for the DINA-CH code validation, for such a complex system like the tokamak there are inevitably differences between the DINA code and the real tokamak in operation. Thus, since the RZIP model is derived form experimental data there is inevitably a discrepancy between the RZIP model and the DINA-CH code. This discrepancy could be avoided by deriving an RZIP model from DINA simulation data.

  2. **The intrinsic nonlinearities in the DINA-CH code or in a tokamak in operation**
     Since the state reconstruction uses a linear model these intrinsic nonlinearities can lead to an inaccurate state reconstruction. If this reveals to be true then a nonlinear state reconstruction and perhaps a new nonlinear controller which

take into consideration the intrinsic tokamak nonlinearities would be indispensable. Note that the main problem of such an investigation would be linked to the specification of the intrinsic tokamak nonlinearities.

The validations provided by Scibile [49, 48] and the simulations carried out by Schuster [47] seem to demonstrate that the observation of the unstable state is not falsified by the intrinsic nonlinearities of the tokamak. Therefore, it is more likely that the reconstruction problem is due to the discrepancy between the linear RZIP model and the DINA-CH code.

There is a supplementary problem linked to the use of the DINA-CH code. For some discharges the DINA-CH simulations show intrinsic disturbances which cannot be observed on tokamaks in operation. This problem has to be studied in future investigations.

- **Tradeoff between different controllers**
  One of the most important findings that can be derived from this thesis is the fact that there is always a tradeoff between the stability properties, the performance and the reduction of AC losses. Table 10.1 illustrates this tradeoff by comparing different controllers.

	Stability properties	Local performance	AC loss reduction	Application to higher order systems	Simple design
Standard linear feedback controller	weak $\mathcal{A} \subset \mathcal{C}$	$\checkmark$	$\checkmark$	$\checkmark$	$\checkmark$
Unstable state feedback controller	enhanced $\mathcal{A} = \mathcal{C}$	$-$	$\checkmark$	$\checkmark$	$\checkmark$
Unstable state bang-bang controller	best $\mathcal{A} = \mathcal{C}$	$-$	$-$	$\checkmark$	$\checkmark$
Near time optimal VSC controller (DANTOC, [49, 48])	enhanced $\mathcal{A} = \mathcal{C}$	$\checkmark$	$-$	$-$ has to be investigated	$-$
CNGSC controller	enhanced $\mathcal{A} = \mathcal{C}$	$\checkmark$	$\checkmark$	$\checkmark$	$\checkmark$

Table 10.1: Tradeoff between different controllers.

A standard linear controller can provide local performance and AC loss reduction but the stability properties are weak since the region of attraction is smaller than the null controllable region ($\mathcal{A} \subset \mathcal{C}$). The stability properties can be enhanced by focusing on the feedback of the unstable state. This idea is best represented by considering a linear state feedback controller for which only the unstable state is fed back. For such a controller the enhancement of stability is linked to the fact that the region of attraction is equal to the null controllable region ($\mathcal{A} = \mathcal{C}$). But since only

a single state is fed back the local performance might be lost. When we consider ELM-like disturbances then we have shown that the best stability properties can be achieved by applying a bang-bang controller for which only the unstable state is fed back. Additionally to the loss of local performance, a reduction of the AC losses can no longer be achieved since bang-bang controllers generate control signals with high-frequency oscillations and large amplitudes. The DANTOC controller proposed by Scibile [49, 48] enhances the stability and simultaneously ensures local performance in the sense of a time optimal controller. But since this controller is a sliding mode bang-bang controller it is susceptible to generate large AC losses. The CNGSC controller proposed in this thesis can handle the three requirements: it enhances the stability and can simultaneously take into consideration the local performance and the AC loss reduction. Note that when we consider ELM-like disturbances then both controllers, the DANTOC and the CNGSC, possess weaker stability properties than the unstable state bang-bang controller. In this case we have shown that the stability properties of the CNGSC controller can be improved by increasing the feedback gain of the unstable state. By doing this the resulting modified CNGSC controller adopts more and more the characteristics of the unstable state bang-bang controller which inevitably reduces the local performance and increases AC losses.

Note that all controllers except for the DANTOC controller are applicable to arbitrary high order systems and the controller design is kept simple. The application of the DANTOC controller to systems of higher order than two is not impossible but would require further investigation.

From this tradeoff discussion we can derive an additional important finding: The incorporation of the unstable state into the control law is essential for enhancing the stability of a tokamak closed-loop system. Therefore, an accurate unstable state reconstruction is indispensable.

10.2   Perspective

Several issues concerning the analysis and the design of controllers and the state reconstruction can be considered in future studies:

- **Unstable state reconstruction**
  A primordial issue consists of solving the problem of the unstable state reconstruction. As mentioned before, this problem is most probably due to the discrepancy between the linear RZIP model and the DINA code induced by the fact that both models are derived from experimental data. This problem could be resolved by deriving an RZIP model from DINA simulation data.

  In this context the robustness study of the state reconstruction requires further and more rigorous investigations.

- **Analytic proof of the global stability of the CNGSC controller**
  For arbitrary high order systems the global stability, i.e. the region of attraction is equivalent to the null controllable region, of the CNGSC controller has so far only been demonstrated by means of simulations. A formal analytic proof is therefore required. One possibility is the analysis by means of Lyapunov functions and by considering slightly more conservative stability conditions, i.e. a formal proof which is only valid for a subclass of all possible CNGSC controllers.

- **Extension for multiple saturated inputs**
  The extension of the analysis presented in this thesis to systems with several saturated inputs constitutes a challenging task for future work.

Appendix A

Control theory

A.1 Poincaré's and Bendixson's theorems

In this section we present three classic results for predicting limit cycles in second order systems [50, 32]. We consider autonomous nonlinear second order system of the form

$$\dot{x}_1 = f_1(x_1, x_2) \qquad\qquad\qquad\qquad\qquad (A.1)$$
$$\dot{x}_2 = f_2(x_1, x_2),$$

where x_1 and x_2 are the states of the system and f_1 and f_2 are nonlinear functions of the states.

The first theorem presented indicates a relationship between the existence of a limit cycle and the number of equilibrium points it encircles (encloses). In the statement of this theorem we will use N to represent the number of equilibrium points, which are not saddle points, encircled by a limit cycle. On the other hand, S represents the number of saddle points encircled by a limit cycle.

Theorem A.1
Poincaré's theorem
If a limit cycle exists in the second order system (A.1), then $N = S + 1$.

The second theorem indicates the asymptotic properties of a trajectory of a second order system.

Theorem A.2
Poincaré-Bendixson's theorem
If a trajectory of the second order system (A.1) remains in a closed bounded region $\mathcal{B}$, then one of the following statements is true:

1. *the trajectory converges to an equilibrium point*

2. *the trajectory tends to an asymptotically stable limit cycle*

3. *the trajectory is itself a limit cycle*

The third theorem provides a sufficient condition for the non-existence of a limit cycle.

Theorem A.3
Bendixson's theorem

For the second order system (A.1), no limit cycle can exist in a region $\mathcal{B}$ of the phase plane in which

$$\frac{\partial f_1}{\partial x_1} + \frac{\partial f_2}{\partial x_2}$$

does not vanish and does not change sign.

Proof: Because

$$\frac{\dot{x}_2}{\dot{x}_1} = \frac{dx_2}{dx_1} = \frac{f_2(x_1, x_2)}{f_1(x_1, x_2)}$$

is always satisfied for system (A.1), we have the relation

$$f_1 \, dx_2 - f_2 \, dx_1 = 0. \tag{A.2}$$

This relation is true for any system trajectory, including a limit cycle.

   Assume that a limit cycle exists. The line integral of (A.2) along the closed curve C of the limit cycle is

$$\int_C (f_1 \, dx_2 - f_2 \, dx_1) = 0. \tag{A.3}$$

Applying Stoke's theorem in vector analysis results in

$$\int_C (f_1 \, dx_2 - f_2 \, dx_1) = \int\int_S \left(\frac{\partial f_1}{\partial x_1} + \frac{\partial f_2}{\partial x_2} \right) dx_1 dx_2, \tag{A.4}$$

where the integration on the right-hand side is carried out on the area S enclosed by the limit cycle C.

   From equation (A.3), the left-hand side has to vanish. However, the right-hand side cannot be equal zero since

$$\frac{\partial f_1}{\partial x_1} + \frac{\partial f_2}{\partial x_2}$$

does not vanish and does not change sign in the region $\mathcal{B}$. This contradiction indicates the non-existence of the limit cycle. ∎

A.2 Contraction analysis of the trajectories of second order linear systems

In this section we give some results concerning the contraction properties of the trajectories of second order linear systems. To be more concrete, we deal with the analysis of the contractive behaviour of two trajectories with respect to one or two lines in the state space. In other terms, we study if the distance between two trajectories with respect to one or two lines decreases (contraction) or increases. To illustrate this, we take as an example the case where we consider only one line. We therefore define a line $fx = \frac{1}{k}$ (or simply $kfx = 1$) in state space, where $x \in \mathbb{R}^2$ represents the state space variable and where $f = \left[\begin{array}{cc} f_1 & f_2 \end{array}\right]$, with $f_1, f_2 \in \mathbb{R}$ and $k \in \mathbb{R} \setminus 0$. We consider two trajectories starting on the line $kfx = 1$ which evolves in state space until they intersect the same line. The starting points are denoted as p_1 and p_2, respectively and the intersection points with the line are denoted as p'_1 and p'_2. Figure A.1 illustrates the line $kfx = 1$ and the considered two trajectories with their starting and intersection points. The main idea is to analyse how the distance between the two trajectories evolves in time with respect to the line $kfx = 1$. We therefore considering the distances $d = \|p_1 - p_2\|$ and $d' = \|p'_1 - p'_2\|$ on the line $kfx = 1$, and state under which conditions the distance between two trajectories decreases $d' < d$ or increases $d' > d$.
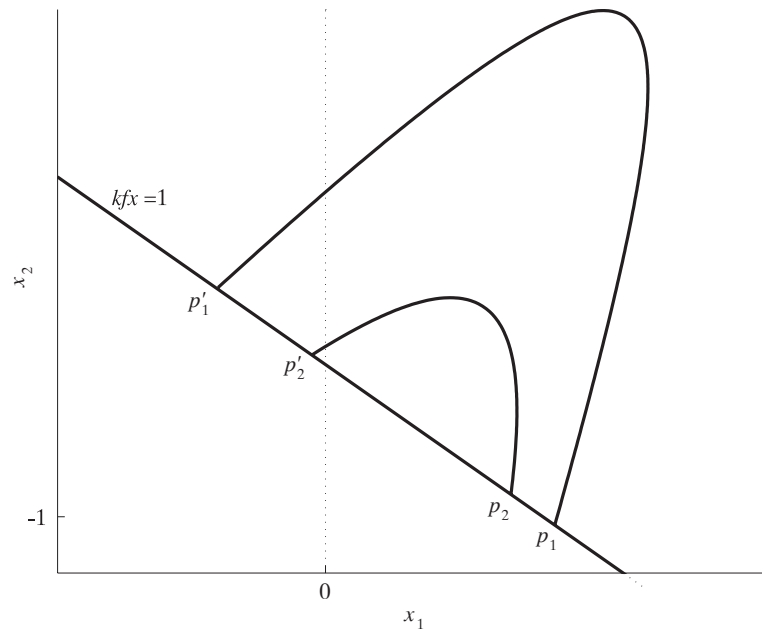
Figure A.1: Illustration of the line $kfx = 1$ and two trajectories with their starting points p_1 and p_2 and their intersection points p'_1 and p'_2.

For our purposes we need to study systems with one stable and one unstable poles. This represents the main contribution of this section and it is provided in Section A.2.1. Since we also need the results for stable systems we present them as a reminder in Section A.2.2.

Without loss of generality, the results are developed by assuming that the considered systems are represented in the observability canonical form, where $f = \left[\begin{array}{cc} 0 & 1 \end{array}\right]$. It will be shown that the contraction results can be generalised for all systems by means of state

transformation.

A.2.1   Unstable systems

First, consider the autonomous second order unstable system

$$\dot{x} = Ax = \begin{bmatrix} 0 & a_1 \\ 1 & a_2 \end{bmatrix} x = \begin{bmatrix} 0 & -\lambda_1\lambda_2 \\ 1 & \lambda_1 + \lambda_2 \end{bmatrix} x, \qquad a_1 > 0 \ , \ a_2 \in \mathbb{R} \tag{A.5}$$

with a positive and negative real eigenvalue $\lambda(A) = \{\lambda_1, \lambda_2\}$ where $\lambda_1 > 0$ and $\lambda_2 < 0$. We will examine its trajectories with respect to a horizontal line $kfx = 1$ where

$$f = \begin{bmatrix} 0 & 1 \end{bmatrix}, \quad k < 0.$$

On this line $x_2 = \frac{1}{k}$ we denote the points

$$p_m = \begin{bmatrix} x_{m1} \\ \frac{1}{k} \end{bmatrix} = \begin{bmatrix} -\frac{\lambda_1}{k} \\ \frac{1}{k} \end{bmatrix}, \quad p'_m = \begin{bmatrix} y_{m1} \\ \frac{1}{k} \end{bmatrix} = \begin{bmatrix} \frac{-\lambda_2}{k} \\ \frac{1}{k} \end{bmatrix}$$

$$\text{and} \quad p_o = p'_o = \begin{bmatrix} x_{o1} \\ \frac{1}{k} \end{bmatrix} = \begin{bmatrix} -\frac{\lambda_1+\lambda_2}{k} \\ \frac{1}{k} \end{bmatrix}.$$

If $x_1 > x_{o1}$, then $\dot{x}_2 > 0$, *i.e.*, the vector $\dot{x}$ points upward. If $x_1 < x_{o1}$, then $\dot{x}_2 < 0$, *i.e.*, the vector $\dot{x}$ points downward. Below the $x_2 = 0$ axis ($x_2 < 0$), $\dot{x}_1 < 0$, hence the trajectories all go to the left.

Then we have

Lemma A.1 *Let $x_{11} \geq x_{o1}$ and*

$$p = \begin{bmatrix} x_{11} \\ \frac{1}{k} \end{bmatrix}$$

be a point on the line $kfx = 1$. The trajectory $x(t) = e^{At}p, t \geq 0$, will return to this line if and only if $x_{11} < x_{m1}$. Let T be the first time when it returns and

$$p' = \begin{bmatrix} y_{11} \\ \frac{1}{k} \end{bmatrix}$$

the corresponding intersection point, i.e., $p' = e^{AT}p$. *This defines two functions: $x_{11} \to y_{11}$ and $x_{11} \to T$. Then for all $x_{11} \in (x_{o1}, x_{m1})$,*

$$y_{11} \in (y_{m1}, x_{o1}), \quad \frac{\partial T}{\partial x_{11}} > 0, \quad \frac{\partial T}{\partial y_{11}} < 0,$$

$$\text{for } \lambda_1 + \lambda_2 > 0: \quad \frac{\partial y_{11}}{\partial x_{11}} \in [-\infty, -1), \quad \frac{\partial^2 y_{11}}{\partial x_{11}^2} < 0 \quad \text{and} \quad |y_{11} - x_{o1}| > |x_{11} - x_{o1}|$$

$$\text{for } \lambda_1 + \lambda_2 < 0: \quad \frac{\partial y_{11}}{\partial x_{11}} \in (-1, 0], \quad \frac{\partial^2 y_{11}}{\partial x_{11}^2} > 0 \quad \text{and} \quad |y_{11} - x_{o1}| < |x_{11} - x_{o1}|$$

$$\tag{A.6}$$

$$\text{for } \lambda_1 + \lambda_2 = 0: \quad \frac{\partial y_{11}}{\partial x_{11}} = -1, \quad \frac{\partial^2 y_{11}}{\partial x_{11}^2} = 0 \quad \text{and} \quad |y_{11} - x_{o1}| = |x_{11} - x_{o1}|.$$

Proof: Since at the intersection p', the trajectory goes downward, it follows that $y_{11} < x_{o1}$. Using the fact that

$$fp = fp' = \frac{1}{k}$$

and

$$p' = e^{AT}p,$$

We have,

$$\begin{bmatrix} 0 & k \end{bmatrix} p' = \begin{bmatrix} 0 & k \end{bmatrix} e^{AT} \begin{bmatrix} x_{11} \\ \frac{1}{k} \end{bmatrix} = 1 \tag{A.7}$$

$$\begin{bmatrix} 0 & k \end{bmatrix} p = \begin{bmatrix} 0 & k \end{bmatrix} e^{-AT} \begin{bmatrix} y_{11} \\ \frac{1}{k} \end{bmatrix} = 1 \tag{A.8}$$

From (A.7) and (A.8), we can also express x_{11} and y_{11} as functions of T. In other words, x_{11} and y_{11} are related to each other through the parameter T.

Let

$$V = \begin{bmatrix} -\lambda_2 & -\lambda_1 \\ 1 & 1 \end{bmatrix}$$

then,

$$e^{AT} = V \begin{bmatrix} e^{\lambda_1 T} & 0 \\ 0 & e^{\lambda_2 T} \end{bmatrix} V^{-1}.$$

From (A.7) and (A.8) we have,

$$x_{11}(T) = \frac{1}{k} \frac{\lambda_1 - \lambda_2 + \lambda_2 e^{\lambda_2 T} - \lambda_1 e^{\lambda_1 T}}{e^{\lambda_1 T} - e^{\lambda_2 T}} \tag{A.9}$$

$$y_{11}(T) = \frac{1}{k} \frac{\lambda_1 - \lambda_2 + \lambda_2 e^{-\lambda_2 T} - \lambda_1 e^{-\lambda_1 T}}{e^{-\lambda_1 T} - e^{-\lambda_2 T}} \tag{A.10}$$

Due to the uniqueness of the trajectory, T is also uniquely determined by x_{11}. Therefore, $x_{11} \leftrightarrow T$, $x_{11} \leftrightarrow y_{11}$ and $y_{11} \leftrightarrow T$ are all one to one maps. From the above two equations, we now that $x_{11}(T)$ and $y_{11}(T)$ are analytic on $T \in (0, \infty)$. It can be verified from (A.9) and (A.10) that

$$\lim_{T \to 0} x_{11} = \lim_{T \to 0} y_{11} = -\frac{\lambda_1 + \lambda_2}{k} = -\frac{a_2}{k} = x_{o1}, \quad \lim_{T \to \infty} x_{11} = \frac{-\lambda_1}{k} = x_{m1}, \quad \lim_{T \to \infty} y_{11} = \frac{-\lambda_2}{k} = y_{m1}$$

So the valid domain of x_{11} is $[x_{o1}, x_{m1})$ and of y_{11} is $(y_{m1}, x_{o1}]$. Since $\lambda_1 > 0$, $\lambda_2 < 0$ and $k < 0$ it follows that $y_{m1} < x_{o1} < x_{m1}$.

The derivatives of (A.9) and (A.10) are

$$\frac{\partial x_{11}}{\partial T} = -\frac{\lambda_1 - \lambda_2}{k \left(e^{\lambda_1 T} - e^{\lambda_2 T} \right)^2} \left[\lambda_1 e^{\lambda_1 T} - \lambda_2 e^{\lambda_2 T} - (\lambda_1 - \lambda_2) e^{(\lambda_1 + \lambda_2)T} \right] \tag{A.11}$$

$$\frac{\partial y_{11}}{\partial T} = \frac{\lambda_1 - \lambda_2}{k \left(e^{-\lambda_1 T} - e^{-\lambda_2 T} \right)^2} \left[\lambda_1 e^{-\lambda_1 T} - \lambda_2 e^{-\lambda_2 T} - (\lambda_1 - \lambda_2) e^{-(\lambda_1 + \lambda_2)T} \right]. \tag{A.12}$$

Since the first parts of (A.11) and (A.12) are

$$-\frac{\lambda_1 - \lambda_2}{k\left(e^{\lambda_1 T} - e^{\lambda_2 T}\right)^2} > 0 \qquad \forall\, T > 0$$

$$\frac{\lambda_1 - \lambda_2}{k\left(e^{-\lambda_1 T} - e^{-\lambda_2 T}\right)^2} < 0 \qquad \forall\, T > 0,$$

and since the second parts of (A.11) and (A.12) are

$$h_{x_T}(T) := \lambda_1 e^{\lambda_1 T} - \lambda_2 e^{\lambda_2 T} - (\lambda_1 - \lambda_2)e^{(\lambda_1 + \lambda_2)T} > 0 \qquad \forall\, T > 0 \tag{A.13}$$

$$h_{y_T}(T) := \lambda_1 e^{-\lambda_1 T} - \lambda_2 e^{-\lambda_2 T} - (\lambda_1 - \lambda_2)e^{-(\lambda_1 + \lambda_2)T} > 0 \qquad \forall\, T > 0, \tag{A.14}$$

because of

$$\frac{\partial h_{x_T}}{\partial T} = \lambda_1{}^2 e^{\lambda_1 T} - \lambda_2{}^2 e^{\lambda_2 T} - (\lambda_1 + \lambda_2)(\lambda_1 - \lambda_2)e^{(\lambda_1 + \lambda_2)T} =$$

$$e^{\lambda_2 T}\left[\lambda_1{}^2 e^{\lambda_1 T}\left(e^{-\lambda_2 T} - 1\right) + \lambda_2{}^2\left(e^{\lambda_1 T} - 1\right)\right] > 0 \qquad \forall\, T > 0\,,$$

$$\left.\frac{\partial h_{x_T}}{\partial T}\right|_{T=0} = 0 \qquad \text{and} \qquad h_{x_T}(0) = 0$$

and

$$\frac{\partial h_{y_T}}{\partial T} = -\lambda_1{}^2 e^{-\lambda_1 T} + \lambda_2{}^2 e^{-\lambda_2 T} + (\lambda_1 + \lambda_2)(\lambda_1 - \lambda_2)e^{-(\lambda_1 + \lambda_2)T} =$$

$$e^{-\lambda_2 T}\left[\lambda_1{}^2 e^{-\lambda_1 T}\left(1 - e^{\lambda_2 T}\right) + \lambda_2{}^2\left(1 - e^{-\lambda_1 T}\right)\right] > 0 \qquad \forall\, T > 0\,,$$

$$\left.\frac{\partial h_{y_T}}{\partial T}\right|_{T=0} = 0 \qquad \text{and} \qquad h_{y_T}(0) = 0$$

we can claim that

$$\frac{\partial x_{11}}{\partial T} > 0 \quad \text{and} \quad \frac{\partial y_{11}}{\partial T} < 0 \qquad \forall\, T \in (0, \infty)$$

or

$$\frac{\partial T}{\partial x_{11}} > 0 \quad \text{and} \quad \frac{\partial T}{\partial y_{11}} < 0 \qquad \forall\, T \in (0, \infty).$$

Denote the gradient

$$g(T) := -\frac{\frac{\partial y_{11}}{\partial T}}{\frac{\partial x_{11}}{\partial T}} = -\frac{\partial y_{11}}{\partial x_{11}}, \tag{A.15}$$

then,

$$g(T) = \frac{\lambda_1 - \lambda_2 - \lambda_1 e^{\lambda_2 T} + \lambda_2 e^{\lambda_1 T}}{\lambda_1 - \lambda_2 - \lambda_1 e^{-\lambda_2 T} + \lambda_2 e^{-\lambda_1 T}}. \tag{A.16}$$

Since $\frac{\partial x_{11}}{\partial T} > 0$ and $\frac{\partial y_{11}}{\partial T} < 0$ it follows that

$$g(T) > 0 \quad \forall\, T \in (0, \infty),$$

for $\lambda_1 + \lambda_2 > 0 : \lim_{T \to \infty} g(T) = \infty$

for $\lambda_1 + \lambda_2 < 0 : \lim_{T \to \infty} g(T) = 0$

for $\lambda_1 + \lambda_2 = 0 : \lim_{T \to \infty} g(T) = 1.$

It can be verified that

$$\lim_{T \to 0} g(T) = 1,$$

and

$$\frac{\partial g}{\partial T} = -\frac{\lambda_1 \lambda_2 \left(e^{\lambda_1 T} - e^{\lambda_2 T}\right)}{\left(\lambda_1 - \lambda_2 - \lambda_1 e^{-\lambda_2 T} + \lambda_2 e^{-\lambda_1 T}\right)^2} h(T),$$

where

$$h(T) = (\lambda_1 - \lambda_2)\left(e^{-(\lambda_1 + \lambda_2)T} - 1\right) - (\lambda_1 + \lambda_2)\left(e^{-\lambda_1 T} - e^{-\lambda_2 T}\right).$$

It can be verified that

$$\lim_{T \to 0} h(T) = 0,$$

and

$$\frac{\partial h}{\partial T} = i(T)j(T),$$

where

$$i(T) = \left(-\lambda_2 e^{\lambda_1 T} + \lambda_1 e^{\lambda_2 T} - \lambda_1 + \lambda_2\right)$$
$$j(T) = (\lambda_1 + \lambda_2)e^{-(\lambda_1 + \lambda_2)T}.$$

Since

$$\lim_{T \to 0} i(T) = 0 \quad \text{and} \quad \frac{\partial i}{\partial T} = -\lambda_1 \lambda_2 \left(e^{\lambda_1 T} - e^{\lambda_2 T}\right) > 0 \qquad \forall T > 0$$

we have $i(T) > 0 \; \forall T > 0$ and therefore it follows that

$$\text{sgn}\left(\frac{\partial h(T)}{\partial T}\right) = \text{sgn}(j(T)) \quad \implies \quad \text{sgn}(h(T)) = \text{sgn}(j(T))$$
$$\implies \quad \text{sgn}\left(\frac{\partial g(T)}{\partial T}\right) = \text{sgn}(h(T)) = \text{sgn}(j(T)) \quad \forall T > 0.$$

This shows by inspecting $j(T)$ for all $T > 0$ that

for $\lambda_1 + \lambda_2 > 0 : \quad j(T) > 0 \quad \implies \quad g(T) > 1 \quad \implies \quad \dfrac{\partial y_{11}}{\partial x_{11}} \in [-\infty, -1)$

for $\lambda_1 + \lambda_2 < 0 : \quad j(T) < 0 \quad \implies \quad 0 \leq g(T) < 1 \quad \implies \quad \dfrac{\partial y_{11}}{\partial x_{11}} \in (-1, 0]$ \quad (A.17)

for $\lambda_1 + \lambda_2 = 0 : \quad j(T) = 0 \quad \implies \quad g(T) = 1 \quad \implies \quad \dfrac{\partial y_{11}}{\partial x_{11}} = -1.$

Furthermore, since

$$\frac{\partial g}{\partial T} = \frac{\partial g}{\partial x_{11}} \frac{\partial x_{11}}{\partial T} = -\frac{\partial^2 y_{11}}{\partial x_{11}^2} \frac{\partial x_{11}}{\partial T} \quad \text{and} \quad \frac{\partial x_{11}}{\partial T} > 0,$$

it follows that

$$\text{for } \lambda_1 + \lambda_2 > 0: \quad j(T) > 0 \quad \implies \quad \frac{\partial g}{\partial T} > 0 \quad \implies \quad \frac{\partial^2 y_{11}}{\partial x_{11}^2} < 0$$

$$\text{for } \lambda_1 + \lambda_2 < 0: \quad j(T) < 0 \quad \implies \quad \frac{\partial g}{\partial T} < 0 \quad \implies \quad \frac{\partial^2 y_{11}}{\partial x_{11}^2} > 0$$

$$\text{for } \lambda_1 + \lambda_2 = 0: \quad j(T) = 0 \quad \implies \quad \frac{\partial g}{\partial T} = 0 \quad \implies \quad \frac{\partial^2 y_{11}}{\partial x_{11}^2} = 0.$$

Since we know that $\lim_{T \to 0} g(T) = 1$ and therefore

$$\lim_{T \to 0} \frac{\partial y_{11}}{\partial x_{11}} = -1,$$

and because oft A.17 it follows that

$$\text{for } \lambda_1 + \lambda_2 > 0: \quad |y_{11} - x_{o1}| > |x_{11} - x_{o1}|$$
$$\text{for } \lambda_1 + \lambda_2 < 0: \quad |y_{11} - x_{o1}| < |x_{11} - x_{o1}|$$
$$\text{for } \lambda_1 + \lambda_2 = 0: \quad |y_{11} - x_{o1}| = |x_{11} - x_{o1}|.$$

∎

An illustration for Lemma A.1 for the case where $\lambda_1 + \lambda_2 > 0$ is given in Figure A.2, where p_1, p_2 and p_3 are three points on $kfx = 1$, *i.e.*,

$$p_i = \begin{bmatrix} x_{11}^i \\ \frac{1}{k} \end{bmatrix}, \quad x_{11}^i \in [x_{o1}, x_{m1}), \quad x_{11}^{i+1} > x_{11}^i, \quad i = 1, 2, 3,$$

and p_1', p_2' and p_3' are the first intersections of the trajectories that start from p_1, p_2 and p_3. Then from Lemma A.1 we can conclude that

$$\text{for } \lambda_1 + \lambda_2 > 0: \quad \frac{\|p_3' - p_2'\|}{\|p_3 - p_2\|} > \frac{\|p_2' - p_1'\|}{\|p_2 - p_1\|} > 1$$

$$\text{for } \lambda_1 + \lambda_2 < 0: \quad \frac{\|p_3' - p_2'\|}{\|p_3 - p_2\|} < \frac{\|p_2' - p_1'\|}{\|p_2 - p_1\|} < 1 \qquad \text{(A.18)}$$

$$\text{for } \lambda_1 + \lambda_2 = 0: \quad \frac{\|p_3' - p_2'\|}{\|p_3 - p_2\|} = \frac{\|p_2' - p_1'\|}{\|p_2 - p_1\|} = 1.$$

Remark:
The results of Lemma A.1 are given for the line $kfx = 1$, where $k < 0$. Since the considered system (A.5) is symmetric the results of Lemma A.1 are also valid for $kfx = -1$ with $k < 0$ which can be expressed as $kfx = 1$ with $k > 0$. Therefore, Lemma A.1 is valid for the line $kfx = 1$, where $k \in \mathbb{R} \setminus 0$.

Consider any state transformation $x = T\hat{x}$ resulting in

$$\dot{\hat{x}} = \hat{A}\hat{x} \quad \text{with} \quad \hat{A} = T^{-1}AT$$

$$\text{and} \quad k\hat{f} = kfT.$$
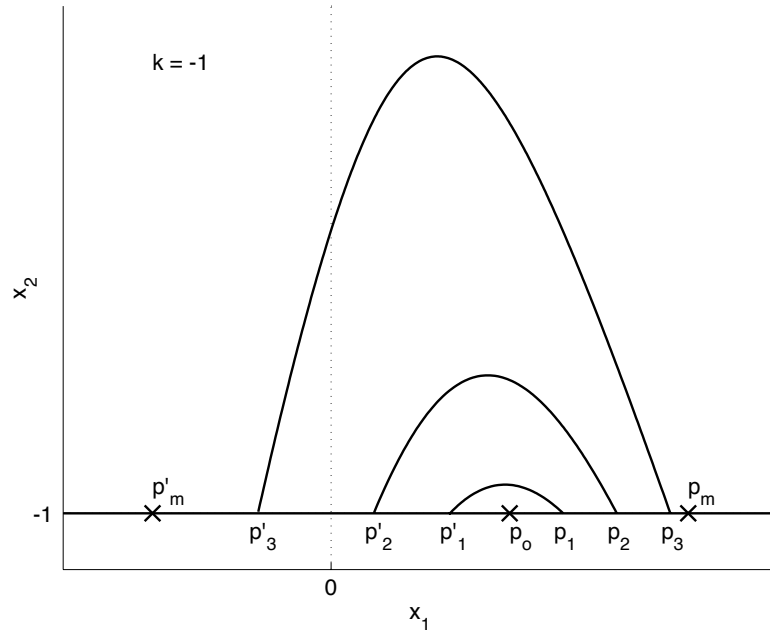
Figure A.2: Illustration of Lemma A.1 for $\lambda_2 < \lambda_1$.

Lemma A.2 *Consider a one pole unstable system $\dot{\hat{x}} = \hat{A}\hat{x}$ and the line $k\hat{f}\hat{x} = 1$, where $k \in \mathbb{R} \setminus 0$ can be arbitrary chosen. Moreover, consider two trajectories $\mathrm{Trj}(\hat{p}_1, \hat{p}_1')$ and $\mathrm{Trj}(\hat{p}_2, \hat{p}_2')$, where the trajectories start at $\hat{p}_1$ and $\hat{p}_2$ on $k\hat{f}\hat{x} = 1$ and end at $\hat{p}_1'$ and $\hat{p}_2'$ on $k\hat{f}\hat{x} = 1$. Then the conditions*

$$
\begin{aligned}
&\text{for } \lambda_1 + \lambda_2 > 0: &&\|\hat{p}_2' - \hat{p}_1'\| > \|\hat{p}_2 - \hat{p}_1\| \\
&\text{for } \lambda_1 + \lambda_2 < 0: &&\|\hat{p}_2' - \hat{p}_1'\| < \|\hat{p}_2 - \hat{p}_1\| \\
&\text{for } \lambda_1 + \lambda_2 = 0: &&\|\hat{p}_2' - \hat{p}_1'\| = \|\hat{p}_2 - \hat{p}_1\|.
\end{aligned}
\tag{A.19}
$$

are verified.

Proof:
We only give the proof for case $\lambda_1 + \lambda_2 > 0$ since the proof is similar for both other cases. The vectors $\hat{p}_1 - \hat{p}_2$ and $\hat{p}_1' - \hat{p}_2'$ are parallel since $\hat{f}(\hat{p}_1 - \hat{p}_2) = 0$ and $\hat{f}(\hat{p}_1' - \hat{p}_2') = 0$. This is due to the fact that $\hat{p}_1$, $\hat{p}_2$, $\hat{p}_1'$ and $\hat{p}_2'$ are elements of the line $k\hat{f}\hat{x} = 1$. Thus, we can express

$$
\hat{p}_1' - \hat{p}_2' = \mu(\hat{p}_1 - \hat{p}_2) \quad \text{with} \quad \mu \in \mathbb{R}.
\tag{A.20}
$$

Consider inequality $\|\mu(\hat{p}_1 - \hat{p}_2)\| > \|\hat{p}_1 - \hat{p}_2\|$ where by state transformation $\hat{p} = Tp$ we obtain

$$
\|\mu(Tp_1 - Tp_2)\| > \|Tp_1 - Tp_2\| \implies |\mu| \|T\| \|p_1 - p_2\| > \|T\| \|p_1 - p_2\| \implies |\mu| \|p_1 - p_2\| > \|p_1 - p_2\|.
\tag{A.21}
$$

Since from the state transformation of (A.20)

$$
Tp_1' - Tp_2' = \mu(Tp_1 - Tp_2) \implies p_1' - p_2' = \mu(p_1 - p_2)
\tag{A.22}
$$

we obtain from (A.21) the inequality

$$
\|p_1' - p_2'\| > \|p_1 - p_2\|
\tag{A.23}
$$

which is a consequence of Lemma A.1 (see equation(A.18)). ■

A.2.2 Stable systems

We consider the autonomous second order stable system

$$\dot{x} = Ax = \begin{bmatrix} 0 & -a_1 \\ 1 & -a_2 \end{bmatrix} x, \qquad a_1, \, a_2 > 0 \tag{A.24}$$

where $a_1 = \lambda_1 \lambda_2$, $a_2 = -(\lambda_1 + \lambda_2)$, $\lambda_1 < 0$ and $\lambda_2 < 0$. We will study the trajectories of (A.24) with respect to two horizontal lines $kfx = 1$ and $kfx = -1$ where

$$f = \begin{bmatrix} 0 & 1 \end{bmatrix}, \quad k > 0.$$

For some points on the line $kfx = 1$, the trajectories of (A.24) starting from these points will enter the region

$$\left\{ x \in \mathbb{R}^2 : |kfx| < 1 \right\}$$

and then intersect the line $kfx = -1$. We will define some functions to relate these points on $kfx = 1$ to the first intersection of the trajectories with $kfx = -1$. The functions will be defined in terms of the point

$$p_0 = \begin{bmatrix} y_{m2} \\ -\frac{1}{k} \end{bmatrix} = \begin{bmatrix} -\frac{a_2}{k} \\ -\frac{1}{k} \end{bmatrix} = \begin{bmatrix} \frac{\lambda_1 + \lambda_2}{k} \\ -\frac{1}{k} \end{bmatrix}$$

on $kfx = -1$. If a point x is on $kfx = -1$ and is to the left of p_0 ($x_1 < y_{m2}$), then the vector $\dot{x}$ points downward $\dot{x}_2 < 0$; if x is to right of p_0 ($x_1 > y_{m2}$), then the vector $\dot{x}$ points upward $\dot{x}_2 > 0$, see Figure A.3.

Definition 10
Let p_0' be the unique point on $kfx = 1$ and $T_d > 0$ be the unique number satisfying

$$e^{AT_d} p_0' = p_0, \quad |kfe^{At}p_0'| \leq 1, \quad \forall\, t \in [0, T_d].$$

Denote the first coordinate of p_0' as x_{m2}, i.e.,

$$p_0' = \begin{bmatrix} x_{m2} \\ \frac{1}{k} \end{bmatrix}.$$

For $x_{11} \in (-\infty, x_{m2}]$, let

$$p' = \begin{bmatrix} x_{11} \\ \frac{1}{k} \end{bmatrix},$$

be a point on $kfx = 1$, then there is a unique

$$p = \begin{bmatrix} y_{11} \\ -\frac{1}{k} \end{bmatrix},$$

on $kfx = -1$, where $y_{11} \in (-\infty, y_{m2}]$ and a unique $T \in (0, T_d]$ such that

$$p = e^{AT_d} p', \quad |kfe^{At}p'| \leq 1, \quad \forall\, t \in [0, T]. \tag{A.25}$$

This defines two functions $x_{11} \to y_{11}$ and $x_{11} \to T$ with $x_{11} \in (-\infty, x_{m2}]$, $y_{11} \in (-\infty, y_{m2}]$ and $T \in (0, T_d]$.

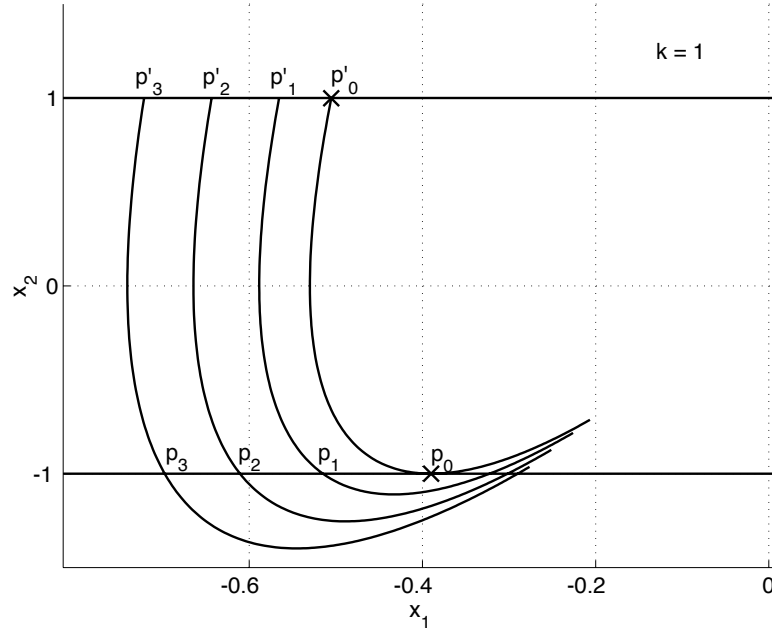Figure A.3: Illustration of Lemma A.3.

Lemma A.3 *For all $x_{11} \in (-\infty, x_{m2})$, we have $x_{11} < y_{11}$ and*

$$\frac{\partial y_{11}}{\partial x_{11}} > 1, \quad \frac{\partial^2 y_{11}}{\partial x_{11}^2} > 0, \quad \frac{\partial T}{\partial x_{11}} > 0.$$

Proof: Similar to the proof of Lemma A.1, from (A.25), we can express x_{11} and y_{11} as function of T, $x_{11}(T)$ and $y_{11}(T)$. Clearly these functions are analytic. Denote

$$g(T) := \frac{\frac{\partial y_{11}}{\partial T}}{\frac{\partial x_{11}}{\partial T}} = \frac{\partial y_{11}}{\partial x_{11}}.$$

It suffice to show that

$$\frac{\partial x_{11}}{\partial T} > 0, \quad g(T) > 1, \quad \frac{\partial g}{\partial T} > 0.$$

We need to break the proof into three different cases.

Case 1. The matrix

$$A = \begin{bmatrix} 0 & -\lambda_1\lambda_2 \\ 1 & \lambda_1 + \lambda_2 \end{bmatrix}$$

has two different real eigenvalues $\lambda_1, \ \lambda_2 < 0$. Assume that $\lambda_1 < \lambda_2$.

Let

$$V = \begin{bmatrix} -\lambda_2 & -\lambda_1 \\ 1 & 1 \end{bmatrix},$$

then,

$$e^{AT} = V \begin{bmatrix} e^{\lambda_1 T} & 0 \\ 0 & e^{\lambda_2 T} \end{bmatrix} V^{-1}.$$

From (A.25) and the fact that $kfp' = 1$, $kfp = -1$, we have, for $T \in (0, T_d)$,

$$x_{11}(T) = \frac{1}{k} \frac{-\lambda_2 + \lambda_1 - \lambda_2 e^{\lambda_2 T} + \lambda_1 e^{\lambda_1 T}}{e^{\lambda_2 T} - e^{\lambda_1 T}} \qquad (A.26)$$

$$y_{11}(T) = \frac{1}{k} \frac{-\lambda_2 + \lambda_1 - \lambda_2 e^{-\lambda_2 T} + \lambda_1 e^{-\lambda_1 T}}{e^{-\lambda_1 T} - e^{-\lambda_2 T}}, \qquad (A.27)$$

and,

$$g(T) = \frac{-\lambda_2 + \lambda_1 - \lambda_2 e^{\lambda_1 T} + \lambda_1 e^{\lambda_2 T}}{-\lambda_2 + \lambda_1 - \lambda_2 e^{-\lambda_1 T} + \lambda_1 e^{-\lambda_2 T}}. \qquad (A.28)$$

By the definition of T_d,

$$y_{11}(T_d) = \frac{\lambda_1 + \lambda_2}{k} = -\frac{a_2}{k} = y_{m2}.$$

It can be shown that as $T \to T_d$, $g(T) \to \infty$. Since $g(0) = 1$ and

$$\frac{\partial g}{\partial T} = \frac{2\lambda_1 \lambda_2}{(\lambda_1 - \lambda_2 + \lambda_1 e^{-\lambda_2 T} - \lambda_2 e^{-\lambda_1 T})^2} \{-(\lambda_1 + \lambda_2)[\text{ch}(\lambda_1 T - \lambda_2 T) - 1]$$
$$+ (\lambda_1 - \lambda_2)[\text{ch}(\lambda_2 T) - \text{ch}(\lambda_1 T)]\} > 0,$$

where

$$\text{ch}(a) = \frac{e^a + e^{-a}}{2} \geq 1$$

is monotonously increasing, we have that

$$g(T) > 1, \quad \forall \, T \in (0, T_d).$$

It can also be verified that

$$\frac{\partial x_{11}}{\partial T} > 0.$$

The remaining proof is similar to the proof of Lemma A.1.

Case 2. The matrix

$$A = \begin{bmatrix} 0 & -\lambda^2 \\ 1 & 2\lambda \end{bmatrix}$$

has two identical real eigenvalues $\lambda < 0$.

Let

$$V = \begin{bmatrix} -\lambda & 1 \\ 1 & 0 \end{bmatrix},$$

then,

$$e^{AT} = V \begin{bmatrix} 1 & T \\ 0 & 1 \end{bmatrix} V^{-1} e^{\lambda T}.$$

In this case , for all $T \in (0, T_d)$, we have,

$$x_{11}(T) = -\frac{1}{kT} \left(1 + \lambda T + e^{-\lambda T} \right),$$

$$y_{11}(T) = -\frac{1}{kT} \left(1 - \lambda T + e^{\lambda T} \right),$$

and

$$g(T) = \frac{1 - \lambda T e^{\lambda T} + e^{\lambda T}}{1 + \lambda T e^{-\lambda T} + e^{-\lambda T}}. \tag{A.29}$$

Since $g(0) = 1$ and

$$\frac{\partial g}{\partial T} = \frac{\lambda^2 T \left(-2\lambda T + e^{-\lambda T} - e^{\lambda T} \right)}{\left(1 + \lambda T e^{-\lambda T} + e^{-\lambda T} \right)^2} > 0,$$

we have $g(T) > 1$ for all $T \in (0, T_d)$. It can be verified that

$$\frac{\partial x_{11}}{\partial T} > 0.$$

Case 3. The matrix

$$A = \begin{bmatrix} 0 & -(\alpha^2 + \beta^2) \\ 1 & 2\alpha \end{bmatrix}$$

has two complex eigenvalues $\alpha \pm j\beta$, where $\alpha < 0$ and $\beta > 0$.

Let

$$V = \begin{bmatrix} \beta & -\alpha \\ 0 & 1 \end{bmatrix},$$

then,

$$e^{AT} = V \begin{bmatrix} \cos(\beta T) & -\sin(\beta T) \\ \sin(\beta T) & \cos(\beta T) \end{bmatrix} V^{-1} e^{\alpha T}.$$

In this case $T_d < \frac{\pi}{\beta}$,

$$x_{11}(T) = -\frac{1}{k \sin(\beta T)} \left(\beta \cos(\beta T) + \alpha \sin(\beta T) + \beta e^{-\alpha T} \right),$$

$$y_{11}(T) = -\frac{1}{k \sin(\beta T)} \left(\beta \cos(\beta T) - \alpha \sin(\beta T) + \beta e^{\alpha T} \right),$$

and

$$g(T) = \frac{\beta + (\beta \cos(\beta T) - \alpha \sin(\beta T)) e^{\alpha T}}{\beta + (\beta \cos(\beta T) + \alpha \sin(\beta T)) e^{-\alpha T}}, \quad T \in (0, T_d). \tag{A.30}$$

Since $g(0) = 1$ and

$$\frac{\partial g}{\partial T} = \frac{(\alpha^2 + \beta^2) \sin(\beta T)}{(\beta + (\beta \cos(\beta T) + \alpha \sin(\beta T)) e^{-\alpha T})^2} \cdot \left[-2\alpha \sin(\beta T) + \beta (e^{-\alpha T} - e^{\alpha T}) \right] > 0,$$

we have $g(T) > 1$ for all $T \in (0, T_d)$. It can be verified that

$$\frac{\partial x_{11}}{\partial T} > 0.$$

For all the above three cases, since $g(T) > 1$, *i.e.*,

$$\frac{\partial y_{11}}{\partial T} > \frac{\partial x_{11}}{\partial T}, \quad \forall\, T \in (0, T_d)$$

and

$$\lim_{T \to 0} \frac{\partial x_{11}}{\partial y_{11}} = 1$$

We thus have $y_{11} > x_{11}$. ∎

This lemma is illustrated with Figure A.3 where p'_1, p'_2 and p'_3 are three points on $kfx = 1$, and p_1, p_2 and p_3 are the three first intersections of $kfx = -1$ with the three trajectories starting from p'_1, p'_2 and p'_3, respectively. Then from Lemma A.3 we can conclude that,

$$\frac{\|p_1 - p_2\|}{\|p'_1 - p'_2\|} > \frac{\|p_2 - p_3\|}{\|p'_2 - p'_3\|} > 1. \tag{A.31}$$

Remark:
The results of Lemma A.3 are given for the line $kfx = 1$, where $k > 0$. Since the considered system (A.24) is symmetric the results of Lemma A.1 are also valid for $kfx = -1$ with $k > 0$ which can be expressed as $kfx = 1$ with $k < 0$. Therefore, Lemma A.3 is valid for the line $kfx = 1$, where $k \in \mathbb{R} \setminus 0$.

Consider any state transformation $x = T\hat{x}$ resulting in

$$\dot{\hat{x}} = \hat{A}\hat{x} \quad \text{with} \quad \hat{A} = T^{-1}AT$$
$$\text{and} \quad k\hat{f} = kfT.$$

Lemma A.4 *Consider a stable system $\dot{\hat{x}} = \hat{A}\hat{x}$ and the lines $k\hat{f}\hat{x} = 1$ and $k\hat{f}\hat{x} = -1$, where $k \in \mathbb{R} \setminus 0$ can be arbitrary chosen. Moreover, consider two trajectories $\mathrm{Trj}(\hat{p}'_1, \hat{p}_1) \subset \mathcal{L}$ and $\mathrm{Trj}(\hat{p}'_2, \hat{p}_2) \subset \mathcal{L}$, where the trajectories start at $\hat{p}'_1$ and $\hat{p}'_2$ on $k\hat{f}\hat{x} = 1$ and end at $\hat{p}_1$ and $\hat{p}_2$ on $k\hat{f}\hat{x} = -1$. Then the condition*

$$\|\hat{p}_1 - \hat{p}_2\| > \|\hat{p}'_1 - \hat{p}'_2\|$$

is verified.

Proof:
The vectors $\hat{p}_1 - \hat{p}_2$ and $\hat{p}'_1 - \hat{p}'_2$ are parallel since $\hat{f}(\hat{p}_1 - \hat{p}_2) = 0$ and $\hat{f}(\hat{p}'_1 - \hat{p}'_2) = 0$. This is due to the fact that $\hat{p}_1$ and $\hat{p}_2$ are elements of the line $k\hat{f}\hat{x} = -1$ and $\hat{p}'_1$ and $\hat{p}'_2$ are elements of the line $k\hat{f}\hat{x} = 1$. Thus, we can express

$$\hat{p}'_1 - \hat{p}'_2 = \mu(\hat{p}_1 - \hat{p}_2) \quad \text{with} \quad \mu \in \mathbb{R}. \tag{A.32}$$

Consider inequality $\|\hat{p}_1 - \hat{p}_2\| > \|\mu(\hat{p}_1 - \hat{p}_2)\|$ where by state transformation $\hat{p} = Tp$ we obtain

$$\|Tp_1 - Tp_2\| > \|\mu(Tp_1 - Tp_2)\| \implies \|T\|\|p_1 - p_2\| > |\mu|\|T\|\|p_1 - p_2\| \tag{A.33}$$
$$\implies \|p_1 - p_2\| > |\mu|\|p_1 - p_2\|.$$

Since from the state transformation of (A.32)

$$T p_1' - T p_2' = \mu(T p_1 - T p_2) \implies p_1' - p_2' = \mu(p_1 - p_2) \tag{A.34}$$

we obtain from (A.33) the inequality

$$\|p_1 - p_2\| > \|p_1' - p_2'\| \tag{A.35}$$

which is a consequence of Lemma A.3 (see equation(A.31)). ∎

A.3   System connections
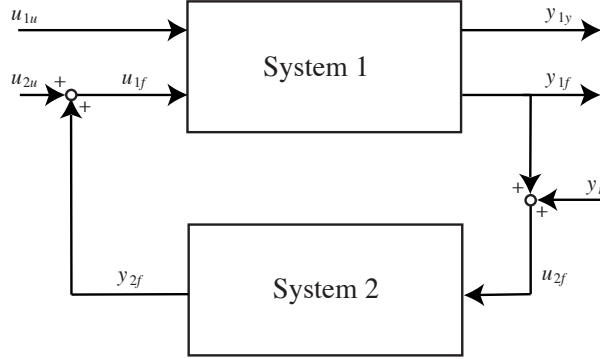
A.3.1   Feedback connection

Figure A.4: Illustration of the feedback connection

Consider two linear state-space systems (System 1 and 2) which constitute a closed-loop system (Figure A.4). We will show how to compute the input-output system of the closed-loop system in function of the two linear system. We pay particular attention to the state variables where we impose that the state vector of the closed-loop system has the structure $\begin{bmatrix} x_1 & x_2 \end{bmatrix}^T$, where x_1 and x_2 denote the state vectors of Systems 1 and 2, respectively. Consider the state-space representation of System 1

$$
\begin{aligned}
\dot{x}_1 &= A_1 x_1 + B_{1f} u_{1f} + B_{1u} u_{1u} \\
y_{1y} &= C_{1y} x_1 + D_{1yf} u_{1f} + D_{1yu} u_{1u} \\
y_{1f} &= C_{1f} x_1 + D_{1ff} u_{1f} + D_{1fu} u_{1u}.
\end{aligned}
\tag{A.36}
$$

The f in the indices denotes the parts of the inputs, outputs and matrices which are used for the feedback and the r denotes input references signals, where u and y denote the parts which are connected to the non-fedbacked inputs and outputs, respectively.

Consider the state-space representation of System 2

$$
\begin{aligned}
\dot{x}_2 &= A_2 x_2 + B_2 u_2 \\
y_2 &= C_2 x_2 + D_2 u_2.
\end{aligned}
\tag{A.37}
$$

To avoid algebraic loops the two conditions

$$
D_{1ff} D_2 = 0 \qquad \text{and} \qquad D_2 D_{1ff} = 0
\tag{A.38}
$$

have to be satisfied.

As a first step we connect the input of System 1 with the output of System 2 and add the second part (u_{2u}) of the input of System 1 $u_{1f} = y_2 + u_{2u}$. By considering the condition (A.38) the system of Equations (A.36) becomes

$$
\begin{aligned}
\dot{x}_1 &= A_1 x_1 + B_{1f}(u_{2u} + D_2 u_2 + C_2 x_2) + B_{1u} u_{1u} \\
y_{1y} &= C_{1y} x_1 + D_{1yf}(u_{2u} + D_2 u_2 + C_2 x_2) + D_{1yu} u_{1u} \\
y_{1f} &= C_{1f} x_1 + D_{1ff}(u_{2u} + C_2 x_2) + D_{1fu} u_{1u}.
\end{aligned}
\tag{A.39}
$$

For the next step we connect the input of System 2 with the output of System 1 $u_2 = y_{1f} + y_r$. By considering the condition (A.38) the system of Equations (A.37) becomes

$$\dot{x}_2 = A_2 x_2 + B_2(C_{1f} x_1 + D_{1ff}(u_{2u} + C_2 x_2) + D_{1fu} u_{1u} + y_r) \tag{A.40}$$
$$y_2 = C_2 x_2 + D_2(C_{1f} x_1 + D_{1fu} u_{1u} + y_r).$$

The last step is to substitute u_2 in the system of Equations (A.39) by $y_{1f} + y_r$, where y_{1f} is given from System (A.39). By still considering the condition (A.38) the system of Equations (A.39) becomes

$$\dot{x}_1 = A_1 x_1 + B_{1f}(u_{2u} + D_2(D_{1fu} u_{1u} + C_{1f} x_1 + y_r) + C_2 x_2) + B_{1u} u_{1u}$$
$$y_{1y} = C_{1y} x_1 + D_{1yf}(u_{2u} + D_2(D_{1fu} u_{1u} + C_{1f} x_1 + y_r) + C_2 x_2) + D_{1yu} u_{1u} \tag{A.41}$$
$$y_{1f} = C_{1f} x_1 + D_{1ff}(u_{2u} + C_2 x_2) + D_{1fu} u_{1u}.$$

This leads to the closed-loop system where we can unite both systems of Equations (A.41) and (A.40)

$$\dot{x} = \begin{bmatrix} A_1 + B_{1f} D_2 C_{1f} & B_{1f} C_2 \\ B_2 C_{1f} & A_2 + B_2 D_{1ff} C_2 \end{bmatrix} x$$
$$+ \begin{bmatrix} B_{1u} + B_{1f} D_2 D_{1fu} & B_{1f} & B_{1f} D_2 \\ B_2 D_{1fu} & B_2 D_{1ff} & B_2 \end{bmatrix} u \tag{A.42}$$
$$y = \begin{bmatrix} C_{1y} + D_{1yf} D_2 C_{1f} & D_{1yf} C_2 \\ C_{1f} & D_{1ff} C_2 \end{bmatrix} x$$
$$+ \begin{bmatrix} D_{1yu} + D_{1yf} D_2 D_{1fu} & D_{1yf} & D_{1yf} D_2 \\ D_{1fu} & D_{1ff} & 0 \end{bmatrix} u,$$

where $x = \begin{bmatrix} x_1 & x_2 \end{bmatrix}^T$, $u = \begin{bmatrix} u_{1u} & u_{2u} & y_r \end{bmatrix}^T$ and $y = \begin{bmatrix} y_{1y} & y_{1f} \end{bmatrix}^T$.
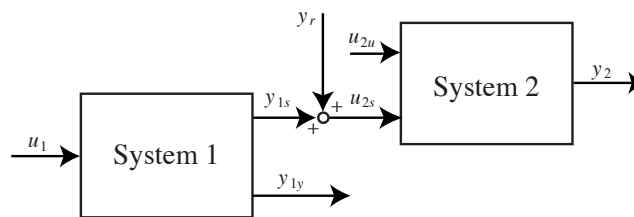
A.3.2 Serial connection

Figure A.5: Illustration of the serial connection

We consider two linear state-space systems which are connected serially (Figure A.5). As in the section above we show how to compute the serial connected input-output system in function of System 1 and System 2. We impose that the state vector of the serial connected system has the structure $\begin{bmatrix} x_1 & x_2 \end{bmatrix}^T$, where x_1 and x_2 denote the state vectors of system 1 and 2, respectively. We denote System 1 as

$$\dot{x}_1 = A_1 x_1 + B_1 u_1 \tag{A.43}$$
$$y_{1s} = C_1 x_1 + D_1 u_1,$$

where only the output y_{1s} connected to the input of System 2 is considered. Similarly, we denote System 2 only by considering its serial connected input u_{2s}

$$\dot{x}_2 = A_2 x_2 + B_2 u_{2s} \tag{A.44}$$
$$y_2 = C_2 x_2 + D_2 u_{2s}.$$

The serially connected system is obtained by substituting u_{2s} by $y_{1s} + y_r$

$$\dot{x} = \begin{bmatrix} A_1 & 0 \\ B_2 C_1 & A_2 \end{bmatrix} x + \begin{bmatrix} B_1 & 0 \\ B_2 D_1 & B_2 \end{bmatrix} u \tag{A.45}$$
$$y = \begin{bmatrix} D_2 C_1 & C_2 \end{bmatrix} x + \begin{bmatrix} D_2 D_1 & D_2 \end{bmatrix} u,$$

where $x = \begin{bmatrix} x_1 & x_2 \end{bmatrix}^T$, $u = \begin{bmatrix} u_1 & y_r \end{bmatrix}^T$ and $y = y_2$.

A.4   Least square solution [44]

Consider the linear problem

$$Bz = c, \tag{A.46}$$

where $z \in \mathbb{R}^n$ and $c \in \mathbb{R}^m$ and with the $m \times n$ matrix B. We want to solve for z.

If $m = n$, and if the inverse of B exist then there is a unique solution, i.e.

$$z = B^{-1}c. \tag{A.47}$$

If $m < n$, then there are infinitely many solutions. We can set arbitrary value, i.e. zero, for $n - m$ elements of z and solve for the others elements with Equation (A.47).

If $m > n$, then we only can find an approximated solution. We can for example seek for the **least square** error of the distance $|Bz - c|$ by finding the minimum of distance square error

$$\min_z \frac{1}{2}(Bz - c)^2. \tag{A.48}$$

We therefore solve for the partial differential of the square error equal to zero,

$$\frac{1}{2}\frac{\partial(Bz - c)^2}{\partial z} = 0.$$

This leads to

$$\frac{1}{2}\frac{\partial}{\partial z}(z^T B^T B z - c^T B z - z^T B^T c + c^T c) = B^T B z - B^T c = 0.$$

If the inverse of $B^T B$ exists then the **least square** solution is given by

$$z = (B^T B)^{-1} B^T c.$$

Note that $(B^T B)^{-1} B^T$ is the pseudo inverse matrix of B referred to as $B^\dagger$ and therefore

$$z = (B^T B)^{-1} B^T c \equiv B^\dagger c. \tag{A.49}$$

Bibliography

[1] R. Albanese, G. Calabrò, M. Mattei, and F. Villone. Plasma response models for current, shape and position control in JET. In *Proc. SOFT 2002, accepted for publication in Fusion Engineering and Design*, Helsinki, Finland, 2002.

[2] R. Albanese and F. Villone. The linearized CREATE-L plasma response model for the control of current, position and shape in tokamaks. *Nuclear Fusion*, 38(5):723–738, 1998.

[3] J. Alvarez, R. Suárez, and J. Alvarez. Planar linear systems with single saturated feedback. *System & Control Letters*, 20:319–326, 1993.

[4] M. Ariola, G. Ambrosino, J.B. Lister, A. Pironti, F. Villone, and P. Vyas. A modern plasma controller tested on the TCV tokamak. *Fusion Technology*, 36(1):126–138, 1999.

[5] M. Ariola, G. Ambrosino, A. Pironti, J.B. Lister, and P. Vyas. Design and experimental testing of a robust multivariable controller on a tokamak. *IEEE Trans. on Control Systems Technol.*, 10(5):646–653, 2002.

[6] M. Ariola, A. Pironti, and A. Portone. Vertical stabilization and plasma shape control in the ITER-FEAT tokamak. In *Proceedings of the 2000 IEEE International Conference on Control Applications*, pages 401–405, Anchorage, Alaska, USA, 2000.

[7] M. Ariola, A. Pironti, and A. Portone. A Reduced-Order Controller for Plasma Position and Shape Control in the ITER-FEAT Tokamak. In *CDC00-REG1452*, 3 May 2000.

[8] C.P. Bean. Magnetization of hard superconductors. *Phys. Rev. Lett.*, 8:250–253, 1962.

[9] E. Bertolini, P.L. Mondino, and P. Noll. The JET magnet power supplies and plasma control systems. *Fusion Technology*, 11(1):71–119, 1987.

[10] D. Bonvin and D.A. Mellichamp. A unified derivation and critical review of modal approaches to model reduction. *International Journal of Control*, 35(5):829–848, 1988.

[11] L. Bottura. A practical fit for the critical surface of NbTi. *IEEE Appl. Supercon.*, 10:2000, 1982.

[12] S.I. Braginskii. Transport Processes in a Plasma. *Reviews of Plasma Physics*, 1:205–311, 1965.

[13] M.S. Branicky. Multiple lyapunov functions and other analysis tools for switched and hybrid systems. *IEEE Transactions on Automatic Control*, 43(4):475–482, 1998.

[14] V.J. Bucek. *Control Systems.* Prentice-Hall, Inc, 1989.

[15] J.B. Burl. *Linear Optimal Control.* Prentice-Hall, Inc, 1998.

[16] A.M. Campbell. A general treatment of losses in multifilamentary superconductors. *Cryogenics*, 22(3), 1982.

[17] A. Coutlis, I. Bandyopadhyay, J.B. Lister, P. Vyas, R. Albanese, D.J.N. Limebeer, F. Villone, and J.P. Wainwright. Measurement of the open loop plasma equilibrium response in TCV. *Nuclear Fusion*, 39(5):663–684, 1999.

[18] J-Y. Favez, B. Srinivasan, Ph. Mullhaupt, and D. Bonvin. Condition for Bifurcation of the Region of Attraction in Linear Planar Systems with Saturated Linear Feedback. In 41th *Conference on Decision and Control*, pages 3918–3923, Las Vegas, USA, 2002.

[19] Y. Gribov. Personal Communications. In *ITER NAKA JWS*, Naka, Japan.

[20] Y. Gribov. Plasma Operation Scenarios. In *ITER NAKA JWS, Issue 3*, Naka, Japan, 24 March 2000.

[21] Y. Gribov. Disturbances for Plasma Control Study in ITER-FEAT. In *ITER NAKA JWS, Issue 1*, Naka, Japan, 6 April 2000.

[22] Y. Gribov. ITER-FEAT CS and PF Coils for PF Control Study. In *ITER NAKA JWS, Issue 2*, Naka, Japan, 7 April 2000.

[23] F. Hofmann, M.J. Dutch, D.J. Ward, M. Anton, I. Furno, J.B. Lister, and J.-M. Moret. Vertical instability in TCV: comparison of experimental and theoretical growth rates. *Nuclear Fusion*, 37(5):681–688, 1997.

[24] F. Hofmann, A. Favre, P.-F. Isoz, Y. Martin, J.-M. Moret, and C. Nieswand. Vertical position control in TCV: Comparison of model predictions with experimental results. *Nuclear Fusion*, 40(4):767–775, 2000.

[25] F. Hofmann, J.-M. Moret, and D.J. Ward. Stability analysis of the vertical position control loop in TCV using rigid and deformable plasma models. *Nuclear Fusion*, 38(12):1767–1778, 1998.

[26] F. Hofmann and G. Tonetti. Tokamak equilibrium reconstruction using Faraday rotation measurements. *Nuclear Fusion*, 28(10):1871–1878, 1988.

[27] T. Hu and Z. Lin. *Control Systems with Actuator Saturation: Analyses and Design.* Birkhauser, Boston, 2000.

[28] T. Hu, Z. Lin, and L. Qiu. Stabilization of Exponentially Unstable Linear Systems with Saturating Actuators. *IEEE Transactions on Automatic Control*, 46(6):973–979, 2001.

[29] D.A. Humphreys, A.G. Kellman, R.R. Khayrutdinov, and V.E. Lukash. Time-dependent simulation of DIII-D plasma evolution and control scenarios. *APS*, 40:1191, 1995.

[30] S.C. Jardin, N. Pomphrey, and J. DeLucia. Dynamic Modelling of Transport and Positional Control in a Tokamak. *Journal of Computational Physics*, 66:418, 1986.

[31] A. Kavin. ITER-FEAT linear models description. In *ITER NAKA JWS, Issue 1*, Naka, Japan, 10 July 2000.

[32] H. K. Khalil. *Nonlinear Systems*. Prentice-Hall, Inc, 1996.

[33] R.R. Khayrutdinov, J.B. Lister, V.E. Lukash, and J.P. Wainwright. Comparing DINA code simulations with TCV experimental plasma equilibrium responses. *Plasma Physics and Controlled Fusion*, 43(3):321–342, 2001.

[34] R.R. Khayrutdinov and V.E. Lukash. Studies of Plasma Equilibrium and Transport in a Tokamak Fusion Device with the Inverse-Variable Technique. *Journal of Computational Physics*, 109(2):193–201, 1993.

[35] E.A. Lazarus, J.B. Lister, and G.H. Neilson. Control of the Vertical Instability in Tokamaks. *Nuclear Fusion*, 30(1):111–141, 1990.

[36] M. Lennholm, D. Campbell, F. Milani, et al. Plasma Vertical Stabilisation at JET using adaptive gain control. In *Proc. 17th Symp. on Fusion Engineering*, pages 539–542, San Diego, USA, 1997.

[37] Z. Lin and A. Saberi. Semi-global exponential stabilization of linear systems subject to input saturation via linear feedback. *System & Control Letters*, 21:225–239, 1993.

[38] J.B. Lister, P. Bruzzone, J-Y. Favez, B. Schärz, L. Bugnion, and E. Zapretilina. Plasma Current, Position and Shape Control, Contract FU05-CT2001-00018 (EFDA/00-551). LRP 741, CRPP, Switzerland, 2002.

[39] J.B. Lister, E.A. Lazarus, A.G. Kellman, J.-M. Moret, J.R. Ferron, F.J. Helton, L.L. Lao, J.A. Leuer, E.J. Strait, T.S. Taylor, and Turnbull A.D. Experimental Study of the Vertical Stability of High Decay Index Plasmas in the DIII-D Tokamak. *Nuclear Fusion*, 30(11):2349–2366, 1990.

[40] J.B. Lister, A. Sharma, D.J.N. Limebeer, Y. Nakamura, J.P. Wainwright, and R. Yoshino. Plasma equilibrium response modelling and validation on JT-60U. *Nuclear Fusion*, 42(6):708–724, 2002.

[41] J.M. Mendels. *Lesson in Digital Estimation Theory*. Prentice-Hall, Inc, 1987.

[42] D.L. Phillips and R.D. Harbor. *Feedback Control Systems*. Prentice-Hall, Inc, 1988.

[43] E.R. Pinch. *Optimal Control and the Calculus of Variations*. Oxford University Press, New York, 1993.

[44] Fletcher R. *Practical Methods of Optimization*. John Wiley & Sons, 1987.

[45] B. Schärz. AC-Loss Minimization in the ITER Tokamak. Diploma Project 40171, Laboratoire d'Automatique, EPFL, Switzerland, 2001.

[46] B. Schärz, P. Bruzzone, J-Y. Favez, J.B. Lister, and E. Zapretilina. The effect of the feedback controller on superconducting tokamak AC losses. LRP 714, CRPP, Switzerland, 2001.

[47] E. Schuster, M.L. Walker, D.A. Humphreys, and M. Krstic. Plasma Vertical Stabilization in Presence of Coil Voltage Saturation in the DIII-D Tokamak. In *American Control Conference ACC 2003*, Denver, Colorado, 2003.

[48] L. Scibile. *Nonlinear control of plasma vertical position in a tokamak*. Thesis, University of Oxford, 1997.

[49] L. Scibile and B. Kouvaritakis. Stability region for a class of open-loop unstable linear systems: theory and application. *Automatica*, 36:37–44, 2000.

[50] J-J. E. Slotine and W. Li. *Applied Nonlinear Control*. Prentice-Hall, Inc, 1991.

[51] H.J. Sussmann, E.D. Sontag, and Y. Yang. A General Result on the Stabilization of Linear Systems Using Bounded Controls. *IEEE Transactions on Automatic Control*, 39(12):2411–2424, 1994.

[52] F. Villone, P. Vyas, J.B. Lister, and R. Albanese. Comparison of the CREATE-L plasma response model with TCV limited discharges. *Nuclear Fusion*, 37(10):1395–1410, 1997.

[53] P. Vyas, F. Villone, J.B. Lister, and R. Albanese. The separatrix response of diverted TCV plasmas compared with the predictions of the CREATE-L model. *Nuclear Fusion*, 38(7):1043–1053, 1998.

[54] J. Wesson. *Tokamaks*. O.U.P., 1987.

[55] M. Wilson. *Superconducting magnets*. Oxford, 1983.

[56] L.E. Zakharov and V.D. Shafranov. Equilibrium of Current-Carrying Plasmas in Toroidal Configurations. *Reviews of Plasma Physics*, 11:153–302, 1986.

[57] E. Zapretilina. Personal Communications. In *ITER NAKA JWS*, Naka, Japan.

[58] K. Zhou, J.C. Doyle, and K. Glover. *Robust and Optimal Control*. Prentice-Hall, Inc, 1996.

Curriculum vitae

Favez Jean-Yves

Chemin de la Forêt 5A
1024 Ecublens
Switzerland

Date of birth: November, 23th 1971
Swiss nationality
Single

021/634 02 85
021/693 34 38

Education

1999-2004 **Ph.D. thesis**
Centre de Recherches en Physique des Plasmas (CRPP) and Laboratoire d'Automatique (LA) at the Swiss Federal Institute of Technology (EPFL)
Ph.D. project: Enhancing the control of tokamaks via a continuous nonlinear control law

1995-1999 **Engineering degree (MS)**
Swiss Federal Institute of Technology (EPFL)
Electrical department: Orientation in electronics and computer science
Master thesis: - Analysis of a PLL for a superregenerative receiver
Semester projects: - Control of a polar pendulum
 - Displacement detection with radio frequency

1992-1995 **Electrical engineering (University of applied sciences)**
School of Engineering and Information Technology, Berne University of Applied Sciences
Diploma work: Digital control system for model railway. Development of a decoder for engines of the firm HAG Modelleisenbahn AG.

1988-1992 **Apprenticeship** in the field of audio-video electronics. Repair and maintenance of audio and video systems. Customer advisory service and after-sales service.

Experience

1997-1998 Development and programming of a micro-controller system for the steering and control of a Stirling engine. A collaboration with the firm Bullag SA, Bulle.

1999-2004 Research and Teaching assistant, Swiss Federal Institute of Technology, Laboratoire d'Automatique (LA) and Centre de Recherches en Physique des Plasmas (CRPP)

Award

2003 Experimental Physics Control Systems Prize of the European Physical Society (EPS - EPCS Prize)
Enhancing tokamak control given power supply voltage saturation
International Conference on Accelerator and Large Experimental Physics Control Systems (ICALEPCS), Gyeongju, Korea.

Publications

Main author:

- **J-Y. Favez**, Ph. Mullhaupt, B. Srinivasan, D. Bonvin, A globally stabilising controller under saturated input for linear planar systems with one unstable pole, American Control Conference ACC 2004, Boston, USA, 2004

- **J-Y. Favez**, Ph. Mullhaupt, B. Srinivasan, J.B. Lister, D. Bonvin, Improving the region of attraction of ITER in the presence of actuator saturation, 42th Conference on Decision and Control, Hawaii, USA, 2003

- **J-Y. Favez**, Ph. Mullhaupt, B. Srinivasan, J.B. Lister, D. Bonvin, Enhancing tokamak control given power supply voltage saturation, International Conference on Accelerator and Large Experimental Physics Control Systems (ICALEPCS), Gyeongju, Korea, 2003

- **J-Y. Favez**, J.B. Lister, Ph. Mullhaupt, B. Srinivasan, F. Villone, Improving tokamak vertical position control in the presence of power supply voltage saturation, 30th EPS Conference on Plasma Physics and Controlled Fusion, St Petersbourg, Russia, July 2003

- **J-Y. Favez**, B. Srinivasan, Ph. Mullhaupt, D. Bonvin, Condition for bifurcation of the region of attraction in linear planar systems with saturated linear feedback, 41th Conference on Decision and Control, pages 3918-3923, Las Vegas, USA, 2002

- **J-Y. Favez**, R.R. Khayrutdinov, J.B. Lister, V.E. Lukash, Comparing TCV experimental VDE responses with DINA code simulations, Plasma Phys. Control. Fusion 44 No 2, pages 171-193, February 2002

- **J-Y. Favez**, R.R. Khayrutdinov, J.B. Lister, V.E. Lukash, Comparing DINA code simulations with TCV experimental VDE responses, 28th EPS Conference on Plasma Physics and Controlled Fusion, Madeira, June 2001

- **J-Y. Favez**, Analyse d'une PLL pour un récepteur super-régénératif, Institut dAutomatique EPFL, February 1999

Co-author:

- V.E. Lukash, D.Raju, V.N. Dokouka, **J-Y. Favez**, R.R. Khayrutdinov, J.B. Lister, DINA simulations of TCV Electron Cyclotron Heating Discharges, 22nd Symposium on Fusion Technology, Helsinki, Finland (9-13 September 2002)

- D. Raju, V.N. Dokouka, **J-Y. Favez**, R.R. Khayrutdinov, J.B. Lister, V.E. Lukash, DINA simulations of TCV Electron Cyclotron Current Drive and Heating, 29th EPS Conference on Plasma Physics and Controlled Fusion, Montreux June 2002

- E. Ronco, B. Srinivasan, **J-Y. Favez**, D. Bonvin, Predictive Control with Added Feedback for Fast Nonlinear Systems, European Control Conference ECC 2001, pages 3167-3172, Porto, Portugal, September 2001

- B. Schärz, P Bruzzone, **J-Y. Favez**, J B Lister, E Zapretilina, The Effect of the Feedback Controller on Superconducting Tokamak AC Losses, submitted to Fusion Engineering and Design

- B. Schärz, L. Bugnion, **J-Y. Favez**, J.B. Lister, Sensitivity of the ITER Tokamak closed loop control system to variations in the assumed model, ITER Report, June 2002

- B. Schärz, J.B. Lister, **J-Y. Favez**, ITER Divertor Sweep AC Loss Estimation, ITER Report, June 2002